Transparent Boundary Conditions for Maxwell's Equations: Numerical Concepts beyond the PML Method

Lin Zschiedrich

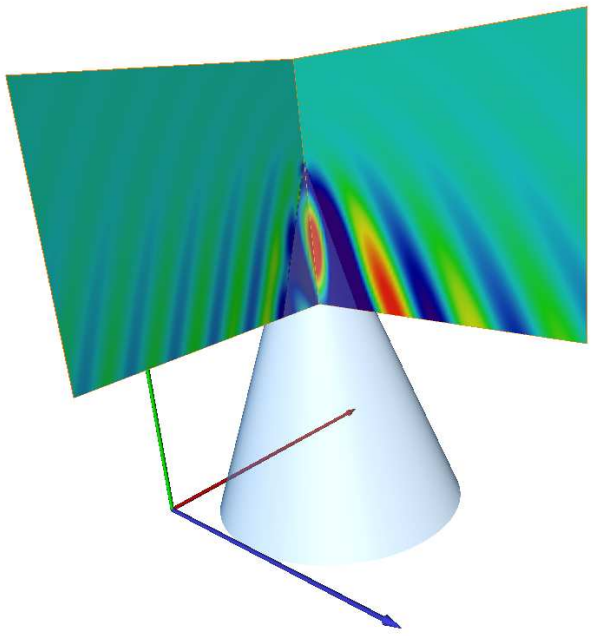

Dissertation

Fachbereich Mathematik und Informatik
Freie Universität Berlin
Februar 2009

Acknowledgment

It is a pleasure to thank all those who helped this thesis to come into existence.

Firstly, I cannot be grateful enough to Peter Deuflhard for his continuous and patient support over so many years. He gave me the freedom to try things for myself but he also pushed me at the right moment to finalize this thesis.

I thank Frank Schmidt for teaching me optics, for the countless discussions on numerics and for proofreading the manuscript.

I wish to acknowledge my gratitude to Sven Burger for the stimulating discussions on real world applications.

Thanks to Benjamin Kettner for giving answers to my numerous questions on the English language. I also thank Daniel Lockau who read the manuscript with great care, and made a lot of suggestions for corrections.

Finally, I thank my family; my parents, Dorit, Tilman, Enno and Jann. It is always a hard burden for them, when the weekend starts at Friday evening with fixing a bug in the code “quickly”.

Supervisor:	Prof. Dr. Dr. h. c. Peter Deuflhard, Fachbereich für Informatik und Mathematik, FU Berlin
Second referee:	Prof. Dr. Ralf Hiptmair, Seminar für Angewandte Mathematik, ETH Zürich
Date of disputation:	October 27, 2009

Contents

Introduction

Optical technologies are ubiquitously used in hi-tech devices. Prominent examples are lasers, glass fibers, optical waveguides in general, optical sensors, solar cells, and measurement systems for various kinds of applications including huge optical metrology systems and consumer products like Blu-ray players. Optics also plays an important role in the production of semiconductor chips. Here, optical projection systems are used to print the circuit pattern onto the wafers. As a common feature of such devices one finds structures with dimensions in the order of the wavelength of the used light. To design and produce such devices the wave nature of light must be taken into account. Accordingly, robust simulation tools are required which are based rigorously on Maxwell's equations, the governing equations of light propagation within macroscopic media. This thesis contributes to the modeling and the numerical computation of light scattering problems.

A light scattering problem is schematically depicted in Figure 1. An incident field $\mathbf{E}_{\text{inc}}$ depending harmonically on time enters the region of interest from above and excites an outgoing field $\mathbf{E}_{\text{out}}$. One could also denote the outgoing field as "scattered field" but this term is reserved for later purposes in a more strict mathematical description of the scattering problem. In Figure 1 the scatterer is embedded into a layered medium. This is a typical situation for optical devices mounted on a glass substrate coated with layers of different materials.

The exterior domain may also contain prolonged structures such as optical waveguides which are best modeled as infinitely extended. In this case so called waveguide modes are often used as incoming source fields. Waveguide modes are strongly confined in the waveguide and are used to transfer the light into the optical device.

For a non–localized illumination, such as a plane wave incident from an arbitrary direction, we must consider the light scattering off the semi-infinite structures in the exterior domain. This will requires a non-trivial extension of the scattering problem formulation which is derived in this thesis. Additionally, we will explain how to evaluate the outgoing wave in the upper

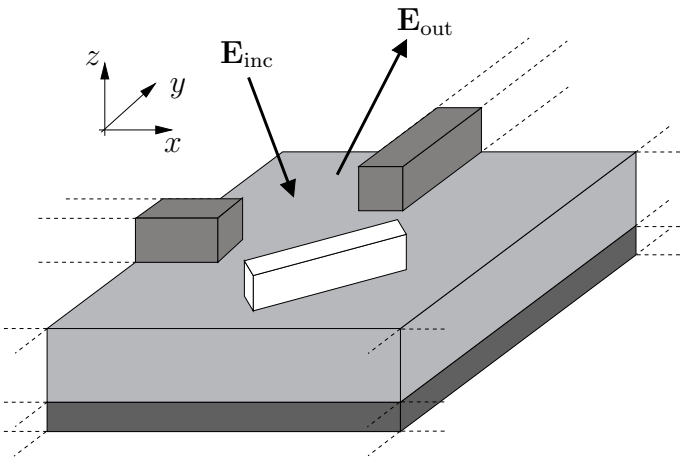

Figure 1: Sketch of a typical simulation setting for a scattering problem. An incident field $\mathbf{E}_{\text{inc}}$ enters the computational domain and excites an outgoing field $\mathbf{E}_{\text{out}}$. The computational domain encloses the scatterer (white). The surrounding medium is typically layered but may contain prolonged structures such as optical waveguides.

half space outside the computational domain. This will provide the far field pattern, i.e. the angular spectrum representation, of the outgoing wave in the upper half space. This is of major importance because the far field is typically the quantity of interest for the abovementioned applications.

To numerically solve a scattering problem one encloses the scatterer in a bounded domain which serves as the computational domain, see Figure 1. *Transparent boundary conditions* are needed on the interface between the computational domain and its surroundings. These transparent boundary conditions must guarantee that the computed light field within the computational domain is identical to the original solution of the scattering problem as posed on the entire space.

Different concepts for the numerical realization of transparent boundary conditions exist. Among them we distinguish between five fundamental approaches [1]:

- Green's tensor methods,
- infinite elements,
- mode matching method,

[1] Approximate transparent boundary conditions are not considered in this thesis, see for example Bayliss, Gunzburger and Turkel [11], Engquist and Majda [45], and Antoine, Darbas et al. [5].

– perfectly matched layers (PML),
– pole condition method.

Green's tensor methods rely on fundamental solutions to Maxwell's equations in the exterior domain which need to be numerically available. Examples are the classical boundary integral methods as treated in Colton and Kress [32], and Nédélec [84]. Green's tensor techniques for stratified media were chiefly developed by Martin et al. [73, 88, 89]. However, geometries as shown in Figure 1 cannot be treated due to the lack of a numerically feasible Green's tensor.

The theoretical foundation for the infinite element method can be traced back to Leis [70]. The starting point is a variational formulation of the scattering problem within a Hilbert space equipped with a weighted Sobolev norm so that an outward radiating field has a finite norm. Demkowicz et al. proposed a numerical discretization of this variational problem which is similar to the finite element method [36, 21, 35]. The idea of the infinite element method is to decompose the exterior domain into non-overlapping *infinite* patches. Analog to the finite element method, an ansatz function is attached to a certain sub-patch of an infinite patch and has support only in those infinite patches which share this sub-patch. These ansatz functions must span a finite dimensional sub-space of the underlying weighted Sobolev space. The major drawback of the infinite element method is that the construction of *conformal* ansatz functions contained in the weighted Sobolev space requires special knowledge on the asymptotic behavior of the outgoing waves. This restricts the applicability of the infinite element method to problems with a homogeneous exterior domain.

In the mode matching method the field in the exterior domain is represented by a series expansion into ansatz functions which satisfy Maxwell's equations on infinite sub-domains of the exterior domain. Typically, the ansatz functions are constructed by solving various kinds of eigenvalue problems stemming from the time–harmonic Maxwell's equations. The corresponding eigensolutions are called *eigenmodes* in the engineering science. Matching conditions of the mode expansions within two adjacent sub-domains are imposed to enforce the field continuity across their common interface. Accordingly, one matches the field data on the boundary of the computational domain. For example, when the computational domain is a ball and the exterior domain is homogeneous, a solution to time–harmonic Maxwell's equations can be expanded into a series of products of spherical harmonics and spherical Bessel functions, see Monk [79, Chap. 10]. In this simple case, the matching conditions on the sphere can be realized by means of a *Dirichlet-to-Neumann*-operator, see Grote and Keller [48]. More complicated

geometries as shown in Figure 1 can also be treated with the mode matching method, see Chew [27, Chap. 6] and Hammer [71, 50]. The major criticism of the mode matching method is that a discretization yields a dense matrix block of a dimension equal to the number of used modes. This is only tolerable as long as the number of required modes for an accurate approximation remains small. Unfortunately, this is not the case for a geometry as given in Figure 1 with a plane wave illumination because one has to deal with a continuum of modes, cf. Chew [27, Section 6.3.2].

The pole condition method proposed by Schmidt [98] as well as Bérenger's perfectly matched layer method (PML) will play a central role throughout this thesis. We will introduce both concepts in greater detail. However, our numerical considerations will focus on the PML method and beyond. Besides the development of an adaptive PML method, we will extend the PML method to cope with complicated scattering problems such as given in Figure 1. Moreover, we will explain how to utilize the PML solution for a field evaluation in the exterior domain. A rough sketch of the involved ideas is given in the outline section below.

In this thesis, the pole condition approach is primarily used for the mathematical description of scattering problems. For numerical aspects on the pole condition method we refer to Schmidt et al. [98, 100], Ruprecht et al. [96], Antoine et al. [4], and Hohage and Nannen [55, 83]. We remark that the pole condition method can be regarded as a generalization of the infinite element method, which remedies the restriction to homogeneous exterior domains.

Outline

In Chapter 1 we will review the required physical background of Maxwell's equations and construct some special solutions. Furthermore, we will introduce the *exterior calculus* which allows for a compact and elegant notation of Maxwell's equations.

After this preparatory work we will regard the mathematical formulation of *time harmonic* scattering problems in Chapter 2. To do so, we will introduce the pole condition concept. We further discuss so called *Calderon maps* which realize the transparent boundary conditions by operators defined on the Sobolev trace spaces of the computational domain's boundary.

The Chapters 3–5 are the core of this thesis and address the following aspects: the construction and implementation of an adaptive PML method, an exterior domain evaluation formula and a novel scattering problem formulation for more complicated exterior domains. We give a more detailed overview to these topics here:

Adaptive PML Bérenger introduced the perfectly matched layer method (PML) in 1994 [15] to realize transparent boundary conditions. In a nutshell, the electromagnetic field in the exterior domain is turned into an exponentially damped function by using a complex continuation. This way a truncation of the "complex stretched" exterior domain (called sponge layer) is justified, see Chew and Weedon [28]. Numerous papers have been published on this topic discussing the mathematical justification of the PML method or proving the convergence of the numerical method, see for example the papers by Lassas and Somersalo [68, 67] which provide a convergence proof for a homogeneous exterior domain. Together with Hohage and Schmidt the author generalized the convergence proof to a certain class of inhomogeneous exterior domains [57]. Furthermore, numerical experiments demonstrated an exponentially fast convergence of the PML method for more general exterior domains like layered media with waveguide inhomogeneities [118, 117].

However, a standard implementation of the PML method fails for periodic grating problems[2] in the presence of so called anomalous modes [120, 117]. For the discussion of periodic gratings see also Elschner et al. [43, 42, 44]. An anomalous mode (also called Rayleigh frequency) corresponds to a wave which travels in the direction of the periodic lattice and which is constant in the outward direction. Due to this constantness a complex continuation has no effect and the exponential convergence of the PML method is broken. This misfeature of the PML method is not restricted to periodic grating problems. We will see that with a standard PML implementation one encounters the same problems for scattering off devices with multiply structured exterior domains as given in Figure 1.

This led the author to the development of the adaptive PML, where the sponge layer thickness is automatically adapted by an *a posteriori* error criterion [120, 117]. Since the PML method acts as a high-frequency filter in the outward radiating direction, it is possible to exponentially increase the mesh width of the finite element discretization in the outward direction. In the presence or in the vicinity of anomalous modes, a PML sponge layer thickness of thousands of wavelengths is needed to achieve relevant accuracies. This thesis summarizes earlier results from 2005 on the adaptive PML method, gives greater details on implementation issues and further validates

[2]The term *periodic grating problem* is used to describe a periodic arrangement of scatterers in one or two space directions. The PML method is only applied in space directions which are perpendicular to the lattice vectors of the periodic arrangement. We do not aim at the construction of transparent boundary conditions at the interface of the computational domain to a semi–infinite periodic exterior domain. This challenging topic is discussed for example in Wilcox et al. [111], Joly et al. [64], Ehrhard et al. [41, 40], Oskooi et al. [87] and Soussi [103].

the method for critical test problems.

We mention that Chen also proposed an adaptive PML method in 2003 [26] with a detailed convergence analysis, see also the subsequent papers by Chen et al. [10, 25]. However, Chen excluded anomalous modes in his analysis. The algorithm Chen proposed uses an adaptive finite element discretization within the PML sponge layer after fixing the sponge layer thickness. A similar approach based on a *hp*–refinement strategy is studied in Michler, Demkowicz et al. [78]. Our approach is complementary to that, since we mainly aim at an automatic adaption of the PML thickness for varying physical input parameters.

Evaluation formula for PML solution Having a Green's tensor at hand, the outgoing field is easily evaluated at any position of the exterior domain. Numerically efficient exterior domain evaluation methods are known for homogeneous exterior domains so far, see for example Monk et al. [82, 80], and Grote and Kirsch [49]. This is not the case for geometries as given in Figure 1. Even an asymptotic formula of the Green's tensor for a far field approximation is not available. To overcome this, the Rayleigh-Sommerfeld diffraction formula, see Singer et al. [102], is commonly used for the evaluation of the scattered electromagnetic field in a homogeneous half space above the computational domain. However, standard numerical methods lack the precise computation of the arising high–frequency integral with infinite integration domain. Together with Schmidt the author presented a numerical method for the computation of the Rayleigh-Sommerfeld integral based on the computed near field data within the computational domain including the perfectly matched layer domain [123]. After deriving the exterior domain evaluation formula we will comment on the numerical computation of the angular spectrum representation of the far field in the upper half space.

Multiply structured exterior domains The incoming light field in Figure 1 is not only scattered at the structures enclosed in the computational domain, but the light is also scattered by the infinite lines in the exterior domain. The scattering problem formulation given in [98, 121] applies only for incoming fields which approximately vanish on the infinite structures outside the computational domain. This is a realistic assumption only when the incident field is a confined waveguide mode or a beam focused on the computational domain. Therefore, dealing with incident plane waves necessitates a non-trivial extension of the scattering problem, recently proposed by the author in [124]. The geometry in Figure 1 is a combination of two infinite lines and a layered medium. In the proposed approach we split the exterior

domain into these three parts and formulate appropriate matching conditions at the interfaces within the PML sponge layer. The theory presented in this thesis generalizes classical results by Wiener and Hopf for ideal geometries like a thin half-screen, see for example Titchmarsh [107], Born and Wolf [18], Noble [85], Clemmow [29] and Meister [77].

It may also be worth mentioning that the scattering problem setting with *multiply structured exterior domains* (Figure 1) is similar to the *rough surface* scattering problem. In a rough surface problem one investigates the scattering off a single infinite surface with a fixed boundary condition. We refer to the detailed discussion on rough surface problems in Chandler–Wilde et al. [23], Meier et al. [76], Arens et al. [6]. Chandler–Wilde et al. also address the case of rough layered media above an unbounded surface, see [24]. A numerical method to solve this type of problems is also proposed by Déchamps, Bourlier et al. [33, 34, 19].

Besides the near field computation, we will tackle the far field extraction above a structure with a multiply structured exterior domain.

Chapter 1

Maxwell's equations

James Clerk Maxwell established the governing equations of light propagation in 1873, see [75]. We give a short summary of Maxwell's electromagnetic field theory as can be found in classical textbooks on electrodynamics, see for example Jackson [60] or the introductory chapters in Jin [63] and Chew [27].

1.1 Maxwell's equations

The electromagnetic field is a pair of an electric field $\mathbf{E}(\mathbf{r},t)$ and a magnetic field $\mathbf{H}(\mathbf{r},t)$, where $\mathbf{r}=(x,y,z)$ is the position in space and t is the time. We further introduce the electric flux density $\mathbf{D}(\mathbf{r},t)$, the magnetic flux density $\mathbf{B}(\mathbf{r},t)$, the electric current density $\mathbf{J}(\mathbf{r},t)$ and the scalar charge density $\rho(\mathbf{r},t)$. Maxwell's equations are

$$\begin{aligned}
\nabla\times\mathbf{E}(\mathbf{r},t) &= -\partial_t\mathbf{B}(\mathbf{r},t), && \text{(1.1a)}\\
\nabla\times\mathbf{H}(\mathbf{r},t) &= \partial_t\mathbf{D}(\mathbf{r},t)+\mathbf{J}(\mathbf{r},t), && \text{(1.1b)}\\
\nabla\cdot\mathbf{B}(\mathbf{r},t) &= 0, && \text{(1.1c)}\\
\nabla\cdot\mathbf{D}(\mathbf{r},t) &= \rho(\mathbf{r},t). && \text{(1.1d)}
\end{aligned}$$

This system of equations is not independent. To allow for a unique solution to a given distribution of currents and charges Maxwell's equations are supplemented by so called material equations also known as constitutive relations. For general time-dependent Maxwell's equations the constitutive relations are rather complicated. In this presentation we assume that all bodies are at rest and that the electromagnetic field exhibits a harmonic dependence on time that is

$$\begin{aligned}
\mathbf{E}(\mathbf{r},t) &= \mathrm{Re}\left(\hat{\mathbf{E}}(\mathbf{r},\omega)e^{-i\omega t}\right),\\
\mathbf{H}(\mathbf{r},t) &= \mathrm{Re}\left(\hat{\mathbf{H}}(\mathbf{r},\omega)e^{-i\omega t}\right),
\end{aligned}$$

and accordingly for $\mathbf{D}$, $\mathbf{B}$, $\mathbf{J}$, and ρ. Here, ω is called angular frequency. The quantities with a hat ($\hat{\mathbf{E}}$, *etc.*) are known as phasors. Under this assumptions the constitutive relations take the form

$$\begin{aligned}
\hat{\mathbf{D}}(\mathbf{r},\omega) &= \varepsilon(\mathbf{r},\omega)\,\hat{\mathbf{E}}(\mathbf{r},\omega), && \text{(1.2a)}\\
\hat{\mathbf{B}}(\mathbf{r},\omega) &= \mu(\mathbf{r},\omega)\,\hat{\mathbf{H}}(\mathbf{r},\omega), && \text{(1.2b)}\\
\hat{\mathbf{J}}(\mathbf{r},\omega) &= \sigma(\mathbf{r},\omega)\,\hat{\mathbf{E}}(\mathbf{r},\omega) + \hat{\mathbf{J}}_i(\mathbf{r},\omega), && \text{(1.2c)}
\end{aligned}$$

with the tensors ε, μ, and σ called permittivity, permeability and conductivity, respectively. $\hat{\mathbf{J}}_i(\mathbf{r},\omega)$ is the impressed current density. For simplicity we will henceforth drop the hats. Introducing the complex permittivity tensor $\varepsilon_c = \varepsilon + i\sigma/\omega$ the time-harmonic Maxwell's equations read as

$$\begin{aligned}
\nabla\times\mathbf{E}(\mathbf{r}) &= i\omega\mu(\mathbf{r})\mathbf{H}(\mathbf{r}), && \text{(1.3a)}\\
\nabla\times\mathbf{H}(\mathbf{r}) &= -i\omega\varepsilon_c(\mathbf{r})\mathbf{E}(\mathbf{r}) + \mathbf{J}_i(\mathbf{r}), && \text{(1.3b)}\\
\nabla\cdot\mu\mathbf{H}(\mathbf{r}) &= 0, && \text{(1.3c)}\\
\nabla\cdot\varepsilon_c\mathbf{E}(\mathbf{r}) &= -\frac{i}{\omega}\nabla\cdot\mathbf{J}_i(\mathbf{r}). && \text{(1.3d)}
\end{aligned}$$

As usual, ε will henceforth denote the complex permittivity tensor ε_c. To derive the last equation (1.3d) we used the equation of continuity $\nabla\cdot\mathbf{J} = i\omega\rho$, which assures the conservation of charge. To transfer the above first order system of equations (1.3) into second order equations for $\mathbf{E}$ and $\mathbf{H}$ separately, we insert equation (1.3a) and equation (1.3b) into each other. For the electric field strength this yields

$$\nabla\times\mu^{-1}\nabla\times\mathbf{E}(\mathbf{r}) - \omega^2\varepsilon\mathbf{E}(\mathbf{r}) = i\omega\mathbf{J}_i(\mathbf{r}), \qquad \text{(1.4)}$$

which is the basic equation we deal with throughout this thesis. The divergence condition for the electric field equation (1.3d) directly follows from equation (1.4) when applying the divergence operator on both sides of equation (1.4).

1.2 Special solutions

We collect some special solutions to time-harmonic Maxwell's equations (1.3) as needed for later purposes. In this subsection we assume transparent materials, so that μ and ε are positive scalars. The material of the section is chiefly taken from Chew [27].

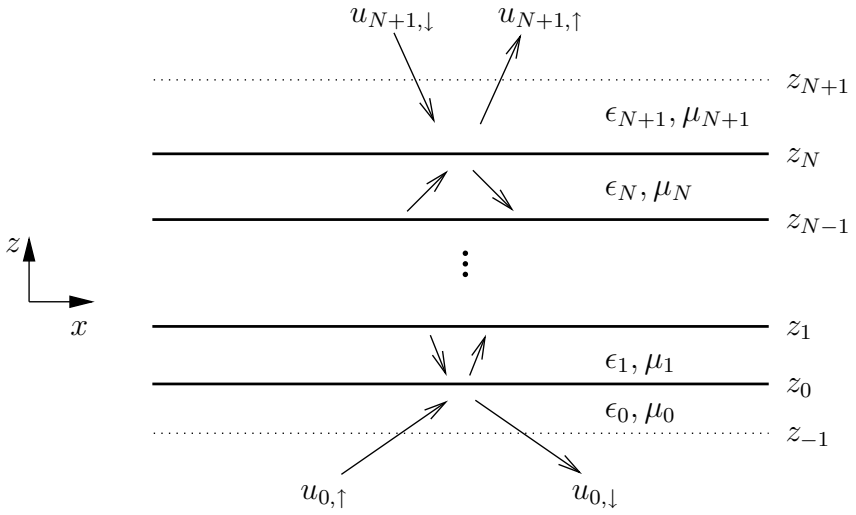

Figure 1.1: Layered media configuration. The dotted lines are introduced for theoretical purposes only.

1.2.1 Plane waves in layered media

In a homogeneous medium with constant μ and ε and without impressed sources, the plane wave

$$\mathbf{E}(\mathbf{r}) \;=\; \widehat{\mathbf{E}} e^{i\mathbf{k}\cdot\mathbf{r}}$$

is a solution to time harmonic Maxwell's equations provided that $\mathbf{k}\cdot\widehat{\mathbf{E}} = 0$, $\mathbf{k} \in \mathbb{C}^3$ and $k_x^2 + k_y^2 + k_z^2 = \omega\sqrt{\mu\varepsilon}$.

We say that a plane wave *propagates* in a direction $\hat{\mathbf{r}}$ if $\mathrm{Re}(\mathbf{k}\cdot\hat{\mathbf{r}}) > 0$. For the case $\mathrm{Im}(\mathbf{k}\cdot\hat{\mathbf{r}}) > 0$ the plane wave is *evanescent* in the direction $\hat{\mathbf{r}}$.

The situation of a layered (or stratified) medium is more complicated. A layered medium is a stack of N parallel plates with different thicknesses and constant materials in each layer. Figure 1.1 shows such a configuration and fixes the notation. The 0th layer is the infinite half space below the stack. The $(N+1)$th layer is the infinite half space above the stack. Layered media configurations are considered in many textbooks on electrodynamics, see for example Chew [27].

We want to construct special solutions in layered media which generalize the plane waves solutions in homogeneous media. We choose a Cartesian coordinate system (x, y, z) so that the normal direction $\mathbf{n}$ of the stack is equal to the z–direction.

Using the ansatz $\mathbf{E}(x,y,z) = \widehat{\mathbf{E}}(z)e^{ik_x x + ik_y y}$ we have

$$\begin{pmatrix} ik_x \\ ik_y \\ \partial_z \end{pmatrix} \times \mu^{-1} \begin{pmatrix} ik_x \\ ik_y \\ \partial_z \end{pmatrix} \times \widehat{\mathbf{E}}(z) - \omega^2 \varepsilon \widehat{\mathbf{E}}(z) \;=\; 0.$$

Hence, Maxwell's equations reduce to an system of ordinary differential equations for fixed $k_x, k_y \in \mathbf{R}$.

In the following we only consider $k_y = 0$ since the case $k_y \neq 0$ follows from a rotation of the coordinate system around the normal axis $\mathbf{n}$. Now, the above ODE system decouples into two *polarizations* namely a single equation for $\widehat{E}_y$,

$$-\partial_z \mu^{-1} \partial_z \widehat{E}_y - (\omega^2 \varepsilon - \mu^{-1} k_x^2)\widehat{E}_y \;=\; 0, \quad \text{(TE)} \tag{1.5}$$

and a system of equations for $(\widehat{E}_x, \widehat{E}_z)$, which we do not derive here. Since $(\widehat{E}_x, \widehat{E}_z) = i/\varepsilon\omega\,(-\partial_z \widehat{H}_y, ik_x \widehat{H}_y)$ we alternatively solve for $\widehat{H}_y$ to determine $(\widehat{E}_x, \widehat{E}_z)$,

$$-\partial_z \varepsilon^{-1} \partial_z \widehat{H}_y - (\omega^2 \mu - \varepsilon^{-1} k_x^2)\widehat{H}_y \;=\; 0. \quad \text{(TM)} \tag{1.6}$$

In the TE (*transversal electric*) case the electric field vector is transverse to the normal direction and lies in the xy–plane (even after a rotation due to $k_y \neq 0$). The term TM (*transversal magnetic*) is motivated accordingly. We deal only with the TE case and denote $u = \widehat{E}_y$.

In each layer, a general solution of the TE–equation (1.5) is given by

$$u_j(z) \;=\; u_{j,\uparrow} e^{ik_{j,z}(z - z_{j-1})} + u_{j,\downarrow} e^{-ik_{j,z}(z - z_j)}, \tag{1.7}$$

with

$$k_{j,z}(k_x) = (\omega^2 \varepsilon_j \mu_j - k_x^2)^{1/2}. \tag{1.8}$$

This is a double–valued function with branch points at $k_x = \pm k_j$, where $k_j = \omega\sqrt{\varepsilon_j \mu_j}$ is the local wave number in the jth layer. We fix the definition of the square root in (1.8) by demanding that

$$\begin{aligned} &\mathrm{Re}(k_{j,z}(k_x)) > 0, \text{ for } |k_x| < k_j \\ &\mathrm{Im}(k_{j,z}(k_x)) > 0, \text{ for } |k_x| > k_j. \end{aligned}$$

This way, $u_{j,\uparrow} e^{ik_x x + ik_{j,z} z}$ is an upward traveling plane wave when $|k_x| < k_j$ and is an exponentially decaying field in the upward direction if $|k_x| > k_j$.

The plane wave $u_{j,\downarrow}e^{ik_x x - ik_{j,z}z}$ has the opposite behavior, i.e. it propagates downwards or decays in the downward direction.

The splitting of $u_j(z)$ in equation (1.7) is not valid when $k_{j,z} = 0$. To cover also this case we switch over to another general solution of the field in the jth layer,

$$u_j(z) = v_{j,0}\cos(k_{j,z}(z - z_{j-1})) + v_{j,1}\frac{\sin(k_{j,z}(z - z_{j-1}))}{k_{j,z}h_j},$$

with $h_j = z_j - z_{j-1}$. This definition also covers the case $k_{j,z} = 0$, as we see from

$$\begin{aligned}\lim_{k_{j,z}\to 0}\cos(k_{j,z}(z - z_{j-1})) &= 1,\\ \lim_{k_{j,z}\to 0}\frac{\sin(k_{j,z}(z - z_{j-1}))}{k_{j,z}h_j} &= (z - z_{j-1})/h_j.\end{aligned}$$

We further remark that this form of the general solution is independent of the branch cuts used in the square root definitions (1.8), because $\cos(k_{j,z}z)$ and $\sin(k_{j,z}z)/k_{j,z}h_j$ are even functions in $k_{j,z}$.

The fields within two adjacent layers must be matched across the common interface in order to satisfy the TE-equation (1.5). From Maxwell's equations one derives the constraints

$$\begin{aligned}u_j(z_j) &= u_{j+1}(z_j),\\ \mu_j^{-1}\partial_z u_j(z_j) &= \mu_{j+1}^{-1}\partial_z u_{j+1}(z_j).\end{aligned} \tag{1.9}$$

Essentially, the matching conditions assure the continuity of the magnetic and electric fields' tangential components across a material interface.

To bring the coupling conditions (1.9) into an algebraic notation for the coefficients $v_{j,0}, v_{j,1}$, $j = 0, \ldots, N+1$, we define

$$\mathbf{A}_{j-1,j} = \begin{bmatrix} 1 & 0 \\ 0 & \mu_j^{-1}/h_j \end{bmatrix}$$

and

$$\mathbf{A}_{j,j} = \begin{bmatrix} \cos(k_{j,z}h_j) & \sin(k_{j,z}h_j)/k_{j,z}h_j \\ -\mu_j^{-1}k_{j,z}\sin(k_{j,z}h_j) & \mu_j^{-1}\cos(k_{j,z}h_j)/h_j \end{bmatrix}.$$

Now, the coupling conditions (1.9) are given by

$$\mathbf{A}_{j,j}\mathbf{v}_j = \mathbf{A}_{j,j+1}\mathbf{v}_{j+1}, \tag{1.10}$$

with $\mathbf{v}_j = [v_{j,0}, v_{j,1}]^{\mathrm{T}}$. As a function of k_x, the matrices $\mathbf{A}_{j,j}(k_x)$ and $\mathbf{A}_{j-1,j}(k_x)$ are single–valued, since all coefficients in these matrices are even functions of $k_{j,z}$.

For $2(N+2)$ unknowns $\mathbf{v}_j$, $j = 0, \ldots N+1$, the field matching conditions (1.10) imposes $2(N+1)$ linear constraints. Hence, we have two free parameters.

Typically, these free parameters are used to prescribe the incoming plane waves from below and from above by setting $u_{0,\uparrow}$ and $u_{N+1,\downarrow}$, respectively. For later purposes we allow for a complex value $k_x \in \mathbb{C}$, and we want to clarify which values of k_x permit unique solutions to the TE equation (1.5) for given coefficients $u_{0,\uparrow}$ and $u_{N+1,\downarrow}$:

To prescribe $u_{0,\uparrow}$ and $u_{N+1,\downarrow}$, the field matching constraints (1.10) are supplemented by

$$\begin{aligned} \mathbf{B}_0 \mathbf{v}_0 &= u_{0,\uparrow}, \\ \mathbf{B}_{N+1} \mathbf{v}_{N+1} &= u_{N+1,\downarrow}, \end{aligned}$$

with

$$\begin{aligned} \mathbf{B}_0 &= 0.5 \begin{bmatrix} 1 & -i/k_{0,z}h_0 \end{bmatrix} \quad \text{and} \\ \mathbf{B}_{N+1} &= 0.5 e^{-ik_{N+1}h_{N+1}} \begin{bmatrix} 1 & i/k_{N+1,z}h_{N+1} \end{bmatrix}. \end{aligned}$$

We arrive at the $2(N+2) \times 2(N+2)$ linear system

$$\begin{bmatrix} \mathbf{A}_{0,0} & -\mathbf{A}_{0,1} & & & & \\ & \mathbf{A}_{1,1} & -\mathbf{A}_{1,2} & & & \\ & & \ddots & \ddots & & \\ & & & \mathbf{A}_{N,N} & \mathbf{A}_{N,N+1} & \\ \mathbf{B}_0 & & & & & \\ & & & & \mathbf{B}_{N+1} & \end{bmatrix} \begin{bmatrix} \mathbf{v}_0 \\ \mathbf{v}_1 \\ \vdots \\ \mathbf{v}_N \\ \mathbf{v}_{N+1} \\ \end{bmatrix} = \begin{bmatrix} 0 \\ 0 \\ \vdots \\ 0 \\ u_{0,\uparrow} \\ u_{N+1,\downarrow} \end{bmatrix}. \tag{1.11}$$

We have already seen that the matrices $\mathbf{A}_{j,j}(k_x)$ and $\mathbf{A}_{j-1,j}(k_x)$ are single–valued functions of k_x. But, the coefficients in the row vectors $\mathbf{B}_0(k_x)$ and $\mathbf{B}_{N+1}(k_x)$ are *not* even functions of $k_{0,z}$ and $k_{N+1,z}$, respectively. This has the important consequence, that we must fix the location of the branch cuts in the definition (1.8) of $k_{j,z}$ for the outermost, infinite layers $j = 0$ and $j = N+1$, and that we do not need to bother about branch cuts for $j = 1, \ldots, N$.

For the definition of the branch cuts we only regard the upper half space. The treatment of the lower half space is alike. In the defining equation (1.8)

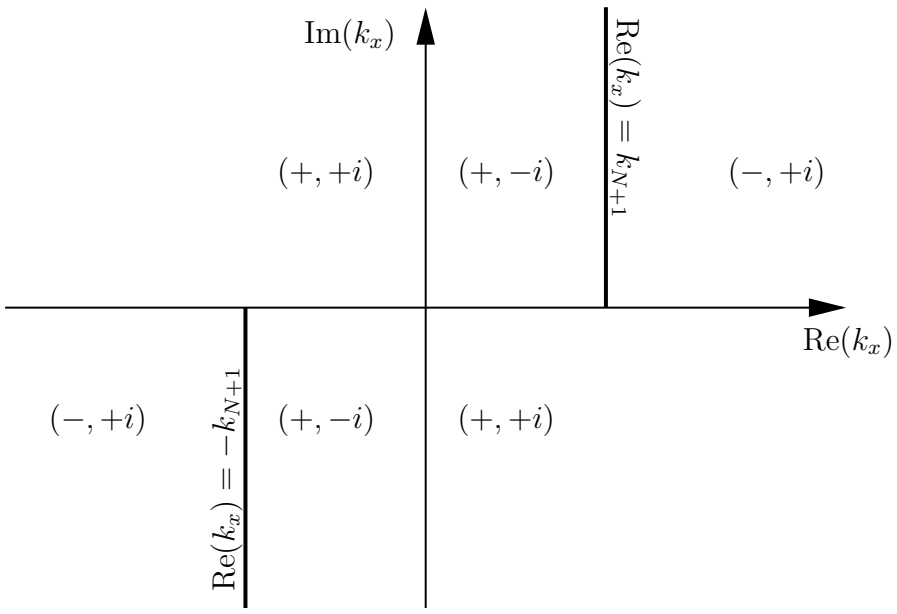

Figure 1.2: Branch cuts for $k_{N+1,z} = (k_{N+1}^2 - k_x^2)^{1/2}$. The complex plane is divided into regions accordingly to the signs of $\mathrm{Re}(k_{N+1,z}(k_x))$ and $\mathrm{Im}(k_{N+1,z}(k_x))$.

for $k_{N+1,z}$, we have already characterized $k_{N+1,z}$ on the real axis:

$$\begin{aligned}\mathrm{Re}(k_{N+1,z}) &= \mathrm{Re}((k_{N+1}^2 - k_x^2)^{1/2}) > 0, \quad |\mathrm{Re}(k_x)| < k_{N+1}\\ \mathrm{Im}(k_{N+1,z}) &= \mathrm{Im}((k_{N+1}^2 - k_x^2)^{1/2}) > 0, \quad |\mathrm{Re}(k_x)| > k_{N+1}.\end{aligned}$$

To meet these conditions, we define $k_{N+1,z}(k_x)$ for a complex value k_x by

$$k_{N+1,z}(k_x) = (k_{N+1}^2 - k_x^2)^{1/2} = i\sqrt{-i(k_{N+1} + k_x)}\sqrt{-i(k_{N+1} - k_x)}.$$

We remind that $\sqrt{\cdot}$ denotes usual root function with the branch cut along the negative real axis.

Figure 1.2 shows the branch cuts of the so defined analytic function $k_{N+1,z}(k_x)$. There, we divided the complex plane into regions accordingly to the signs of $\mathrm{Re}(k_{N+1,z}(k_x))$ and $\mathrm{Im}(k_{N+1,z}(k_x))$. For example, in regions marked with $(+,+i)$ we have $\mathrm{Re}(k_{N+1,z}(k_x)) > 0$, $\mathrm{Im}(k_{N+1,z}(k_x)) > 0$, whereas in the region $(-,+i)$ we have $\mathrm{Re}(k_{N+1,z}(k_x)) < 0$, $\mathrm{Im}(k_{N+1,z}(k_x)) > 0$. Other regions are characterized accordingly. In particular, we have $\mathrm{Re}(k_{N+1,z}(k_x)) = 0$ *exactly* on the interfaces of the regions $(+,\pm i)$ with the regions $(-,\pm i)$.

It is still in front of us to discuss the unique solvability of the linear system (1.11). From linear algebra we know that the system (1.11) is not

uniquely solvable at $k_x = \kappa_x \in \mathbb{C}$ if and only if there exists an eigenvector to this system with eigenvalue equal to zero. The corresponding field $u(z)$ is called an *eigenmode* in physics.

To see when such an eigenmode appears, we multiply the TE–equation for $u(z)$ with $\overline{u}(z)$ and integrate over the interval $z = [z_{-1}, z_{N+1}]$, cf. Figure 1.1. Integration by parts yields

$$\int_{z_{-1}}^{z_{N+1}} \partial_z \overline{u}(z)\mu^{-1}\partial_z u(z) - \overline{u}(z)(\omega^2\varepsilon - \mu^{-1}\kappa_x^2)u(z)\mathrm{d}z \\ - \overline{u}_{N+1}(z_{N+1})\mu_{N+1}^{-1}\partial_z u_{N+1}(z_{N+1}) + \overline{u}_0(z_{-1})\mu_0^{-1}\partial_z u_0(z_{-1}) = 0. \tag{1.12}$$

The boundary terms can be simplified by utilizing that $u_m(z)$ is an eigenmode. The corresponding coefficient vector $\mathbf{v}_m$ solves system (1.11) with a zero right hand side, which means that $u_m(z)$ contains no incoming plane wave from below or from above. Consequently, we have $u(z) = u_{0,\downarrow}e^{-ik_{0,z}(z-z_{-1})}$ in the lower half space and $u(z) = u_{N+1,\uparrow}e^{ik_{N+1,z}(z-z_N)}$ in the upper half space. It holds true that $u_{0,\downarrow} \neq 0$ and $u_{N+1,\uparrow} \neq 0$, because otherwise the field is zero in the lower or upper half space, which would imply that $u(z)$ is zero everywhere. Using this, the boundary terms in (1.12) simplify to

$$-ik_{N+1,z}C_{N+1} - ik_{0,z}C_0,$$

with positive numbers $C_0 = \mu_0^{-1}|u_0(z_{-1})|^2$ and $C_{N+1} = \mu_{N+1}^{-1}|u_{N+1}(z_N)|^2$. Taking the imaginary part of equation (1.12) yields

$$\mathrm{Im}(\kappa_x^2)\int_{z_{-1}}^{z_{N+1}} \mu^{-1}\overline{u}(z)u(z)\mathrm{d}z = \mathrm{Re}(k_{N+1,z})C_{N+1} + \mathrm{Re}(k_{0,z})C_0.$$

For the sake of a simpler notation we normalize the eigenmode $u(z)$ so that $\int_{z_{-1}}^{z_{N+1}} \mu^{-1}\overline{u}(z)u(z)\mathrm{d}z = 1$. The above equation now implies

$$2\mathrm{Re}(\kappa_x)\mathrm{Im}(\kappa_x) = \mathrm{Re}(k_{N+1,z})C_{N+1} + \mathrm{Re}(k_{0,z})C_0. \tag{1.13}$$

Similarly, by taking the real part of equation (1.12), we have

$$\int_{z_{-1}}^{z_{N+1}} \partial_z \overline{u}(z)\mu^{-1}\partial_z u(z)\mathrm{d}z - \sum_{j=-1}^{N} \mathrm{Re}(k_j^2 - \kappa_x^2)\int_{z_j}^{z_{N+1}} \mu^{-1}\overline{u}(z)u(z)\mathrm{d}z = \\ - \mathrm{Im}(k_{N+1,z})\mu_{N+1}^{-1}C_{N+1} - \mathrm{Im}(k_{0,z})\mu_0^{-1}C_0.$$

In arriving at the above, we have used the definition $k_j = \omega\sqrt{\varepsilon_j\mu_j}$. We derive the condition

$$\mathrm{Re}(\kappa_x)^2 - \mathrm{Im}(\kappa_x)^2 \leq k_{\max}^2 - \mathrm{Im}(k_{N+1,z})C_{N+1} - \mathrm{Im}(k_{0,z})C_0, \tag{1.14}$$

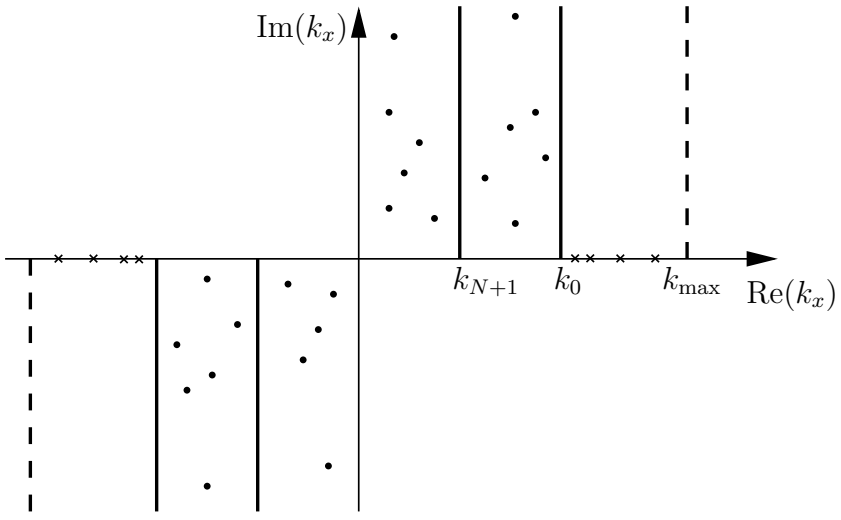

Figure 1.3: Possible loci of eigenvalues κ_x. Eigenvalues marked with crosses correspond to guided modes. Resonances are marked with bullets. The bold, drawn through lines are the branch cuts corresponding to the square root functions $k_{0,z} = (k_0^2 - k_x^2)^{1/2}$ and $k_{N+1,z} = (k_{N+1}^2 - k_x^2)^{1/2}$. The dashed lines bound the real part of the eigenvalues.

with $k_{\max} = \max\{k_j\}$.

With the two conditions (1.13), (1.14) we can *exclude* eigenvalues κ_x within the following regions, where we only consider $\mathrm{Re}(\kappa_x) \geq 0$, since the classification for $\mathrm{Re}(\kappa_x) < 0$ follows from symmetry:

i) $\mathrm{Im}(\kappa_x) < 0$: In this case, $\mathrm{Re}(k_{N+1,z})$ and $\mathrm{Re}(k_{0,z})$ are positive, cf. Figure 1.2. An eigenvalue is excluded in this region by condition (1.13).

ii) $\mathrm{Re}(\kappa_x) > k_{\max}$: Here we have $\mathrm{Im}(k_{N+1,z}) \geq 0$ and $\mathrm{Im}(k_{0,z}) \geq 0$, cf. Figure 1.2, so that $\mathrm{Im}(\kappa_x)^2 > 0$ by condition (1.14). Since we have already excluded eigenvalues with $\mathrm{Im}(\kappa_x) < 0$, this gives $\mathrm{Im}(\kappa_x) > 0$, and from Figure 1.2 we infer $\mathrm{Re}(k_{0,z}), \mathrm{Re}(k_{N+1,z}) < 0$. But this contradicts condition (1.13).

iii) $\mathrm{Re}(\kappa_x) < \max\{k_0, k_{N+1}\}, \mathrm{Im}(k_x) = 0$: This is a refinement of i). Without restriction of generality we assume that $k_0 \geq k_{N+1}$, so that $\kappa_x < k_0$ and $\kappa_x \leq k_{N+1}$. From Figure 1.2 we infer that $\mathrm{Re}(k_{0,z}) > 0$ and $\mathrm{Re}(k_{N+1,z}) \geq 0$, so condition (1.13) exclude an eigenvalue in this case.

Figure 1.3 shows the possible loci of eigenvalues κ_x. We distinguished between two types of eigenvalues κ_x :

An eigenvalue with $\mathrm{Im}(k_{0,z}) > 0$ and $\mathrm{Im}(k_{N+1,z}) > 0$ is called *guided waveguide mode.* Guided waveguide modes propagate within the multi–layer stack and decay exponentially in the outward directions of the lower and upper half space. Guided modes only occur for $\max\{k_0, k_{N+1}\} \leq |\mathrm{Re}(\kappa_x)| < k_{\max}$. Since then $\mathrm{Re}(k_{0,z}), \mathrm{Re}(k_{N+1,z}) \leq 0$, cf. Figure 1.2, we infer from condition (1.13) that guided modes lie on the real axis.

The remaining eigenmodes are called *resonances.* The corresponding fields grow exponentially in the lower or upper half space and are therefore not directly encountered in reality. However, a resonance κ_x close to the real axis has a large impact on the scattering off the layered structure, since it renders the scattering problem ill-conditioned.

For later purposes we need to bound the maximum value of the field $u(x)$ for large values of k_x, when prescribing an incoming field from above, that is $u_{N+1,\downarrow} = u_{\mathrm{inc}}$ and $u_{0,\uparrow} = 0$ with a given scalar u_{inc}.

For the sake of a simpler notation we set $\mu = 1$, here, and introduce the notation

$$\begin{aligned} q(z) &= -(\omega^2\varepsilon - \kappa_x^2), \\ \kappa_0 &= ik_{0,z}, \\ \kappa_{N+1} &= ik_{N+1,z}. \end{aligned}$$

$q(z)$, κ_0 and κ_{N+1} are positive for sufficiently large values of k_x. We assume $u_{\mathrm{inc}} \in \mathbf{R}$, so that the problem is posed in the real arithmetic. The solution $u(z)$ satisfies

$$\begin{aligned} \int_{z_{-1}}^{z_{N+1}} &\partial_z u(z)\partial_z u(z) + q(z)u(z)u(z)\mathrm{d}z \\ &- u(z_{N+1})\partial_z u(z_{N+1}) + u(z_{-1})\partial_z u(z_{-1}) = 0 \end{aligned} \tag{1.15}$$

At the upper and lower interfaces we have

$$\begin{aligned} u(z_{N+1}) &= u_{\mathrm{inc}} + u_{N+1,\uparrow}e^{-\kappa_{N+1}h_{N+1}} \\ \partial_z u(z_{N+1}) &= \kappa_{N+1}u_{\mathrm{inc}} - \kappa_{N+1}u_{N+1,\uparrow}e^{-\kappa_{N+1}h_{N+1}} \\ \partial_z u(z_{-1}) &= \kappa_0 u_{z_{-1}}. \end{aligned}$$

Inserting this into (1.15) and denoting $u_{\mathrm{out}} = u_{N+1,\uparrow}e^{-\kappa_{N+1}h_{N+1}}$ we get

$$\begin{aligned} \int_{z_{-1}}^{z_{N+1}} &\partial_z u(z)\partial_z u(z) + q(z)u(z)u(z)\mathrm{d}z + \kappa_0|u(z_{-1})|^2 + \kappa_{N+1}|u_{\mathrm{out}}|^2 \\ &= \kappa_{N+1}u(z_{N+1})u_{\mathrm{inc}} - \kappa_{N+1}u_{\mathrm{inc}}u_{\mathrm{out}} \end{aligned} \tag{1.16}$$

To start with the bound on $|u(z)|$, we quote the Sobolev embedding theorem, which states that $u(z)$ is bounded by its H^1–norm, see for example Renardy and Rogers [93, Sec. 6.4.6]. We perform the estimations

$$\begin{aligned}\|u\|_\infty^2 &\le C\|u\|_{H^1}^2 \\ &\le C\Big(\int_{z_{-1}}^{z_{N+1}} \partial_z u(z)\partial_z u(z) + q(z)u(z)u(z)\mathrm{d}z + \\ &\qquad \kappa_0|u(z_{-1})|^2 + \kappa_{N+1}|u_{\text{out}}|^2\Big).\end{aligned}$$

Utilizing equation (1.16) gives

$$\begin{aligned}\|u\|_\infty^2 &\le \kappa_{N+1} C\Big(u(z_{N+1})u_{\text{inc}} + u_{\text{inc}}u_{\text{out}}\Big) \\ &\le \kappa_{N+1} C\|u\|_\infty |u_{\text{inc}}| + \kappa_{N+1} C|u_{\text{out}}||u_{\text{inc}}|.\end{aligned} \tag{1.17}$$

To bound the second term we need an estimate $|u_{\text{out}}| \le C\|u\|_\infty$. At the interface of the $(N+1)$th layer we have

$$\begin{aligned}u(z_N) &= u_{\text{inc}} e^{-\kappa_{N+1}h_{N+1}} + u_{\text{out}}, \\ u(z_{N+1}) &= u_{\text{inc}} + u_{\text{out}}.\end{aligned}$$

Multiplying the second equation with $\epsilon = e^{-\kappa_{N+1}h_{N+1}}$ and subtracting the second from the first equation gives

$$u(z_N) - \epsilon u(z_{N+1}) = u_{\text{out}}(1-\epsilon).$$

Since $\epsilon < 1$ for sufficiently large $|k_x|$ this leads to the bound

$$|u_{\text{out}}| \le C\max\{u(z_N), u(z_{N+1})\} \le C\|u\|_\infty,$$

which completes the estimation in (1.17) together with dividing by $\|u\|_\infty$:

$$\|u\|_\infty \le \kappa_{N+1} C|u_{\text{inc}}| \le C|k_x||u_{\text{inc}}|. \tag{1.18}$$

1.2.2 Point source

We want to solve Maxwell's equations in a homogeneous medium with an idealized point dipole placed at position $\mathbf{r}' \in \mathbf{R}^3$,

$$\nabla \times \mu^{-1}\nabla \times \mathbf{E}(\mathbf{r}) - \omega^2 \varepsilon \mathbf{E}(\mathbf{r}) \;=\; i\omega\delta(\mathbf{r}-\mathbf{r}')\mathbf{J}_{\text{p}}. \tag{1.19}$$

Here, $\mathbf{J}$ is the dipole direction of the point source.

The solution to the point source problem (1.19) is given by

$$\mathbf{E}(\mathbf{r}) = i\omega \mathbf{G}_+(\mathbf{r}, \mathbf{r}')\mathbf{J}_\mathrm{p}, \tag{1.20}$$

where $\mathbf{G}_+(\mathbf{r}, \mathbf{r}')$ is the outward radiating Green's tensor, which satisfies

$$\nabla \times \mu^{-1} \nabla \times \mathbf{G}_+(\mathbf{r}, \mathbf{r}') - \omega^2 \varepsilon \mathbf{G}_+(\mathbf{r}, \mathbf{r}') \;\; = \;\; \delta(\mathbf{r} - \mathbf{r}')\mathbf{1}.$$

Here, $\mathbf{1}$ is the 3×3 unit matrix, also called unit dyad in this context. The curl operator acts on $\mathbf{r}$.

From Martin and Piller [73] we take that

$$\mathbf{G}_+(\mathbf{r}, \mathbf{r}') = \mu \left(\mathbf{1} + \frac{\nabla \nabla^\mathrm{T}}{k_\mathrm{b}^2} \right) g_+(\mathbf{r}, \mathbf{r}'), \tag{1.21}$$

with the background wave number $k_\mathrm{b} = \omega\sqrt{\mu\varepsilon}$ and the scalar Green's function

$$g_+(\mathbf{r}, \mathbf{r}') = \frac{e^{ik_\mathrm{b}|\mathbf{r}-\mathbf{r}'|}}{4\pi|\mathbf{r} - \mathbf{r}'|}.$$

The scalar Green's function $g_+(\mathbf{r}, \mathbf{r}')$ is the outward radiating fundamental solution to the Helmholtz equation,

$$-\Delta_\mathbf{r} g_+(\mathbf{r}, \mathbf{r}') - k_\mathrm{b}^2 g_+(\mathbf{r}, \mathbf{r}') = \delta(\mathbf{r} - \mathbf{r}').$$

We quote the Fourier transform of the Green's tensor on a hyperplane with constant z–coordinate. Before we start with this, we need to fix the prefactor in the Fourier transform. For a function $f : \mathbf{R}^n \to \mathbb{C}$ we define the Fourier transform as

$$f^\wedge(\mathbf{k}) = \frac{1}{(2\pi)^n} \int_{\mathbf{R}^n} f(\mathbf{x}) e^{-i\mathbf{k}\cdot\mathbf{x}} \mathrm{d}\mathbf{x}. \tag{1.22}$$

For the inverse Fourier transform this means

$$f(\mathbf{x}) = (f^\wedge)^\vee(\mathbf{x}) = \int_{\mathbf{R}^n} f^\wedge(\mathbf{k}) e^{+i\mathbf{k}\cdot\mathbf{x}} \mathrm{d}\mathbf{k}.$$

From Weyl [110] or Singer et al. [102, p.55], we take Weyl's representation of a scalar, diverging spherical wave

$$g_+^\wedge(\mathbf{k}_{xy}, z, \mathbf{r}') = \frac{i}{8\pi^2} \frac{e^{ik_z|z-z'|}}{k_z} \cdot e^{-i\mathbf{k}_{xy}\cdot\mathbf{r}'_{xy}}, \tag{1.23}$$

with $\mathbf{r}'_{xy} = (r'_x, r'_y)^{\mathrm{T}}$, $\mathbf{k}_{xy} = (k_x, k_y)^{\mathrm{T}}$ and $k_z = \sqrt{k_{\mathrm{b}}^2 - |\mathbf{k}_{xy}|^2}$. The Fourier transform is performed only in the x- and y-coordinates and is singular at $\mathbf{k}_{xy}$ with $|\mathbf{k}_{xy}| = k_{\mathrm{b}}$. Therefore, the above formula is understood in the distributational sense, cf. Rudin [94, p. 166].

To move on to the vectorial case we exploit the following relations,

$$\begin{aligned}(\partial_{x/y} g_+)^\wedge(\cdot, z, \mathbf{r}') &= ik_{x/y} g_+^\wedge(\cdot, z, \mathbf{r}') \\ \partial_z g_+^\wedge(\cdot, z, \mathbf{r}') &= i\mathrm{sgn}(z - z') k_z g_+^\wedge(\cdot, z, \mathbf{r}') \\ \partial_{zz} g_+^\wedge(\cdot, z, \mathbf{r}') &= -k_z^2 g_+^\wedge(\cdot, z, \mathbf{r}') - \frac{1}{4\pi^2}\delta(z - z') e^{-i\mathbf{k}_{xy}\cdot\mathbf{r}'_{xy}},\end{aligned}$$

From equation (1.21) we now derive the Green's tensor version of Weyl's representation formula

$$\begin{aligned}\mathbf{G}_+^\wedge(\mathbf{k}_{xy}, z, \mathbf{r}') = \mu \left(\mathbf{1} - \frac{\mathbf{k}\mathbf{k}^{\mathrm{T}}}{k_{\mathrm{b}}^2}\right) g_+^\wedge(\mathbf{k}_{xy}, z, \mathbf{r}') - \\ \frac{\mu}{4\pi^2}\frac{\mathbf{n}_z \mathbf{n}_z^{\mathrm{T}}}{k_{\mathrm{b}}^2}\delta(z) \cdot e^{-i\mathbf{k}_{xy}\cdot\mathbf{r}'_{xy}},\end{aligned} \tag{1.24}$$

with the notations $\mathbf{k} = (k_x, k_y, \mathrm{sgn}(z - z')k_z)^{\mathrm{T}}$, $\mathbf{n}_z = (0, 0, 1)^{\mathrm{T}}$.

To give the Fourier transform a physical meaning we regard a point source placed above the $z = 0$ hyperplane, that is $z' > 0$. For $z < z'$, we have

$$\mathbf{G}_+^\wedge(\mathbf{k}_{xy}, z, \mathbf{r}') = e^{-ik_z z}\mathbf{G}_+^\wedge(\mathbf{k}_{xy}, 0, \mathbf{r}').$$

Applying the inverse Fourier transform yields

$$\begin{aligned}\mathbf{G}_+(\mathbf{r}, \mathbf{r}') &= (\mathbf{G}_+^\wedge(\mathbf{k}_{xy}, 0, \mathbf{r}')e^{-ik_z z})^\vee(\mathbf{r}) \\ &= \int_{z=0} \mathbf{G}_+^\wedge(\mathbf{k}_{xy}, 0, \mathbf{r}')e^{i\mathbf{k}_{xy}\cdot\mathbf{r}_{xy}}e^{-ik_z z}\mathrm{d}\mathbf{k}_{xy}.\end{aligned}$$

We recall that k_z is a real, positive number for $|\mathbf{k}_{xy}| < k_{\mathrm{b}}$, whereas for $|\mathbf{k}_{xy}| \geq k_{\mathrm{b}}$ we have $\mathrm{Re}(k_z) = 0$ and $\mathrm{Im}(k_z) \geq 0$. Hence, the above representation formula for $\mathbf{G}_+(\mathbf{r}, \mathbf{r}')$ in the lower half space can be seen as an "integral summation" of downward traveling or evanescent plane waves.

In general, such a Fourier transform–based representation formula of an electromagnetic field in a half space is commonly called *angular spectrum representation*.

1.2.3 Line source

The setting is as in the previous subsection but instead of a point source we impose a line source $\delta(\mathbf{r}_{xz} - \mathbf{r}'_{xz})e^{ik_y y}\mathbf{J}_{\mathrm{l}}$ at position $\mathbf{r}'_{xz} = (x', z')^{\mathrm{T}}$:

$$\nabla \times \mu^{-1}\nabla \times \mathbf{E}(\mathbf{r}) - \omega^2\varepsilon\mathbf{E}(\mathbf{r}) = i\omega\delta(\mathbf{r}_{xz} - \mathbf{r}'_{xz})e^{ik_y y}\mathbf{J}_{\mathrm{l}}.$$

Again, we want to construct the solution by a Green's tensor $\mathbf{G}_{k_y,+}(\mathbf{r}, \mathbf{r}'_{xz})$,

$$\mathbf{E}(\mathbf{r}) = i\omega \mathbf{G}_+(\mathbf{r}, \mathbf{r}')\mathbf{J}_\mathrm{l}. \tag{1.25}$$

Using

$$\int_{-\infty}^{\infty} \delta(\mathbf{r} - \mathbf{r}')e^{ik_y y'}\mathrm{d}y' = \delta(\mathbf{r}_{xz} - \mathbf{r}'_{xz})e^{ik_y y}$$

the corresponding Green's tensor is readily constructed from the 3D Green's tensor (1.21):

$$\begin{aligned}\mathbf{G}_{k_y,+}(\mathbf{r}, \mathbf{r}'_{xz}) &= \int_{-\infty}^{\infty} \mathbf{G}_+(\mathbf{r}, \mathbf{r}')e^{ik_y y'}\mathrm{d}y' \\ &= \mu\left(\mathbf{1} + \frac{\nabla\nabla^\mathrm{T}}{k^2}\right)\int_{-\infty}^{\infty} g_+(\mathbf{r}, \mathbf{r}')e^{ik_y y'}\mathrm{d}y' \\ &= \mu\left(\mathbf{1} + \frac{\nabla\nabla^\mathrm{T}}{k^2}\right)\frac{i}{4}H_{0,+}(k_{xz}|\mathbf{r}_{xz} - \mathbf{r}'_{xz}|)e^{ik_y y},\end{aligned} \tag{1.26}$$

where $H_{0,+}$ is the zeroth order Hankel function of first kind. $k_{xz} = \sqrt{k_\mathrm{b}^2 - k_y^2}$ is the cross section wave number. For the last identity in the equation above we refer to Martin and Piller [73]. We remark that the function

$$g_+^{(\mathrm{2D})}(\mathbf{r}_{xz}, \mathbf{r}'_{xz}) = \frac{i}{4}H_{0,+}(k_{xz}|\mathbf{r}_{xz} - \mathbf{r}'_{xz}|)$$

is the scalar Green's function to the 2D Helmholtz equation,

$$-\Delta_{\mathbf{r}_{xz}} g_+^{(\mathrm{2D})}(\mathbf{r}_{xz}, \mathbf{r}'_{xz}) - k_{xz}^2 g_+^{(\mathrm{2D})}(\mathbf{r}_{xz}, \mathbf{r}'_{xz}) = \delta(\mathbf{r}_{xz} - \mathbf{r}'_{xz}).$$

Again, we want to provide the Fourier transform of $\mathbf{G}_{k_y,+}(\mathbf{r}, \mathbf{r}'_{xz})$ for a constant z–coordinate. Essentially, the derivation is a repetition of the considerations made for the point source case. Since $\mathbf{G}_{k_y,+}(\mathbf{r}, \mathbf{r}'_{xz})$ trivially depends on y, the Fourier integrals can be restricted to the x–coordinate. The 2D Weyl's representation formula reads as

$$(g_+^{(\mathrm{2D})})^\wedge(k_x, z, \mathbf{r}'_{xz}) = \frac{i}{4\pi}\frac{e^{ik_z|z-z'|}}{k_z}e^{-ik_x x'}, \tag{1.27}$$

with $k_z = \sqrt{k_{xz}^2 - k_x^2} = \sqrt{k_\mathrm{b}^2 - |\mathbf{k}_{xy}|^2}$. Inserting this into equation (1.26) we finally arrive at

$$\begin{aligned}\mathbf{G}^\wedge_{k_y,+}(\mathbf{k}_{xy}, z, \mathbf{r}'_{xz}) = \mu\left(\mathbf{1} - \frac{\mathbf{k}\mathbf{k}^\mathrm{T}}{k_\mathrm{b}^2}\right)(g_+^{(\mathrm{2D})})^\wedge(k_x, z, \mathbf{r}'_{xy})\delta(k_y) - \\ \frac{\mu}{4\pi^2}\frac{\mathbf{n}_z\mathbf{n}_z^\mathrm{T}}{k_\mathrm{b}^2}\delta(k_y)\delta(z - z'),\end{aligned} \tag{1.28}$$

which has the same form as the Fourier transform of a point source solution in equation (1.24).

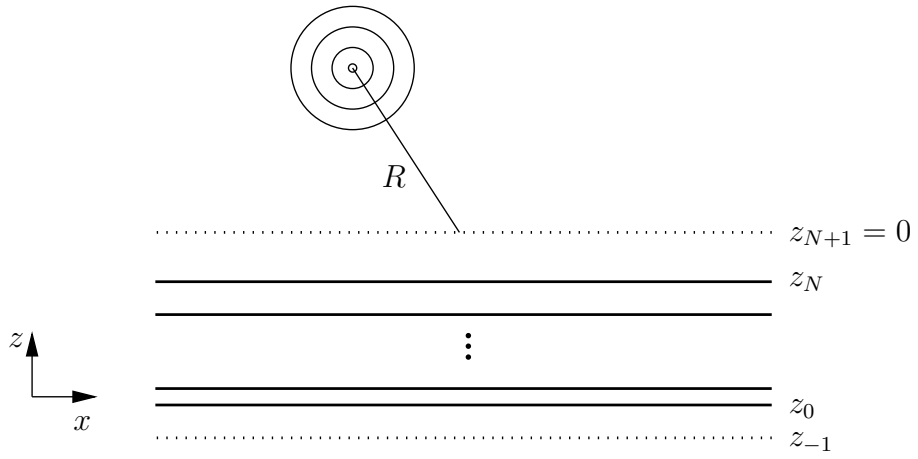

Figure 1.4: A point source placed above a layered media.

1.2.4 Point and line sources above layered media

The configuration shown in Figure 1.4 is a combination of the previous examples. We seek the solution to a point or line source placed at position $\mathbf{r}'$ above a layered media,

$$\nabla \times \mu^{-1} \nabla \times \mathbf{E}(\mathbf{r}) - \omega^2 \varepsilon \mathbf{E}(\mathbf{r}) = i\omega \mathbf{J}(\mathbf{r}), \tag{1.29}$$

where

$$\mathbf{J} = \begin{cases} \delta(\mathbf{r} - \mathbf{r}')\mathbf{J}_{\mathrm{p}}, & (\text{point dipole}), \\ \delta(\mathbf{r}_{xz} - \mathbf{r}'_{xz}) e^{ik_y y} \mathbf{J}_{\mathrm{l}}, & (\text{line source}). \end{cases}$$

We adopt the notation of Section 1.2.1, where we discussed the propagation of plane waves in a layered media.

Disregarding the layered media, the source in the upper half space emits an electromagnetic field $\mathbf{E}_{\mathrm{inc}}$ which satisfies

$$\nabla \times \mu_{N+1}^{-1} \nabla \times \mathbf{E}_{\mathrm{inc}}(\mathbf{r}) - \omega^2 \varepsilon_{N+1} \mathbf{E}_{\mathrm{inc}}(\mathbf{r}) = i\omega \mathbf{J}(\mathbf{r}).$$

An analytic expression for $\mathbf{E}_{\mathrm{inc}}$ by means of the Green's tensor was given in equations (1.20) and (1.21) for the point source case and in equations (1.25), (1.26) for the line source case.

Physically spoken, the source field $\mathbf{E}_{\mathrm{inc}}$ hits the layered media from above and is scattered by the multilayer stack. To construct the solution $\mathbf{E}$ we evoke the angular spectrum representation of the field $\mathbf{E}_{\mathrm{inc}}$, equations (1.24)

and (1.28), which permits to decompose $\mathbf{E}_{\text{inc}}$ into downward traveling and evanescent waves,

$$\begin{aligned}\mathbf{E}_{\text{inc}}(\mathbf{r}) &= \int \mathbf{E}^{\wedge}_{\text{inc}}(\mathbf{k}_{xy},0)e^{i\mathbf{k}_{xy}\cdot\mathbf{r}_{xy}}e^{-ik_{N+1,z}z}\mathrm{d}\mathbf{k}_{xy} \\ &= \int \mathbf{E}^{\wedge}_{\text{inc}}(\mathbf{k}_{xy},0)e^{i\mathbf{k}_{N+1,\downarrow}\cdot\mathbf{r}}\mathrm{d}\mathbf{k}_{xy},\end{aligned} \tag{1.30}$$

with the notation $\mathbf{k}_{j,\downarrow} = (k_x, k_y, -k_{j,z})$, $j = 0, \dots N+1$, and $\mathbf{k}_{j,\uparrow}$ defined accordingly. Equation (1.30) is valid below the source position, that is $z < z'$.

With the angular spectrum representation (1.30) at hand we separately compute the light fields stimulated by the Fourier modes $\mathbf{E}^{\wedge}_{\text{inc}}(\mathbf{k}_{xy},0)e^{i\mathbf{k}_{j,\downarrow}\cdot\mathbf{r}}$ within the layered media. Afterwards we superimpose these contributions by inverse Fourier transforming with respect to $\mathbf{k}_{xy}$ in order to gain the sought field $\mathbf{E}$. After doing so, we will verify that the so constructed field $\mathbf{E}$ indeed satisfies Maxwell's equations (1.29).

In Section 1.2.1 we have derived that the field within the layered media stimulated by a plane wave $\mathbf{E}^{\wedge}_{\text{inc}}(\mathbf{k}_{xy}0)e^{i\mathbf{k}_{j,\downarrow}\cdot\mathbf{r}}$ from above has the following form in the jth layer:

$$\mathbf{E}^{\wedge}_{j}(\mathbf{k}_{xy},z)e^{i\mathbf{k}_{xy}\cdot\mathbf{r}_{xy}} = \mathbf{E}^{\wedge}_{j,\uparrow}(\mathbf{k}_{xy})e^{i\mathbf{k}_{j,\uparrow}\cdot\mathbf{r}} + \mathbf{E}^{\wedge}_{j,\downarrow}(\mathbf{k}_{xy})e^{i\mathbf{k}_{j,\downarrow}\cdot\mathbf{r}}.$$

In the lower half space ($j = 0$) we have $\mathbf{E}_{0,\uparrow}(\mathbf{k}_{xy}) = 0$ which excludes incoming waves from below. In the upper half space ($j = N+1$) we have $\mathbf{E}_{N+1,\downarrow}(\mathbf{k}_{xy}) = \mathbf{E}^{\wedge}_{\text{inc}}(\mathbf{k}_{xy},0)$ which prescribes the stimulating field.

Now, the solution $\mathbf{E}$ is given in the jth layer and for $z < z'$ by the integral over the plane waves contributions $\mathbf{E}^{\wedge}_{j}(\mathbf{k}_{xy},z)$, which is exactly the inverse Fourier transform,

$$\begin{aligned}\mathbf{E}_{j}(\mathbf{r}) &= \int \mathbf{E}^{\wedge}_{j}(\mathbf{k}_{xy},z)e^{i\mathbf{k}_{xy}\cdot\mathbf{r}_{xy}}\mathrm{d}\mathbf{k}_{xy}, \\ &= \int \mathbf{E}^{\wedge}_{j,\uparrow}(\mathbf{k}_{xy})e^{i\mathbf{k}_{j,\uparrow}\cdot\mathbf{r}} + \mathbf{E}^{\wedge}_{j,\downarrow}(\mathbf{k}_{xy})e^{i\mathbf{k}_{j,\downarrow}\cdot\mathbf{r}}\mathrm{d}\mathbf{k}_{xy}.\end{aligned} \tag{1.31}$$

Integral representations of this type are called Sommerfeld integrals, see Chew [27]. We mention that the integral in (1.31) requires a careful definition in the distributational sense, because the integral is singular, when $\|\mathbf{k}_{xy}\|$ is equal to k_0, or k_{N+1}, or is equal to a guided mode of the layered media. We refer to the discussion on the unique solvability of the layered media problem with a stimulating plane wave in Section 1.2.1.

To properly define the integral representation (1.31) and for a numerical evaluation of the Sommerfeld integral it is possible to apply a complex integral deformation, see [27] and Paulus et al. [88]. To exemplify this, we

restrict ourselves to the case of a y-polarized and y–independent line source, that is

$$\mathbf{J}(\mathbf{r}) = \delta(\mathbf{r}_{xz} - \mathbf{r}'_{xz}) \begin{pmatrix} 0, & 1, & 0 \end{pmatrix}^{\mathrm{T}}.$$

Then, the fields $\mathbf{E}_{\mathrm{inc}}$ and $\mathbf{E}$ have only y-components and Maxwell's equations collapse to the Helmholtz equation in 2D,

$$-\nabla^{\mathrm{T}}\mu^{-1}\nabla E_y(x,z) - \omega^2\epsilon E_y(x,z) = i\omega\delta(\mathbf{r}_{xz} - \mathbf{r}'_{xz}). \tag{1.32}$$

The source field $E_{\mathrm{inc},y}$ can be computed from the line source Green's tensor, equations (1.25) and (1.26), with $k_y = 0$:

$$E_{\mathrm{inc},y} = i\omega\mu H_{0,+}(k_{xz}|\mathbf{r}_{xz} - \mathbf{r}'_{xz}|).$$

Accordingly, the angular spectrum representation (1.30) of $\mathbf{E}_{\mathrm{inc}}$ reduces to an integral over k_x,

$$\begin{aligned} E_{\mathrm{inc},y}(x,z) &= \mu_{N+1}\int_{\mathbf{R}} (g_+^{(2\mathrm{D})})^{\wedge}(k_x, 0, \mathbf{r}'_{xy}) e^{-ik_{N+1,z}z} e^{ik_x x}\mathrm{d}k_x \\ &= \frac{i\mu_{N+1}}{4\pi}\int_{\mathbf{R}} \frac{e^{ik_{N+1,z}z'}e^{-ik_x x'}}{k_{j,z}} e^{-ik_{N+1,z}z} e^{ik_x x}\mathrm{d}k_x, \end{aligned}$$

for $z < z'$, and the Sommerfeld integral (1.31) becomes

$$\begin{aligned} E_{j,y}(x,z) = \int_{\mathbf{R}} & u_{j,\uparrow}(k_x) e^{ik_{j,z}(z - z_{j-1})} e^{ik_x x} + \\ & u_{j,\downarrow}(k_x) e^{-ik_{j,z}(z - z_j)} e^{ik_x x}\mathrm{d}k_x, \end{aligned} \tag{1.33}$$

with scalar coefficients $u_{j,\uparrow}(k_x)$, $u_{j,\downarrow}(k_x)$ as introduced in equation (1.7). In the upper half space ($j = N+1$) we prescribe the stimulating field by setting

$$\begin{aligned} u_{N+1,\downarrow}(k_x) &= \mu_{N+1}(g_+^{(2\mathrm{D})})^{\wedge}(k_x, 0, \mathbf{r}'_{xy}) \\ &= \frac{i\mu_{N+1}}{4\pi}\frac{e^{-ik_{N+1,z}z'}e^{-ik_x x'}}{k_{N+1,z}}. \end{aligned} \tag{1.34}$$

We exclude incoming waves from below by setting $u_{0,\uparrow} = 0$.

With equation (1.34) we can replace the Sommerfeld integral (1.33) in the upper half space by

$$E_{N+1,y}(x,z) = E_{\mathrm{inc},y}(x,z) + \int_{\mathbf{R}} u_{N+1,\uparrow}(k_x) e^{ik_{N+1,z}(z - z_N)} e^{ik_x x}\mathrm{d}k_x. \tag{1.35}$$

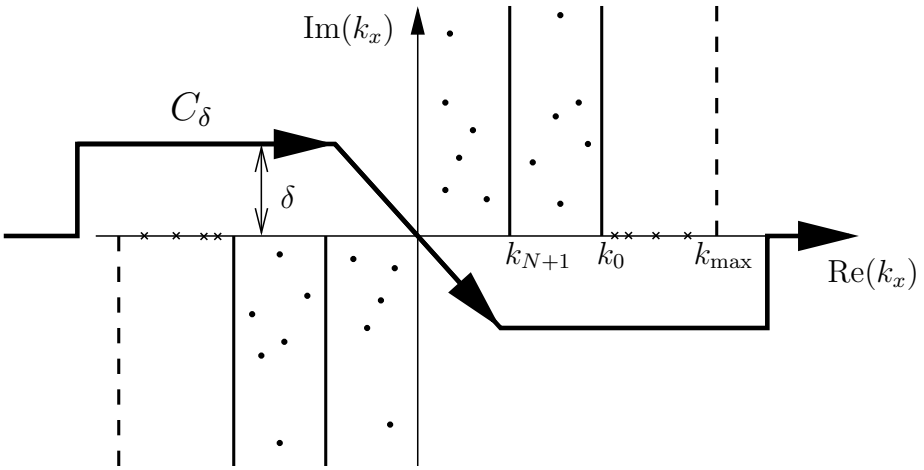

Figure 1.5: Complex integration path for the numerical evaluation of the Sommerfeld integral. For the pole loci and the branch cuts (vertical lines) we refer to Figure 1.3.

The coefficient functions $u_{j,\uparrow}(k_x)$ and $u_{j,\downarrow}(k_x)$ are analytic functions of k_x with poles and branch cuts as shown in Figure 1.3. To circumvent an integration over a singularity or across a branch cut in the Sommerfeld integral (1.33) we use a complex integration path C_δ as given in Figure 1.5,

$$E_{j,y}(x,z) = \int_{C_\delta} u_{j,\uparrow}(k_x) e^{ik_{j,z}(z-z_{j-1})} e^{ik_x x} + u_{j,\downarrow}(k_x) e^{-ik_{j,z}(z-z_j)} e^{ik_x x} \mathrm{d}k_x. \tag{1.36}$$

In the upper half space, equation (1.35) with a complex integration path C_δ reads as

$$E_{N+1,y}(x,z) = E_{\mathrm{inc},y}(x,z) + \int_{C_\delta} u_{N+1,\uparrow}(k_x) e^{ik_{N+1,z}(z-z_N)} e^{ik_x x} \mathrm{d}k_x. \tag{1.37}$$

We will show soon that this integral is absolutely integrable. This way it is clear, that the integral value in (1.36) is independent of δ, so that it delivers a numerically feasible expression for the Sommerfeld integral (1.33).

To show the absolute integrability of the integral in (1.36) we use equation (1.18), which gives a bound on the coefficients $u_{j,\uparrow}(k_x)$ and $u_{j,\downarrow}(k_x)$ for large values $|k_x|$:

$$|u_{j,\uparrow\downarrow}(k_x)| \le C \frac{|u_{N+1,\downarrow}(k_x)|}{|k_x|} \le C |e^{ik_{N+1,z}z'}|.$$

We remind the definition of the square root function $k_{N+1,z} = (k_{N+1}^2 - k_x^2)^{1/2}$ with branch cuts as shown in Figure 1.2. For large values of $|k_x|$ we have that $\mathrm{Im}(k_{N+1,z}) \sim |k_x|$, which yields the bound

$$|u_{j,\uparrow\downarrow}(k_x)| \leq Ce^{-|k_x|z'}.$$

This gives the following bound for the first integrand in the Sommerfeld integral (1.36)

$$\begin{aligned} |\int_{C_\delta} u_{j,\uparrow}(k_x)e^{ik_{j,z}(z-z_{j-1})}e^{ik_x x}\mathrm{d}k_x| &\leq C\int_{C_\delta} e^{-|k_x|z'}e^{-|k_x|(z-z_{j-1})}|\mathrm{d}k_x| \\ &\leq C\int_{C_\delta} e^{-|k_x|z'}|\mathrm{d}k_x|. \end{aligned}$$

The last estimate holds for $j > 0$, because $z - z_{j-1}$ is positive. For $j = 0$ we have that $u_{j,\uparrow}(k_x) = 0$ by definition, since we ruled out incoming waves from below.

Similar, one shows for the second integrand in the Sommerfeld integral (1.36), that

$$|\int_{C_\delta} u_{j,\downarrow}(k_x)e^{ik_{j,z}(z-z_j)}e^{ik_x x}\mathrm{d}k_x| \leq C\int_{C_\delta} e^{-|k_x|z'}e^{|k_x|(z-z_j)}|\mathrm{d}k_x|. \tag{1.38}$$

This shows the absolute integrability of the Sommerfeld integral (1.36) provided that $z - z_j$ is negative. This is the case for layers with $j \leq N$. In the upper half space with $j = N + 1$, absolute integrability is only guaranteed for $z < z'$. However, equation (1.35) is valid in the entire upper half space, so that an integration of the second integrand in the Sommerfeld integral (1.33) can be avoided for $j = N + 1$.

It remains to verify that the field E_y defined by the Sommerfeld integral (1.36) and (1.37) indeed solves the Helmholtz equation (1.32). Since all integrals on the complex integration path C_δ are now absolutely integrable, we can differentiate under the integral sign and one readily confirms that E_y solves the Helmholtz equation (1.32).

Far distance source

We now want to derive the asymptotic approximation of the field within the layered media for a source located in a far distance position. We will see that the asymptotic field is equal to the field stimulated by a plane wave incident from the direction of the source position.

Again, we only deal with the line source case in the Helmholtz equation (1.32). However, a generalization of the results to the Maxwell case is straightforward, but requires a tedious notation.

Let the position of the line source be given by $(x', z') = R(\hat{x}, \hat{z})$ with $|(\hat{x}, \hat{z})| = 1$. We want to discuss the limit $R \to \infty$. Equation (1.34) relates the angular spectrum representation of the incoming field with the coefficients $u_{j,\uparrow}(k_x, R)$, $u_{j,\downarrow}(k_x, R)$ in the Sommerfeld integral (1.36). Here, we added the dependency on the distance R. We infer that

$$\begin{aligned} u_{j,\uparrow}(k_x, R) &= u_{N+1,\downarrow}(k_x, R) \frac{u_{j,\uparrow}(k_x, 1)}{u_{N+1,\downarrow}(k_x, 1)} \\ &= u_{N+1,\downarrow}(k_x, R) \tilde{u}_{j,\uparrow}(k_x), \end{aligned}$$

where we introduced $\tilde{u}_{j,\uparrow}(k_x) = u_{j,\uparrow}(k_x, 1)/u_{N+1,\downarrow}(k_x, 1)$. The coefficients of the downward traveling waves $\tilde{u}_{j,\downarrow}(k_x)$ are defined accordingly. Note that $\tilde{u}_{N+1,\downarrow}(k_x) = 1$, so that the coefficients $\tilde{u}_{j,\uparrow}(k_x)$, $\tilde{u}_{j,\downarrow}(k_x)$ corresponds to the plane wave solution in the layered media with normalized incoming field from above.

The Sommerfeld integral (1.36) now reads as

$$\begin{aligned} E_{j,y}(x, z) = \int_{C_\delta} & \tilde{u}_{j,\uparrow}(k_x) e^{ik_{j,z}(z - z_{j-1})} e^{ik_x x} u_{N+1,\downarrow}(k_x, R) + \\ & \tilde{u}_{j,\downarrow}(k_x) e^{ik_{j,z}(z - z_j)} e^{ik_x x} u_{N+1,\downarrow}(k_x, R) \mathrm{d}k_x. \end{aligned} \tag{1.39}$$

In the following we only discuss the first integrand, since the treatment of the second integrand follows in an analog way. With the angular spectrum representation of the source field, equation (1.34),

$$u_{N+1,\downarrow}(k_x, R) = \frac{i\mu_{N+1}}{4\pi} \frac{e^{-ik_{N+1,z}R\hat{z}} e^{-ik_x R\hat{x}}}{k_{N+1,z}},$$

the considered integral is given by

$$I_\uparrow = \frac{i\mu_{N+1}}{4\pi} \int_{C_\delta} \tilde{u}_{j,\uparrow}(k_x) e^{ik_{j,z}(z - z_{j-1})} e^{ik_x x} \frac{e^{-ik_{N+1,z}R\hat{z}} e^{-ik_x R\hat{x}}}{k_{N+1,z}} \mathrm{d}k_x$$

The parameter R renders the above expression into a highly oscillatory integral as $R \to \infty$. Following Chew [27, Sec. 2.5] we apply the method of stationary phase, cf. Maslov and Fedoriuk [74, Sec. 1.1].

We split the above integrand into an highly oscillatory part with phase function $S(k_x)$ and a smooth part $\varphi(k_x)$:

$$I_\uparrow = \frac{i\mu_{N+1}}{4\pi} \int_{C_\delta} \varphi_\uparrow(k_x) e^{iRS(k_x)} \mathrm{d}k_x,$$

with

$$\begin{aligned}\varphi(k_x) &= \frac{i\mu_{N+1}}{4\pi}\tilde{u}_{j,\uparrow}(k_x)e^{ik_{j,z}(z-z_{j-1})}e^{ik_x x}/k_{N+1,z} \quad \text{and} \\ S(k_x) &= -k_{N+1,z}\hat{z} - k_x\hat{x}.\end{aligned} \tag{1.40}$$

Reminding the definition $k_{N+1,z} = (k_{N+1}^2 - k_x^2)^{1/2}$, we see that the phase function $S(k_x)$ has a stationary point, $S'(k_x') = 0$ only at $k_x' = -k_{N+1}\hat{x}$.

Now, the method of stationary phase method yields the following first order asymptotic approximation for large values R,

$$I_\uparrow \sim \varphi(k_x') \int_{C_\epsilon} e^{iRS(k_x)} \mathrm{d}k_x$$

We denote $k_{j,z}' = k_{j,z}(k_x')$. Undoing the substitutions from equations (1.40), we are led to

$$\begin{aligned}I_\uparrow &\sim \tilde{u}_{j,\uparrow}(k_x')e^{ik_{j,z}'(z-z_{j-1})}e^{ik_x' x} \cdot \frac{i\mu_{N+1}}{4\pi k_{N+1,z}'} \int_{C_\epsilon} e^{iRS(k_x)} \mathrm{d}k_x \\ &= A \cdot \tilde{u}_{j,\uparrow}(k_x')e^{ik_{j,z}'(z-z_{j-1})}e^{ik_x' x},\end{aligned}$$

with the prefactor

$$A = \frac{i\mu_{N+1}}{4\pi k_{N+1,z}'} \int_{C_\epsilon} e^{iRS(k_x)} \mathrm{d}k_x. \tag{1.41}$$

Repeating the above consideration for the second integrand in the Sommerfeld integral (1.39) we finally arrive at

$$\begin{aligned}E_{j,y}(x,z) \sim A \cdot \tilde{u}_{j,\uparrow}(k_x')e^{ik_{j,z}'(z-z_{j-1})}e^{ik_x' x} + \\ A \cdot \tilde{u}_{j,\downarrow}(k_x')e^{-ik_{j,z}'(z-z_j)}e^{ik_x' x}.\end{aligned} \tag{1.42}$$

Using that

$$k_{N+1,z}' = (k_{N+1}^2 - k_{N+1}^2\hat{x}^2)^{1/2} = k_{N+1}\hat{z},$$

we see that this is the solution to the layered media problem with an incoming plane wave $Ae^{i(-k_x' x - k_{N+1,z}' z)}$ from direction $(-\hat{x}, -\hat{z})$.

To fix the prefactor A we help us with a trick: Since only the material properties of the upper half space are involved in the definition of A, equation (1.41), we regard a blank material stack with $\mu_j = \mu_{N+1}$, $\varepsilon_j = \varepsilon_{N+1}$. Then we trivially have $E_{j,y}(x,z) = E_{\mathrm{inc},y}(x,z)$ and $\tilde{u}_{j,\uparrow}(k_x') = 0$, $\tilde{u}_{j,\downarrow}(k_x') = e^{-k_z' z_j}$ for all j. From equation (1.42) we conclude,

$$A \sim E_{\mathrm{inc},y}(0,0) = i\omega\mu H_{0,+}(k_{N+1}R).$$

Together with the asymptotic behavior of the Hankel functions, see Abramowitz and Stegun [1, p. 108], this gives

$$A = \sqrt{\frac{2}{\pi k_{N+1} R}} e^{i(k_{N+1}R - \pi/4)}.$$

Remarks 1.1

i) To compute Sommerfeld integrals for a point source in 3D by utilizing a complex integration path in the $\mathbf{k}_{xy}$–space, it is easier to use cylinder coordinates (ρ, ϕ, z). Then, the complex path integration is performed in the variable $k_\rho = \sqrt{k_x^2 + k_y^2}$, cf. Chew [27, Sec. 2.7], Paulus et al. [88].

ii) A point or line source embedded in the layered media can also be treated with little modifications, see again [27, 88].

1.2.5 Waveguide modes

We assume that the material properties are invariant in the z–direction, $\varepsilon(x, y, z) = \varepsilon(x, y, 0)$ and $\mu(x, y, z) = \mu(x, y, 0)$ for all $z \in \mathbf{R}$. A waveguide mode has the form $\mathbf{E}(x, y, z) = \mathbf{E}(x, y)e^{ik_z z}$. So, Maxwell's equations in the $(x,\ y)$–cross section read as

$$\begin{pmatrix} \partial_x \\ \partial_y \\ ik_z \end{pmatrix} \times \mu^{-1} \begin{pmatrix} \partial_x \\ \partial_y \\ ik_z \end{pmatrix} \times \mathbf{E}(x, y) - \omega^2 \varepsilon \mathbf{E}(x, y) \quad = \quad 0.$$

As demonstrated in Jin [63], see also Schmidt et al. [99], this yields after some manipulations an eigenvalue problem for k_z^2 in the cross-section. To solve the eigenmode problem numerically one either imposes radiating boundary conditions in the cross-section or truncates the computational domain in the cross-section. The latter approach is justified when the eigenmode is confined by a *waveguide* structure in the cross–section as it often happens in applications. A layered medium as described above may also exhibit waveguide modes. These eigenmodes appear when for a chosen k_z the ODE system permits a non-trivial solution for zero incoming fields $u_{0,+} = 0$ and $u_{N+1,-} = 0$.

line integrals:	$\int_\gamma \mathbf{E}\cdot\mathrm{dl},\ \int_\gamma \mathbf{H}\cdot\mathrm{dl}$
surface integrals:	$\int_A \mathbf{D}\cdot\mathrm{dS},\ \int_A \mathbf{B}\cdot\mathrm{dS},\ \int_A \mathbf{J}\cdot\mathrm{dS}$
volume integrals:	$\int_V \rho\,\mathrm{dV}$

Table 1.1: Integrals in classical notation as they appear in electrodynamics.

1.3 Exterior calculus

The exterior calculus provides a consistent view on many types of differential equations like the Helmholtz equation in acoustics or Maxwell's equations. Classical integral identities like Green's theorems for scalar fields and Stokes's theorem for vector fields, see Monk [79, p. 52] or Nédélec [84, p. 73], are direct consequences of a central theorem also called Stokes's theorem. This way, Maxwell and Helmholtz scattering problems can be treated within one theory. Besides its mathematical elegancy, the exterior calculus allows for a much simpler notation. Especially we will extensively make use of the simple transformation rules under coordinate changes, when introducing the perfectly matched layer method or when using cylindrical coordinates. It is not the objective of this thesis to introduce the exterior calculus in greater detail. Here we only collect the relevant notations and formulas. We refer to Jänich [61] for a comprehensive treatment of differential forms.

E, D, H, B, J and ρ as differential forms

In the previous section Maxwell's equations (1.1) were given in a differential representation. The integral representation of Maxwell's equations as introduced for example in Chew [27], are closer related to the data measured in physical experiments. Table 1.1 collects involved integrals in classical notation. One regains the field values $\mathbf{E}$, $\mathbf{D}$, *etc.* at a position $\mathbf{r}$ as the limit for shrinking integration domains (lines, surfaces or volumes). Consequently, in the exterior calculus the field quantities are defined as their response on infinitesimal small integration volumes. For example we have

$$\begin{aligned}
\mathbf{e}(\mathbf{r})[\mathbf{t}] &= \lim_{\varepsilon\to 0}\frac{1}{|\varepsilon\mathbf{t}|}\int_{[\mathbf{r},\mathbf{r}+\varepsilon\mathbf{t}]}\mathbf{E}\cdot\mathrm{dl} = \mathbf{E}(\mathbf{r})\cdot\mathbf{t},\\
\mathbf{b}(\mathbf{r})[\mathbf{t}_1,\mathbf{t}_2] &= \lim_{\varepsilon\to 0}\frac{1}{|[\varepsilon\mathbf{t}_1,\varepsilon\mathbf{t}_2]|}\int_{\mathbf{r}+[\varepsilon\mathbf{t}_1,\varepsilon\mathbf{t}_2]}\mathbf{B}\cdot\mathrm{dS} = \mathbf{B}(\mathbf{r})\cdot(\mathbf{t_1}\times\mathbf{t_2}),\\
\rho(\mathbf{r})[\mathbf{t}_1,\mathbf{t}_2,\mathbf{t}_3] &= \lim_{\varepsilon\to 0}\frac{1}{|[\varepsilon\mathbf{t}_1,\varepsilon\mathbf{t}_2,\varepsilon\mathbf{t}_3]|}\int_{\mathbf{r}+[\varepsilon\mathbf{t}_1,\varepsilon\mathbf{t}_2,\varepsilon\mathbf{t}_3]}\rho\,\mathrm{dV} = \rho(\mathbf{r})\det(\mathbf{t_1},\mathbf{t_2},\mathbf{t_3}),
\end{aligned}$$

electric field energy density:	u_{elec}	$=$	$\mathbf{E}\cdot\mathbf{D}/2$
magnetic field energy density:	u_{magn}	$=$	$\mathbf{H}\cdot\mathbf{B}/2$
energy flux density(Poynting-vector):	$\mathbf{S}$	$=$	$\mathbf{E}\times\mathbf{H}$

Table 1.2: Field products in classical notation. For time-harmonic fields the values are averaged in time, see Jackson [60].

where $[\varepsilon\mathbf{t}_1, \varepsilon\mathbf{t}_2]$ denotes the oriented surface in $\mathbf{R}^3$ spanned by $\varepsilon\mathbf{t}_1$ and $\varepsilon\mathbf{t}_2$ with area size $|[\varepsilon\mathbf{t}_1, \varepsilon\mathbf{t}_2]|$. The volume $[\varepsilon\mathbf{t}_1, \varepsilon\mathbf{t}_2, \varepsilon\mathbf{t}_3]$ is defined accordingly. Here, the position vector $\mathbf{r}$ and the vector $\mathbf{t}$ are elements in $\mathbf{R}^3$, but in the differential geometry theory $\mathbf{r}$ and $\mathbf{t}$ are defined in different spaces. The position $\mathbf{r}$ lives on an oriented manifold M (here $M = \mathbf{R}^3$) and $\mathbf{t}$ lives in the linear tangential space $T_{\mathbf{r}}M$ to M at $\mathbf{r}$, see Jänich [61].

We denote the space of alternating k-forms on the vector space $T_{\mathbf{r}}M$ by $\text{Alt}^k T_{\mathbf{r}}M$ and the space of differential k-forms by $\Omega^k M$, see again Jänich [61]. The above equations define the electric field as a differential 1-form $\mathbf{e} \in \Omega^1 M$, the magnetic flux density as a differential 2-form $\mathbf{b} \in \Omega^2 M$, and the charge density as a differential 3-form $\rho \in \Omega^3 M$. Differential 0-forms are the scalar functions on the manifold M.

In the following we will often restrict a differential form on the boundary of a domain. The boundary of a sufficiently smooth manifold $M \subset \mathbf{R}^3$ is a 2-dimensional sub-manifold $N = \partial M$. The tangent space $T_{\mathbf{r}}N$ to N at $\mathbf{r}$ is a sub-space of $T_{\mathbf{r}}M$ and so the restriction (or trace) of a k-form $\eta \in \Omega^k M$ as a k-form $\eta_{|\partial M} \in \Omega^k N$ is naturally defined by $\eta_{|\partial M}(\mathbf{r})[t_1, \ldots, t_k] = \eta(\mathbf{r})[t_1, \ldots, t_k]$, with $t_1, \ldots, t_k \in T_{\mathbf{r}}N \subset T_{\mathbf{r}}M$.

The exterior calculus defines the integral of a k-form in $\Omega^k N$ over a k-dimensional manifold $N \subset \mathbf{R}^3$. The integrals in Table 1.1 are notated as

$$\int_\gamma \mathbf{e}, \quad \int_A \mathbf{b}, \quad \int_V \rho, \quad \textit{etc.}$$

Here, γ is an oriented curve (1D-manifold), A is an oriented surface (2D-manifold) and V is an oriented volume.

Wedge products and exterior derivatives

Table 1.2 gives bilinear field products as they appear in electromagnetic field theory. The first two examples are products between a 1-form and a 2-form with a 3-form as result. The last example is a product of two 1-forms. The result is a 2-form (flux density) which gives the energy flux of the electromagnetic field through an infinitesimal surface. These examples are special

cases of wedge products defined within the exterior calculus,

$$\begin{aligned} \wedge_{r,s} : \Omega^r M \times \Omega^s M &\rightarrow \Omega^{r+s} M \\ (\eta, \zeta) &\mapsto \eta \wedge_{r,s} \zeta. \end{aligned}$$

As usual, we drop the sub-indices for the product $\wedge$ in the following. The product of a 0-form with a k-form is the scalar multiplication. The wedge product is associative, $(\eta \wedge \zeta) \wedge \zeta = \eta \wedge (\zeta \wedge \zeta)$, and anti-commutative, $\zeta \wedge \eta = (-1)^{r \cdot s} \eta \wedge \zeta$.

As a next step we transfer the classical differential operators ∇, $\nabla\times$, and $\nabla\cdot$ to the exterior calculus. A look on Maxwell's equations (1.1) reveals that applying the $\nabla\times$ operator on a 1-form gives a 2-form, see equation (1.1a) or equation (1.1b). Applying the $\nabla\cdot$ operator on a 2-form yields a 3-form, see equation (1.1c) or equation (1.1d). Additionally, from electrostatics we know that $\mathbf{E}_{\text{stat}} = \nabla\phi(\mathbf{r})$, with the scalar potential function ϕ which is a 0-form. Hence a 0-form is mapped to a 1-form by applying the gradient operator. We observe that for a k-form the action of a specific differential operators yields a $(k+1)$-form. In general the exterior calculus defines the exterior derivatives,

$$d_k : \Omega^k M \rightarrow \Omega^{k+1} M.$$

Again, we will henceforth drop the sub-index for the exterior derivative d. Later we will make use of the following identities:

$$d \circ d\eta = 0, \tag{1.43a}$$

$$d(\eta \wedge \zeta) = d\eta \wedge \zeta + (-1)^k \eta \wedge d\zeta, \text{ for } \eta \in \Omega^k M. \tag{1.43b}$$

The first equation (1.43a) reflects that a gradient field is curl free ($\nabla \times \nabla = 0$) and that a rotational field is divergence free ($\nabla \cdot \nabla\times = 0$). The second equation (1.43b) covers the classical product rules in one single equation that is, $\nabla(fg) = \nabla f g + f \nabla g$, $\nabla \times (f\mathbf{E}) = \nabla f \times \mathbf{E} + f \nabla \times \mathbf{E}$, $\nabla \cdot (f\mathbf{D}) = \nabla f \cdot \mathbf{D} + f \nabla \cdot \mathbf{D}$, $\nabla \cdot (\mathbf{E} \times \mathbf{H}) = \nabla \times \mathbf{E} \cdot \mathbf{H} - \mathbf{E} \cdot \nabla \times \mathbf{H}$.

Material tensors ε, μ and the Hodge operator

The constitutive equations (1.2) give us a hint of how the material tensors μ and ε act on the differential forms. From equation (1.2a) we see that the permittivity tensor ε maps the 1-form $\mathbf{e}$ on the 2-form $\mathbf{d}$ and we therefore consider ε as an operator $\varepsilon : \Omega^1 M \rightarrow \Omega^2 M$. The permeability tensor μ acts in the same way (equation (1.2b)).

We are now in the position to write Maxwell's equation (1.4) and the divergence condition (1.3d) for the electric field in differential form,

$$d\mu^{-1}d\mathbf{e} - \omega^2\varepsilon\mathbf{e} = i\omega\mathbf{j}_i, \tag{1.44a}$$

$$d\varepsilon\mathbf{e} = -\frac{i}{\omega}d\mathbf{j}_i. \tag{1.44b}$$

The expression on the right hand side of equation (1.44a) is a 2-form and so is the expression on the left hand side as one concludes when observing the action of the operators μ^{-1} and d. The expressions on both sides of equation (1.44b) are 2-forms.

The scalar Helmholtz equation in acoustics, see for example Ihlenburg [59], is given by

$$-\nabla \cdot c_{2,H}\nabla u - \omega^2 c_{0,H}u = 0.$$

From the types of the differential operators involved (∇ and $\nabla\cdot$), we conclude that u is a (scalar) 0-form and that $c_{2,H}\nabla u$ is a 2-form. Consequently, $c_{0,H}u$ is a 3-form. In exterior calculus we can cast the Helmholtz equation and Maxwell's equations (1.44a) into the form

$$(-1)^{k+1}dc_2 d\eta - \omega^2 c_0\eta = 0.$$

Here, the k–form η is a 0-form for the Helmholtz case and a 1-form for the Maxwell case. In a unified way the material operators act like

$$\begin{aligned} c_0 : \Omega^k M &\rightarrow \Omega^{n-k}M, \\ c_2 : \Omega^{k+1} M &\rightarrow \Omega^{n-k-1}M. \end{aligned}$$

We remark that the material tensors are closely related to the Hodge operator $*$ defined on Riemann manifolds, see Jänich [61] and Teixeira [46, 104]. With the introduction of the co-derivative δ the classical Maxwell's equations can be cast into the exterior calculus in a slightly different way than above. As in [118] we prefer to use the explicit definition of the material tensors c_0 and c_2 given above in order to restrict the theoretical considerations to a minimum.

Together with Stokes's theorem (Jänich [61]),

$$\int_M d\eta = \int_{\partial M}\eta,$$

the product rule (1.43b) yields the *partial integration formula*

$$(-1)^{k+1}\int_M \eta \wedge dc_2 d\mathbf{e} = \int_M d\eta \wedge c_2 d\mathbf{e} - \int_{\partial M}\eta \wedge c_2 d\mathbf{e}. \tag{1.45}$$

In the following we only deal with Maxwell's equations in 3D thus setting $k = 1$. We also prefer to use the notation ε and μ^{-1} for the material tensors.

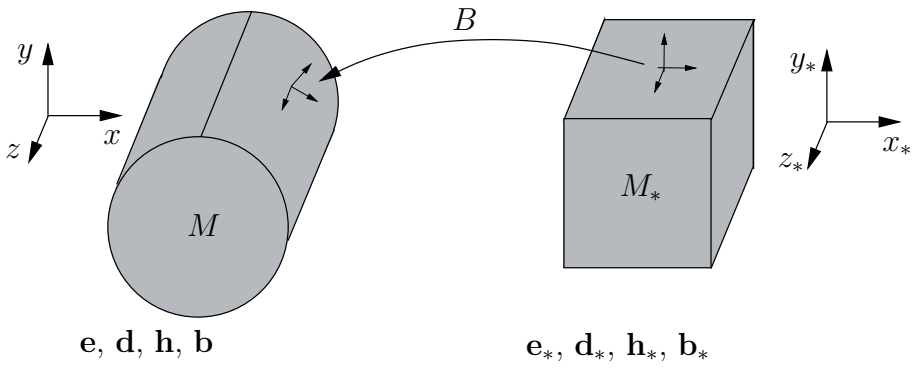

Figure 1.6: Sketch of a coordinate transform. Here, we consider the manifold M as a physical body embedded into $\mathbf{R}^3$ with coordinates (x, y, z). The manifold M_* together with the isomorphism B is used to define new coordinates (x_*, y_*, z_*) for M. The isomorphism B defines locally a linear mapping of the tangent spaces at identified points. The transformed fields $\mathbf{e}_*$, *etc.* yield the same observable data, e.g. the same integral values.

Coordinate transformations

The definition of a k-form by its action on the tangential vectors $\mathbf{t}_1, \ldots, \mathbf{t}_k \in T_{\mathbf{r}}M$ is independent of the chosen coordinate system. However, when doing numerics one is forced to fix a coordinate system. We will see that the definition and implementation of transparent boundary conditions are often easier when not using the standard Euclidean coordinate system $\mathbf{r} = (x, y, z)$.

To define the coordinate change for differential forms we regard two manifolds M and M_* of same dimension n, see Figure 1.6. Both manifolds are identified via a piecewise smooth isomorphism B. We assume that M and M_* are embedded in $\mathbf{R}^3$ equipped with Euclidean coordinates $\mathbf{r} = (x, y, z)$ and $\mathbf{r}_* = (x_*, y_*, z_*)$, respectively. At each point the isomorphism $\mathbf{r} = B(\mathbf{r}_*)$ defines a linear mapping $J(\mathbf{r}_*) : T_{\mathbf{r}_*}M_* \to T_{\mathbf{r}}M$ from the tangent space to M_* at $\mathbf{r}_*$ onto the tangent space to M at $\mathbf{r}$. Clearly, this is the Jacobian when $n = 3$. For a k-form $\eta \in \Omega^k M$ the transformed (*pulled back*) k-form $\eta_* \in \Omega^k M_*$ is defined as

$$\eta_*(\mathbf{r}_*)[\mathbf{t}_{1,*}, \ldots, \mathbf{t}_{k,*}] \quad = \quad \eta(\mathbf{r})[J(\mathbf{r}_*)\mathbf{t}_1, \ldots, J(\mathbf{r}_*)\mathbf{t}_k], \forall \mathbf{t}_{1,*}, \ldots, \mathbf{t}_{k,*} \in T_{\mathbf{r}_*}M_*,$$

so it gives the same result when applied on the transformed tangent vectors as the original k-form applied on the original tangent vectors. One shows the

following important identities (see Jänich [61]),

$$\begin{aligned} \int_{N_*} \eta_* &= \int_N \eta, && (1.46a)\\ d\eta_* &= d\eta, && (1.46b)\\ \eta_* \wedge \zeta_* &= (\eta \wedge \zeta)_*. && (1.46c) \end{aligned}$$

In the first equation (1.46a) $N \subset M$ is a k-dimensional sub-manifold of M and $\eta \in \Omega^k M$.

Equation (1.46a) reflects the fact that the physical observables (=real numbers) are independent on the chosen coordinates. The two last equations (1.46b), (1.46c) guarantee that the application of the wedge operators and the differential operators does not depend on the coordinate system.

It remains to transform the material tensor ε and μ. We define

$$\begin{aligned} \varepsilon_* \eta_* &= (\varepsilon\eta)_*, && (1.47a)\\ \mu_* \eta_* &= (\mu\eta)_*. && (1.47b) \end{aligned}$$

Hence, applying a material tensor and pulling back commutes. With this definition the transformed electric field $\mathbf{e}_*$ to a solution $\mathbf{e} \in \Omega^3 M$ of Maxwell's equations (1.44) meets the transformed Maxwell's equations,

$$\begin{aligned} d\mu_*^{-1} d\mathbf{e}_* - \omega^2 \varepsilon_* \mathbf{e}_* &= i\omega \mathbf{j}_{i,*}, && (1.48)\\ d\varepsilon_* \mathbf{e}_* &= -\frac{i}{\omega} d\mathbf{j}_{i,*}. && (1.49) \end{aligned}$$

Remark 1.1 For completeness we bring the transformed Maxwell's equations back to classical notation. The electric field (1-form) is transformed as $\mathbf{E}_* = J^T \mathbf{E}$ and a 2-form is transformed as $\mathbf{D}_* = |J| J^{-1} \mathbf{D}$, where J is the Jacobian as defined above. For simplicity we assume $\mathbf{j}_i = 0$. and introduce $\nabla_* = (\partial x_*, \partial y_*, \partial z_*)^T$. We have

$$\nabla_* \times \left(|J| J^{-1} \mu J^{-T} \right)^{-1} \nabla_* \times \mathbf{E}_* - \omega^2 |J| J^{-1} \varepsilon J^{-T} \mathbf{E}_* = 0.$$

Here, we used the *canonical* transformed vector $\mathbf{E}_*$. When using the original vector $\mathbf{E}(\mathbf{r}_*) = \mathbf{E}(\mathbf{r})$ one gets,

$$\nabla_* \times \left(|J| J^{-1} \mu J^{-T} \right)^{-1} \nabla_* \times J^T \mathbf{E} - \omega^2 |J| J^{-1} \varepsilon \mathbf{E} = 0.$$

Chapter 2

Scattering problems

A scattering problem consists of three major components: the illumination system, the scattering object and the detector. This chapter is devoted to the mathematical description of the light scattering off the considered object. The illumination system is reduced to an idealized light source and the detector is not considered at all. However, for later purposes when we deal with the far field extraction it indispensable to develop a basic understanding of the involved length scales in a scattering experiment.

We refer to Figure 2.1. The overall scattering problem setup is very complicated. In reality, the illumination system and the detector consist of a complex arrangement of a large number of lenses, apertures and other opto-electronical devices, cf. Wong [114]. This way, light traveling in different directions is collected in the detector and focused on a photosensitive device. To deal with a scattering problem numerically a cascade of idealizations is necessary. A keystone for these simplifications is the separation of the microscopic and macroscopic length scale effects.

Our first idealization concerns the nature of the emitted light. As in the previous chapter we only consider a monochromatic light source, so that the electromagnetic field depends harmonically on time with an angular frequency ω. In practice, such a pure, perfectly coherent light source is never encountered due to transient effects, thermal fluctuation, *etc.* Therefore, a realistic illumination model requires a statistical description of the light source as explained in Wolf and Mandel [72, 112].

As a second idealization we separate the scatterer from its surroundings. We suppress any interferences of the outgoing field $\mathbf{e}_{\text{out}}$ with the illumination system and the detector. Since the scatterer is directly placed on a substrate it is necessary to take the interactions with the substrate into account. But we also disregard any interactions with other obstacles placed on the substrate as well.

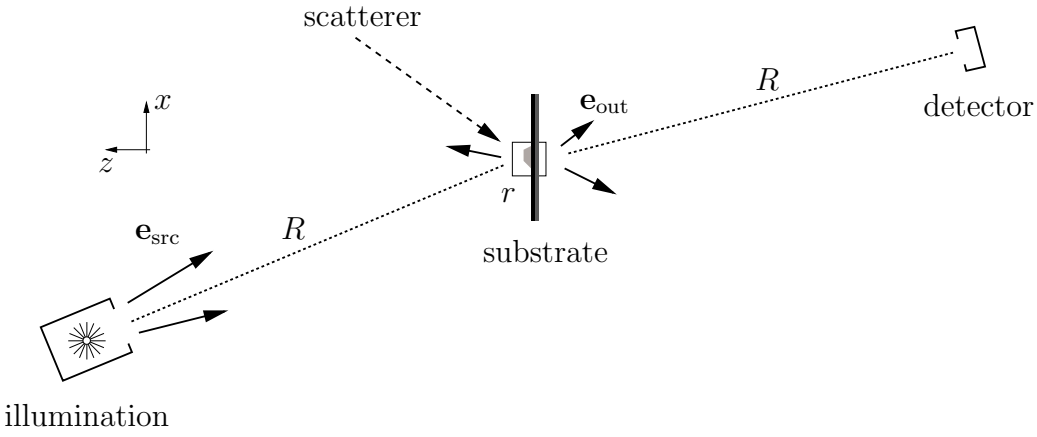

Figure 2.1: Principle setup of a scattering experiment. The scatterer has a microscopic length scale r, whereas the illumination system and the detector are placed in a far distance $R \gg r$ to the scatter.

The third idealization utilizes that $r \ll R$ so that we are allowed to replace the source field $\mathbf{e}_{\text{src}}$ by its asymptotic expansion $\mathbf{e}_{\text{inc}} \sim \mathbf{e}_{\text{src}}$. For example, a divergent spherical wave emanated from a far distant dipole looks like a plane wave front in the vicinity of the scatterer.

After applying these idealizations we are in the situation as depicted in Figure 2.2 in case of a 2D problem. Since no impressed sources are present, the total electric field $\mathbf{e}$ stimulated by the incoming field $\mathbf{e}_{\text{inc}}$ satisfy equation (1.44a) in the entire space $\mathbf{R}^3$ with a zero right hand side,

$$d\mu^{-1}d\mathbf{e} - \omega^2\varepsilon\mathbf{e} \;=\; 0. \tag{2.1}$$

We drop the divergence condition (1.44b) since a solution $\mathbf{e}$ to the above equation satisfies $d\varepsilon\mathbf{e} = 0$ as a consequence of the identity $d \circ d = 0$, see equation (1.43a).

Since the incoming field $\mathbf{e}_{\text{inc}}$ is the asymptotic form of the idealized illumination it does not satisfy Maxwell's equations within the substrate. Consequently, the outgoing field $\mathbf{e}_{\text{out}} = \mathbf{e} - \mathbf{e}_{\text{inc}}$ is not a solution to Maxwell's equations in the exterior domain as well. This makes the outgoing field $\mathbf{e}_{\text{out}}$ unsuitable for a discretization with the PML method or the pole condition method. To cure that we choose a different splitting of the total field, $\mathbf{e} = \mathbf{e}_{\text{ref}} + \mathbf{e}_{\text{sc}}$, into a *reference field* and a *scattered field* as follows:

The reference field $\mathbf{e}_{\text{ref}}$ is the field which is stimulated by the incoming field in the substrate without the scatterer. Hence, $\mathbf{e}_{\text{ref}}$ is a solution to Maxwell's equations in the entire exterior domain and comprises the incoming field $\mathbf{e}_{\text{inc}}$. It may contain outward traveling waves but no incoming traveling wave other

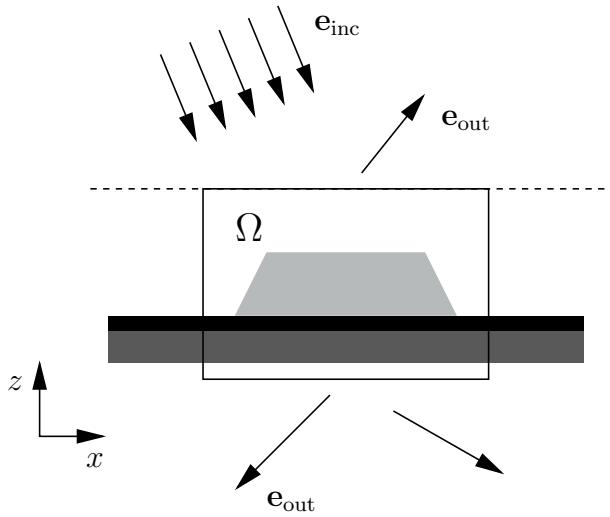

Figure 2.2: Idealized scattering problem: The incoming field is given as the asymptotic form of a complex light source. The scatterer painted in light gray only interacts with the substrate.

than the prescribed field $\mathbf{e}_{\text{inc}}$. To give an example, we regard Figure 2.2 and assume that the incoming field $\mathbf{e}_{\text{inc}}$ is a plane wave. Without the scatterer, the incoming plane wave propagates through the layered media. We derived the exact solution to this propagation in a layered medium in Section 1.2 of the previous chapter. This gives our reference field $\mathbf{e}_{\text{ref}}$ which is indeed a solution to Maxwell's equations in the entire exterior domain and which comprises the original incoming field $\mathbf{e}_{\text{inc}}$.

We are now in the position to give a first definition of a scattering problem.

Problem 2.1 (scattering problem)**.** *Let a reference field* $\mathbf{e}_{\text{ref}}$ *be given, which satisfies Maxwell's equations in the exterior of a bounded domain* $\Omega \subset \mathbf{R}^3$,

$$d\mu^{-1} d\mathbf{e}_{\text{ref}} - \omega^2 \varepsilon \mathbf{e}_{\text{ref}} \;=\; 0 \text{ in } \Omega_{\text{ext}} = \mathbf{R}^3 \setminus \Omega.$$

We seek the total field solution $\mathbf{e}$ *satisfying Maxwell's equations in the entire space* $\mathbf{R}^3$,

$$d\mu^{-1} d\mathbf{e} - \omega^2 \varepsilon \mathbf{e} \;=\; 0 \text{ in } \mathbf{R}^3$$

so that the scattered field $\mathbf{e}_{\text{sc}} = \mathbf{e} - \mathbf{e}_{\text{ref}}$ *defined in the exterior domain* Ω_{ext} *is outward radiating.*

The precise definition of the term *outward radiating* is discussed in the section after next. In the next section we will restrict the shape of the computational domain Ω to *admissible geometries.*

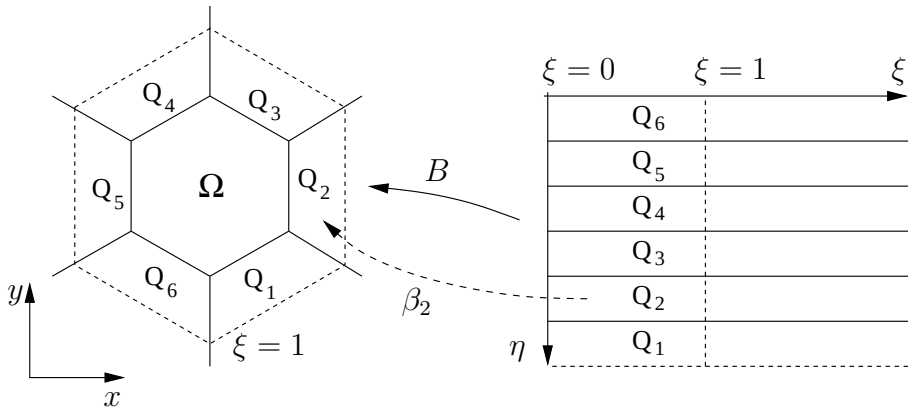

Figure 2.3: Admissible geometry for a 2D domain. The exterior domain is composed of infinite quadrilaterals. Each quadrilateral Q_j is the image of an infinite reference quadrilateral under an affine bilinear mapping β_j. These local mappings are combined to a global mapping $B : [\eta_{\min}, \eta_{\max}]_\pi \times [0, \infty) \to \Omega_{\text{ext}}$ so that a distance coordinate ξ and an angular–like coordinate η are globally defined.

2.1 Admissible geometries

In the scattering problem formulation it is a crucial point to decompose the electromagnetic field into outgoing and incoming waves. Before we can start with this, it is necessary to define outward coordinate directions in a geometrical sense. For examples, if Ω is a ball, one may equip the exterior domain with a spherical coordinate system (φ, ϑ, r), where r is the distance to the sphere and serves as the outward coordinate direction.

To generalize this, we will regard geometries which allows for the definition of a generalized distance coordinate ξ in the exterior domain. We restrict ourselves to domains Ω which can be represented by a finite element mesh with straight edges and plane faces.

For the definition of admissible geometries with a single outward coordinate direction we refer to Schmidt [98] and Kettner [66]. To cover tensor product-like exterior domains as well, we propose a more general approach here. In these cases we use multiple distance coordinates, which are not defined in the entire exterior domain.

The definition of admissible geometries given below for 3D domains is very technical. We therefore exemplify the construction for the 2D case first. Figure 2.3 shows an admissible geometry in 2D. The computational domain is a convex polygon. Each boundary segment is an edge of an infinite

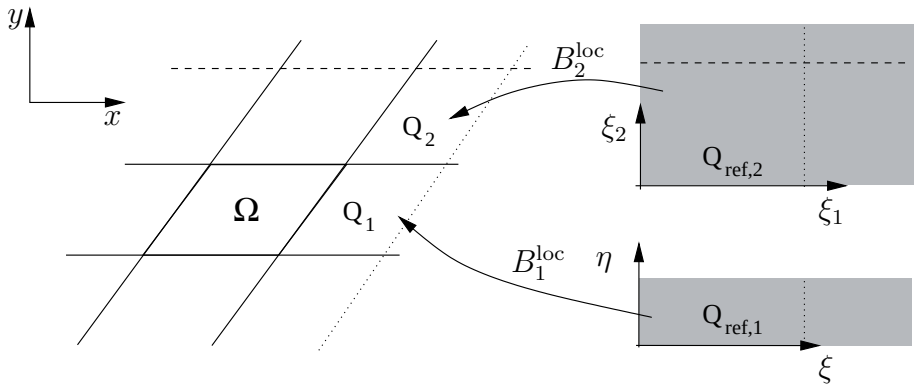

Figure 2.4: Admissible geometry for a 2D domain (tensor product geometry). We allow for quadrilaterals with two infinite coordinate directions. Multiple distance–like coordinate directions are present. As indicated by the dashed and dotted lines these distance–like coordinates are continuous across quadrilateral boundaries.

quadrilateral. Two adjacent quadrilaterals share a common infinite edge. We demand that there exists a continuous and piecewise affine bilinear coordinate transformation $B : [\eta_{\min}, \eta_{\max}]_\pi \times [0, \infty) \to \Omega_{\mathrm{ext}}$, cf. Figure 2.3. $[\eta_{\min}, \eta_{\max}]$ is a periodified interval ($\eta_{\min}$ and $\eta_{\max}$ are identified). The coordinate $\eta \in [\eta_{\min}, \eta_{\max}]_\pi$ is a generalized angle parameterizing the polygonal boundary $\partial\Omega$. ξ is a globally defined distance variable.

Another type of an admissible geometry in 2D is depicted in Figure 2.4. There the exterior domain is split into compartments, which are mapped locally on simply infinite reference quadrilaterals $Q_{1,\mathrm{ref}} = \{(\eta, \xi) \in \mathbf{R}^2 \,|\, \eta, \xi \geq 0,\, \eta \leq 1\}$ or on doubly infinite reference quadrilaterals $Q_{2,\mathrm{ref}} = \{(\xi_1, \xi_2) \in \mathbf{R}^2 \,|\, \xi_1, \xi_2 \geq 0\}$. This way on each quadrilateral one or two distance–like coordinates are defined locally. We again demand that these coordinates match continuously for adjacent quadrilaterals.

We now address the 3D case and give a general definition of the admissible geometries. We introduce the following infinite *reference elements*:

$$
\begin{aligned}
P_{\mathrm{ref}} &= \{(\eta_1, \eta_2, \xi_1) \in \mathbf{R}^3 \,|\, 1 - \eta_1 - \eta_2 \leq 1,\, \eta_1, \eta_2, \xi_1 \geq 0\} \quad \textit{(infinite prism)},\\
B^{(1)}_{\mathrm{ref}} &= \{(\eta_1, \eta_2, \xi_1) \in \mathbf{R}^3 \,|\, \eta_1, \eta_2 \leq 1,\, \eta_1, \eta_2, \xi_1 \geq 0\} \quad \textit{(simply infinite brick)},\\
B^{(2)}_{\mathrm{ref}} &= \{(\eta, \xi_1, \xi_2) \in \mathbf{R}^3 \,|\, \eta \leq 1,\, \eta, \xi_1, \xi_2 \geq 0\} \quad \textit{(doubly infinite brick)},\\
B^{(3)}_{\mathrm{ref}} &= \{(\xi_1, \xi_2, \xi_3) \in \mathbf{R}^3 \,|\, \xi_1, \xi_2, \xi_3 \geq 0\} \quad \textit{(triply infinite brick)}.
\end{aligned}
$$

An *infinite cell* is a sub–manifold $T \subset \mathbf{R}^3$ which is the image of an orientation preserving, multi-linear isomorphism β_T from an infinite reference element into $\mathbf{R}^3$.

A cell T gives rise to the definition of rays. For example, if T is a doubly infinite brick a ray $r : [0, \infty) \to \mathbf{R}^3$ is defined by $r(\cdot) = T(\eta_1, \xi_1, \cdot)$ for fixed coordinates η_1, ξ_1. Other rays are defined accordingly by selecting an infinite coordinate ξ_k and fixing the other coordinates.

We call an edge, triangle, quadrilateral finite if it is bounded.

Definition 2.1 (admissible geometries)**.** *A domain Ω is admissible, if the following conditions are satisfied:*

1. *Ω is connected, convex and bounded.*
2. *The exterior domain $\Omega_{\text{ext}} = \mathbf{R}^3 \setminus \Omega$ is a finite union of non-overlapping infinite cells such that,*
   - *i) The intersection of two infinite cells is a common vertex, edge or quadrilateral.*
   - *ii) An infinite cell's vertices, finite edges, finite triangles and finite quadrilaterals lie on the boundary $\partial\Omega$.*
   - *iii) Common rays of adjacent cells have the same parameterization. More precisely, let r_1 and r_2 denote rays defined on different cells. If $\text{rg}(r_1) = \text{rg}(r_2)$ then $r_1 = r_2$ that is, $r_1(\tau) = r_2(\tau)$ for all $\tau \in [0, \infty)$.*
   - *iv) The material tensors ε and μ are constant scalars on each infinite cell.*

Condition 2iii) is called *ray matching condition* and assures that a distance like variable ξ_k defined on a cell is continuous across cell boundaries. Figure 2.5 sketches an admissible domain in 3D.

2.2 The pole condition

The pole condition concept as introduced by Schmidt [98] allows for a characterization of outgoing waves for admissible geometries.

Before we start with the pole condition concept, we regard the homogeneous exterior domain, so that ε and μ are constant scalars. This yields a constant wave number $k = \omega\sqrt{\mu\varepsilon}$ in the entire exterior domain. From physics, one sees that a field $\mathbf{e}$ is outward radiating if and only if it satisfies the radiation condition

$$\lim_{\xi \to \infty} \xi^{\frac{d-1}{2}} \mu^{-1} (d\mathbf{e}(\xi\hat{x}) - ik\hat{x} \wedge \mathbf{e}(\xi\hat{x})) \;=\; 0, \tag{2.2}$$

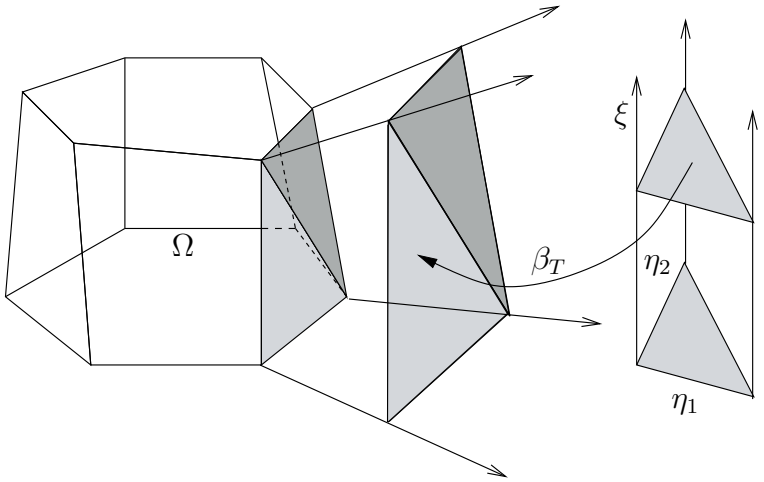

Figure 2.5: Sketch of an admissible geometry in 3D. An infinite cell is mapped onto the corresponding reference element. Here a prism is mapped onto P_{ref} by the transformation β_T^{-1}.

uniformly for any direction $\hat{x} \in \mathbf{R}^d$, $\|\hat{x}\| = 1$. Here $d = 1, 2, 3$ is the space dimension. This equation comprises the Sommerfeld radiation condition for the scalar case as well as the Silver–Müller radiation condition for Maxwell's equations, see Monk [79, p. 226].

In a numerical simulation, the radiation condition (2.2) can be used to impose boundary conditions on a truncated domain. However, this boundary condition is not transparent, because an outgoing wave only satisfies the Sommerfeld condition (2.2) asymptotically for large computational domains. This renders a numerical simulation intractable.

From a theoretical point of view, the Sommerfeld radiation condition (2.2) characterized outgoing waves and is the corner stone for a mathematical theory on scattering problems in many textbooks, see for example Colton and Kress [32] or Nédélec [84]. Since a Sommerfeld-like radiation condition is not available for general inhomogeneous exterior domains, a new approach towards the characterization of outgoing waves is needed for numerical simulations and theoretical purposes as well. This gives the motivation for the pole condition concept.

To explain the principle idea of the pole condition concept we consider the 1D case,

$$\begin{aligned} -u''(x) - k^2 u(x) &= 0, \quad x \in [0, \infty) \\ u(0) &= 1. \end{aligned}$$

The solution has the form $u(x) = Ae^{ikx} + Be^{-ikx}$ with $A + B = 1$. Clearly, for u to satisfy the above radiation condition (2.2) we conclude that $B = 0$, so that $A = 1$.

We see that the general solution decomposes into an outgoing wave Ae^{ikx} and an incoming wave Be^{-ikx}. For this simple example the decomposition into outgoing and incoming parts is explicitly given. Because this is not the case for general geometries, we look for another characterization of outgoing and incoming waves.

As observed by Schmidt, the Laplace transform of u reflects this decomposition into outgoing and incoming waves, as we will explain now. The Laplace transform

$$U(s) = \int_0^\infty u(x)e^{-sx}dx = \frac{A}{s - ik} + \frac{B}{s + ik}$$

exhibits two poles $s_\pm = \pm ik$ and we conclude that a wave is outgoing when its Laplace transform is holomorphic in the lower complex half space.

We now generalize this idea to higher space dimensions and to Maxwell's equations. We assume within this subsection that the exterior domain is equipped with coordinates which define a global distance–like coordinate ξ. Let us regard a cell T of Ω_{ext} as in Definition 2.1 for admissible geometries. For $\tau > 0$ we define the displaced cell T_τ by

$$T_\tau \;=\; \{\mathbf{x} \in \Omega_{\text{ext}} \,|\, \mathbf{x} = \beta_T(\eta_1, \eta_2, \xi + \tau),\ (\eta_1, \eta_2, \xi) \in \beta_T^{-1}(T)\}.$$

The displaced exterior domain $\Omega_{\text{ext},\tau}$ is defined piecewise. The ray matching condition in Definition 2.1 assures that the so defined isomorphism $D_\tau : \Omega_{\text{ext}} \to \Omega_{\text{ext},\tau}$ is continuous and piecewise affine bilinear.

For a field $\mathbf{e}$ defined in Ω_{ext}, $\mathbf{e}_\tau$ denotes the differential form pulled back from $\Omega_{\text{ext},\tau}$ to Ω_{ext} via the isomorphism D_τ. The pulled back material tensor ε_τ is defined as in equation (1.47a). Given a test function φ we define the scalar function

$$u_{\mathbf{e},\varepsilon,\varphi}(\tau) \;=\; \int_{\Omega_{\text{ext}}} \overline{\varphi} \wedge \varepsilon_\tau \mathbf{e}_\tau. \tag{2.3}$$

Definition 2.2 (pole condition)**.** *Let a field $\mathbf{e}_{\text{sc}}$ be given which solves Maxwell's equations in the exterior of an admissible domain $\Omega \subset \mathbf{R}^3$,*

$$d\mu^{-1}d\mathbf{e}_{\text{sc}} - \omega^2\varepsilon\mathbf{e}_{\text{sc}} \;=\; 0 \text{ in } \Omega_{\text{ext}} = \mathbf{R}^3 \setminus \Omega.$$

$\mathbf{e}_{\text{sc}}$ is called outward radiating if the Laplace transform

$$U_{\mathbf{e},\varepsilon,\varphi}(s) \;=\; \int_0^\infty u_{\mathbf{e}_{\text{sc}},\varepsilon,\varphi}(\tau)e^{-s\tau}d\tau$$

of $u_{\mathbf{e}_{\mathrm{sc}},\varepsilon,\varphi}$ as defined in equation (2.3) has a holomorphic extension into the lower complex half plane for all test functions φ.

As shown in Hohage et al. [56] the pole condition is equivalent to the *Sommerfeld radiation condition* for homogeneous exterior domains and the scalar Helmholtz equation. Arens and Hohage [7] showed that for rough surface problems the pole condition is equivalent to the *upward propagating radiation condition*.

We now address the inverse Laplace transformation of $U_{\mathbf{e}_{\mathrm{sc}},\varepsilon,\varphi}(s)$ to recover $u_{\mathbf{e}_{\mathrm{sc}},\varepsilon,\varphi}(\tau)$. The results will be useful for the theoretical motivation of the adaptive PML method later. Because the field $\mathbf{e}_{\mathrm{sc}}$ is bounded in the exterior domain for non-active materials we are allowed to apply the inverse Laplace transform theorem. This yields

$$u_{\mathbf{e}_{\mathrm{sc}},\varepsilon,\varphi}(\tau) = \frac{1}{2\pi i}\int_{\epsilon-i\infty}^{\epsilon+i\infty} U_{\mathbf{e}_{\mathrm{sc}},\varepsilon,\varphi}(s)e^{s\tau}\mathrm{d}s.$$

In the following we use that $|U_{\mathbf{e}_{\mathrm{sc}},\varepsilon,\varphi}(s)| \leq C/|s|$ for large values of $|s|$ without giving a proof for this estimate here, cf. Schmidt [98]. We further assume that $U_{\mathbf{e}_{\mathrm{sc}},\varepsilon,\varphi}(s)$ is holomorphic in the upper complex half space for $\mathrm{Im}(s) > k_{\max}$. We deform the integration path in the above inverse Laplace transform integral as shown in Figure 2.6. Precisely, we have

$$\begin{aligned}
2\pi i u_{\mathbf{e}_{\mathrm{sc}},\varepsilon,\varphi}(\tau) &= \lim_{R\to\infty}\int_{\epsilon-iR}^{\epsilon+iR} U_{\mathbf{e}_{\mathrm{sc}},\varepsilon,\varphi}(s)e^{s\tau}\mathrm{d}s \\
&= \lim_{R\to\infty}\int_{\epsilon-R-i\epsilon}^{\epsilon-i\epsilon} U_{\mathbf{e}_{\mathrm{sc}},\varepsilon,\varphi}(s)e^{s\tau}\mathrm{d}s + \int_{\epsilon-i\epsilon}^{\epsilon+ik_{\max}+i\epsilon} U_{\mathbf{e}_{\mathrm{sc}},\varepsilon,\varphi}(s)e^{s\tau}\mathrm{d}s + \\
&\qquad \int_{\epsilon+ik_{\max}+i\epsilon}^{\epsilon-R+ik_{\max}+i\epsilon} U_{\mathbf{e}_{\mathrm{sc}},\varepsilon,\varphi}(s)e^{s\tau}\mathrm{d}s + \int_C U_{\mathbf{e}_{\mathrm{sc}},\varepsilon,\varphi}(s)e^{s\tau}\mathrm{d}s.
\end{aligned}$$

For $\tau > 0$, the integral over the two arcs C disappears for $R \to \infty$. This gives

$$\begin{aligned}
2\pi i u_{\mathbf{e}_{\mathrm{sc}},\varepsilon,\varphi}(\tau) = &\int_{-\infty-i\epsilon}^{\epsilon-i\epsilon} U_{\mathbf{e}_{\mathrm{sc}},\varepsilon,\varphi}(s)e^{s\tau}\mathrm{d}s + \int_{\epsilon+ik_{\max}+i\epsilon}^{-\infty+ik_{\max}+i\epsilon} U_{\mathbf{e}_{\mathrm{sc}},\varepsilon,\varphi}(s)e^{s\tau}\mathrm{d}s + \\
&\int_{\epsilon-i\epsilon}^{\epsilon+ik_{\max}+i\epsilon} U_{\mathbf{e}_{\mathrm{sc}},\varepsilon,\varphi}(s)e^{s\tau}\mathrm{d}s.
\end{aligned}$$

For the sake of a simpler notation we now set $\epsilon = 0$. The arising integrals are understood as the limit values for $\epsilon \searrow 0$. With a change of the integration

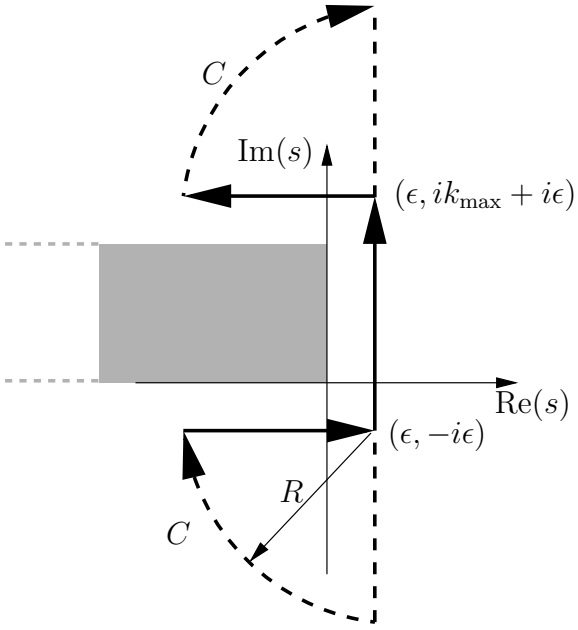

Figure 2.6: Contour as used for the inverse Laplace transform.

variables we end up with

$$u_{\mathbf{e}_{\mathrm{sc}},\varepsilon,\varphi}(\tau) = \frac{1}{2\pi i}\int_0^\infty \Big(U_{\mathbf{e}_{\mathrm{sc}},\varepsilon,\varphi}(-\kappa) - U_{\mathbf{e}_{\mathrm{sc}},\varepsilon,\varphi}(-\kappa + ik_{\max})\tau)e^{ik_{\max}\tau}\Big)e^{-\kappa\tau}\mathrm{d}\kappa + \frac{1}{2\pi}\int_0^{k_{\max}} U_{\mathbf{e}_{\mathrm{sc}},\varepsilon,\varphi}(ik)e^{ik\tau}\mathrm{d}k. \tag{2.4}$$

This formula admits an interesting interpretation: The first integral is an "infinite summation" over evanescent waves. Whereas the second integral gives rise to propagating waves.

2.3 Coupled interior–exterior domain problem

We want to bring the scattering problem (Problem 2.1) into a weak form. We search the total field $\mathbf{e}$ in the space $H_{\mathrm{loc}}(\mathrm{curl}, \mathbf{R}^3)$ such that it satisfies

$$\int_{\mathbf{R}^3} \overline{d\varphi} \wedge \mu^{-1} d\mathbf{e} - \omega^2 \overline{\varphi} \wedge \varepsilon \mathbf{e} \;=\; 0$$

for all $\overline{\varphi} \in H(\mathrm{curl}, \mathbf{R}^3)$ with compact support. We split this integral into an interior and an exterior part and use that $\mathbf{e} = \mathbf{e}_{\mathrm{sc}} + \mathbf{e}_{\mathrm{ref}}$ in Ω_{ext},

$$\int_\Omega \overline{d\varphi} \wedge \mu^{-1} d\mathbf{e} - \omega^2 \overline{\varphi} \wedge \varepsilon \mathbf{e} + \int_{\Omega_{\mathrm{ext}}} \overline{d\varphi} \wedge \mu^{-1} d\mathbf{e}_{\mathrm{sc}} - \omega^2 \overline{\varphi} \wedge \varepsilon \mathbf{e}_{\mathrm{sc}} = - \int_{\Omega_{\mathrm{ext}}} \overline{d\varphi} \wedge \mu^{-1} d\mathbf{e}_{\mathrm{ref}} - \omega^2 \overline{\varphi} \wedge \varepsilon \mathbf{e}_{\mathrm{ref}}.$$

On the right hand side of this equation one finds the prescribed, exciting field $\mathbf{e}_{\mathrm{ref}}$. Since $\mathbf{e}_{\mathrm{ref}}$ satisfies Maxwell's equations in Ω_{ext} the last term in the equation above can be transformed to a boundary term by applying the partial integration formula (1.45),

$$\int_{\Omega_{\mathrm{ext}}} \overline{d\varphi} \wedge \mu^{-1} d\mathbf{e}_{\mathrm{ref}} - \omega^2 \overline{\varphi} \wedge \varepsilon \mathbf{e}_{\mathrm{ref}} = \int_{\partial\Omega_{\mathrm{ext}}} \overline{\varphi} \wedge \mu^{-1} d\mathbf{e}_{\mathrm{ref}} = - \int_{\partial\Omega} \overline{\varphi} \wedge \mu^{-1} d\mathbf{e}_{\mathrm{ref}}.$$

Putting all together we get the coupled exterior–interior domain problem in variational form:

Problem 2.2 (scattering problem in variational form)**.** *Let a reference field* $\mathbf{e}_{\mathrm{ref}} \in H_{\mathrm{loc}}(\mathrm{curl}, \Omega_{\mathrm{ext}})$ *be given which satisfies Maxwell's equations in the exterior of an admissible domain* $\Omega \subset \mathbf{R}^3$,

$$\int_{\Omega_{\mathrm{ext}}} \overline{d\varphi} \wedge \mu^{-1} d\mathbf{e}_{\mathrm{ref}} - \omega^2 \overline{\varphi} \wedge \varepsilon \mathbf{e}_{\mathrm{ref}} = \int_{\partial\Omega_{\mathrm{ext}}} \overline{\varphi} \wedge \mu^{-1} d\mathbf{e}_{\mathrm{ref}}$$

for all test functions $\varphi \in H(\mathrm{curl}, \Omega_{\mathrm{ext}})$ *with compact support. We seek a pair* $(\mathbf{e},\, \mathbf{e}_{\mathrm{sc}}) \in H(\mathrm{curl}, \Omega) \times H_{\mathrm{loc}}(\mathrm{curl}, \Omega_{\mathrm{ext}})$ *such that* $\mathbf{e}_{\mathrm{sc}}$ *is outward radiating and*

$$\int_\Omega \overline{d\varphi} \wedge \mu^{-1} d\mathbf{e} - \omega^2 \overline{\varphi} \wedge \varepsilon \mathbf{e} + \int_{\Omega_{\mathrm{ext}}} \overline{d\varphi} \wedge \mu^{-1} d\mathbf{e}_{\mathrm{sc}} - \omega^2 \overline{\varphi} \wedge \varepsilon \mathbf{e}_{\mathrm{sc}} = \int_{\partial\Omega} \overline{\varphi} \wedge \mu^{-1} d\mathbf{e}_{\mathrm{ref}}, \tag{2.5a}$$

$$(\mathbf{e} - \mathbf{e}_{\mathrm{sc}})|_{\partial\Omega} = \mathbf{e}_{\mathrm{ref}}|_{\partial\Omega} \tag{2.5b}$$

for all $\overline{\varphi} \in H(\mathrm{curl}, \mathbf{R}^3)$ *with compact support.*

We will explain later how to incorporate the Dirichlet jump condition (2.5b) into a modified variational equation.

Remark 2.1 Impressed current sources $\mathbf{j}_i$ can be easily taken into account in an extension of Problem 2.2. For a source not compactly supported in the interior domain Ω the reference field $\mathbf{e}_{\mathrm{ref}}$ must already comprise the sources in the exterior domain Ω_{ext}. This way, one can treat for example δ–distributed sources located in the exterior domain.

2.4 Dirichlet–to–Neumann operator

Our aim is to restrict the interior–exterior domain problem (2.5) onto the bounded domain Ω. To account for the radiation of the field into the exterior domain we need to formulate transparent boundary conditions on $\partial\Omega$. This is done by the so called *Dirichlet–to–Neumann operator* (also named *Calderon map*), see Monk [79, p. 248]. We mention that the numerical methods we will discuss in later chapters do not rely on the DtN–operator. However, the formal restriction of the scattering problem to a bounded domain is very useful for an existence and stability analysis of the scattering problem. Furthermore the effect of the PML method on the interior domain solution can be understood as a perturbation of the exact DtN–operator, see Lassas et al. [68] and Hohage et al. [56].

Let us start with the variational scattering problem (2.5a). We transform the integral over Ω_{ext} into a boundary integral by applying the partial integration formula (1.45),

$$\int_{\Omega_{\text{ext}}} \overline{d\varphi} \wedge \mu^{-1} d\mathbf{e}_{\text{sc}} - \omega^2 \overline{\varphi} \wedge \varepsilon \mathbf{e}_{\text{sc}} = \int_{\partial\Omega} \overline{\varphi} \wedge \mu^{-1} d\mathbf{e}_{\text{sc}} + \int_{\Omega_{\text{ext}}} \overline{\varphi} \wedge d\mu^{-1} d\mathbf{e}_{\text{sc}} - \omega^2 \overline{\varphi} \wedge \varepsilon \mathbf{e}_{\text{sc}}.$$

The last integral term is equal to zero because $\mathbf{e}_{\text{sc}}$ satisfies Maxwell's equations in the exterior domain Ω_{ext}. Inserting this into equation (2.5a) gives

$$\int_{\Omega} \overline{d\varphi} \wedge \mu^{-1} d\mathbf{e} - \omega^2 \overline{\varphi} \wedge \varepsilon \mathbf{e} + \int_{\partial\Omega} \overline{\varphi} \wedge \mu^{-1} d\mathbf{e}_{\text{sc}} = \int_{\partial\Omega} \overline{\varphi} \wedge \mu^{-1} d\mathbf{e}_{\text{ref}}. \qquad (2.6)$$

This equation is only posed on the interior domain Ω but the unknown Neumann–data of the scattered field solution $\mathbf{e}_{\text{sc}}$ is still involved. To proceed with, we assume that an outgoing field in the exterior domain Ω_{ext} is uniquely defined by its Dirichlet data on $\partial\Omega$. This way, we can formally define the DtN–operator

$$\begin{aligned} \text{DtN} : H^{1/2} &\to H^{-1/2} \\ \mathbf{g} &\mapsto (\mu^{-1} d\mathbf{e}_{\text{out}})_{|\partial\Omega}, \end{aligned}$$

where $\mathbf{e}_{\text{out}}$ solves

$$\begin{aligned} d\mu^{-1} d\mathbf{e}_{\text{out}} - \omega^2 \varepsilon \mathbf{e}_{\text{out}} &= 0, \\ \mathbf{e}_{\text{out}}|_{\partial\Omega} &= \mathbf{g} \end{aligned}$$

and is *outward radiating*. Here, $H^{1/2}$ denotes the space of Dirichlet data (trace space) and $H^{-1/2}$ its dual space. For Maxwell's equations the definition

of these spaces is very technical. Now, we eliminate the Neumann term of $\mathbf{e}_{\text{sc}}$ in the above equation (2.6),

$$\begin{aligned}\int_{\partial\Omega} \overline{\varphi} \wedge \mu^{-1} d\mathbf{e}_{\text{sc}} &= \int_{\partial\Omega} \overline{\varphi} \wedge \text{DtN}[\mathbf{e}_{\text{sc}}] \\ &= \int_{\partial\Omega} \overline{\varphi} \wedge \text{DtN}[\mathbf{e} - \mathbf{e}_{\text{ref}}],\end{aligned}$$

and end up with the sought variational problem

$$\begin{aligned}\int_{\Omega} \overline{d\varphi} \wedge \mu^{-1} d\mathbf{e} - \omega^2 \overline{\varphi} \wedge \varepsilon \mathbf{e} + \int_{\partial\Omega} \overline{\varphi} \wedge \text{DtN}(\mathbf{e}) = \\ \int_{\partial\Omega} \overline{\varphi} \wedge (\mu^{-1} d\mathbf{e}_{\text{ref}} + \text{DtN}(\mathbf{e}_{\text{ref}}))\end{aligned} \tag{2.7}$$

for all $\varphi \in H(\text{curl}, \Omega)$.

Remarks 2.1

i) The DtN–operator can be constructed explicitly for a homogeneous exterior domain, see Monk [79, p. 248].

ii) For separable coordinate systems the DtN–operator is numerically available, see for example Keller and Givoli [65] and Grote and Keller [48]. The DtN–operator is a non–local operator on $\partial\Omega$. In a numerical discretization with finite elements or finite differences this leads to a dense block with a dimension equal to the number of discretization points on the boundary.

iii) One may also define a Neumann–to–Dirichlet operator $H^{-1/2} \to H^{1/2}$. In this case one needs to solve the exterior domain problem for given Neumann-data on $\partial\Omega$. Similar to equation (2.7) one derives a variational problem in $H_0(\text{curl}, \Omega)$.

2.5 Geometries with symmetries

When the geometry and the incoming field exhibit a symmetry, Maxwell's equations in 3D can be restricted to a smaller domain. We will even see that a 3D problem may collapse to a 2D or 1D problem. In the following we discuss various symmetries often present in real life applications. The definition of admissible geometries in Definition 2.1 is too strict to deal with

symmetries, since we need to impose certain boundary conditions on symmetry planes. For the following cases it is obvious how to treat the extra boundary conditions.

Periodicity

We assume periodic material tensors $\varepsilon(\mathbf{r}+\mathbf{a}) = \varepsilon(\mathbf{r})$, and $\mu(\mathbf{r}+\mathbf{a}) = \mu(\mathbf{r})$ for a lattice vector $\mathbf{a}$. If the reference field is *Bloch periodic* that is,

$$\mathbf{e}_{\text{ref}}(\mathbf{r}+\mathbf{a}) \quad = \quad e^{i\mathbf{k}_{\text{B}}\cdot\mathbf{a}}\mathbf{e}_{\text{ref}}(\mathbf{r}),$$

then the total field and hence the scattered field are also Bloch periodic with the same Bloch vector $\mathbf{k}_{\text{B}} \in \mathbf{R}^3$. The scattering problem can be restricted to $\mathbf{R}^3_{\mathbf{a}} = \{\mathbf{r} \in \mathbf{R}^3 \,|\, 0 \leq \mathbf{a}\cdot\mathbf{r} \leq \|\mathbf{a}\|^2\}$ which looks like an infinite plate with faces $\Gamma_0 = \{\mathbf{r} \in \mathbf{R}^3 \mid \mathbf{a}\cdot\mathbf{r} = 0\}$ and $\Gamma_a = \{\mathbf{r} \in \mathbf{R}^3 \mid \mathbf{a}\cdot\mathbf{r} = \|\mathbf{a}\|^2\}$. According to the Bloch periodicity of the fields we use the space with Bloch periodic boundary conditions on Γ_0 and Γ_a,

$$H_{\text{loc}}(\text{curl}, \mathbf{R}^3_a, \mathbf{k}_{\text{B}}) \quad = \quad \{\mathbf{e} \in H_{\text{loc}}(\text{curl}, \mathbf{R}^3_a) \,|\, \mathbf{e}_{|\Gamma_a} = e^{i\mathbf{k}_{\text{B}}\cdot\mathbf{a}}\mathbf{e}_{|\Gamma_0}\},$$

as the ansatz space in the variational scattering formulation Problem 2.2. The test functions are chosen accordingly with compact support in $\mathbf{R}^3_a$. A twofold periodicity can be treated in an analogous way. In this case the scattering problem is posed on an infinite cylinder which has a bounded cross–section with twofold periodic boundary conditions.

Remark 2.2 Dobson and Pasciak [39] analyzed the Bloch eigenmode problem. They used standard periodic function spaces and modified the differential operators to account for the phase–shifting behavior of a Bloch mode. Doing so, Nédélec's finite elements do not preserve the *de Rham* properties of the modified operators. To cure this, Dobson and Pasciak adapted the finite element spaces. On a discrete level this yields exactly the same algebraic problem as in the above approach, where the Bloch phase jumps are incorporated into the function spaces.

Translation invariance

We assume that the geometry is invariant in the z-direction so that $\varepsilon(x,y,z) = \varepsilon(x,y,0)$ and $\mu(x,y,z) = \mu(x,y,0)$ for all $z \in \mathbf{R}$. We further assume that the reference field and thus all other fields have the form

$$\mathbf{e}(x,y,z) \quad = \quad e^{ik_z z}\mathbf{e}(x,y,0).$$

This condition is general enough to allow for an oblique incoming plane wave with a wave vector $\mathbf{k}$ not lying in the xy–plane. We will see that this special geometry allows for a restriction of the scattering problem onto the cross-section $z = 0$. Since all field components $\mathbf{e} = e_x dx + e_y dy + e_z dz$ are non-trivial the restricted 2D problem exceeds the framework of differential forms in 2D. Dealing with the field in the cross–section only,

$$\mathbf{e}(x, y, 0) = \begin{bmatrix} \mathbf{e}_\perp(x, y) \\ e_z(x, y) \end{bmatrix},$$

the 2D Maxwell's equations have the following form in classical notation,

$$\begin{pmatrix} \partial_x \\ \partial_y \\ ik_z \end{pmatrix} \times \mu^{-1} \begin{pmatrix} \partial_x \\ \partial_y \\ ik_z \end{pmatrix} \times \begin{bmatrix} \mathbf{e}_\perp \\ e_z \end{bmatrix} - \omega^2 \varepsilon \begin{bmatrix} \mathbf{e}_\perp \\ e_z \end{bmatrix} = 0. \tag{2.8}$$

The curl–operator $(\partial_x, \partial_y, ik_z)^{\mathrm{T}}\times$ acts in the following way

$$\begin{pmatrix} \partial_x \\ \partial_y \\ ik_z \end{pmatrix} \times \begin{bmatrix} \mathbf{e}_\perp \\ e_z \end{bmatrix} = \begin{bmatrix} P(\nabla e_z - ik_z \mathbf{e}_\perp) \\ \partial_x e_y - \partial_y e_x \end{bmatrix},$$

with $P = [0\ 1; -1\ 0]$. Formally, $\mathbf{e}_\perp$ is a 1–form in 2D and e_z is a 0–form for which the gradient operator is defined. One therefore may regard the above 2D Maxwell's equations as a coupled system of a 1-form $\mathbf{e}_\perp$ and a 0–form e_z. Finite elements are constructed accordingly, see for example Jin [63] and [118]. The derivation of a scattering problem for the 2D Maxwell's equations is analog to the general 3D case. Radiating boundary conditions (pole conditions) are imposed for all field components.

We want to derive the variational formulation of the 2D cross section Maxwell's equations (2.8). Instead of using the above splitting $\mathbf{e} = (\mathbf{e}_\perp, e_z)$ we find it more intuitive to start with the 3D variational form and to restrict the ansatz and test space. Given an admissible 2D geometry Ω_{2D} with exterior domain $\Omega_{\mathrm{ext,2D}} = \mathbf{R}^2 \setminus \Omega_{\mathrm{2D}}$, we define $\Omega = \Omega_{\mathrm{2D}} \times \mathbf{R}$ and the ansatz and test space as

$$H_{\mathrm{loc}}(\mathrm{curl}, \mathbf{R}^3, k_z) = \{\mathbf{e} \in H_{\mathrm{loc}}(\mathrm{curl}, \mathbf{R}^3) \,|\, \mathbf{e}(x, y, z) = e^{ik_z z}\mathbf{e}(x, y, 0)\}.$$

The test functions φ are chosen in $H_{\mathrm{loc}}(\mathrm{curl}, \mathbf{R}^3, k_z)$ with compact support

in the xy–plane. We integrate over $\mathbf{R}^2 \times [0, \delta]$, with $\delta > 0$,

$$\int_{\Omega_{2D}\times[0,\delta]} \overline{d\varphi} \wedge \mu^{-1} d\mathbf{e} - \omega^2 \overline{\varphi} \wedge \varepsilon \mathbf{e} + \int_{\Omega_{\text{ext},2D}\times[0,\delta]} \overline{d\varphi} \wedge \mu^{-1} d\mathbf{e}_{\text{sc}} - \omega^2 \overline{\varphi} \wedge \varepsilon \mathbf{e}_{\text{sc}} =$$
$$\int_{\partial\Omega_{2D}\times[0,\delta]} \overline{\varphi} \wedge \mu^{-1} d\mathbf{e}_{\text{ref}} +$$
$$\int_{\Omega_{2D}\times\{0\}} \overline{\varphi} \wedge \mu^{-1} d\mathbf{e} + \int_{\Omega_{2D}\times\delta} \overline{\varphi} \wedge \mu^{-1} d\mathbf{e} +$$
$$\int_{\Omega_{\text{ext},2D}\times\{0\}} \overline{\varphi} \wedge \mu^{-1} d\mathbf{e}_{\text{sc}} + \int_{\Omega_{\text{ext},2D}\times\delta} \overline{\varphi} \wedge \mu^{-1} d\mathbf{e}_{\text{sc}}.$$

Due to the special choice of the ansatz and test space, each integrand is independent of the z-coordinate. The two terms in the last line cancel each other since the cross-sections $\Omega_{2D} \times \{0\}$ and $\Omega_{2D} \times \delta$ have opposite orientations. The same holds true for the last but one line. Hence after dividing by δ we end up with a 2D variational problem.

Rotational symmetry

Equipping the space $\mathbf{R}^3$ with cylinder coordinates (r, y, ϕ) gives rise to the isomorphism

$$\begin{aligned} \mathcal{T} : (0,\infty) \times \mathbf{R} \times [0, 2\pi) &\rightarrow \mathbf{R}^3 \setminus (\{0\} \times \mathbf{R} \times \{0\}) \\ (r, y, \phi) &\mapsto (r\cos(\phi), y, r\sin(\phi)). \end{aligned}$$

We use the isomorphism $\mathcal{T}$ to transform Maxwell's equations from the Cartesian coordinate system (x, y, z) to the cylinder coordinate system. As derived in Section 1.3, transforming Maxwell's equation results only in a change of the material tensors. We recall equation (1.48)

$$d\mu_*^{-1} d\mathbf{e}_* - \omega^2 \varepsilon_* \mathbf{e}_* = 0,$$

where $\mathbf{e}_*$ denotes the pulled back differential form and μ_*, ε_* denote the pulled back material tensors. For a rotational symmetric problem the material tensors do not depend on ϕ. With an expansion of the reference field into Fourier modes,

$$\mathbf{e}_{\text{ref},*} = \sum_{n=-\infty}^{\infty} \mathbf{e}_{\text{ref},n}(r, y) e^{in\phi},$$

the transformed problem separates into 2D Maxwell's equations as described in the previous paragraph, cf. [122]. The only difference is that special care

needs to be taken at the cylinder axis $r = 0$ where the transformed material tensors have singularities. The ϕ–component of the transformed differential form $\mathbf{e}_*$ vanishes at $r = 0$ since $e_{*,\phi} = re_z$. Therefore one must enforce the boundary condition $e_{*,\phi} = 0$ at $r = 0$ which is readily done in the finite element context. More delicate is the assembling of the stiffness and mass matrices near $r = 0$ due to arising $1/r$ terms. To overcome these difficulties, Hiptmair and Ledger [53] proposed to use extra high numerical quadrature rules near the cylinder axis without giving a full theoretical justification.

The reduction of a cylinder symmetric problem to a set of 2D problems is possible due to the separability of Maxwell's equations after a coordinate change. More general configurations which allow for a separation are considered in Pollok [90].

Chapter 3

Adaptive perfectly matched layers

The perfectly matched layer (PML) method is widely used for the numerical implementation of transparent boundary conditions. For the application on Maxwell's equations it goes back to Bérenger who proposed the method for Cartesian coordinates and planar interfaces of the computational domain in 1994 [15]. [1] The method has been generalized to curvilinear coordinates by Teixeira, Chew [105] and Collino, Monk [31]. More general and systematic approaches are reported in Teixeira et al. [106, 46], see also [118, 121]. To introduce the perfectly matched layer concept and to establish the notation we exemplify the principle ideas for the 1D problem,

$$\begin{aligned} -u''(x) - k^2(x)u(x) &= 0, \quad x \in [-a, \infty) \\ u(-a) &= 1. \end{aligned}$$

We assume that the local wave number $k(x)$ is constant outside the bounded interval $\Omega = [-a, 0]$, that is, $k(x) = k_{\text{ext}}$ in $\Omega_{\text{ext}} = (0, \infty)$. In this introductory example we assume $k_{\text{ext}} > 0$. We denote the field in the exterior domain by u_{sc} and demand that u_{sc} is outward radiating. This problem directly allows for a restriction on the bounded interval Ω by imposing the Sommerfeld radiation condition (2.2) at $x = a$, that is, $u'(a) = ik_{\text{ext}}u(a)$. But, a local transparent boundary condition is not available in higher space dimensions and so we do not exploit this special property here. We write the above problem as a

[1] The PML method is related to the "spectral deformation theory" developed in the early 70's for the definition and the computation of quantum resonances, cf. Aguilar and Combes [2], Hislop and Sigal [54].

coupled interior–exterior domain problem

$$\begin{aligned} -u''(x) - k^2(x)u(x) &= 0, \quad x \in [-a, 0] && \text{(3.1a)} \\ -u''_{\mathrm{sc}}(\xi) - k^2_{\mathrm{ext}} u_{\mathrm{sc}}(\xi) &= 0, \quad \xi \in (0, \infty) && \text{(3.1b)} \\ u(0) &= u_{\mathrm{sc}}(0), && \text{(3.1c)} \\ u'(0) &= u'_{\mathrm{sc}}(0). && \text{(3.1d)} \end{aligned}$$

As in the above system of equations we will henceforth denote a coordinate direction with an infinite range $[0, \infty)$ by ξ. The general solution in the exterior domain is $u_{\mathrm{sc}}(\xi) = Ae^{ik\xi} + Be^{-ik\xi}$ and with $B = 0$ the field is outward radiating.

In a numerical simulation it is not possible to truncate the exterior domain to a bounded domain $\Omega^{(\rho)}_{\mathrm{ext}} = [0, \rho]$ with a zero boundary condition at $\xi = \rho$ (Neumann or Dirichlet), since then $|A| = |B|$ which results in serious artificial reflections. The principle idea of the PML method is to replace the scattered field with a numerically more favorable field allowing for a truncation to a bounded domain. In order to not affect the interior field solution we need to *perfectly match* the interface conditions (3.1c), (3.1d).

Complex continuation is the mathematical tool for the construction of such a perfectly matching field. Any solution in the exterior domain is defined in the complex plane, $u_{\mathrm{sc}}(\hat{\xi}) = Ae^{ik\hat{\xi}} + Be^{-ik\hat{\xi}}$ with $\hat{\xi} \in \mathbb{C}$. The complex function $u_{\mathrm{sc}}(\hat{\xi})$ still satisfies the system of equations (3.1) with the complex differentiation as derivatives.

The important observation is that the outgoing wave $Ae^{ik\xi}$ and the incoming wave $Be^{-ik\xi}$ behave very differently under the complex continuation. For $\mathrm{Im}(\hat{\xi}) \to \infty$ the outgoing wave is exponentially damped, whereas the incoming wave grows exponentially.

Let us regard a C^1–path $\hat{\xi}(\cdot) : [0, \infty) \to \mathbb{C}$ of the form

$$\hat{\xi}(\xi) = \int_0^{\xi} \gamma(s) \mathrm{d}s,$$

with $\hat{\xi}'(\xi) = \gamma(\xi)$. For notation purposes we will use γ to label a path and we will call γ the *path parameter*. The field $u_{\mathrm{sc},\gamma}$ on a path is given by

$$u_{\mathrm{sc},\gamma}(\xi) = u_{\mathrm{sc}}(\hat{\xi}(\xi)), \quad \xi \in [0, \infty).$$

We assume $\mathrm{Im}(\gamma(\xi)) > \sigma_0$ with a positive number σ_0. Then $u_{\mathrm{sc},\gamma}$ decays exponentially,

$$|u_{\mathrm{sc},\gamma}(\xi)| = |Ae^{ik_{\mathrm{ext}}\hat{\xi}(\xi)}| = |A|e^{-k_{\mathrm{ext}}\mathrm{Im}(\hat{\xi}(\xi))} \leq |A|e^{-k_{\mathrm{ext}}\sigma_0\xi}.$$

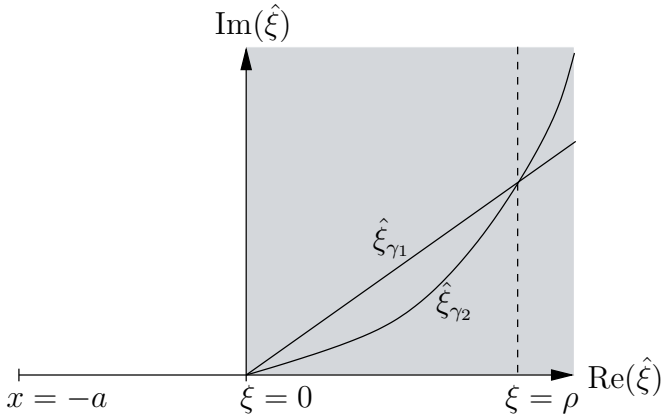

Figure 3.1: Principle idea of the PML method. The field in the exterior domain $\xi > 0$ is oscillatory and numerically not feasible. To overcome this one deforms the real axis path into a path in the complex plane ($\hat{\xi}_{\gamma_1}$ or $\hat{\xi}_{\gamma_2}$). An outward radiating field is exponentially damped on the shown paths.

Figure 3.1 shows two admissible paths $\hat{\xi}_{\gamma_1}$ and $\hat{\xi}_{\gamma_2}$.

With

$$u'_{\mathrm{sc},\gamma}(\xi) = \frac{d}{d\xi} u_{\mathrm{sc}}(\hat{\xi}(\xi)) = \frac{d}{d\hat{\xi}} u_{\mathrm{sc}}(\hat{\xi}(\xi)) \cdot \gamma(\xi)$$

one verifies that the pair $(u,\, u_{\mathrm{sc},\gamma})$ solves the coupled interior–exterior problem

$$\begin{aligned} -u''(x) - k^2(x)u(x) &= 0, \quad x \in [-a, 0] \\ -\frac{1}{\gamma(\xi)}\left(\frac{1}{\gamma(\xi)} u'_{\mathrm{sc},\gamma}(\xi)\right)' - k_{\mathrm{ext}}^2 u_{\mathrm{sc},\gamma}(\xi) &= 0, \quad \tilde{\xi} \in (0, \infty) \\ u(0) &= u_{\mathrm{sc},\gamma}(0), \\ u'(0) &= \frac{1}{\gamma} u'_{\mathrm{sc},\gamma}(0). \end{aligned}$$

Here the interior field solution $u(x)$ is still the exact solution. Since the field $u_{\mathrm{sc},\gamma}$ decays exponentially a truncation of the exterior domain to a bounded domain $\Omega_{\mathrm{ext}}^{(\rho)} = [0, \rho]$ seems appropriate. One indeed proves that the solution $(u_\gamma^{(\rho)},\, u_{\mathrm{sc},\gamma}^{(\rho)})$ of the truncated problem converges exponentially fast to the exact solution in Ω with increasing thickness ρ of the absorbing *sponge layer*,

$$\|u - u_\gamma^{(\rho)}\|_{H^1(\Omega)} \leq C e^{-i\sigma_0 \rho}.$$

The truncation error of the PML method only depends on the endpoint $\hat{\xi}(\rho)$ of the complex path. In numerics two paths $\hat{\xi}_{\gamma_1}$ and $\hat{\xi}_{\gamma_2}$ as shown in Figure 3.1

with the same endpoint behave differently because the regularity of $u_{\mathrm{sc},\gamma}$ depends on the specific choice of the path. Improving the PML method by choosing an optimal path parameter γ is widely discussed in literature, Collino and Monk [31] and Bermúdez et al. [16]. As an alternative approach towards an optimal PML we prefer to use a straight line in the complex plane in combination with an adaptive finite element method to find an efficient discretization on this path. This topic is detailed in a later subsection.

Remark 3.1 Typically one chooses a path $\hat{\xi}_\gamma$ with

$$\gamma(\xi) = 1 + i\frac{\sigma(\xi)}{\omega},$$

where ω is the angular frequency of the underlying time-harmonic scattering problem. The $1/\omega$ term is motivated from the time-dependent Maxwell's equations where an attenuation factor necessarily exhibits a $1/\omega$ dependency in the frequency domain. However, from a numerical point of view the ω dependency of the path $\hat{\xi}_\gamma$ has the undesirable effect that the scaling invariance of the time-harmonic Maxwell's equations $\mathbf{r} \to s\mathbf{r}$, $\omega \to \omega/s$ is broken.

3.1 Complex coordinate stretching

We now derive the PML system in 2D/3D. We start from the variational scattering formulation Problem 2.2. This will directly yield a variational problem well suited for a discretization with standard vectorial finite elements. In the following we assume for simplicity that any cell T is the image of the infinite reference prism P_{ref}. As will become clear from the following, simply, doubly and triply infinite reference bricks $B^{(1)}_{\mathrm{ref}}$, *etc.* are treated in an obvious way.

For an infinite cell T let $\beta_T(\eta_1, \eta_2, \xi)$ denote the transformation of the infinite reference prism P_{ref} onto T. This defines the pulled back differential form $\mathbf{e}^{(T)}_{*,\mathrm{sc}}$. Hence on each unit prism the situation is very similar to the above 1D case. We have coordinates (η_1, η_2, ξ), where ξ is a distance coordinate with infinite range $\xi \in [0, \infty)$. According to the 1D motivation we want to use a complex stretching in the ξ direction on each prism. We assume that $\mathbf{e}^{(T)}_{*,\mathrm{sc}}$ permits a complex continuation in ξ, but as we will see soon, we only use that integral values as in the pole condition (2.3) allow for a complex continuation. On the reference prism and with the notation of the previous

section we define the stretching

$$\begin{aligned} S_{\mathrm{ref},h} : P_{\mathrm{ref}} &\rightarrow P_{\mathrm{ref}} \\ (\eta_1, \eta_2, \xi) &\rightarrow (\eta_1, \eta_2, \hat{\xi}_{\gamma_h}(\xi)), \end{aligned}$$

where

$$\hat{\xi}_{\gamma_h}(\xi) = \int_0^\xi \gamma_h(s)\mathrm{d}s = \int_0^\xi \sigma_R(s) + h\sigma_I(s)\mathrm{d}s.$$

Here $\sigma_{R/I} : [0,\infty) \rightarrow [0,\infty)$ are smooth, positive and monotone growing functions. h is a homotopy parameter. We will use this homotopy parameter to make the transition from a real value coordinate stretching to a complex value coordinate stretching. Since h is a single scalar we are allowed to make use of standard function theory of one complex variable in the following.

Let us first assume that h is a real and positive value. The stretching on the reference prism defines a stretching for each cell $T \subset \Omega_{\mathrm{ext}}$. The ray matching condition 2iii in Definition 2.1 for admissible geometries assures that the infinite distance coordinate ξ is globally defined. Therefore we can define a global stretching

$$\begin{aligned} S_h : \Omega \cup \Omega_{\mathrm{ext}} &\rightarrow \Omega \cup \Omega_{\mathrm{ext}} \\ \mathbf{r} &\mapsto \begin{cases} \mathbf{r}, & \mathbf{r} \in \Omega \\ \beta_T \circ S_{\mathrm{ref},h} \circ \beta_T^{-1}(\mathbf{r}), & \mathbf{r} \in T \end{cases} \end{aligned}$$

which is continuous and C^∞ on each cell. The stretching S_h is a simple coordinate transformation when the homotopy parameter h is positive and real. Hence we are allowed to apply transformation rules for differential forms. Let $\mathbf{e}_{\mathrm{sc},h}$, μ_h, *etc.* denote the *pulled back* quantities. Here we abandon the dependence on the PML path parameter γ in the notation for a while. In the interior domain Ω we have $\mathbf{e}_h = \mathbf{e}$ since S_h is the identity in Ω. Accordingly $(\mu^{-1} d\mathbf{e}_{\mathrm{ref}})|_{\partial\Omega} = (\mu^{-1} d\mathbf{e}_{\mathrm{ref}})|_{\partial\Omega}$ because the transformation S_h is also the identity on $\partial\Omega$ and hence the tangential space to a boundary point is not changed. The transformation rules (1.46), (1.47a) (1.48) imply that

$$\begin{aligned} \int_\Omega \overline{d\varphi_h} \wedge \mu^{-1} d\mathbf{e} - \omega^2 \overline{\varphi_h} \wedge \varepsilon \mathbf{e} \; + \int_{\Omega_{\mathrm{ext}}} \overline{d\varphi_h} \wedge \mu_h^{-1} d\mathbf{e}_{h,\mathrm{sc}} - \omega^2 \overline{\varphi_h} \wedge \varepsilon_h \mathbf{e}_{h,\mathrm{sc}} = \\ \int_{\partial\Omega} \overline{\varphi_h} \wedge \mu^{-1} d\mathbf{e}_{\mathrm{ref}} \end{aligned} \tag{3.2}$$

for all $\varphi \in H_{\mathrm{loc}}(\mathrm{curl}, \Omega \cup \Omega_{\mathrm{ext}})$. We emphasis that this equation is still equivalent to the original scattering problem. Since φ was chosen arbitrarily and

the transformation S_h gives rise to an isomorphism in $H_{\rm loc}(\mathrm{curl}, \Omega \cup \Omega_{\rm ext})$ we can suppress a transformation of the test function φ and are allowed to replace φ_h with φ in the above variational equation. This way all integral expressions are holomorphic functions in the homotopy parameter h. Since the above equation is valid for all h on the positive real axis we conclude that the equation is also valid for $h \in \mathbb{C}$ with $\mathrm{Re}(h) > 0$. We now fix $h = i$ which yields the PML equation.

It remains to incorporate the matching condition

$$(\mathbf{e} - \mathbf{e}_{\rm sc})|_{\partial\Omega} \;=\; \mathbf{e}_{\rm ref}|_{\partial\Omega}.$$

into the variational equation. Note that this matching condition involves only tangential components of the electric field on $\partial\Omega$. The coordinate stretching does not affect the tangential field data of $\mathbf{e}_{\rm sc}$ since the tangent space $T_{\mathbf{r}}M$ for a point $\mathbf{r} \in \partial\Omega$ is not stretched. Hence the above Dirichlet matching condition also holds true for $\mathbf{e}_{\rm sc}$ replaced with $\mathbf{e}_{i,\rm sc}$. Let $\mathcal{I}\mathbf{e}_{\rm ref}$ denote a field in $H_{\rm loc}(\mathrm{curl}, \Omega_{\rm ext})$ with support in a vicinity of $\partial\Omega$ which interpolates the Dirichlet data of $\mathbf{e}_{\rm ref}$ on $\partial\Omega$. Surely, $\mathcal{I}$ is an extension operator of the Dirichlet data space into $H_{\rm loc}(\mathrm{curl}, \Omega_{\rm ext})$. In the finite element context such an operator is easily constructed. We define

$$\mathbf{e}_\gamma \;=\; \begin{cases} \mathbf{e} & \text{in } \Omega, \\ \mathbf{e}_{i,\rm sc} + \mathcal{I}\mathbf{e}_{\rm ref} & \text{in } \Omega_{\rm ext}. \end{cases}$$

One checks that $\mathbf{e}_\gamma \in H_{\rm loc}(\mathrm{curl}, \Omega \cup \Omega_{\rm ext})$ provided that the complex stretched field $\mathbf{e}_{i,\rm sc}$ exists in $H_{\rm loc}(\mathrm{curl}, \Omega_{\rm ext})$. From equation (3.2) one easily derives a variational equation for $\mathbf{e}_\gamma$ as given later for a truncated domain in Problem 3.1.

In the following we denote $\varepsilon_\gamma = \varepsilon_i$ and $\mu_\gamma = \mu_i$. For $\rho > 0$ we define the truncated exterior domain $\Omega_{\rm ext}^{(\rho)} \subset \Omega_{\rm ext}$,

$$\Omega_{\rm ext}^{(\rho)} = \{\mathbf{r} \in \Omega_{\rm ext} \,|\, \beta_T^{-1}(\mathbf{r}) \in P_{\rm ref}^{(\rho)}\},$$

where $P_{\rm ref}^{(\rho)}$ is the truncated prism with ξ–coordinate smaller ρ. The ray matching condition guarantees that $\Omega_{\rm ext}^{(\rho)}$ is a convex polyhedron.

Problem 3.1 (scattering problem with PML)**.** *Let a reference field* $\mathbf{e}_{\rm ref} \in H_{\rm loc}(\mathrm{curl}, \Omega_{\rm ext})$ *be given which satisfies Maxwell's equations in the exterior of an admissible domain* $\Omega \subset \mathbf{R}^3$,

$$\int_{\Omega_{\rm ext}} \overline{d\varphi} \wedge \mu^{-1} d\mathbf{e}_{\rm ref} - \omega^2 \overline{\varphi} \wedge \varepsilon \mathbf{e}_{\rm ref} \;=\; \int_{\partial\Omega_{\rm ext}} \overline{\varphi} \wedge \mu^{-1} d\mathbf{e}_{\rm ref}$$

for all test functions $\varphi \in H(\mathrm{curl}, \Omega_{\mathrm{ext}})$ *with compact support. For a given path* $\hat{\xi}_\gamma$*, a given thickness of the sponge layer* ρ *and with the notations above we seek* $\mathbf{e}_\gamma^{(\rho)} \in H(\mathrm{curl}, \Omega \cup \Omega_{\mathrm{ext}}^{(\rho)})$ *such that*

$$\begin{aligned} \int_{\Omega \cup \Omega_{\mathrm{ext}}^{(\rho)}} \overline{d\varphi} \wedge \mu_\gamma^{-1} d\mathbf{e}_\gamma^{(\rho)} - \omega^2 \overline{\varphi} \wedge \varepsilon_\gamma \mathbf{e}_\gamma^{(\rho)} = \\ \int_{\partial\Omega} \overline{\varphi} \wedge \mu^{-1} d\mathbf{e}_{\mathrm{ref}} + \int_{\Omega_{\mathrm{ext}}^{(\rho)}} \overline{d\varphi} \wedge \mu_\gamma^{-1} d\mathcal{I}\mathbf{e}_{\mathrm{ref}} - \omega^2 \overline{\varphi} \wedge \varepsilon_\gamma \mathcal{I}\mathbf{e}_{\mathrm{ref}} \end{aligned} \tag{3.3}$$

for all $\varphi \in H(\mathrm{curl}, \Omega \cup \Omega_{\mathrm{ext}}^{(\rho)})$.

The unique solvability of (3.3) was shown by Lassas and Somersalo [68, 69, 67] for homogeneous exterior domains and complex paths $\hat{\xi}_\gamma$ which behaves asymptotically like straight lines. Furthermore they proved an exponential convergence of $u_\gamma^{(\rho)}$ with growing ρ in the interior domain. Slightly more general exterior domains are considered in Hohage, Schmidt and Zschiedrich [56], where we showed that an outward radiating solution satisfying the pole condition also permits a complex continuation with damping properties similar to the homogeneous case. For more general exterior domain such as layered media a convergence proof is still missing. However, with the help of Green's functions in layered media as constructed in Martin and Piller [73] one proves that a complex continuation of the scattered field exists and exhibits the desired damping properties.

The above PML variational equation (3.3) is well suited for a discretization with standard, vectorial finite elements. We do not go into details about finite elements in this thesis. For finite element aspects we refer to Demkowicz [37], Ainsworth [3] and Zaglmayr [116].

After the finite element discretization of the scattering problem the arising linear system of equations calls for a numerical solution. For large scale problems the discretized scattering problem is highly indefinite and standard iterative methods suffer from extremely slow convergence rates.[2] For the numerical examples in this thesis we rely on the sparse LU solver Pardiso by Schenk and Gärtner [97]. The development of an efficient linear solver in combination with improved finite elements for high–frequency Maxwell's equations is a topic of vivid research [51, 81, 17].

[2]This is in contrast to other types of equations also stemming from Maxwell's equations like eddy-current problems, electro/magneto-static problems or when computing an implicit time step for the time-dependent Maxwell's equations. In these cases efficient preconditioners like multilevel methods (Beck et al. [13], Hiptmair et al. [52], Arnold et al. [8]), algebraic multigrid methods (Beck [12], Reitzinger [92]) and domain decomposition preconditioners (e.g. Toselli [108]) are available.

3.2 Relation of the PML method to the pole condition

The PML method relies on the decay of the complex deformed field $\mathbf{e}_\gamma$ in the exterior domain with an increasing distance ξ to the coupling boundary $\partial\Omega_{\text{ext}}$. We argued that the splitting of the general solution to Maxwell's equations in the exterior domain into outgoing and incoming parts manifests under a complex deformation: outgoing parts are damped, whereas incoming parts are amplified. By demanding that $\mathbf{e}_\gamma \in H(\text{curl}, \mathbf{R}^3)$ we filter out the unwanted incoming waves.

With the Definition 2.2 of the pole condition we already have characterized outgoing and incoming waves. Our aim is to justify the PML method by the pole condition. We want to show that an outgoing wave (in terms of the pole condition) possesses a complex continuation which indeed exhibits the desired exponential decay.

In the definition of the pole condition we regarded scalar functions of the form

$$u_{\mathbf{e},\varepsilon,\varphi}(\tau) \quad = \quad \int_{\Omega_{\text{ext}}} \overline{\varphi} \wedge \varepsilon_\tau \mathbf{e}_\tau.$$

φ is a test function and $\mathbf{e}_\tau$ is the field pulled back under a displacement isomorphism D_τ. Here, we demand that $\overline{\varphi}$ is holomorphic and rapidly decreasing in the ξ direction, e.g. $\overline{\varphi}(\cdot,\cdot,\xi) = p(\xi)\exp(-c(\xi-\xi_0))\cdot\phi(\cdot,\cdot)$, where p is a polynomial.

The pole condition states that the scalar function $u_{\mathbf{e},\varepsilon,\varphi}(\tau)$ possesses a Laplace transform $U_{\mathbf{e},\varepsilon,\varphi}(\tau)(s)$ which is holomorphic outside the strip

$$\mathcal{S} = \{s \in \mathbb{C} \,|\, 0 \le \text{Im}(s) \le k_{\max}, \text{Re}(s) \le 0\},$$

where $k_{\max} > 0$ is problem specific, cf. Figure 2.6 in the pole condition section 2.2.

Additionally we make the conjecture that $U_{\mathbf{e},\varepsilon,\varphi}(\tau)(s)$ is holomorphic outside

$$\mathcal{S}_\kappa = \mathcal{S} \setminus \{s \in \mathbb{C} \,|\, |s| \le \kappa\}, \tag{3.4}$$

with $\kappa > 0$. The domain $\mathcal{S}_\kappa$ is sketched in gray on the left hand side of Figure 3.2. We further assume that $|U_{\mathbf{e},\varepsilon,\varphi}(\tau)(s)| \le M/|s|$ for large $|s|$. These assumptions can be justified by using that $\mathbf{e}$ solves Maxwell's equations in the exterior domain.

To link the PML method to the pole condition we combine the displacement isomorphism D_τ with the complex coordinate stretching S_γ. We restrict

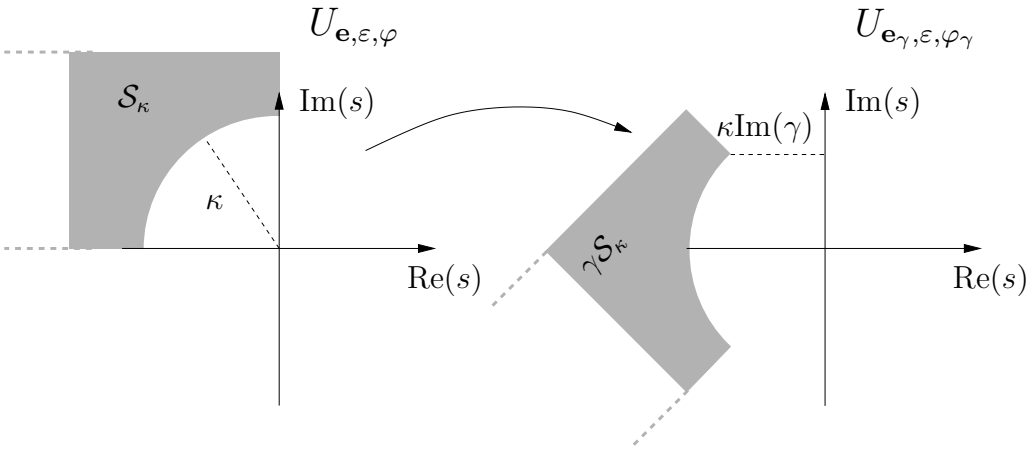

Figure 3.2: Holomorphic regions of $U_{\mathbf{e},\varepsilon,\varphi}$ and $U_{\mathbf{e}_\gamma,\varepsilon_\gamma,\varphi_\gamma}$. Regions in which the functions are *not* holomorphic are painted in gray. The gray dashed lines indicate that the gray regions are unbounded. We demand that the function $U_{\mathbf{e},\varepsilon,\varphi}$ satisfies the pole condition and is holomorphic outside $\mathcal{S}_\kappa$ (left). The Laplace transform $U_{\mathbf{e}_\gamma,\varepsilon_\gamma,\varphi_\gamma}$ which corresponds to the PML solution is holomorphic outside the rotated domain $\gamma\mathcal{S}_\kappa$ (right).

the PML path to a straight line $\hat{\xi}(\xi) = \gamma\xi$ with $|\gamma| = 1$ and $\mathrm{Re}(\gamma), \mathrm{Im}(\gamma) > 0$. We have that $S_\gamma \circ D_\tau = D_{\gamma\tau} \circ S_\gamma$ and hence

$$D_{\gamma\tau} = S_\gamma \circ D_\tau \circ S_{\gamma^{-1}}.$$

This gives

$$\begin{aligned} u_{\mathbf{e},\varepsilon,\varphi}(\gamma\tau) &= \int \overline{\varphi} \wedge \varepsilon_{\gamma\tau}\mathbf{e}_{\gamma\tau} \\ &= \int \overline{\varphi} \wedge \left((\varepsilon_\gamma)_\tau(\mathbf{e}_\gamma)_\tau\right)_{\gamma^{-1}} \\ &= \int \overline{\varphi}_\gamma \wedge (\varepsilon_\gamma)_\tau(\mathbf{e}_\gamma)_\tau. \end{aligned}$$

In the last line we used that the $\overline{\varphi}$ is analytic in ξ. We have derived that the PML solution $\mathbf{e}_\gamma$ satisfies

$$u_{\mathbf{e}_\gamma,\varepsilon_\gamma,\varphi_\gamma}(\tau) = u_{\mathbf{e},\varepsilon,\varphi}(\gamma\tau), \tag{3.5}$$

and we want to show that $u_{\mathbf{e}_\gamma,\varepsilon_\gamma,\varphi_\gamma}(\tau)$ exponentially decays when $u_{\mathbf{e},\varepsilon,\varphi}(\tau)$ meets the pole condition. The Laplace transform of $u_{\mathbf{e}_\gamma,\varepsilon_\gamma,\varphi_\gamma}(\tau)$ is given by

$$U_{\mathbf{e}_\gamma,\varepsilon_\gamma,\varphi_\gamma}(s) = \frac{1}{\gamma} U_{\mathbf{e},\varepsilon,\varphi}(\frac{s}{\gamma}). \tag{3.6}$$

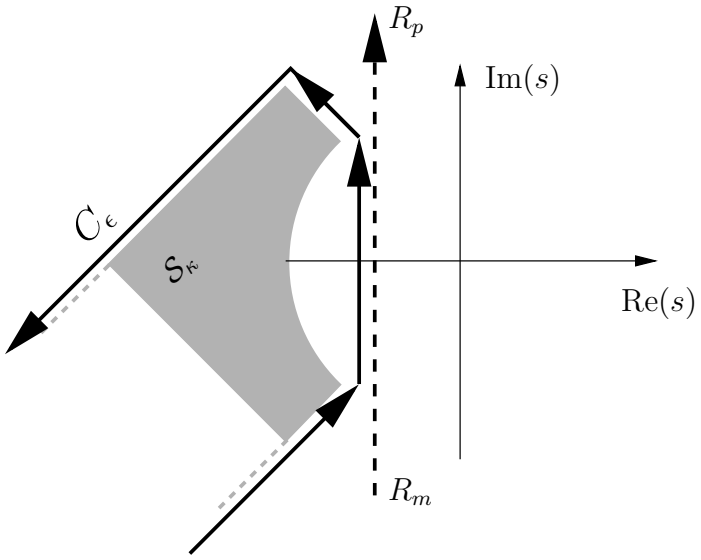

Figure 3.3: Complex contours used in the Laplace inversion of the function $U_{\mathbf{e}_\gamma,\varphi_\gamma}$.

Since we assumed $|\gamma| = 1$ the Laplace transform $U_{\mathbf{e}_\gamma,\varepsilon_\gamma,\varphi_\gamma}$ is just a rotated version of $U_{\mathbf{e},\varepsilon,\varphi}$, see Figure 3.2. Hence, $U_{\mathbf{e}_\gamma,\varepsilon_\gamma,\varphi_\gamma}$ is holomorphic in $\mathbb{C} \setminus \gamma\mathcal{S}_\kappa$ which contains the half space $\mathrm{Re}(s) > -\kappa\mathrm{Im}(\gamma)$.

For a $\epsilon > 0$, we apply the Laplace inversion on an integration path as indicated by the dashed line in Figure 3.3

$$u_{\mathbf{e}_\gamma,\varepsilon_\gamma,\varphi_\gamma}(\tau) = \lim_{R\to\infty} \frac{1}{2\pi i} \int_{R_m}^{R_p} U_{\mathbf{e}_\gamma,\varepsilon_\gamma,\varphi_\gamma}(s) e^{s\tau} \mathrm{d}s,$$

where $R_m = -iR - \kappa\mathrm{Im}\gamma + \epsilon$ and $R_p = iR - \kappa\mathrm{Im}\gamma + \epsilon$. Repeating the arguments which led to the Laplace inversion formula (2.4) in the non-PML case, we are allowed to use the integration path C_ϵ,

$$u_{\mathbf{e}_\gamma,\varepsilon_\gamma,\varphi_\gamma}(\tau) = \frac{1}{2\pi i} \int_{C_\epsilon} U_{\mathbf{e}_\gamma,\varepsilon_\gamma,\varphi_\gamma}(s) e^{s\tau} \mathrm{d}s. \tag{3.7}$$

Since this integral is absolutely convergent for $\tau > 0$ we can perform the estimate

$$|u_{\mathbf{e}_\gamma,\varepsilon_\gamma,\varphi_\gamma}(\tau)| \le e^{-(\kappa\mathrm{Im}\gamma-\epsilon)\tau} \frac{1}{2\pi} \int_{C_\epsilon} |U_{\mathbf{e}_\gamma,\varepsilon_\gamma,\varphi_\gamma}(s)| e^{(\mathrm{Re}(s)+\kappa\mathrm{Im}(\gamma)-\epsilon)\tau} |\mathrm{d}s|.$$

Fixing a $\tau_* > 0$ gives

$$|u_{\mathbf{e}_\gamma,\varepsilon_\gamma,\varphi_\gamma}(\tau)| \le e^{-(\kappa\mathrm{Im}\gamma-\epsilon)\tau} \frac{1}{2\pi} \int_{C_\epsilon} |U_{\mathbf{e}_\gamma,\varepsilon_\gamma,\varphi_\gamma}(s)| e^{(\mathrm{Re}(s)+\kappa\mathrm{Im}(\gamma)-\epsilon)\tau_*} |\mathrm{d}s|,$$

for $\tau > \tau_*$. This yields the desired estimate

$$|u_{\mathbf{e}_\gamma,\varepsilon_\gamma,\varphi_\gamma}(\tau)| \leq Ce^{-(\kappa \mathrm{Im}\gamma - \epsilon)\tau}.$$

For a formal discussion of this estimate we regard the 1D case, so that $\mathbf{e}_\gamma$ is a scalar field and $\mathbf{e}_\gamma(\xi) = \mathbf{e}(\gamma\xi)$. We have

$$u_{\mathbf{e}_\gamma,\varepsilon_\gamma,\varphi_\gamma}(\tau) = \int_0^\infty \overline{\varphi_\gamma}(\xi)\varepsilon \mathbf{e}(\gamma(\xi+\tau))\mathrm{d}\xi.$$

In the context of the PML variational formulation (3.3) we see that the contribution of the field $\mathbf{e}_\gamma$ decays exponentially with the distance to the boundary when tested with the same test function φ_γ.

Surely, to show rigorously the exponential convergence of the PML variational problem many further steps are required. For example, we need to remedy the restriction that the test function φ is holomorphic and we need to show that the exponential decay is uniform in all test functions. But this is not in the scope of this thesis and we content ourselves with the gained insight on the relation of the PML method to the pole condition.

3.3 Analysis of periodic grating problems

In the introductory 1D example at the beginning of this chapter we considered an exterior domain with a fixed wave number k_{ext}. For 2D/3D scattering problems it is important that the PML method is efficient not only for a fixed k_{ext} but for general k_{ext} with $\mathrm{Re}(k_{\mathrm{ext}}) \geq 0$ and $\mathrm{Im}(k_{\mathrm{ext}}) \geq 0$. To demonstrate this we analyze the PML method for a periodic grating. For simplicity we restrict ourselves to the scalar Helmholtz equation. We will pay special attention to the case $k_{\mathrm{ext}} = 0$.

A periodic grating is sketched in Figure 3.4. The scattering problem is posed on $[0,a] \times \mathbf{R}$ with computational domain $\Omega = [0,a] \times [-b,0]$. The exterior domain separates into two disjoint sets $\Omega_{\mathrm{ext},-} = [0,a] \times (-\infty,-b]$ and $\Omega_{\mathrm{ext},+} = [0,a] \times [0,\infty)$. We assume that the reference field exhibits a Bloch periodicity,

$$u_{\mathrm{ref}}(x+a,z) \quad = \quad u_{\mathrm{ref}}(x,z)e^{ik_x a}.$$

We introduce the Sobolev space of Bloch periodic functions

$$H^1_{k_x}(\Omega) \quad = \quad \{u \in H^1(\Omega) \,|\, u_{\mathrm{ref}}(x+a,z) = u_{\mathrm{ref}}(x,z)e^{ik_x a}\}.$$

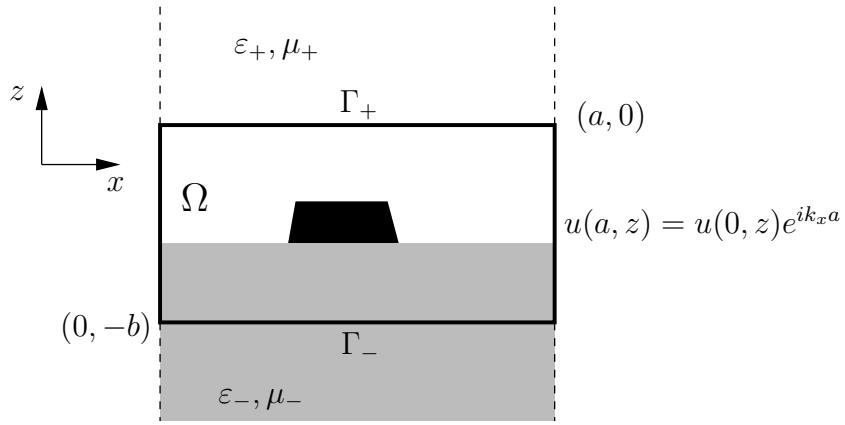

Figure 3.4: Sketch of a periodic grating problem. The structure is periodically repeated in the x–direction. The fields are Bloch periodic (quasi-periodic) that is $u(x+a,z) = u(x,z)e^{ik_x a}$.

Γ_- and Γ_+ denote the lower and upper boundary of Ω. The scattering problem in the DtN–operator formulation is to find $u \in H^1_{k_x}(\Omega)$ such that

$$\begin{aligned}\int_\Omega \nabla\overline{\varphi}\mu^{-1}\nabla u - \omega^2\varepsilon u - \int_{\Gamma_-}\overline{\varphi}\mathrm{DtN}_-[u] - \int_{\Gamma_+}\overline{\varphi}\mathrm{DtN}_+[u] = \\ \int_{\Gamma_-}\overline{\varphi}(\mathrm{DtN}_-[u_{\mathrm{ref}}] + \mu^{-1}\partial_n u_{\mathrm{ref}}) + \int_{\Gamma_+}\overline{\varphi}(\mathrm{DtN}_-[u_{\mathrm{ref}}] + \mu^{-1}\partial_n u_{\mathrm{ref}})\end{aligned} \tag{3.8}$$

for all $\varphi \in H^1_{k_x}(\Omega)$.

In the following we only regard the upper exterior domain and write $\Omega_{\mathrm{ext}} = \Omega_{\mathrm{ext},+}$, $\Gamma = \Gamma_+$, and $\mathrm{DtN} = \mathrm{DtN}_+$. We will explicitly construct the DtN–operator for the case that μ and ε are positive real numbers. Formally the DtN–operator is defined as

$$\begin{aligned}\mathrm{DtN} : H^{1/2}_{k_x}(\Gamma) &\to H^{-1/2}_{k_x}(\Gamma) \\ v &\mapsto \mu^{-1}\partial_z u_{\mathrm{sc}},\end{aligned}$$

where u_{sc} is the outward radiating solution to the exterior domain problem

$$\begin{aligned}-\nabla\mu^{-1}\nabla u_{\mathrm{sc}} - \omega^2\varepsilon u_{\mathrm{sc}} &= 0, \\ u_{|\Gamma} &= v.\end{aligned}$$

To construct the DtN–operator we use that $u_{\mathrm{sc}}e^{-ik_x x}$ and $v(x)e^{-ik_x x}$ are periodic functions in x with periodicity length a. With $g = 2\pi/a$ we expand

these fields into Fourier modes,

$$\begin{aligned} v(x) &= \sum_{j=-\infty}^{\infty} v_j e^{i(k_x+jg)x}, \\ u_{\rm sc}(x,z) &= \sum_{j=-\infty}^{\infty} u_{{\rm sc},j}(z) e^{i(k_x+jg)x} \end{aligned}$$

and conclude that the Fourier coefficients $u_{{\rm sc},j}(z)$ satisfy the 1D problem

$$\begin{aligned} -u''_{{\rm sc},j}(z) - k_j^2 u_{{\rm sc},j}(z) &= 0, \\ u_{{\rm sc},j}(0) &= v_j, \end{aligned}$$

with $k_j = \sqrt{\omega^2\mu\varepsilon - (k_x+jg)^2}$. Except for a coordinate change we have already discussed this equation as the introductory model problem at the beginning of this chapter with $k_{\rm ext} = k_j$. The outward radiating solution is given by

$$u_{{\rm sc},j}(z) = v_j e^{i(k_x+jg)x} e^{ik_j z}.$$

The exterior domain solution behaves very differently in z–direction depending on the sign of $\omega^2\mu\varepsilon - (k_x+jg)^2$. We distinguish three situations:

i) $\mathrm{Re}(k_z) > 0$, $\mathrm{Im}(k_z) = 0$ *(propagating mode)*: The Fourier mode is an undamped and upward propagating plane wave.

ii) $\mathrm{Re}(k_z) = 0$, $\mathrm{Im}(k_z) > 0$ *(evanescent mode)*: The Fourier mode decays exponentially in the outward direction.

iii) $\mathrm{Re}(k_z) = 0$, $\mathrm{Im}(k_z) = 0$ *(anomalous mode)*: The Fourier mode is constant in the outward direction. In this case we have $(k_x+jg)^2 = k_0^2$ so that the wave propagates perpendicular to the outward direction.

Computing the normal derivative of $u_{\rm sc}$ on Γ, the DtN–operator becomes

$$\mathrm{DtN}[\sum_{j=-\infty}^{\infty} v_j e^{i(k_x+jg)x}] = \mu^{-1} \sum_{j=-\infty}^{\infty} (ik_j v_j) e^{i(k_x+jg)x}.$$

It is more comfortable to write the action of the DtN–operator as a mapping of the Fourier coefficients, $(v_j) \mapsto a\mu^{-1}(ik_j v_j)$. More precisely, the Fourier series expansion defines an isomorphism between $H^{1/2}_{k_x}(\Gamma)$ and the sequence space $h^{1/2}$ defined by

$$h^{1/2} = \{(c_j) \,|\, c_j \in \mathbb{C}, \sum_{j=-\infty}^{\infty} (1+|j|)|c_j|^2 < \infty\}$$

with norm $\|(c_j)\|_{h^{1/2}} = (\sum(1+|j|)|c_j|^2)^{1/2}$. The dual space of $h^{1/2}$ is denoted by $h^{-1/2}$. In the following we denote the DtN–operator as a mapping $h^{1/2} \to h^{-1/2}$,

$$\mathrm{DtN}[(v_j)] \;=\; a\mu^{-1}(ik_j v_j).$$

Here we understand the series on the right hand side as the functional $(w_j) \in h^{1/2} \mapsto a\mu^{-1}\sum ik_j v_j w_j$. The factor a is the periodicity length and is needed to assure that $(\mathrm{DtN}[(v_j)])(w_j) = \int_\Gamma w(x)\mathrm{DtN}[v(x)]$, where $w(x), v(x) \in H^{1/2}(\Gamma)$ correspond to the Fourier series (w_j) and (v_j), respectively. For the sake of a simpler notation we set $a = 1$ and $\mu = 1$.

Anomalous modes do not necessarily affect the unique and stable solvability of the above scattering problem (3.8). It is sufficient that the DtN_-–operator *or* the DtN_+– operator has no anomalous mode. The proof is similar to Proposition 3 in Hohage et al. [56]. One uses that a solution to the above problem (3.8) with $u = 0$ and $\partial_n u = 0$ on one part of the boundary Γ_+ or Γ_- is necessarily zero everywhere. Furthermore unique solvability is also guaranteed when $\mathrm{Im}(\varepsilon)$ is strictly positive on a sub-domain within Ω.

We now want to study the affect of the PML method on the interior field solution u. Following Lassas et al. [68] and Hohage et al. [57] we interpret the application of the PML method as a perturbation of the DtN–operator. We define the perturbed DtN–operator $\mathrm{DtN}_\gamma^{(\rho)}$ in the same way as the original DtN–operator but with the exterior domain problem replaced by the truncated PML system. As shown in [57] the error $\|u - u_\gamma^{(\rho)}\|_{H^1_{k_x}(\Omega)}$ is then proportional to the error of the DtN–operator $\|\mathrm{DtN} - \mathrm{DtN}_\gamma^{(\rho)}\|$.

The separability of the problem into Fourier modes is not affected by the PML method since the complex continuation only acts on the z–coordinate. To define the $\mathrm{DtN}_\gamma^{(\rho)}$–operator we solve for each Fourier mode j the problem

$$\begin{aligned} -\frac{1}{\gamma}\Big(\frac{1}{\gamma}u'_{\gamma,j}\Big)' - k_j^2 u_{\gamma,j} &= 0, \\ u_{\gamma,j}(0) &= v_j, \\ u_{\gamma,j}(\rho) &= 0. \end{aligned} \tag{3.9}$$

Let $\hat{z}_\mathrm{e} = \hat{z}_\gamma(\rho)$ denote the endpoint of the PML path. The solution to this problem is given by

$$u_{\gamma,j}(z) = T_j e^{ik_j\hat{z}(z)} + R_j^{-ik_j\hat{z}(z)}$$

with

$$\begin{aligned} T_j &= \frac{-v_j e^{-ik_j\hat{z}_\mathrm{e}}}{e^{ik_j\hat{z}_\mathrm{e}} - e^{-ik_j\hat{z}_\mathrm{e}}}, \\ R_j &= \frac{v_j e^{+ik_j\hat{z}_\mathrm{e}}}{e^{ik_j\hat{z}_\mathrm{e}} - e^{-ik_j\hat{z}_\mathrm{e}}}. \end{aligned}$$

This gives

$$\mathrm{DtN}_\gamma^{(\rho)}[(v_j)] \;=\; (ik_j v_j p_{\gamma,k_j}^{(\rho)})$$

with the perturbation factor

$$p_{\gamma,k_j}^{(\rho)} \;=\; -\frac{e^{ik_j\hat{z}_\mathrm{e}}+e^{-ik_j\hat{z}_\mathrm{e}}}{e^{ik_j\hat{z}_\mathrm{e}}-e^{-ik_j\hat{z}_\mathrm{e}}}.$$

Note that $\mathrm{DtN}_\gamma^{(\rho)}$ needs a careful definition for an anomalous mode since the denominator of the perturbation factor is zero in this case. This is done by the limit $k_j \to 0$:

$$\begin{aligned}(\mathrm{DtN}_\gamma^{(\rho)}[(v_j)])_l &= iv_l \lim_{\epsilon\to 0}(\epsilon p_{\gamma,\epsilon}^{(\rho)}) \\ &= -v_l\frac{1}{\hat{z}_\mathrm{e}}.\end{aligned}$$

We now want to estimate the error $\|\mathrm{DtN}-\mathrm{DtN}_\gamma^{(\rho)}\|$. In the operator norm we have

$$\|\mathrm{DtN}-\mathrm{DtN}_\gamma^{(\rho)}\| \;=\; \sup_{\|(v_j)\|=1}\Big(\sup_{\|(w_j)\|=1}|\sum_j ik_jv_j(1-p_{\gamma,k_j}^{(\rho)})w_j|\Big).$$

With $|k_j| \sim j$, we immediately obtain the estimate $\|\mathrm{DtN}-\mathrm{DtN}_\gamma^{(\rho)}\| \le C\max_j|1-p_{\gamma,k_j}^{(\rho)}|$. But this estimate is too rough to allow for a bound of anomalous modes. We define $\delta_{\gamma,k_j}^{(\rho)} = 1-p_{\gamma,k_j}^{(\rho)}$ and proceed with the estimates

$$\begin{aligned}|\sum k_jv_j\delta_\gamma^{(\rho)}w_j| &\le |\sum_{|k_j|\le 1}k_jv_j\delta_{\gamma,k_j}^{(\rho)}w_j| + |\sum_{|k_j|>1}k_jv_j\delta_{\gamma,k_j}^{(\rho)}w_j| \\ &\le \left(\max_{|k_j|\le 1}|k_j\delta_{\gamma,k_j}^{(\rho)}| + C\max_{|k_j|>1}|\delta_{\gamma,k_j}^{(\rho)}|\right)\cdot\|(v_j)\|\cdot\|(w_j)\|,\end{aligned}$$

and we obtain $\|\mathrm{DtN}-\mathrm{DtN}_\gamma^{(\rho)}\| \le \max_{|k_j|\le 1}|k_j\delta_{\gamma,k_j}^{(\rho)}| + C\max_{|k_j|>1}|\delta_{\gamma,k_j}^{(\rho)}|$. Assuming $\mathrm{Im}(\hat{z}_\mathrm{e}) > 1$ and with $\delta_{\gamma,k_j}^{(\rho)} = 2e^{ik_j\hat{z}_\mathrm{e}}/(e^{ik_j\hat{z}_\mathrm{e}}-e^{-ik_j\hat{z}_\mathrm{e}})$ we estimate

$$\begin{aligned}\max_{|k_j|\le 1}|k_j\delta_{\gamma,k_j}^{(\rho)}| &\le \max_{|k_j|\le 1}\Big|\frac{2k_j}{e^{ik_j\hat{z}_\mathrm{e}}-e^{-ik_j\hat{z}_\mathrm{e}}}\Big|e^{-\mathrm{Im}(k_j\hat{z}_\mathrm{e})} \\ &\le C\frac{1}{|\hat{z}_\mathrm{e}|}\max_{|k_j|\le 1}e^{-\mathrm{Im}(k_j\hat{z}_\mathrm{e})}.\end{aligned}$$

The estimate of the term $\max_{|k_j|>1}|\delta_{\gamma,k_j}^{(\rho)}|$ is straightforward and we get the error bound

$$\|\mathrm{DtN}-\mathrm{DtN}_\gamma^{(\rho)}\| \;\le\; C\left(\frac{1}{|\hat{z}_\mathrm{e}|}\max_{|k_j|\le 1}e^{-\mathrm{Im}(k_j\hat{z}_\mathrm{e})} + \max_{|k_j|>1}e^{-\mathrm{Im}(k_j\hat{z}_\mathrm{e})}\right) \quad (3.10)$$

and hence

$$\|u - u_\gamma^{(\rho)}\|_{H^1\Omega} \;\leq\; C\left(\frac{1}{|\hat{z}_\mathrm{e}|}\max_{|k_j|\leq 1} e^{-\mathrm{Im}(k_j\hat{z}_\mathrm{e})} + \max_{|k_j|>1} e^{-\mathrm{Im}(k_j\hat{z}_\mathrm{e})}\right) \quad (3.11)$$

If no anomalous mode is present that is, $k_j \neq 0$ for all $j \in \mathbb{Z}$, we observe an exponential convergence

$$\|\mathrm{DtN} - \mathrm{DtN}_\gamma^{(\rho)}\| \;\leq\; \max_j e^{-\mathrm{Re}(k_j)\mathrm{Im}(\hat{z}_\mathrm{e})-\mathrm{Im}(k_j)\mathrm{Re}(\hat{z}_\mathrm{e})}.$$

To observe an exponential convergence for $\rho \to \infty$ along a PML path $\hat{z}_\gamma$ it is necessary that $\mathrm{Re}(\hat{z}_\gamma(\rho)), \mathrm{Im}(\hat{z}_\gamma(\rho)) \to \infty$.

As a mode approaches an anomalous mode, that is $k_j \to 0$, the exponential convergence degrades. Only the $1/\hat{z}_\gamma(\rho)$–factor in the error bound (3.10) guarantees convergence of the PML method.

Remark 3.2 For the definition of the $\mathrm{DtN}_\gamma^{(\rho)}$–operator we used the exterior domain problem (3.9) with zero Dirichlet boundary condition at $\hat{z}_\gamma(\rho)$. Alternatively, it is possible to pose a Sommerfeld like boundary condition $\partial_n u_\gamma(\rho) = i\tilde{k}u_\gamma(\rho)$ at the outer boundary of the PML sponge layer. Using $\tilde{k} = k_j$ the PML system yields the exact transparent boundary condition for the jth Fourier mode. Especially, with a zero Neumann boundary condition $\partial_n u_\gamma(\rho) = 0$ the anomalous mode is treated exactly.

Unfortunately, for Maxwell's equations it is generally not possible to treat anomalous modes exactly by imposing appropriate boundary condition on the outer PML boundary. For twofold periodic problems or for 2D problems with a conical light incidence ($k_y \neq 0$) several anomalous modes may appear. It is only possible to treat one of same exactly for all polarization of the scattered field. Therefore it is indeed necessary that the PML method copes with anomalous modes.

Regularity of the PML solution

The truncation error of the PML system (3.3) only depends on the chosen end-point $\hat{\xi}(\rho)$ of the PML. Besides this truncation error the discretization error within the PML also affects the interior field solution. In a finite element approximation this discretization error is related to the regularity of the solution u_γ on the path $\hat{\xi}$. Therefore we study the derivatives of u_γ along a path $\hat{\xi}(\xi)$. Since the notation is nasty for higher derivatives we restrict

ourselves to the analysis of the first derivative which is given by

$$u'_\gamma(\xi) \;=\; \sum_j v_j i k_j \hat{\xi}'(\xi) e^{i k_j \hat{\xi}(\xi)}.$$

Let J_p denote the set of propagating and anomalous modes and let J_e denote the set of evanescent modes. Since we only consider positive scalar material parameters $\mu > 0$ and $\varepsilon > 0$ we are allowed to introduce $\kappa_j \geq 0$ with $k_j = \kappa_j$ for $j \in J_p$ and $k_j = i\kappa_j$ for $j \in J_e$. We recall that $k_j = \sqrt{\omega^2 \mu\varepsilon - (k_x + jg)^2}$ which gives $\kappa_j \sim |j|$. We start with a trivial estimate of $|u'_\gamma(\xi)|$ for $\xi \geq 0$,

$$\begin{aligned} |u'_\gamma(\xi)| &\leq \sum_{j\in J_p} |v_j|\kappa_j |\hat{\xi}'(\xi)| e^{-\kappa_j \mathrm{Im}(\hat{\xi}(\xi))} + \sum_{j\in J_e} |v_j|\kappa_j |\hat{\xi}'(\xi)| e^{-\kappa_j \mathrm{Re}(\hat{\xi}(\xi))} \\ &\leq C \|(v_j)\|_{h^2} |\hat{\xi}'(\xi)| \left(\max_{j\in J_p} e^{-\kappa_j \mathrm{Im}(\hat{\xi}(\xi))} + \max_{j\in J_e} e^{-\kappa_j \mathrm{Re}(\hat{\xi}(\xi))} \right), \end{aligned} \tag{3.12}$$

where we assumed that the Dirichlet data (v_j) have regularity in $H^2_{k_x}(\Gamma)$ to make the estimate

$$\begin{aligned} \sum_j |v_j|\kappa_j &\leq C \sum_j |v_j| (1+|j|)^2 \cdot \frac{1}{1+|j|} \\ &\leq C \Big(\sum_j |v_j|^2 (1+|j|)^4 \Big)^{1/2} \Big(\sum_j \frac{1}{(1+|j|)^2} \Big)^{1/2} \leq C \|(v_j)\|_{h^2}. \end{aligned}$$

This is not a severe assumption because one shows that $u_\gamma|_\Gamma \in H^\infty_{k_x}(\Gamma)$ when the scatterer within the computational domain does not intersect the boundary Γ. This can be enforced in any case by shifting the coupling boundary.

The above estimate (3.12) tells us that we observe an exponential decay of the derivative when $\kappa_j \neq 0$ for all j. However, we are not satisfied with the above estimate (3.12) for the following reason: As κ_j approaches zero the estimate (3.12) only guarantees boundedness of the derivative $u'_\gamma(\xi)$. But as we learned in the previous section a small value $\kappa_j \sim 0$ necessitates a large PML thickness. To keep the number of unknowns small in an adaptive finite element discretization requires a successive "gain" of regularity with growing ξ which we cannot prove uniformly for $\kappa_j \geq 0$ by the given estimate.

We now want to sharpen up our estimate of the derivative $u'_\gamma(\xi)$ for small values of κ_j. We have

$$\begin{aligned} |u'_\gamma(\xi)| &\leq \sum_{j\in J_p} |v_j|\kappa_j |\hat{\xi}'(\xi)| e^{-\kappa_j \mathrm{Im}(\hat{\xi}(\xi))} + \sum_{j\in J_e} |v_j|\kappa_j |\hat{\xi}'(\xi)| e^{-\kappa_j \mathrm{Re}(\hat{\xi}(\xi))} \\ &\leq C \|(v_j)\|_{l^1} |\hat{\xi}'(\xi)| \left(\max_{j\in J_p} \kappa_j e^{-\kappa_j \mathrm{Im}(\hat{\xi}(\xi))} + \max_{j\in J_e} \kappa_j e^{-\kappa_j \mathrm{Re}(\hat{\xi}(\xi))} \right) \end{aligned} \tag{3.13}$$

The l_1–norm of the series (v_j) is bounded by the estimate

$$\sum_j |v_j| = \sum_j |v_j|(1+|j|)\frac{1}{1+|j|} \leq C\|(v_j)\|_{h_1}.$$

To derive a uniform bound for $\kappa_j \geq 0$ from inequality (3.13) we compute that

$$\max_{\kappa \geq 0} \kappa e^{-\kappa\alpha} = \frac{1}{e\alpha}.$$

for any $\alpha > 0$. Using this in inequality (3.13) with $\alpha = \mathrm{Im}(\hat{\xi})$ and $\alpha = \mathrm{Re}(\hat{\xi})$ gives

$$|u'_\gamma(\xi)| \quad \leq \quad C_\epsilon \frac{|\hat{\xi}'|}{\max\{\mathrm{Re}(\hat{\xi}), \mathrm{Im}(\hat{\xi})\}} \|(v_j)\|_{h^1} \leq C_\epsilon \frac{|\hat{\xi}'|}{|\hat{\xi}|} \|(v_j)\|_{h^1}. \quad (3.14)$$

3.4 Discussion of various PML paths

The convergence property (3.11) and the regularity estimation (3.14) have important consequences for the numerics in the presence of an anomalous mode. Let us assume that we want to keep the PML error below a threshold $tol > 0$. Since in the presence of an anomalous mode the convergence rate of the PML method in equation (3.11) degrades to $1/|\hat{\xi}|$ we are forced to select a PML thickness $\rho > 0$ so that $|\hat{\xi}(\rho)| \sim 1/tol$. For example to bound the error to $tol = 10^{-4}$ the length $|\hat{\xi}(\rho)|$ is approximately equal to ten thousands of wavelengths!

To handle this numerically the PML solution $u_\gamma^{(\rho)}(\cdot, \xi)$ must allow for an efficient approximation within the truncated domain $\Omega_{\mathrm{ext}}^{(\rho)}$. At this point the regularity of the PML solution $u_\gamma^{(\rho)}(\cdot, \xi)$ for $\xi \in [0, \rho]$ comes into play. The smaller the derivatives of $u_\gamma^{(\rho)}(\cdot, \xi)$ with respect to ξ the less discretization points are needed. We see the need for a treat–off between the thickness ρ of the PML and the regularity of $u_\gamma^{(\rho)}(\cdot, \xi)$ in $[0, \rho]$. We will discuss this issue for various PML paths. In the following discussion we consider the regularity estimate (3.14) as a *sharp* estimate.

Straight line $\hat{\xi}(\xi) = \gamma\xi$

We first discuss the straight line path $\hat{\xi}(\xi) = \gamma\xi$ with $\gamma = (1+i)/\sqrt{2}$. Similar to the estimate of the first derivative in equation (3.14) one computes $|\partial_\xi^n u(\xi)| \leq Cn/|\xi|^n$. We want to develop a simple heuristics for the choice of the mesh width $h(\xi)$ in dependency of $\xi \in [0, \rho]$ as required for a finite

element discretization. The local discretization error for the kth order finite element method is proportional $h^{k+1}|\partial_\xi^{k+1}u(\xi)|$. We therefore demand that

$$h(\xi) \quad \sim \quad |\partial_\xi^{k+1}u(\xi)|^{-1/(k+1)} \sim |\xi|.$$

Hence we are allowed to use a discretization $\{\xi_0 = 0, \ldots, \xi_N = \rho\}$ of the interval $[0, \rho]$ so that the number of discretization points only grows logarithmically with ρ. Since $\rho \sim 1/tol$ we conclude that the number of discretization points is proportional to $-\ln(tol)$. In a combination with an adaptive finite element method we expect an exponential convergence of the PML method with the number of unknowns.

Polynomial paths $\hat{\xi}(\xi) = (a_e + i\sigma\xi^n)\xi$

These paths are discussed for example in Collino [30]. The motivation for using polynomial paths is to increase the damping of modes with smaller propagation in the outward direction. However, this extra damping is paid with regularity losses of the evanescent modes. For an evanescent mode $k_j = i\kappa$ the PML solution still exponentially decays ($u_{\gamma,j}(\xi) \sim e^{-\kappa\xi}e^{i\kappa\xi^{n+1}}$) but exhibits higher oscillations as ξ increases. For $\kappa_j \to 0$ it follows from the regularity estimate (3.14) that the regularity is not improved with growing ξ. Hence one is not allowed to use a coarser grid for large distances ξ. Since $\kappa_j \to 0$ requires to use a PML thickness of $\rho \sim tol^{-1/(n+1)}$. We expect the need for $N_{\text{dof}} \sim tol^{-1/(n+1)}$ discretization points.

Paths with blow–ups

PML paths $\hat{\xi}(\xi)$ which reach infinity for a finite value ξ are used in Hugonin and Lalanne [58] and Bermudez et al. [16]. Bermudez proposed a path with $\hat{\xi}(\rho) = a_e + i\infty$ for a finite value $\rho > 0$ and a method parameter $a_e > 0$. With this choice of the PML path evanescent modes are not treated correctly since $\text{Re}(\hat{\xi}(\rho))$ does not reach infinity, cf. equation (3.10). To damp the evanescent modes below a given threshold one must either use a sufficiently large computational domain or increases the parameter a_e.

Hugonin and Lalanne [58] also use PML paths which reach infinity for a finite value $\rho > 0$. Hugonin and Lalanne aim at the usage of the *rigorous coupled wave analysis* method (RCWA) which rely on the expansion of the field into a Fourier series. The usage of a Fourier series necessitates the transformation on a finite domain which is numerically treated as a periodic domain. The path proposed by Hugonin and Lalanne lie asymptotically on a line in the complex plane with a non-linear parameterization so that $\hat{\xi}(\xi_e) = \infty + i\infty$. Evanescent and propagating modes are transformed to fields

$u_j(\xi)$ with finite norm in $H(\mathrm{curl}, \Omega \cup \Omega_{\mathrm{ext}}^{(\rho)})$. However for $k_j \sim 0$ the regularity of the transformed field is affected as can be concluded from our regularity estimate (3.14).

3.5 A practical algorithm

As proposed by the author in [120, 117] we avoid the choice of a sophisticated PML path. Instead, we use the straight line $\hat{\xi} = (1 + i\sigma)\xi$ as the PML path in combination with a finite element discretization which adapts well to the various situations one encounters in scattering problems. The numerical parameters are the thickness ρ of the PML layer and the discretization points $\{\xi_0 = 0, \ldots, \xi_N = \rho\}$.

Chen et al. [26, 10, 25] fixed in an *a priori* way the parameter ρ and used a standard adaptive finite element strategy to determine an accurate discretization in the ξ–direction by an *a posteriori* error estimator.

As in [120, 117] we propose a different strategy. Since the field is smooth in ξ–direction we avoid a costly *a posteriori* mesh control in the exterior domain. Instead we determine the discretization points in the ξ–direction by an *a priori* strategy discussed later in this section. As we learned in the sections before, the required thickness ρ of the PML layer depends sensitively on the physical situation. We therefore want to determine automatically the required PML thickness by an *a posteriori* criterion. In the following we assume that the interior domain is discretized with finite elements of order l. We want to determine the PML parameters ρ and $\{\xi_0 = 0, \ldots, \xi_N = \rho\}$. Our algorithm for an PML consists of the following building blocks:

1. *Find goal accuracy:* We analyze the interior domain discretization on the coupling boundary to estimate the discretization error ϵ_{int} in the interior domain. Furthermore the minimum mesh width h_Γ on the coupling boundary is extracted. We want to bound the PML error *tol* by the discretization error in the interior domain that is, $tol < \epsilon_{\mathrm{int}}$.

2. *Find PML thickness ρ:* This parameter has to be chosen large enough so that the truncation error is smaller than *tol*. The required thickness ρ is not known *a priorily*. We choose ρ such that $tol \leq e^{-2\kappa_{\min}\rho}$, where $\kappa_{\min}$ is the weakest damping factor which is determined iteratively as explained later in Step 4. As the initial guess we set $\kappa_{\min}$ equal to the minimum wave number $k_{\min}$ in the exterior domain. Hence a wave which travels perpendicular to the coupling boundary is sufficiently damped by this initial guess.

3. *Find discretization points:* We determine the discretization points $\{\xi_0 = 0, \ldots, \xi_N = \rho\}$ heuristically in the following way. The field $u_\gamma(\cdot, \xi)$ is a holomorphic function in the ξ direction and we assume that $u_\gamma(\cdot, \xi)$ can be written as

$$\begin{aligned} u_\gamma(\cdot, \xi) &= \int_0^{k_{\max}} U_\gamma(\cdot, k) e^{ik(1+i\sigma)\xi} \mathrm{d}k + \\ &\quad \int_0^{\infty} U_\gamma(\cdot, \kappa) e^{-\kappa(1+i\sigma)\xi} \mathrm{d}\kappa. \end{aligned}$$

The first integral corresponds to propagating waves in the outward ξ–direction and the second integral corresponds to evanescent waves. For periodic grating problems we have verified such a representation formula, with the integrals replaced by sums. For the general case we remark that the above equation can be motivated from equation (2.4) which we derived by an inverse Laplace transform, when we discussed the pole condition.

It is not necessary to take the whole evanescent spectrum $\kappa \in [0, \infty)$ into account, because modes with a large damping factor κ cannot be resolved by the mesh in the interior domain. Hence we do not allow for a smaller mesh width in the exterior domain than the minimum mesh width h_Γ on the coupling boundary. The cutoff factor $\kappa_{\max}$ is determined from the condition that the $H^1([0, \rho])$ approximation error of a function $e^{-\kappa\xi}$ with $\kappa \leq \kappa_{\max}$ is smaller than *tol* on a uniform mesh with mesh width h_Γ.

Let us regard the 1D reference problem

$$\begin{aligned} -v'' + \tilde{k}^2 v &= 0, \\ v(0) &= 1, \\ v'(\rho) &= 0 \end{aligned}$$

for $\tilde{k} \in [0, k_{\max}] \cap i[0, \kappa_{\max}]$. To fix the discretization points $\{\xi_0 = 0, \ldots, \xi_N = \rho\}$ we demand that the $H^1([0, \rho])$ discretization error of the above 1D reference problems is smaller than *tol* for all $\tilde{k} \in [0, k_{\max}] \cap i[0, \kappa_{\max}]$. Practically, we solve the above 1D problem with an adaptive mesh refinement for a few number of test values for $\tilde{k}$. This provides us the desired discretization points.

4. *A posteriori accuracy check:* After we have solved the discrete scattering problem we check if the field is sufficiently small on the outer boundary of the PML. In our implementation this is done by a comparison of the finite element coefficients on the outer PML boundary and

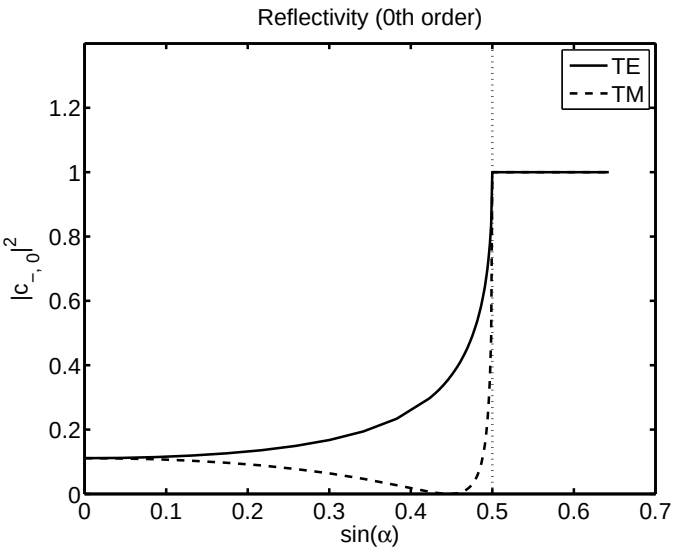

Figure 3.5: Plane material interface: Computed reflectivity. $c_{-,0}(\alpha)$ denotes the 0th order reflected diffraction mode in dependence on the incident angle α.

the coupling boundary. To each finite element coefficient c_j attached to a boundary patch on the coupling boundary corresponds a finite element coefficient c_J on the outer PML boundary. We demand that $|c_J|/|c_j| \leq tol$. If the damping criterion is not satisfied we decrease the weakest damping factor in Step 2 by a fixed rate $\kappa_{\min} \to \kappa_{\min} - \delta\kappa$ and go back to Step 2. In our implementation we set $\delta\kappa = k_{\min}/10$, where $k_{\min}$ is the initial choice for κ_{min} as described in Step 2. If $\kappa_{\min} = 0$ is reached an anomalous mode is present and the iteration stops.

3.6 Numerical examples

It is a major feature of the adaptive PML algorithm that the PML thickness and the discretization within the PML are determined accordingly to the quality of the finite element solution in the interior domain. Therefore we want to verify by numerical experiments that the algorithm behaves efficiently under a successive refinement of the interior domain even in critical situation when an anomalous mode appears.

3.6.1 Plane material interface

We regard a plane material interface at $z = 0$. The material properties in the lower half space are $\mu_- = 1$ and $\varepsilon_- = 4$. This gives a refractive index $n_- = 2$ in the lower domain. In the upper half space we assume $\mu_+ = 1$ and $\varepsilon_+ = 1$ and hence $n_+ = 1$. As incoming fields we use TE/ TM–polarized plane waves with vacuum wave number equal to one and coming from below with incident angles (α, ϑ). Precisely, we have

$$\mathbf{k}_{\text{inc}} = \frac{2\pi n_-}{\lambda_0} \begin{pmatrix} -\cos(\vartheta)\sin(\alpha) \\ \sin(\vartheta)\sin(\alpha) \\ \cos(\alpha) \end{pmatrix}. \tag{3.15}$$

The two orthogonal polarizations $\mathbf{E}_{\text{TM}}$ and $\mathbf{E}_{\text{TE}}$ are given by

$$\mathbf{E}_{\text{TE}} = \begin{pmatrix} \sin(\vartheta) \\ \cos(\vartheta) \\ 0 \end{pmatrix}, \ \mathbf{E}_{\text{TM}} = \begin{pmatrix} \cos(\vartheta)\cos(\alpha) \\ -\sin(\vartheta)\cos(\alpha) \\ \sin(\alpha) \end{pmatrix}. \tag{3.16}$$

The analytic solution to this problem is given by the Fresnel equations.

This configuration is periodic in the x–direction with any period and is invariant in the y–direction. We use a cross-section computational domain $\Omega = [-1, 1] \times \{0\} \times [-2, 2]$ with periodic boundary conditions in the x–direction. In the following we fix $\vartheta = 20^\circ$ and we vary the angle α from 0° to 40°. For $\alpha \geq 30^\circ$ one observes a total internal reflection of the incoming plane wave at the material interface. An anomalous mode appears in the upper half space at the critical angle $\alpha_C = 30^\circ$.

Figure 3.5 shows the intensity $|c_{-,0}|^2$ of the computed 0th order reflected mode. The critical angle α_C is marked by the dotted vertical line. As expected we observe a total reflection for angles larger than the critical angle. In the computation we used a fixed finite element grid in the interior domain and fourth order finite elements.

The PML discretization $\{\xi_0 = 0, \ldots, \xi_N = \rho\}$ was steered by our adaptive PML method with a tolerance requirement $tol = 1.2 \cdot 10^{-3}$. Figure 3.6 shows the number of grid points N in the lower and upper exterior domain. In the upper domain the PML thickness varies in the range from 1.8 wavelengths to circa 500 wavelengths at the critical angle α_C (not plotted). The number of mesh points in the PML varies only in the range from 4 points to 18 points (Figure 3.6).

In Figure 3.7 we compared the computed 0th order mode $c_{0,j}$ with the exact solution. The error has its maximum $err_{max} = 4 \cdot 10^{-3}$ at the critical angle α_C. This seems to be a discouraging result because our aim was to

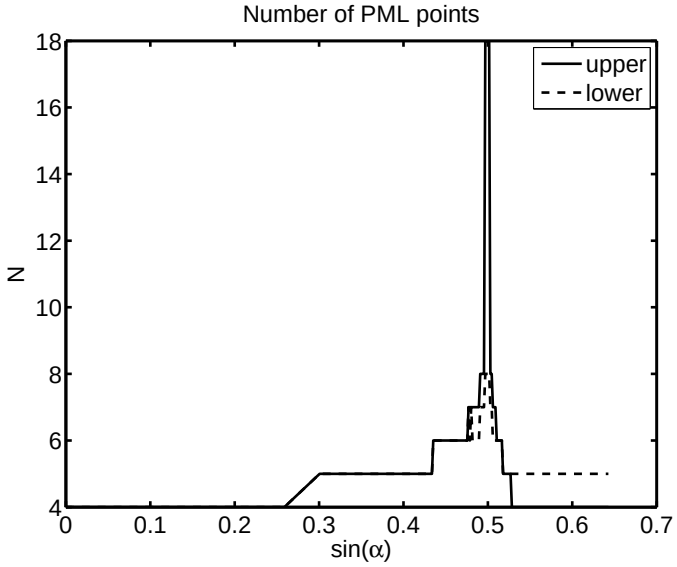

Figure 3.6: Plane material interface: Number of mesh points, N, in the PML in dependence on the incident angle α. The PML is steered individually for the upper and lower exterior domain.

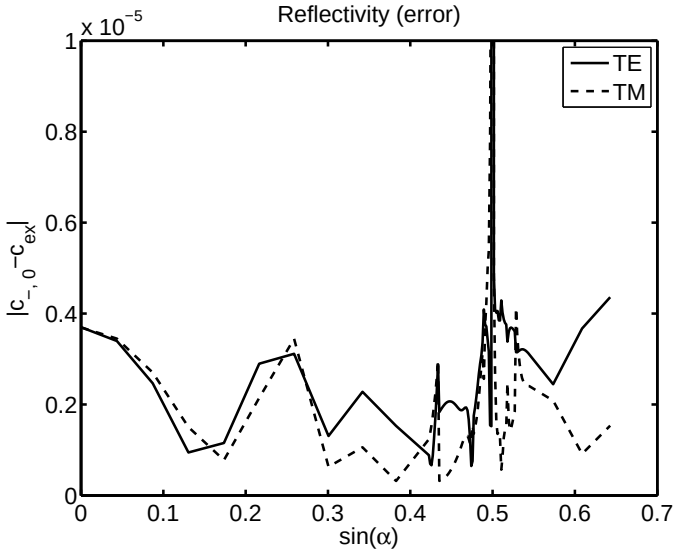

Figure 3.7: Plane material interface: Error of the computed reflected diffraction mode $c_{-,0}$. We observe a maximum error $err_{\max} = 4 \cdot 10^{-3}$ at the critical angle.

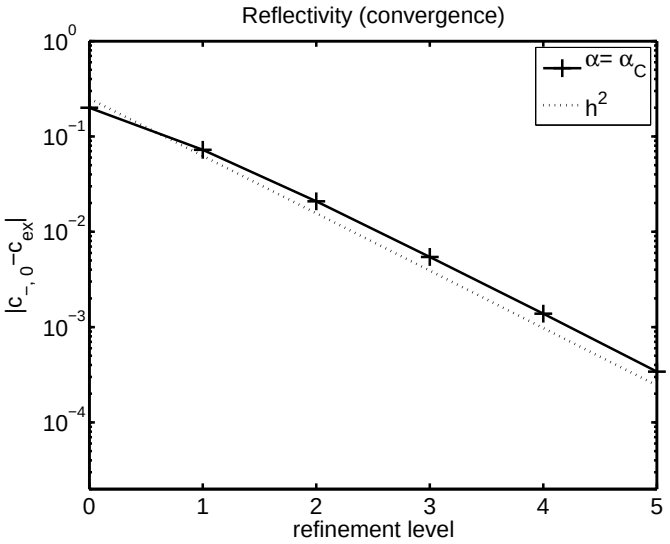

Figure 3.8: Plane material interface: Convergence of the reflected diffraction mode $c_{-,0}$ with the finite element mesh refinement level. In this case we fixed the PML discretization and refined the interior finite element mesh only. At the critical angle α_C one observes the theoretical given convergence rate of the second order finite element discretization (dotted line).

construct an algorithm which shows no convergence degradation at the critical angle. But the error at the critical angle remains below the prescribed tolerance. The higher accuracy for $\alpha \neq \alpha_c$ can be explained as follows:

For $\alpha \neq \alpha_C$ the PML method converges exponentially with the layer thickness. Since we increase the layer thickness by finite intervals we typically use a larger layer as needed to satisfy the prescribed tolerance condition. Only for $\alpha = \alpha_C$ the PML truncation error directly corresponds to the prescribed tolerance. In addition, we observed a better convergence than theoretically expected for $\alpha \neq \alpha_C$. This "super"–convergence (the problem and the functional $c_{-,0}$ are smooth) is not observed at the critical angle α_C. In Figure 3.8 we verified the convergence of the finite element solution at the critical angle α_C. We fixed a sufficiently large PML discretization and studied the convergence of a second order finite element discretization under a refinement of the finite element mesh in the interior domain. The theoretical convergence rate is given by the dotted line. The convergence rate is in a good agreement with the theoretical given convergence rate of the second order finite element discretization.

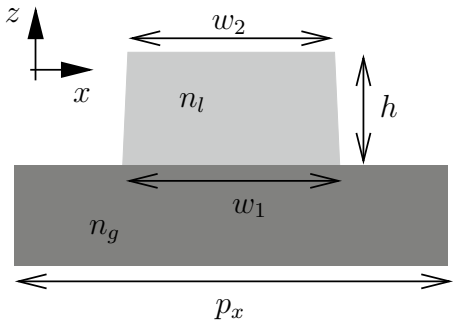

Figure 3.9: Photomask with periodic line structure. The geometry is invariant in the y–direction and periodic in the x–direction with period $p_x = 400$. The lower domain is glass with refractive index $n_g = 1.56306$. The upper domain consists of air. The line placed on top of the glass has a height $h = 65.4$, widths $w_1 = 200$, $w_2 = 191$ and refractive index $n_l = 2.52 + 0.596i$.

3.6.2 Periodic line mask

This realistic example is taken from Burger et al. [20]. We refer to Figure 3.9 for the definition of the material properties and the geometry configuration. The structure is illuminated from below by TE/ TM–polarized plane waves with vacuum wavelength $\lambda_0 = 193$, and incident angles (α, ϑ), cf. equations (3.15) and (3.16) in the previous paragraph.

In the following we fix $\vartheta = 20°$ and vary the angle α from $-25°$ to $25°$. We denote the wave number in the lower and upper domains by k_- and k_+, respectively. An anomalous mode appears in the upper/lower domain when

$$k_{\mathrm{inc},x}(\alpha_C) + j\frac{2\pi}{p_x} = \sqrt{k_{+/-}^2 - k_{\mathrm{inc},y}^2(\alpha_C)}$$

for some $j \in \mathbb{N}$ and a critical angle α_C.

Figure 3.10 shows the computed intensity of the transmitted 0th order diffraction mode $c_{+,0}$. In the computation we used a fixed finite element grid in the interior domain and quadratic finite elements. Incident angles α_C which give rise to an anomalous modes are marked by dotted, vertical lines and are contained in the sampling grid for α. As expected the transmission behaves non-smooth at these points.

The PML discretization $\{\xi_0 = 0, \ldots, \xi_N = \rho\}$ was steered by our adaptive PML method with a tolerance requirement $tol = 3 \cdot 10^{-3}$. As shown in Figure 3.11 the thickness of the PML layer varies between 1.7–$3.8 \cdot 10^3$ wavelengths. The number of discretization points N varies only in the moderate range from 8 to 27 (not plotted).

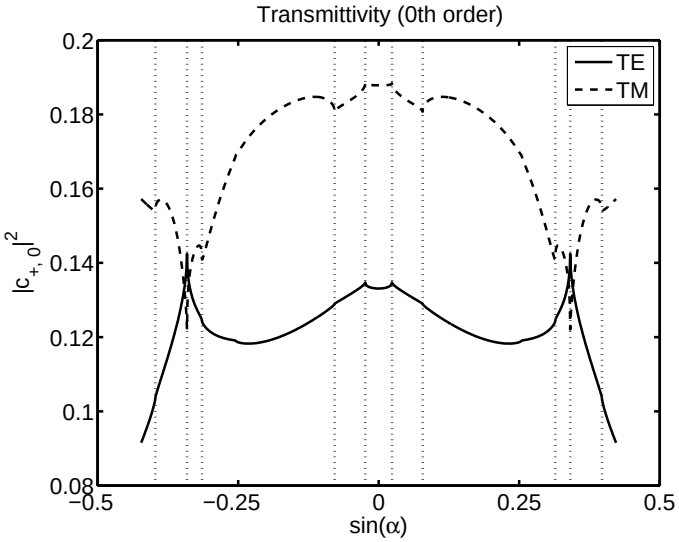

Figure 3.10: Periodic line mask: Transmission in dependence on the incident angle α. $c_{+,0}$ denotes the 0th order transmitted diffraction mode. Incident angles which give rise to an anomalous modes are marked by dotted, vertical lines.

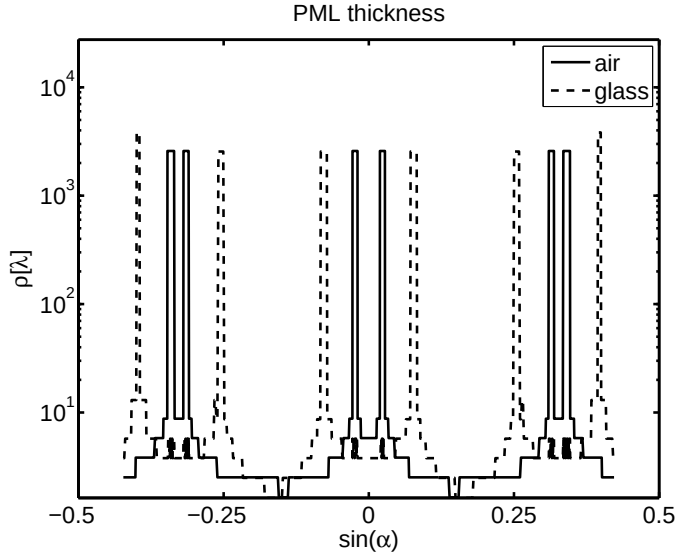

Figure 3.11: Periodic line mask: PML thickness. The PML thickness is chosen individually for the upper (air) and lower (glass) exterior domain. As an anomalous mode appears a huge PML is required.

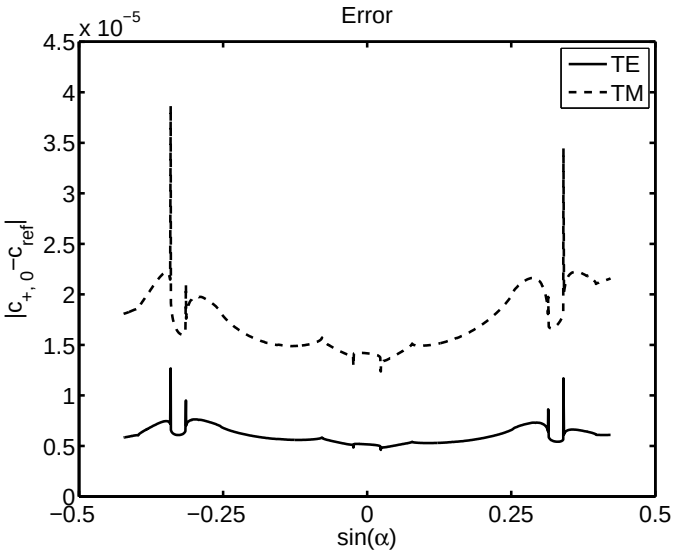

Figure 3.12: Periodic line mask: Computed 0th order transmitted diffraction mode $c_{+,0}$ compared to a reference solution c_{ref}. The reference solution is obtained on a larger computational domain with higher finite element degree and smaller mesh width.

To verify the accuracy we computed the same results on a larger computational domain with third order finite and halved mesh width, see Figure 3.12. Again, we observe the maximum errors at the position of the anomalous modes but the error remains below the prescribed tolerance. Furthermore the error is not so drastically increased at the critical angles as in the previous example with a smooth solution.

After focusing on the behavior of the adaptive PML method at the pathological cases with an anomalous mode we also want to study the performance of the method in a non-critical situation.

Figure 3.13 gives the convergence of the method for $\alpha = 0°$. We used a second order finite element discretization. The grid in the interior domain was uniformly refined whereas the PML discretization was steered by our adaptive PML method. The reference solution was obtained with third order finite elements with a finer mesh on an enlarged computational domain. From Figure 3.13 we see that the finite element convergence under an uniform mesh refinement is not affected by the adaptive PML method. This demonstrates the accuracy of the method. To check the efficiency of the adaptive PML method we regard Figures 3.14 and 3.15. Theoretically we

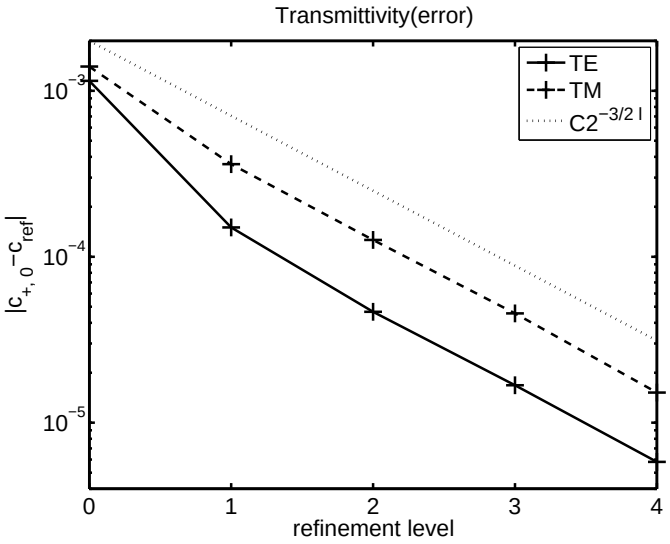

Figure 3.13: Periodic line mask: Convergence at $\alpha = 0°$ for second order finite discretization with refinement level l. The finite element mesh was uniformly refined in the interior domain. The PML discretization was steered fully automatically. The dotted line corresponds to the expected convergence behavior of the interior finite element discretization.

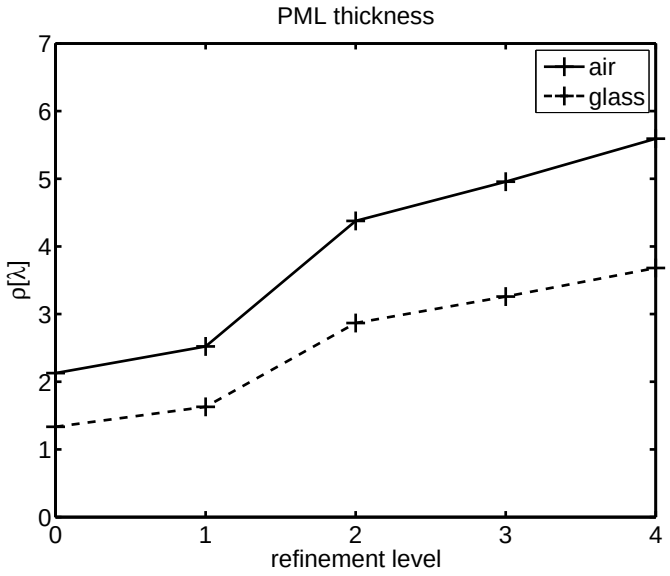

Figure 3.14: Periodic line mask: PML thickness for non-critical incidence angle $\alpha = 0°$.

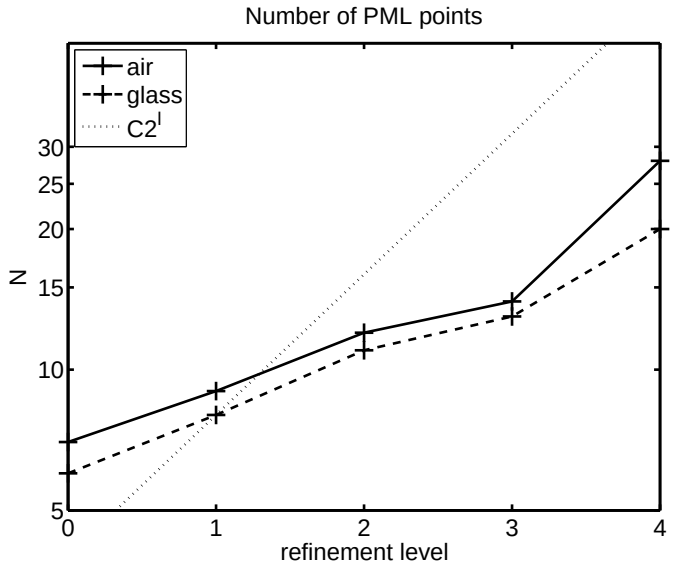

Figure 3.15: Line mask example: Number of PML discretization points, N, for non-critical incidence angle $\alpha = 0°$. The dotted line gives the theoretically expected optimum grow.

expect a linear grows of the PML thickness with the refinement level. Indeed, the thickness as determined by the adaptive PML method grows moderately with the refinement level (Figure 3.14).

More important for the efficiency is the number N of discretization points used in the PML. With an uniform refinement of the interior domain we also expect an uniform refinement of the PML discretization to improve the finite element discretization error within the PML. Therefore, the number of discretization points in the PML is allowed to grow like $N \sim 2^l$, with the refinement level l. As can be seen in Figure 3.15 the number of discretization points in the PML remains even smaller than expected in the beginning of the refinement process.

Chapter 4

Exterior domain evaluation formula for PML solutions

A computation of the near–field only is often of little practical interest. Instead one needs to know the field in the exterior domain in a large distance to the scatterer. Since this distance typically measures hundreds or more of wavelengths it is not a choice to increase the computational domain size so that it contains the evaluation point. Figure 4.1 shows two typical situations in 2D. We assume that the material parameters μ and ε are constant scalars above the hyperplane $z = 0$. Below this hyperplane the structure has a complicated geometry.

The famous Rayleigh–Sommerfeld diffraction integral [47, p. 46] provides an evaluation formula for points with $z > 0$. The Rayleigh–Sommerfeld diffraction integral only involves the field data on the hyperplane $z = 0$. This integral representation has two numerical disadvantages. Firstly, the integrand decays only very slowly with the distance $r = |(x, y, 0)|$. Secondly, the integrand is oscillatory in r. Often a truncated integration volume is used, see for example Veerman et al [109] and Shen and Wang [101]. This may allow for fast integration methods but due to the slow decay of the integrand a truncation is awkward. In [123] the author proposed a new way to evaluate the Rayleigh–Sommerfeld diffraction formula which relies on a complex deformation of the integration path. As in the PML method the oscillatory factor of the integrand is transformed into an evanescent function making the integral feasible for standard integration method. Not surprisingly, the so *complexed stretched* Rayleigh–Sommerfeld diffraction integral involves the field data within the PML.

In the next section we will derive a PML based exterior domain evaluation formula, which covers the Maxwell's case as well and which is more general than the Rayleigh–Sommerfeld diffraction integral. The Rayleigh–

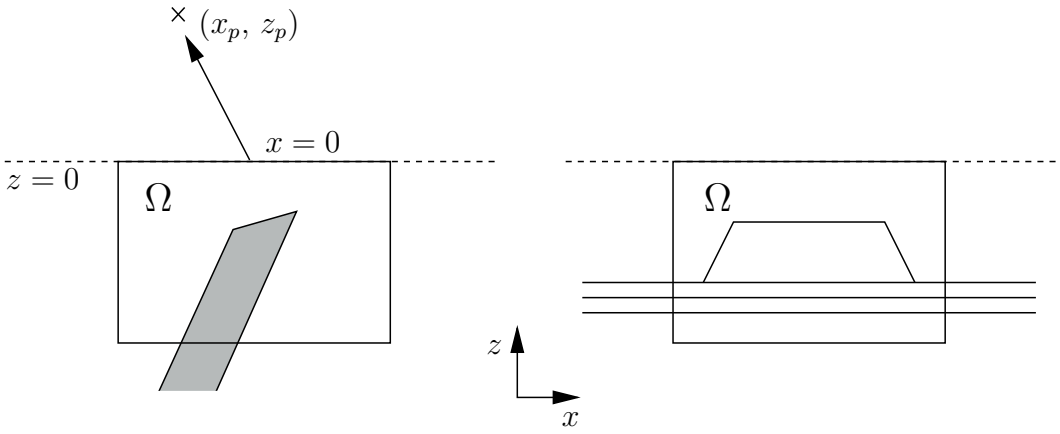

Figure 4.1: Exterior domain evaluation. This figure shows two typical situations. The evaluation point (x_p, z_p) lies above the scatterer. We assume homogeneous materials above the hyperplane $z = 0$. The structure below this hyperplane is arbitrary.

Sommerfeld diffraction integral, or *Stratton-Chu diffraction integral* for the Maxwell case, is afterwards discussed in greater details.

4.1 Exterior domain evaluation formula based on Green's tensors

Let us regard Figure 4.2. The computational domain is admissible in the sense of Definition 2.1, so that there exists a globally defined, generalized distance coordinate ξ in the exterior domain. The dashed line in Figure 4.2 indicates a $\xi = \rho > 0$ isoline.

The exterior domain is split into two sub-domains $\Omega_{\text{ext},1}$ and $\Omega_{\text{ext},2}$. In Figure 4.2, the common interface $\Omega_{\text{ext},1} \cap \Omega_{\text{ext},2}$ is shown by the bold black lines. In the following $\Omega_{\text{ext}}^{(\rho)}$ denotes the bounded domain $\Omega_{\text{ext}}^{(\rho)} \subset \Omega_{\text{ext}}$ enclosed by the $\xi = \rho$ hypersurface. Further, we define the bounded domains $\Omega^{(\rho)} = \Omega \cup \Omega_{\text{ext}}^{(\rho)}$, $\Omega_{\text{ext},1}^{(\rho)} = \Omega_{\text{ext},1} \cap \Omega_{\text{ext}}^{(\rho)}$ and $\Omega_{\text{ext},2}^{(\rho)}$ accordingly.

Let us assume that an outward radiating Green's tensor $\mathbf{g}_{\mathbf{x}_p}$ is available for an evaluation point $\mathbf{x}_p \in \Omega_{\text{ext},1}^{(\rho)}$ within $\Omega_{\text{ext},1}$, that is

$$d\mu^{-1} d\mathbf{g}_{\mathbf{x}_p}(\mathbf{x}) - \omega^2 \varepsilon \mathbf{g}_{\mathbf{x}_p}(\mathbf{x}) = \delta(\mathbf{x} - \mathbf{x}_p)\mathbf{1}, \quad \mathbf{x} \in \Omega_{\text{ext},1}. \tag{4.1}$$

In the situation as depicted in Figure 4.2, the domain $\Omega_{\text{ext},1}$ is a stack of three layers, so that the Green's tensor can be computed by means of the

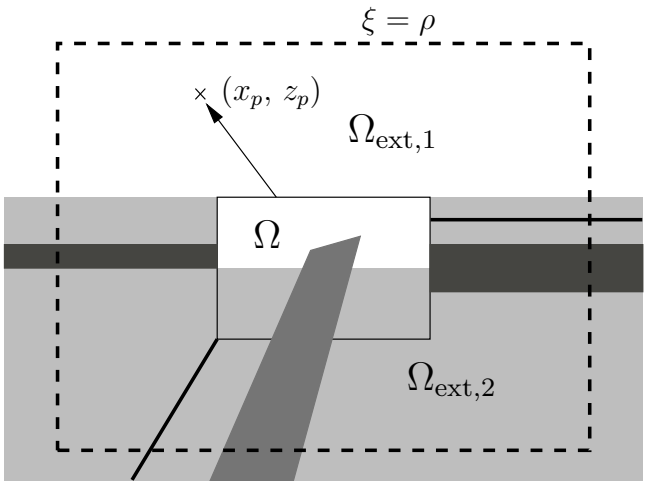

Figure 4.2: Exterior domain evaluation with partially known Green's tensor. We assume that the Green's tensor corresponding to an evaluation point (x_p, z_p) is known in the sub-domain $\Omega_{\text{ext},1}$ of the exterior domain. The evaluation formula involves field data on the interface $\Omega_{\text{ext},1} \cap \Omega$ and on the interface $\Omega_{\text{ext},1} \cap \Omega_{\text{ext},2}$ (black lines). On the latter interface complex deformed boundary integrals are evaluated which uses the PML solution.

Sommerfeld integrals as explained in Section 1.2.4.

We now apply the wedge product with the scattered field $\mathbf{e}_{\text{sc}}$ on both sides equation (4.1) and integrate over $\Omega^{(\rho)}_{\text{ext},1}$. We have

$$\mathbf{e}_{\text{sc}}(\mathbf{x}_p) = \int_{\Omega^{(\rho)}_{\text{ext},1}} \mathbf{e}_{\text{sc}} \wedge \left(d\mu^{-1} d\mathbf{g}_{\mathbf{x}_p} - \omega^2 \varepsilon \mathbf{g}_{\mathbf{x}_p} \right),$$

and applying the partial integration formula (1.45) we get

$$\mathbf{e}_{\text{sc}}(\mathbf{x}_p) = \int_{\Omega_{\text{ext},1}} d\mathbf{e}_{\text{sc}} \wedge \mu^{-1} d\mathbf{g}_{\mathbf{x}_p} - \omega^2 \mathbf{e}_{\text{sc}} \wedge \varepsilon \mathbf{g}_{\mathbf{x}_p} - \int_{\partial\Omega^{(\rho)}_{\text{ext},1}} \mathbf{e}_{\text{sc}} \wedge \mu^{-1} d\mathbf{g}_{\mathbf{x}_p}$$

Partially integrating once more yields

$$\mathbf{e}_{\text{sc}}(\mathbf{x}_p) = \int_{\partial\Omega^{(\rho)}_{\text{ext},1}} \mu^{-1} d\mathbf{e}_{\text{sc}} \wedge \mathbf{g}_{\mathbf{x}_p} - \mathbf{e}_{\text{sc}} \wedge \mu^{-1} d\mathbf{g}_{\mathbf{x}_p}. \tag{4.2}$$

To bring the PML solution into play, we evoke the stretching automorphism

$$\begin{aligned} S_\gamma : \Omega_{\text{ext}} &\to \Omega_{\text{ext}} \\ (\cdot, \cdot, \xi) &\mapsto (\cdot, \cdot, \gamma\xi), \end{aligned}$$

for $\gamma \in \mathbf{R}_+$. This mapping gives rise to an isomorphism

$$S_{\gamma,\rho} : \Omega_{\text{ext},1}^{(\rho/\gamma)} \to \Omega_{\text{ext},1}^{(\rho)},$$

and pull backing the right hand side of equation (4.2) gives

$$\mathbf{e}_{\text{sc}}(\mathbf{x}_p) = \int_{\partial\Omega_{\text{ext},1}^{(\rho/\gamma)}} \mu_\gamma^{-1} d\mathbf{e}_{\text{sc},\gamma} \wedge \mathbf{g}_{\mathbf{x}_p,\gamma} - \mathbf{e}_{\text{sc},\gamma} \wedge \mu_\gamma^{-1} d\mathbf{g}_{\mathbf{x}_p,\gamma},$$

where $\mathbf{e}_{\text{sc},\gamma}$, $\mathbf{g}_{\mathbf{x}_p,\gamma}$, *etc.* denote the pulled back quantities under the isomorphism $S_{\gamma,\rho}$. Since $\rho > 0$ was considered to be large but arbitrary, we are allowed to switch back to the integration domain $\Omega_{\text{ext},1}^{(\rho)}$ in equation (4.2), so that

$$\mathbf{e}_{\text{sc}}(\mathbf{x}_p) = \int_{\partial\Omega_{\text{ext},1}^{(\rho)}} \mu_\gamma^{-1} d\mathbf{e}_{\text{sc},\gamma} \wedge \mathbf{g}_{\mathbf{x}_p,\gamma} - \mathbf{e}_{\text{sc},\gamma} \wedge \mu_\gamma^{-1} d\mathbf{g}_{\mathbf{x}_p,\gamma}. \tag{4.3}$$

We are now in a similar position as in the derivation of the PML equation, cf. Section 3.1. To prove that equation (4.3) is also valid for the PML solution with a complex γ, we consider the right hand side of equation (4.3) as a complex valued function of $I(\gamma)$. Provided that $I(\gamma)$ is analytic in a simply connected subset of the complex plane containing the actual PML path parameter, say $\gamma = 1 + i\sigma$, and the point $\gamma = 1$, we are done. To guarantee this, we must pay special attention on the branch cuts of the complex continued Green's tensor $\mathbf{g}_{\mathbf{x}_p,\gamma}$. We will see later in Section 4.4, that the arising branch cuts of the Green's tensor constrain the PML damping value σ depending on the position of the evaluation point. However, in most situations that is not a severe restriction.

To derive a numerically feasible evaluation formula from equation (4.3) we split the boundary integral:

$$\begin{aligned}\mathbf{e}_{\text{sc}}(\mathbf{x}_p) = &\int_{\partial\Omega_{\text{ext},1}^{(\rho)} \cap \partial\Omega} \mu_\gamma^{-1} d\mathbf{e}_{\text{sc},\gamma} \wedge \mathbf{g}_{\mathbf{x}_p,\gamma} - \mathbf{e}_{\text{sc},\gamma} \wedge \mu_\gamma^{-1} d\mathbf{g}_{\mathbf{x}_p,\gamma} + \\ &\int_{\partial\Omega_{\text{ext},1}^{(\rho)} \cap \Omega_{\text{ext},2}^{(\rho)}} \mu_\gamma^{-1} d\mathbf{e}_{\text{sc},\gamma} \wedge \mathbf{g}_{\mathbf{x}_p,\gamma} - \mathbf{e}_{\text{sc},\gamma} \wedge \mu_\gamma^{-1} d\mathbf{g}_{\mathbf{x}_p,\gamma} + \\ &\int_{\partial\Omega_{\text{ext},1}^{(\rho)} \cap \partial\Omega^{(\rho)}} \mu_\gamma^{-1} d\mathbf{e}_{\text{sc},\gamma} \wedge \mathbf{g}_{\mathbf{x}_p,\gamma} - \mathbf{e}_{\text{sc},\gamma} \wedge \mu_\gamma^{-1} d\mathbf{g}_{\mathbf{x}_p,\gamma}.\end{aligned}$$

The latter integral only involves the PML solution $\mathbf{e}_{\text{sc},\gamma}$ and the complex continued Green's tensor $\mathbf{g}_{\mathbf{x}_p,\gamma}$ for distance $\xi = \rho$. Since both functions decay exponentially with ξ, taking the limit $\rho \to \infty$ yields the desired formula

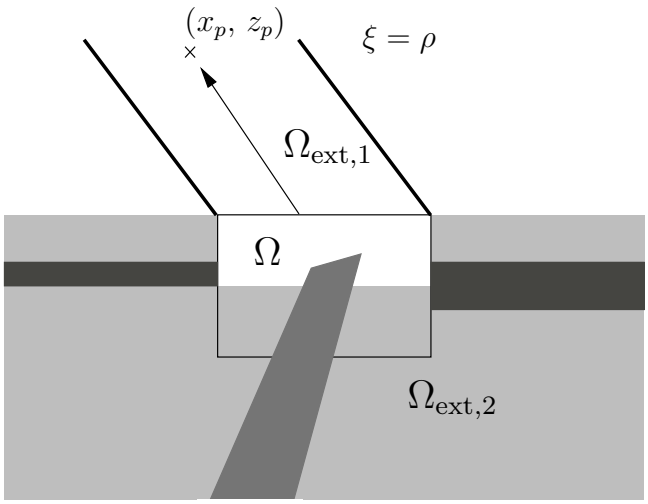

Figure 4.3: Inappropriate splitting of the exterior domain into $\Omega_{\text{ext},1}$ and $\Omega_{\text{ext},2}$.

$$\begin{aligned}\mathbf{e}_{\text{sc}}(\mathbf{x}_p) = &\int_{\partial\Omega_{\text{ext},1}\cap\partial\Omega} \mu_\gamma^{-1} d\mathbf{e}_{\text{sc},\gamma} \wedge \mathbf{g}_{\mathbf{x}_p,\gamma} - \mathbf{e}_{\text{sc},\gamma} \wedge \mu_\gamma^{-1} d\mathbf{g}_{\mathbf{x}_p,\gamma} + \\ &\lim_{\rho\to\infty} \int_{\partial\Omega_{\text{ext},1}^{(\rho)}\cap\partial\Omega_{\text{ext},2}^{(\rho)}} \mu_\gamma^{-1} d\mathbf{e}_{\text{sc},\gamma} \wedge \mathbf{g}_{\mathbf{x}_p,\gamma} - \mathbf{e}_{\text{sc},\gamma} \wedge \mu_\gamma^{-1} d\mathbf{g}_{\mathbf{x}_p,\gamma}.\end{aligned} \tag{4.4}$$

The first integral is defined on a bounded domain and can be numerically integrated by standard quadrature rules.

The second integral (4.4) involves the PML solution and is defined on the infinite interface of the first and second exterior domains. However, by the damping property of the PML solution and the complex continued Green's tensor, the integrand decays exponentially with the PML thickness ρ, rendering the integral into an well defined, absolutely convergent integral even for $\rho = \infty$.

Unfortunately, one does not necessarily benefit from the exponentially decay of the second integrand in (4.4). For an efficient numerical integration of the second integral in (4.4), it is particularly required that the integrand stays harmless for small values of ξ. We will see in Section (4.4) that this depends strongly on the position of the evaluation point and the chosen interface $\Omega_{\text{ext},1} \cap \Omega_{\text{ext},2}$.

To see that at a glance, we refer to Figure 4.3 as a counter example. Now, the domains $\Omega_{\text{ext},1}$, $\Omega_{\text{ext},2}$ are chosen, so that their common interface

is directed towards the evaluation point. The domain $\Omega_{\text{ext},1}$ is homogeneous and an outward radiating Green's tensor is given by formula (1.21). One immediately verifies that for small values of ξ, the Green's tensor contribution in the evaluation formula (4.4) grows exponentially fast. For an efficient numerical evaluation of the second integral in (4.4) it is required that the decay of the PML solution overcompensates the possible grow of the Green's tensor for small ξ values. In Section 3.1 we will derive a criterion for when this happens.

In contrast to the inappropriate splitting in Figure 4.3, our original splitting in Figure 4.2 is well suited for the evaluation formula (4.4), since the Green's tensor decays exponentially fast also for small values of ξ.

Far field evaluation When the decay of the PML solution overcompensates the possible growth of the Green's tensor in the evaluation formula (4.4), a truncation of the infinite boundary integration domain $\Omega_{\text{ext},1} \cap \Omega_{\text{ext},2}$ to $\Omega_{\text{ext},1}^{(\rho)} \cap \Omega_{\text{ext},2}^{(\rho)}$ results in an exponentially decreasing error with growing ρ. Furthermore, the approximation quality only depends on the direction of the evaluation point. This allows to replace the Green's tensor by its asymptotic approximation for a far distance evaluation point.

This may simplify the numerical evaluation. Often the asymptotic expansion of the Green's tensor for far distance evaluation points is numerically available even when the exact Green's tensor is hard to construct, e.g. when the media in $\Omega_{\text{ext},1}$ are stratified as sketched in Figure 4.2, and one wants to avoid a costly evaluation of the Sommerfeld integrals.

It is well-known that for a homogeneous upper half space, the far field value of the scattered field in direction $\hat{x} = (x, y, z)$ is related to its Fourier transform with respect to xy. This way, the asymptotic form of the evaluation formula (4.4) can be used to compute the angular spectrum representation of the scattered field in the upper half space. We will come back this in greater detail in Section 4.6. The special case that the Green's tensor is valid on the entire exterior domain, that is $\Omega_{\text{ext},1} = \Omega_{\text{ext}}$, is treated in Janssen, Haver et al. [62].

4.2 Stratton–Chu diffraction integral

We regard the special configuration with $\Omega_{\text{ext},1}$ to be the upper half space $z \geq 0$, cf. Figure 4.4. In the evaluation formula (4.4) we use an outward radiating Green's tensor in the upper half space $\widetilde{\mathbf{g}}_{\mathbf{x}_p}$ which has zero Dirichlet boundary values on the hyperplane $z = 0$. This Green's tensor $\widetilde{\mathbf{g}}_{\mathbf{x}_p}$ can be constructed by mirroring the Green's tensor $\mathbf{g}_{\mathbf{x}_p}$ related to the entire space

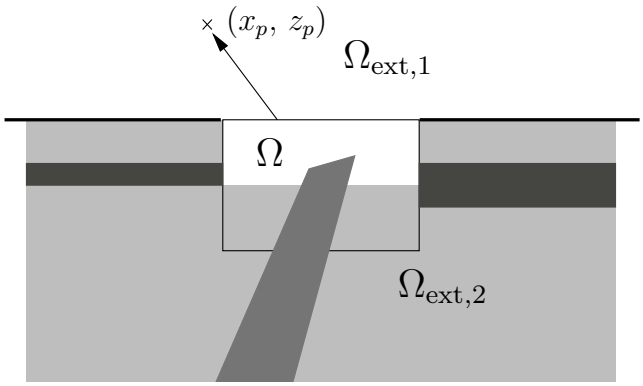

Figure 4.4: Splitting into upper and lower half space as used for the Stratton–Chu, respectively Rayleigh–Sommerfeld diffraction integral.

at the hyperplane $z = 0$,

$$\widetilde{\mathbf{g}}_{\mathbf{x}_p}(x, y, z) = \mathbf{g}_{\mathbf{x}_p}(x, y, z) - s\mathbf{g}_{\mathbf{x}_p}(x, y, -z),$$

with the field mirror operator $s_{i,j} = \text{diag}([1, 1, -1])$. Dropping Dirichlet boundary terms in equation (4.4) yields

$$\mathbf{e}_{\text{sc}}(\mathbf{x}_p) = -\int_{\partial\Omega_{\text{ext},1}\cap\partial\Omega} \mathbf{e}_{\text{sc},\gamma} \wedge \mu_\gamma^{-1} d\widetilde{\mathbf{g}}_{\mathbf{x}_p,\gamma} - \lim_{\rho\to\infty} \int_{\partial\Omega^{(\rho)}_{\text{ext},1}\cap\partial\Omega^{(\rho)}_{\text{ext},2}} \mathbf{e}_{\text{sc},\gamma} \wedge \mu_\gamma^{-1} d\widetilde{\mathbf{g}}_{\mathbf{x}_p,\gamma}.$$

To derive the Stratton–Chu diffraction integral we regard the non-PML case $\gamma = 0$ and use an orientation of the hyperplane $z = 0$ with upward normal. Using that $d\widetilde{\mathbf{g}}_{\mathbf{x}_p,\gamma} = 2\mathbf{g}_{\mathbf{x}_p,\gamma}$ on the hyperplane $z = 0$, we end up with the Stratton–Chu diffraction integral

$$\mathbf{e}_{\text{sc}}(\mathbf{x}_p) = 2\int_{z=0} \mathbf{e}_{\text{sc}} \wedge \mu^{-1} d\mathbf{g}_{\mathbf{x}_p}. \tag{4.5}$$

4.3 Rayleigh–Sommerfeld diffraction integral for Helmholtz equation

To gain deeper insight into the exterior domain evaluation formula (4.4) and to discuss the pitfalls related to the arising branch cuts of the Green's tensor,

we restrict ourselves to the scalar Helmholtz equation in two and three space dimensions,

$$-\Delta u_{\rm sc} - k_+^2 u_{\rm sc} = 0,$$

with $k_+ = \omega\sqrt{\varepsilon_+\mu_+}$ and μ_+, ϵ_+ the material parameters in the upper half space.

To derive the scalar analog of the Stratton–Chu diffraction integral (4.5), we may formally switch from the one form $\mathbf{e}_{\rm sc}$ to the zero form $u_{\rm sc}$. To do this, let G_{z_p} denote the shifted Green function to the Helmholtz equation above,

$$-\Delta G_{z_p}(\mathbf{x}, z) - k_+^2 G_{z_p}(\mathbf{x}, z) = \delta(\mathbf{0}, z - z_p),$$

given by

$$G_{z_p}(x, z) = \frac{i}{4} H_0^{(1)}(k_+|(x, z - z_p)|) \qquad \text{(2D)},$$

$$G_{z_p}(x, y, z) = \frac{e^{ik_+|(x,y,z-z_p)|}}{4\pi|(x, y, z - z_p)|} \qquad \text{(3D)},$$

with the zeroth Hankel function $H_0^{(1)}$ of first kind.

Eventually, one gets the first Rayleigh–Sommerfeld diffraction integral

$$u_{\rm sc}(\mathbf{x}_{\perp,p}, z_p) = -2 \int_{\mathbf{R}^{d-1}} u_{\rm sc}(\mathbf{x}'_\perp, 0) \partial_{z_p} G_{z_p}(\mathbf{x}_{\perp,p} - \mathbf{x}'_\perp, 0) \mathrm{d}\mathbf{x}'_\perp. \tag{4.6}$$

Chandler [22] called this representation formula *upward propagating radiation condition*.

In the following we use the notation $r_p(\mathbf{x}'_\perp) = k_+|(\mathbf{x}_{\perp,p} - \mathbf{x}'_\perp, z_p)|$. We first discuss the convergence of the above Rayleigh–Sommerfeld diffraction integral for the two dimensional case. With

$$\partial_{z_p} G_{z_p}(\mathbf{x}_{\perp,p} - \mathbf{x}'_\perp, 0) = -\frac{i z_p k_+}{4 r_p(\mathbf{x}'_\perp)} H_1^{(1)}(k_+ r_p(\mathbf{x}'_\perp))$$

and with the asymptotic behavior of the Hankel function $|H_1^{(1)}(r)| \sim r^{-1/2}$ for large values r, one proves that the Rayleigh–Sommerfeld diffraction integral (4.6) is absolutely convergent,

$$\int_{-\infty}^{\infty} |u_{\rm sc}(x', 0) \frac{i z_p}{4 r_p(x')} H_1^{(1)}(k_+ r_p(x'))| \mathrm{d}x' \le C_0 + C \cdot \int_1^{\infty} (r')^{-3/2} \mathrm{d}r' < \infty$$

for any bounded field $u_{\rm sc}(x', 0)$. The constants C_0 and C_1 depend on the evaluation point (x_p, z_p).

To evaluate the Rayleigh–Sommerfeld diffraction integral (4.6) in 3D we use polar coordinates (R, φ) in the hyper plane $z = 0$. With

$$\partial_{z_p} G_{z_p}(\mathbf{x}_{\perp,p} - \mathbf{x'}_{\perp}, 0) = \frac{1}{4\pi}\left(ik_+ - \frac{1}{r_p}\right)\frac{e^{ik_+ r_p}}{r_p}\frac{z_p}{r_p} \tag{4.7}$$

one gets

$$u_{\mathrm{sc}}(\mathbf{x}_{\perp,p}, z_p) = -\frac{1}{2\pi}\int_0^\infty \int_0^{2\pi} u_{\mathrm{sc}}(R, \varphi, 0)\left(ik_+ - \frac{1}{r_p}\right)\frac{e^{ik_+ r_p}}{r_p}\frac{z_p}{r_p} R\,\mathrm{d}\varphi\,\mathrm{d}R.$$

Since $r_p \sim R$ for large values R the integral above is absolutely convergent for $z_p > 0$ provided that $|u_{\mathrm{sc}}(R, \varphi, 0)| \leq CR^{-\epsilon}$ for large values R and $\epsilon > 0$:

$$\begin{aligned}\int_0^\infty \int_0^{2\pi} \left| u_{\mathrm{sc}}(R, \varphi, 0)\left(ik_+ - \frac{1}{r_p}\right)\frac{e^{ik_+ r_p}}{r_p}\frac{z_p}{r_p} R\right| \mathrm{d}\varphi \mathrm{d}R \\ \leq C_0 + C_1 \int_1^\infty R^{-1-\epsilon}\mathrm{d}R < \infty.\end{aligned}$$

4.4 Complex deformed Rayleigh–Sommerfeld diffraction integral

A direct numerical evaluation of the Rayleigh–Sommerfeld diffraction integral (4.6) is cumbersome due to the slow decay of the integration kernel $\partial_{z_p} G_{z_p}(\mathbf{x}_{\perp,p} - \mathbf{x}', 0) \sim (r_p)^{-(d+1)/2}$. To overcome this we will use a complex deformation of Rayleigh–Sommerfeld diffraction integral. The so complex deformed integral exhibits an exponentially fast convergence with the size of the integration domain. Furthermore the arising integrand is available from a near field simulation with perfectly matched layers (PML).

To keep the notation simple we only deal with the 2D case

$$u_{\mathrm{sc}}(x_p, z_p) \;=\; -2\int_{\mathbf{R}} u_{\mathrm{sc}}(x, 0)\frac{iz_p}{4r_p(x')}H_1^{(1)}(r_p(x'))\mathrm{d}x'. \tag{4.8}$$

As depicted in Figure 4.1 the intersection of the computational domain Ω and the hyperplane $z = 0$ is an interval $[-a_l, a_r]$. We split the 2D Rayleigh–Sommerfeld diffraction integral into three parts,

$$\begin{aligned}\int_{-\infty}^{\infty} u_{\mathrm{sc}}(x', 0)\frac{iz_p H_1^{(1)}(r_p(x'))}{4r_p(x')}\mathrm{d}x' = \int_{-\infty}^{-a_l} u_{\mathrm{sc}}(x', 0)\frac{iz_p}{4r_p(x')}H_1^{(1)}(r_p(x'))\mathrm{d}x' + \\ \int_{-a_l}^{a_r} u_{\mathrm{sc}}(x', 0)\frac{iz_p}{4r_p(x')}H_1^{(1)}(r_p(x'))\mathrm{d}x' + \\ \int_{a_r}^{\infty} u_{\mathrm{sc}}(x', 0)\frac{iz_p}{4r_p(x')}H_1^{(1)}(r_p(x'))\mathrm{d}x'.\end{aligned}$$

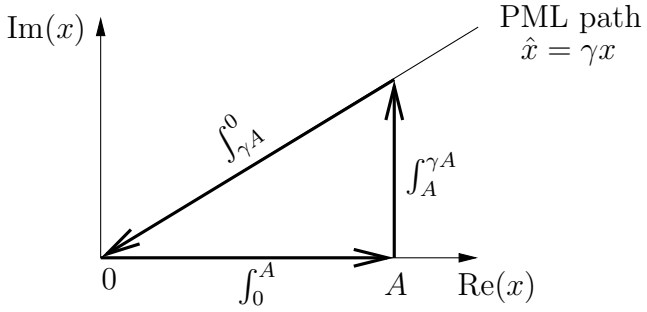

Figure 4.5: Integral deformation for the numerical evaluation of Rayleigh–Sommerfeld diffraction integral. The Rayleigh–Sommerfeld diffraction integral is originally defined on the real axis $x \in [0, \infty)$. The integrand, i.e. the scattered field, is numerically not available on that integration domain but on the PML path $\hat{x} = \gamma x$. Using Cauchy's contour integral theorem and showing that the integral from A to γA vanishes as $A \to \infty$ we replace the original Rayleigh–Sommerfeld integral by a complex deformed integral involving the PML solution.

The second term has a finite integration domain and is numerically evaluated by means of a standard quadrature rule. The first and third integral are oscillatory integrals defined on infinite integration domains. Since both integrals are of the same form we only consider the third integral.

Without loss of generality we set $a_r = 0$ and assume that the Dirichlet data $u_{\rm sc}(x', 0)$ possesses a complex extension $u_{\rm sc}(s, 0)$ with $\mathrm{Re}(s) > 0$ and $\mathrm{Im}(s) \geq 0$ which is bounded in $\mathbb{C}_{++} = \{s \in \mathbb{C} \ : \ \mathrm{Re}(s) > 0, \mathrm{Im}(s) \geq 0\}$. This assumption was also needed for the justification of the PML method in the previous chapter. Accordingly, a near field simulation as in Problem 3.1 delivers the PML solution $u_\gamma(\xi, 0)$ which is equal to the complex continuation of the original field, $u_\gamma(\xi) = u_{\rm sc}(\gamma\xi)$, up to the PML truncation error and the finite element discretization error. Therefore the complex deformed field $u_{\rm sc}(s, 0)$ is available for $s = \gamma\xi$ and with $\xi \geq 0$.

To evaluate the above third integral term we use Cauchy's contour integral theorem. We use the notation from Figure 4.5. We have,

$$\int_0^A u_{\rm sc}(x', 0) \frac{iz_p}{4r_p(x')} H_1^{(1)}(r_p'(s))\mathrm{d}x' = \int_0^{\gamma A} u_{\rm sc}(s, 0) \frac{iz_p}{4r_p(s)} H_1^{(1)}(r_p(s))\mathrm{d}s + \int_{\gamma A}^{A} u_{\rm sc}(s, 0) \frac{iz_p}{4r_p(s)} H_1^{(1)}(r_p(s))\mathrm{d}s, \tag{4.9}$$

with $r_p(s) = \sqrt{(x_p - s)^2 + z_p^2}$. Before we show that the integral in vertical direction,

$$I_v = \int_{\gamma A}^{A} u_{\mathrm{sc}}(s,0) \frac{i z_p}{4 r_p(s)} H_1^{(1)}(r_p(s)) \mathrm{d}s, \tag{4.10}$$

tends to zero as $A \to \infty$ we must assure that the function

$$r_p(s) = k_+ \sqrt{(x_p - s)^2 + z_p^2}$$

is holomorphic in $\mathbb{C}_\gamma = \{s \in \mathbb{C}_{++} \,|\, \mathrm{Im}(s)/\mathrm{Re}(s) \leq \mathrm{Im}(\gamma)/\mathrm{Re}(\gamma)\}$. The set $\mathbb{C}_\gamma$ is the simply connected domain enclosed by the real axis and the PML path. We introduce $f(s) = (x_p - s)^2 + z_p^2$ and apply a theorem from Rudin [95, Th. 13.11, p. 274] which states that $r_p(s)$ is properly defined if $1/f$ is holomorphic in $\mathbb{C}_\gamma$. Hence it is sufficient to demand that $f(s) \neq 0$ in $\mathbb{C}_\gamma$. The roots of f are given by $s_\pm = x_p \pm i z_p$. $s_- \notin \mathbb{C}_\gamma$ and $s_+ \notin \mathbb{C}_\gamma$ requires that

$$\frac{x_p}{z_p} \leq \frac{\mathrm{Re}(\gamma)}{\mathrm{Im}(\gamma)}.$$

This formula has an important impact on the numerics since it restricts the position of an evaluation point (x_p, z_p) to a certain domain which depends on the used numerical parameter γ of the PML path in the near field simulation. To understand that in greater detail we re-introduce the right computational domain's boundary coordinate a_r which we previously set equal to zero for conveniences. Together with an analogous consideration for the left infinite integration domain $(-\infty, a_l]$ we derive

$$\begin{aligned} \frac{x_p - a_r}{z_p} &\leq \frac{\mathrm{Re}(\gamma)}{\mathrm{Im}(\gamma)}, \\ \frac{a_l - x_p}{z_p} &\leq \frac{\mathrm{Re}(\gamma)}{\mathrm{Im}(\gamma)}. \end{aligned}$$

This condition restricts the angles $\vartheta_r = \mathrm{atan2}(x_p - a_r, z_p)$, $\vartheta_l = \mathrm{atan2}(a_r - x_p, z_p)$ under which an evaluation point is "seen" from the points $(a_r, 0)$ and $(a_l, 0)$, respectively. As usual in optics we express this condition in terms of the numerical aperture $\sin(\vartheta_{l/r})$:

$$\sin(\vartheta_{l/r}) \leq \sin(\vartheta_\gamma), \tag{4.11}$$

with $\vartheta_\gamma = \mathrm{atan2}(\mathrm{Re}(\gamma), \mathrm{Im}(\gamma))$. We have summarized the discussion in Figure 4.6 where we painted "forbidden" evaluation regions in gray.

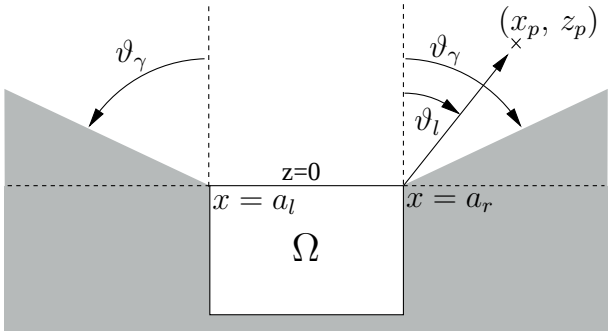

Figure 4.6: Region of allowed positions (x_p, z_p) for exterior domain field evaluation with the deformed Rayleigh–Sommerfeld diffraction integral. "Forbidden" regions are painted in gray. For $z_p \leq 0$ field values are available only within the computational domain. For $z_p > 0$ an evaluation by means of the deformed Rayleigh–Sommerfeld integral is restricted to points (x_p, z_p) that satisfy $\sin(\vartheta_{l/r}) \leq \sin(\vartheta_\gamma)$, with $\vartheta_\gamma = \text{atan2}(\text{Re}(\gamma), \text{Im}(\gamma))$. γ is the PML stretching parameter used in the near field simulation. The numerical efficiency for the evaluation of the deformed Rayleigh–Sommerfeld integral degrades as the evaluation points approaches the forbidden region.

We now resume our discussion on the deformed Rayleigh–Sommerfeld integral (4.9) and show that the vertical integral I_v defined in equation (4.10) vanishes for $A \to \infty$. We have

$$\begin{aligned} |I_v| &= |\int_{\gamma A}^{A} u_{\text{sc}}(s,0) \frac{iz_p}{4r_p(s)} H_1^{(1)}(r_p(s))\mathrm{d}s| \\ &\leq CA \max_{s\in[A,\gamma A]} \frac{1}{|r_p(s)|} \cdot \max_{s\in[A,\gamma A]} |H_1^{(1)}(r(s))|, \end{aligned}$$

where $[A, \gamma A]$ defines the line in the complex plane from A to γA. Since $r_p(s) \sim s$ for $|s| \to \infty$ we conclude $A/|r_p(s)| \leq C$ for $s \in [A, \gamma A]$ and A large enough. Together with the asymptotic behavior of the Hankel functions $|H_1^{(1)}(s)| \sim 1/\sqrt{|s|}$ (Abramowitz and Stegun [1, p. 108]) in the first quadrant of the complex plane this proves that I_v tends to zero in the limit $A \to \infty$.

We now want to rewrite the deformed Rayleigh–Sommerfeld integral (4.9) so that the relation to the PML solution is more apparent. A near field computation yields the PML solution data $u_{r,\gamma}(\xi)$ on the half infinite line $[a_r, \infty)$ and the PML field $u_{l,\gamma}(\xi)$ on $(-\infty, a_l]$. Inserting the complex deformed integral (4.9) into the original exterior domain evaluation formula (4.8) gives

the final formula

$$\begin{aligned} u_{\mathrm{sc}}(x_p, z_p) = &- 2\gamma \int_0^{\infty} u_{l,\gamma}(\xi, 0) \frac{i z_p}{4 r_{l,p}(\xi)} H_1^{(1)}(r_{l,p}(\xi)) \mathrm{d}\xi \\ &- 2 \int_{-a_l}^{a_r} u_{\mathrm{sc}}(x', 0) \frac{i z_p}{4 r_p(x')} H_1^{(1)}(r_p(x')) \mathrm{d}x' \\ &- 2\gamma \int_0^{\infty} u_{r,\gamma}(\xi, 0) \frac{i z_p}{4 r_{r,p}(\xi)} H_1^{(1)}(r_{r,p}(\xi)) \mathrm{d}\xi, \end{aligned} \tag{4.12}$$

with $r_{l/r,p}(\xi) = \sqrt{(x_p - a_{l/r} \mp \gamma\xi)^2 + z_p^2}$.

It remains to discuss whether the involved infinite integrals admit an efficient numerical evaluation. We know from the previous discussion that the above formula losses its validity as the evaluation point (x_p, z_p) approaches the forbidden region as sketched in Figure 4.6. Therefore we suspect a degradation of the numerical efficiency near the forbidden region. This is indeed the case. But before we explain this, we show that the integrands of the infinite integrals in the evaluation formula (4.12) exponentially decay.

Again, we only consider the third integral in equation (4.12). We set $a_r = 0$ and drop the subscript 'r' in the following. For large values of ξ we have $r_p(\xi) \sim \gamma\xi$ and with the asymptotic form of Hankel's function (see Abramowitz and Stegun [1, p.108]),

$$H_1^{(1)}(s) \quad \sim \quad \sqrt{\frac{2}{\pi s}} e^{i(s - \frac{3}{4}\pi)}, \tag{4.13}$$

we conclude that the integrand on the right hand side of the equation above decreases asymptotically with an exponential rate,

$$|u_{r,\gamma}(\xi, 0) \frac{i z_p}{4 r_p(\xi)} H_1^{(1)}(r_p(\xi))| \leq C e^{-\kappa \mathrm{Im}(\gamma)\xi} e^{-k_+ \mathrm{Im}(\gamma)\xi}. \tag{4.14}$$

The first exponential factor stems from the PML solution with exponential decay rate $\kappa\,\mathrm{Im}(\gamma)$. The precise value of κ depends on the actual problem. The second exponential term reflects the asymptotic behavior of Hankel's functions.

At a first glance this is a promising estimate which justifies a truncation of the infinite integrals in a numerical approximation of the complex deformed Rayleigh–Sommerfeld diffraction formula (4.12). However, the estimate (4.14) is only an asymptotic result for large values $|\xi|$. For an efficient numerical evaluation of the involved integrals, the behavior of the term $H_1^{(1)}(r_p(\xi))$ for small values of ξ matters since the truncated integration interval's length should be of the same order as the computational domain diameter. We therefore want to sharpen up the above estimate.

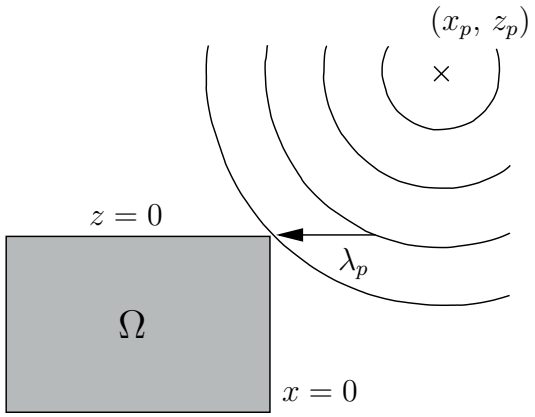

Figure 4.7: Behavior of a diverging spherical wave on the integration domain of the diffraction integral. We integrate on the real axis $x > 0$. One factor in the Rayleigh–Sommerfeld diffraction integral is proportional to the field values of a diverging spherical wave emanated from the evaluation point (x_p, z_p). Under a complex deformation we expect an exponential growth rate proportional to the directed "effective" wavelength λ_p. For $x > x_p$ we observe an exponential decay.

We assume that the evaluation point (x_p, z_p) is placed sufficiently far away from the hyperplane $z = 0$ so that we are allowed to replace $H_1^{(1)}(r_p(\xi))$ with $Ce^{ir_p(\xi)}$ for a qualitative discussion. The integrand estimate in equation (4.14) now reads as

$$|u_{r,\gamma}(\xi, 0)\frac{iz_p}{4r_p(\xi)}H_1^{(1)}(r_p(\xi))| \leq Ce^{-\kappa \mathrm{Im}(\gamma)\xi}e^{-\mathrm{Im}(r_p(\xi))}. \tag{4.15}$$

Before we start with the elementary but tedious analysis of the exponent $-\mathrm{Im}(r_p(\xi))$ we want to develop some intuitive insight into the behavior of the two involved exponential terms.

The second exponential term stems from a point source placed at (x_p, z_p). As sketched in Figure 4.7 the phase fronts of this field hit the integration domain $x > 0$ under an angle depending on the position of the evaluation point. For $x > 0$ we define the "effective" wavelength $\lambda_p = 2\pi z_p/k_+(x - x_p)$ as in Figure 4.7. λ_p is negative for $x < x_p$ and switches its sign at $x = x_p$. The restriction of the spherical wave emanated from (x_p, z_p) essentially behave like $H_1^{(1)}(r_p(x)) \sim \exp(ik_p(x)x)$, with $k_p = 2\pi/\lambda_p(x)$. Under a complex deformation $x \to \gamma\xi$ of the integrand this term has a local growth rate roughly given by $k_p(\xi)\mathrm{Im}(\gamma)$. For $\mathrm{Re}(\xi) \leq x_p$ we expect an exponential growth which switches to an exponential decay for $\mathrm{Re}(\xi) > x_p$.

As already mentioned above the first exponential term in the estimate (4.15) corresponds to the decay of the PML solution. The overall integrand decreases exponentially when the decay of the PML solution overcompensate the possible growth of the second exponential term. In many application we observe that $\kappa \geq k_+$ but the actual decay rate of the PML solution has to be monitored in a numerical implementation.

For the precise analysis of the exponent $-\mathrm{Im}(r_p(\xi))$ we recall the definition of $r_p(\xi)$,

$$r_p(\xi) = k_+\sqrt{(x_p - \gamma\xi)^2 + z_p^2}.$$

For $\xi > x_p/\mathrm{Re}(\gamma)$ we have $\mathrm{Im}((x_p - \gamma\xi)^2 + z_p^2) > 0$ and hence the second exponential term in the above estimate (4.15) is bounded by one. We now aim at finding a constant κ_γ with $-\mathrm{Im}(r_p(\xi)) \leq \kappa_\gamma\xi$ for $\xi \leq x_p/\mathrm{Re}(\gamma)$. In other words we want to bound the slope $|-d/d_\xi \mathrm{Im}(r_p(\xi))| \leq \kappa_\gamma$. To do so we differentiate $-\mathrm{Im}\,(r_p(\xi))$ with respect to ξ,

$$\begin{aligned} -\frac{d}{d\xi}\mathrm{Im}\,(r_p(\xi)) &= -\mathrm{Im}\left(\frac{-k_+^2\gamma(x_p - \gamma\xi)}{r_p(\xi)}\right) \\ &= \mathrm{Im}\left(\frac{k_+^2\gamma(x_p - \gamma\xi)}{r_p(\xi)}\right). \end{aligned}$$

At $\xi = 0$ we have

$$-\frac{d}{d\xi}\mathrm{Im}\,(r_p(\xi)) = \mathrm{Im}(\gamma)k_+\frac{x_p}{\sqrt{x_p^2 + z_p^2}}.$$

We will verify that $-\mathrm{Im}(r_p(\xi))$ has its maximum slope at $\xi = 0$ in the considered interval $[0, x_p/\mathrm{Re}(\gamma)]$. So, we infer from equation (4.15) that

$$|u_{r,\gamma}(\xi, 0)\frac{iz_p}{4r_p(\xi)}H_1^{(1)}(r_p(\xi))| \leq Ce^{-(\kappa-\kappa_p)\mathrm{Im}(\gamma)\xi}, \tag{4.16}$$

with $\kappa_p = k_+x_p/\sqrt{x_p^2 + z_p^2}$. This is the estimate we needed. Provided that $\kappa \geq \kappa_p$ the overall integrand is exponentially damped since the exponential decay rate of the PML solution overcompensate the exponential growth rate of Hankel's function with complex arguments. The decay rate $(\kappa - \kappa_p)\,\mathrm{Im}(\gamma)$ depends on the evaluation point. The larger the angle $\sin(\vartheta_r) = x_p/\sqrt{x_p^2 + z_p^2}$ the larger κ_p. Hence the decay rate of the integrand gets worse with the angle ϑ_r of the evaluation point. We will come back to this point when we detail the numerical implementation of the exterior domain evaluation.

We have postponed to verify that the slope of $-\mathrm{Im}(r_p(\xi))$ has its maximum at $\xi = 0$ in the interval $[0, x_p/\mathrm{Re}(\gamma)]$. It is sufficient to show that the second derivative of $-\mathrm{Im}(r_p(\xi))$ with respect to ξ is non-positive in the interval $[0, x_p/\mathrm{Re}(\gamma)]$. Without restriction of generality we set $k_+ = 1$. We compute

$$\begin{aligned} -\frac{d^2}{d^2\xi}\mathrm{Im}\left(r_p(\xi)\right) = & \ \mathrm{Im}\left(\frac{-\gamma^2}{r_p(\xi)} + \frac{\gamma^2(x_p - \gamma\xi)^2}{r_p^3(\xi)}\right) \\ = & \ \mathrm{Im}\left(\frac{-\gamma^2}{r_p(\xi)} + \frac{\gamma^2(r_p^2 - z_p^2)}{r_p^3(\xi)}\right) \\ = & -z_p^2 \ \mathrm{Im}\left(\frac{\gamma^2}{r_p^3(\xi)}\right). \end{aligned}$$

To show that $\mathrm{Im}(\gamma^2/r_p^3(\xi)) > 0$ one easily checks that this condition only depends on the direction of the evaluation point (x_p, z_p) and the PML path direction $(\mathrm{Re}(\gamma), \mathrm{Im}(\gamma)$. We are therefore allowed to set $\gamma = 1 + i\sigma$ and $x_p = 1$ without restriction of generality. The numerical aperture condition (4.4) now states that $\sigma \leq z_p$ and we must show

$$\mathrm{Im}\left(\frac{(1+i\sigma)^2}{\left((1-(1+i\sigma)\xi)^2 + z_p^2\right)^{3/2}}\right) \geq 0 \tag{4.17}$$

for $\xi \in [0, 1]$. We introduce $f(\xi) = (1-(1+i\sigma)\xi)^2 + z_p^2$ and write

$$\begin{aligned} 1 + i\sigma = & A_\sigma e^{i\vartheta_\sigma} \\ f(\xi) = & A_\xi e^{i\vartheta_\xi} \end{aligned}$$

with positive numbers A_σ, A_ξ. Condition (4.17) now reads as

$$0 \leq 2\vartheta_\sigma - 3/2\vartheta_\xi \leq \pi.$$

From now we assume that $\sigma > 0$ is chosen small enough so that $\vartheta_\sigma \leq \pi/8$. We introduce $f_i(\xi) = \mathrm{Im}(f(\xi)) = 2\sigma(\xi^2 - \xi)$ and $f_r(\xi) = \mathrm{Re}(f(\xi)) = (1 - \sigma^2)\xi^2 - 2\xi + z_p^2 + 1$. We have that $f_i(\xi) \leq 0$ and $f_r(\xi) \geq 0$ for $\xi \in [0, 1]$ using that $\sigma \leq \max(1, z_p)$. This gives $-\pi/2 \leq \vartheta_\xi \leq 0$ and proves condition (4.17).

4.5 Complex deformed evaluation integrals in 3D

In this section we generalize the results obtained for the complex deformed 1D Rayleigh–Sommerfeld diffraction integral in 2D to scattering problems

in three space dimensions. As we will see soon the estimates we tediously gained in the previous section are directly valid in 3D.

Let us first consider an arrangement as given in Figure 4.8. The hyperplane $z = 0$ is equipped with an "angle-radius"–like coordinate system (η, ξ). We find a globally defined, smooth "radial"–like distance coordinate ξ and a quadrilateral–wise defined "angle"–like coordinate η. We use this (η, ξ)–coordinate system to map each quadrilateral $Q_j \times \{0\}$ onto the reference infinite quadrilateral $[0, 1] \times [0, \infty)$. We denote this bilinear transformation by $\mathrm{T}_j : [0, \infty) \to Q_j$. The Rayleigh–Sommerfeld diffraction integral (4.6) is transformed accordingly quadrilateral–wise. On each quadrilateral we gain an integral

$$I_j = -2 \int_0^1 \int_0^\infty u_{\mathrm{sc}}(\mathrm{T}_j(\eta, \xi), 0) \left[\partial_{z_p} G_{z_p}\right] (\mathbf{x}_{\perp,p} - \mathrm{T}_j(\eta, \xi), 0) |\mathrm{T}_j| \mathrm{d}\xi \mathrm{d}\eta.$$

The outer integral is numerically tackled by standard quadrature rules. The inner integral has a similar structure as in the two dimensional case and we are allowed to use a complex coordinate stretching in the ξ–direction. This way the original scattered field $u_{\mathrm{sc}}(\mathrm{T}_j(\eta, \xi), 0)$ is replaced by its PML counterpart $u_\gamma(\eta, \xi)$ and the Green's function is evaluated with complex arguments. To show the exponential decay of the integrand one needs to balance out the behavior of the two factors $u_\gamma(\eta, \xi)$ and $[\partial_{z_p} G_{z_p}](\mathbf{x}_{\perp,p} - \mathrm{T}_j(\eta, \gamma\xi), 0)$ as in the two dimensional case. We do not detail this here and refer to Figure 4.7 for an intuitive understanding of the expected exponential decay rate.

As a generalization to the "radial–distance"–like (η, ξ)–coordinate system one encounters situation where the hyperplane is equipped with a tensor product like coordinate system as shown in Figure 4.9. Now, we find quadrilaterals $Q_{2,j} \times \{0\}$ with two distance–like coordinates ξ_1 and ξ_2 which gives rise to a bilinear mapping $T_{2,j} : [0, \infty) \times [0, \infty) \to Q_{2,j} \times \{0\}$ from the doubly infinite reference quadrilateral onto the considered quadrilateral. The transformed integral contribution of a doubly infinite quadrilateral to the Rayleigh–Sommerfeld integral has the form

$$I_{2,j} = -2 \int_0^\infty \int_0^\infty u_{\mathrm{sc}}(\mathrm{T}_j(\xi_1, \xi_2), 0) \left[\partial_{z_p} G_{z_p}\right] (\mathbf{x}_{\perp,p} - \mathrm{T}_j(\xi_1, \xi_2), 0) |\mathrm{T}_j| \mathrm{d}\xi_1 \mathrm{d}\xi_2.$$

To evaluate this integral we use a complex deformation in both variables ξ_1 and ξ_2 in a now obvious manner.

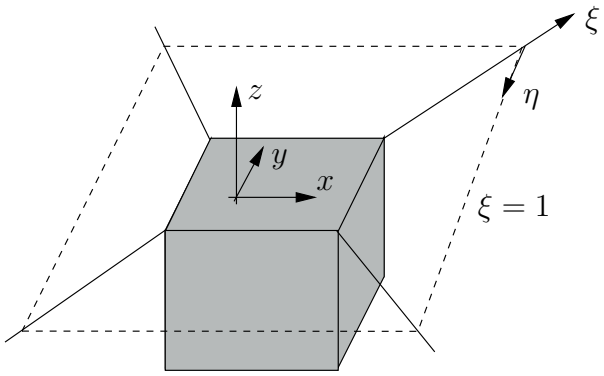

Figure 4.8: 3D geometry configuration for field evaluation in the exterior domain. The computational domain painted in gray is placed beyond the hyperplane $z = 0$. An evaluation point $(\mathbf{x}_{\perp,p}, z_p)$ needs to lie above this hyperplane. We equip the hyperplane $z = 0$ with an "angle-radius"–like coordinate system (η, ξ). The dashed line indicates the $\xi = 1$ isoline. To evaluate the Rayleigh–Sommerfeld diffraction integral numerically we use a complex deformation in the ξ–direction.

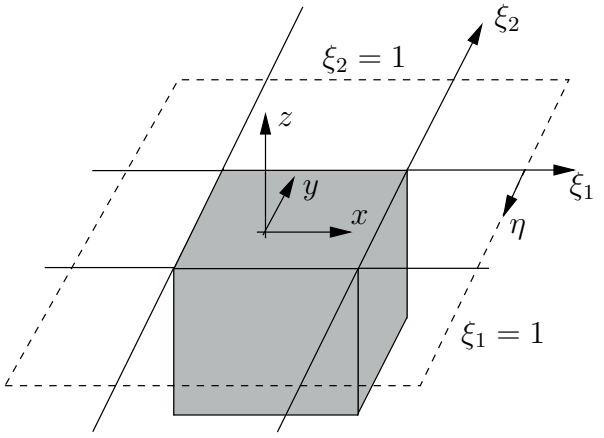

Figure 4.9: 3D geometry configuration for field evaluation in the exterior domain with tensor product coordinate system in the hyperplane $z = 0$. In contrast to the situation in Figure 4.8 the hyperplane $z = 0$ is not equipped with a globally defined distance–like coordinate ξ. As a generalization an quadrilateral may possesses two distance–like coordinates ξ_1 and ξ_2. To evaluate the Rayleigh–Sommerfeld integral it is necessary to use a complex deformation in both infinite coordinate directions ξ_1 and ξ_2.

4.6 Far field pattern and the Fourier transform

There exists a well-known relationship between the far field behavior of the scattered field $\mathbf{e}_{\rm sc}(\mathbf{x}_\perp, z)$ and the Fourier transform with respect to $\mathbf{x}_\perp$. Given a far distance evaluation point $(\mathbf{x}_{\perp,p}, z_p) = R \cdot (\mathbf{n}_\perp, n_z)$ with normal vector $(\mathbf{n}_\perp, n_z)$ and $R \gg 1$ the Green's function in the Rayleigh–Sommerfeld diffraction integral (4.6) only appears with large arguments. Hence in the limit $R \to \infty$ it is possible to replace the Green's function by its asymptotic expansion.

For the two dimensional case we use the asymptotic form of Hankel's function (see Abramowitz and Stegun [1, p.108]),

$$\begin{aligned}
\partial_{z_p} G_{z_p}(\mathbf{x}_\perp - \mathbf{x'}_\perp, 0) &= -\frac{i z_p k_+}{4 r_p(x')} H_1^{(1)}(k_+ r_p(x')) \\
&\sim -\frac{i z_p k_+}{4 r_p(x')} \sqrt{\frac{2}{\pi (k_+ r_p(x'))}} e^{-i3\pi/4} e^{i k_+ r_p(x')} \\
&\sim -\frac{z_p k_+}{r_p(x')^{3/2}} \sqrt{\frac{1}{8\pi k_+}} e^{-i\pi/4} e^{i k_+ r_p(x')}.
\end{aligned}$$

Since $r_p(x') \sim R$ we can replace $r_p(x')$ with R in the denominator. With $\cos\vartheta = z_p/R$ we get

$$\partial_{z_p} G_{z_p}(\mathbf{x}_\perp - \mathbf{x'}_\perp, 0) \sim -k_+ \sqrt{\frac{1}{8\pi k_+ R}} e^{-i\pi/4} e^{i k_+ r_p(x')} \cos\vartheta = C_2 \cdot e^{i k_+ r_p(x')} \cos\vartheta.$$

The three dimensional case yields a similar expression. For large values of R we drop the $1/r_p^3(\mathbf{x}'_\perp)$ term in the formula (4.7) for $\partial_{z_p} G_{z_p}(\mathbf{x}_\perp - \mathbf{x'}_\perp, 0)$. After performing operations similar to the two dimensional case we get

$$\begin{aligned}
\partial_{z_p} G_{z_p}(\mathbf{x}_\perp - \mathbf{x'}_\perp, 0) &= \frac{1}{4\pi} \left(i k_+ - 1/r_p(\mathbf{x}'_\perp)\right) \frac{e^{i k_+ r_p(\mathbf{x}'_\perp)}}{r_p(\mathbf{x}'_\perp)} \frac{z_p}{r_p(\mathbf{x}'_\perp)} \\
&\sim \frac{i k_+}{4\pi R} e^{i k_+ r_p(\mathbf{x}'_\perp)} \cos\vartheta = C_3 \cdot e^{i k_+ r_p(\mathbf{x}'_\perp)} \cos\vartheta.
\end{aligned}$$

A further asymptotic expansion concerns the calculation of $r_p(\mathbf{x}'_\perp)$,

$$\begin{aligned}
r_p(\mathbf{x}'_\perp) &= \sqrt{|R\mathbf{n}_\perp - \mathbf{x'}_\perp|^2 + (R n_z)^2} = R\sqrt{|\mathbf{n}_\perp - \mathbf{x'}_\perp/R|^2 + n_z^2} \\
&= R\sqrt{1 - 2\mathbf{n}_\perp \cdot \mathbf{x'}_\perp/R + |x'|^2/R^2} \sim R(1 - \mathbf{n}_\perp \cdot \mathbf{x'}_\perp/R).
\end{aligned}$$

Now Rayleigh–Sommerfeld diffraction integral (4.6) has the following asymptotic expansion for large values of R,

$$\begin{aligned} u_{\mathrm{sc}}(\mathbf{x}_{\perp,p}, z_p) &= -2\int_{\mathbf{R}^{d-1}} u_{\mathrm{sc}}(\mathbf{x}'_\perp, 0)\partial_{z_p} G_{z_p}(\mathbf{x}_\perp - \mathbf{x}'_\perp, 0)\mathrm{d}\mathbf{x}'_\perp \\ &\overset{!}{\sim} -2C_d \int_{\mathbf{R}^{d-1}} u_{\mathrm{sc}}(\mathbf{x}'_\perp, 0)\cdot e^{ik_+ r_p(\mathbf{x}'_\perp)}\cos\vartheta \mathrm{d}\mathbf{x}'_\perp \\ &\sim -2C_d \int_{\mathbf{R}^{d-1}} u_{\mathrm{sc}}(\mathbf{x}'_\perp, 0)\cdot e^{ik_+ R(1-\mathbf{n}_\perp\cdot\mathbf{x}'_\perp/R)}\cos\vartheta \mathrm{d}\mathbf{x}'_\perp \\ &\sim -2C_d e^{ik_+R}\cos(\vartheta)\int_{\mathbf{R}^{d-1}} u_{\mathrm{sc}}(\mathbf{x}'_\perp, 0)\cdot e^{-i\mathbf{k}_\perp\cdot\mathbf{x}'_\perp}\mathrm{d}\mathbf{x}'_\perp, \end{aligned} \tag{4.18}$$

where we defined $\mathbf{k}_\perp = k_+\mathbf{n}_\perp$. We will comment on the step from the first line to the second line later. The integral on the right hand side in the last line above has the form of a Fourier integral. Defining $k_z = k_+ n_z = \sqrt{k_+^2 - \mathbf{k}_\perp\cdot\mathbf{k}_\perp}$ and using $\cos(\theta) = k_z/k_+$ we are led to the formula

$$\hat{u}(\mathbf{k}_\perp, 0) \sim \frac{-k_+}{2(2\pi)^{(d-1)}k_z C_d} e^{-ik_+R}\cdot u_{\mathrm{sc}}\left(\frac{R}{k_+}(\mathbf{k}_\perp, k_z)\right),\ R\to\infty. \tag{4.19}$$

The step marked with "$\overset{!}{\sim}$" in the above derivation (4.18) requires a careful justification. In this step we make the transition from the absolutely convergent Rayleigh–Sommerfeld diffraction integral to the improper Fourier integral. We will not give the details here. Instead we derive a formula which allows for a direct evaluation of the Fourier transform. We only consider the scalar 2D case. For $\epsilon > 0$ we define

$$u_\epsilon(x) = \begin{cases} u_{\mathrm{sc}}(x,0)e^{-\epsilon(a_r - x)}, & x\in(\infty, a_r] \\ u_{\mathrm{sc}}(x,0), & x\in[a_l, a_r] \\ u_{\mathrm{sc}}(x,0)e^{-\epsilon(x-a_l)}, & x\in[a_l,\infty) \end{cases},$$

where $[a_l, a_r]$ is the top face of the computational domain as defined in Section 4.4. $u_\epsilon(x)$ is a $L^1(\mathbf{R})$–function. Its Fourier transform is given as

$$\begin{aligned} 2\pi\hat{u}_\epsilon(k_x) = \int_{\mathbf{R}} u_\epsilon(x')e^{-ik_x x'}\mathrm{d}x' = &\int_{-\infty}^{a_l} u_\epsilon(x')e^{-ik_x x'}\mathrm{d}x' + \\ &\int_{a_l}^{a_r} u_\epsilon(x')e^{-ik_x x'}\mathrm{d}x' + \\ &\int_{a_r}^{\infty} u_\epsilon(x')e^{-ik_x x'}\mathrm{d}x'. \end{aligned}$$

In the following we only discuss the third infinite integral and assume $a_r = 0$. We use a complex deformation of the integral. For $\gamma = 1 + i\sigma$ with $\sigma > 0$ one proves that

$$\begin{aligned}\int_0^\infty u_\epsilon(\xi)e^{-ik_x\xi}\mathrm{d}\xi &= \int_0^{\gamma\infty} u_\epsilon(s)e^{-ik_x s}\mathrm{d}s \\ &= \frac{1}{\gamma}\int_0^\infty u_\epsilon(\gamma\xi)e^{-ik_x\gamma\xi}\mathrm{d}\xi \\ &= \frac{1}{\gamma}\int_0^\infty u_\gamma(\xi)e^{-\epsilon\gamma\xi}e^{-ik_x\gamma\xi}\mathrm{d}\xi.\end{aligned} \tag{4.20}$$

In the last line the PML solution u_γ has entered the stage. The rest of the discussion is similar to the consideration on the convergence of the complex deformed Rayleigh–Sommerfeld integral. We assume that the PML–solution $u_\gamma(\xi)$ exhibits a decay $|u_\gamma(\xi)| \sim e^{-\kappa\sigma}$. We want that this decay overcompensates the growth of the exponential function $e^{\sigma k_x}$ stemming form the Fourier transform. This gives the restriction

$$k_x < \kappa. \tag{4.21}$$

In this case the last integral in (4.20) is absolutely convergent also for $\epsilon = 0$. Using the same assumption for the left infinite integral

$$\int_{-\infty}^{a_l} u_\epsilon(x')e^{-ik_x x'}\mathrm{d}x'$$

we conclude that the Fourier transform $\hat{u}_{\mathrm{sc}}(k_x)$ is a continuous function in $k_x \in (-\kappa, \kappa)$ and can be computed by the above deformed Fourier integrals.

Remark 4.1 In a real world application the scattered field is not directly projected on a screen. Rather, the light enters a detector which forms an image on a photosensitive device.

In the Abbe theory the optical imaging is described by a *coherent transfer function* $h(\mathbf{k}_\perp)$, see Singer [102, Chapt. 21]. The image field $u_{\mathrm{I}}(x)$ is formed by inverse Fourier transforming the product of $\hat{u}(\mathbf{k}_\perp, 0)$ and the transfer function,

$$u_{\mathrm{I}}(x) = (\hat{u}(\mathbf{k}_\perp, 0) \cdot h(\mathbf{k}_\perp))^\vee(x).$$

The transfer function $h(\mathbf{k}_\perp)$ accounts for wavefront aberrations, amplitude attenuations and has a bounded support in $\|\mathbf{k}_\perp\| \leq \mathrm{NA} \cdot k_+$, with a numerical aperture $\mathrm{NA} < 1$. Hence, for optical imaging purposes we only require the

Fourier transform $\hat{u}(\mathbf{k}_\perp, 0)$ in the band $\|\mathbf{k}_\perp\| \leq \mathrm{NA} \cdot k_+$ Fortunately, we typically have that $\kappa > \mathrm{NA} \cdot k_+$, where κ is the minimum PML damping factor, cf. inequality (4.21).

The most simple optical imaging system is given by the band pass filter

$$h(\mathbf{k}_\perp) = \chi_{\|\mathbf{k}_\perp\| \leq \mathrm{NA} \cdot k_+},$$

where ξ is the characteristic function.

4.7 Numerical implementation and examples

The exterior domain evaluation by means of the Rayleigh–Sommerfeld diffraction integral relies on the field data in the PML. These data need to be available with a sufficient accuracy to guarantee a precise evaluation of the complex deformed Rayleigh–Sommerfeld integral. This is contradictory to the concept of the adaptive PML (Chapter 3) where we only took care for the accuracy in the interior domain. It is possible to steer the adaptive PML method so that the accuracy of the PML data is improved. But this is paid with higher costs for the near field computation.

As an alternative, we compute the field data as needed for the complex deformed Rayleigh–Sommerfeld diffraction integral in a subsequent simulation step. We explain this concept for a scalar field $u(x, z)$ and refer to Figure 4.10: A near field simulation provides the Dirichlet data $u_{\tilde{\gamma}}|_\Gamma(0, z)$ of the scattered field on the vertical interface Γ. $\tilde{\gamma}$ is the PML path parameter used in the near field simulation. The field $u_{\tilde{\gamma}}|_\Gamma$ corresponds to a wave which propagates in $+x$–direction. We choose a $\gamma = 1 + i\sigma$ which satisfies the numerical aperture condition (4.4) for the given evaluation points. Selecting a $\delta > 0$ we apply the PML method to compute the following field:

$$u_{\gamma,\tilde{\gamma}}(\xi, z) = \begin{cases} u_{\mathrm{sc}}(\gamma\xi, z)), & \xi < \delta, z \in [-a, 0] \\ u_{\mathrm{sc}}(\gamma\xi, \tilde{\gamma}(z + a)), & \xi \leq \delta, z < -a \\ u_{\mathrm{sc}}(\gamma\xi, \tilde{\gamma}z), & \xi \leq \delta, z > 0 \\ u_{\mathrm{sc}}(\gamma\delta + \tilde{\gamma}(\xi - \delta), z), & \xi > \delta, z \in [-a, 0] \\ u_{\mathrm{sc}}(\gamma\delta + \tilde{\gamma}(\xi - \delta), \tilde{\gamma}(z + a)), & \xi > \delta, z < -a \\ u_{\mathrm{sc}}(\gamma\delta + \tilde{\gamma}(\xi - \delta), \tilde{\gamma}z), & \xi > \delta, z > 0 \end{cases}$$

We have that $u_\gamma(\xi, 0) = u_{\gamma,\tilde{\gamma}}(\xi, 0)$ for $\xi \in [0, \delta]$. This way, the field data $u_\gamma(\xi, 0)$ as needed in the complex deformed Rayleigh–Sommerfeld integral are available in the interval $[0, \delta]$. Extracting the Dirichlet data $u_{\gamma,\tilde{\gamma}}|_{\Gamma_\delta}(\delta, z)$ we repeat this step and gain $u_\gamma(\xi, 0)$ on the interval $(\delta, 2\delta)$ and so on. This

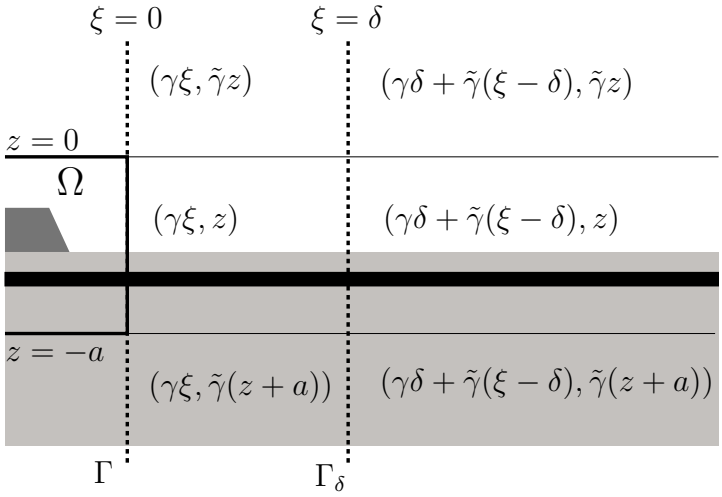

Figure 4.10: Extension of scattered field into the right exterior domain. The near field simulation provides the Dirichlet data of the PML solution $u_{\tilde{\gamma}}$ on the line Γ with $\xi = 0$. We use this data to compute the complex continuation $u_{\gamma,\tilde{\gamma}}$ of the scattered field u_{sc} in the right exterior domain with complex coordinates as given above.

way we are able to evaluate the complex deformed Rayleigh–Sommerfeld integral on the truncated integration interval $[0, j\delta]$.

For the numerical computation of $u_{\gamma,\tilde{\gamma}}$ we choose a discretization of the interval $[0, \delta]$ so that $u_\gamma(\xi, 0)$ allows for an accurate evaluation of the complex deformed Rayleigh–Sommerfeld integral. The PML discretization in $\xi > \delta$ is inherited from the near field simulation. This guarantees that the PML truncation error is of the order of the near field accuracy. The computational costs for computing $u_{\gamma,\tilde{\gamma}}(\xi, 0)$ in the interval $[0, \delta]$ decrease the smaller $\delta > 0$ is chosen.

4.7.1 Waveguide notch

With this test example we want to verify the accuracy of the exterior domain evaluation formula. The geometry and the material parameters to the scattering problem are given in Figure 4.11 The incoming field u_{inc} is the y–polarized fundamental mode of the waveguide which is used as the reference field within the entire exterior domain.

We used a cross–section computational domain $\Omega = [-1, 1] \times \{0\} \times [-2.6, 0]$. For test purposes we used evaluation points (x_p, z_p) in the exterior domain with $z_p = 2$ and $x \in [-11, 11]$. The angles $\theta_{l/r}$ as given in Figure 4.11

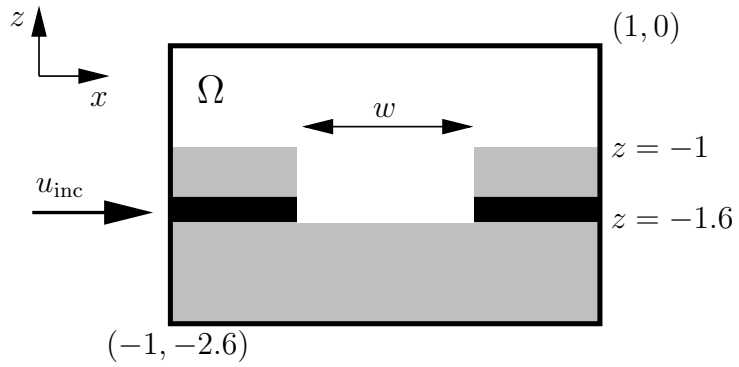

Figure 4.11: Waveguide notch: The upper half space consists of air. The lower half space is glass with permittivity $\epsilon_{\mathrm{g}} = 10.05$. A waveguide (black layer) with thickness $d_{\mathrm{wg}} = 0.2$ and permittivity ($\epsilon_{\mathrm{wg}} = 11.45$) is buried in the glass with a distance 0.4 to the air layer. The incoming field u_{inc} is the y–polarized fundamental mode of the waveguide with $\omega = 2\pi/1.55$. The propagation of the waveguide mode is disturbed by a notch of width $w = 0.5$.

are in the range $[0, 80\,^{\circ}]$.

In Figure 4.12 and 4.13 we compare the exterior domain values u_{ext} with a quasi–exact solution. The quasi–exact solution u_{QE} was obtained on a sufficiently large computational domain containing all evaluation points. In the near field simulations we used third order finite elements. We observe an excellent agreement of u_{ext} with u_{QE}. Both data u_{ext} and u_{QE} are polluted by a finite element discretization error. As can be seen from Figure 4.13 the relative error $|u_{\mathrm{ext}} - u_{\mathrm{QE}}|/|u_{\mathrm{ext}}|$ decreases under an uniform mesh refinement.

4.7.2 Point source above material interface

This example serves as a verification of the Fourier transform computation by means of a complex deformation. As a source we place a dipole at position $(x_d, z_d) = (0, -1.5)$ in the computational domain (Figure 4.14). We solve the Helmoltz equation

$$-\nabla \mu^{-1} \nabla E_y - \omega^2 \epsilon E_y = \delta(x - x_d, z - z_d), \tag{4.22}$$

with $\omega = 2\pi/\lambda_0$ and $\lambda_0 = 1.55$.

The regularity of E_y is poor and a finite element discretization of E_y would suffer from a slow convergence. To cure that we use the subtraction approach, see Awada et al. [9], Wolters [113] and [119]. We split the field E_y into a singular field $E_{y,s}$ and a correction field $E_{y,c}$ that is $E_y = E_{y,s} + E_{y,c}$.

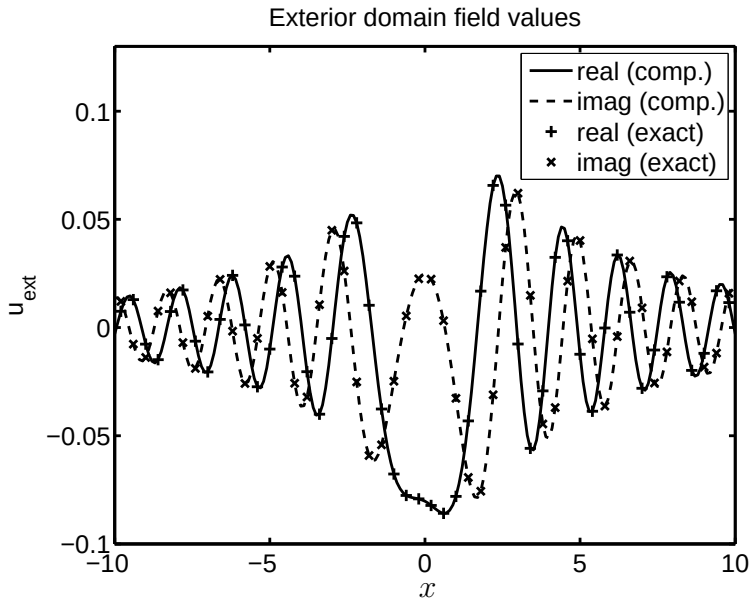

Figure 4.12: Waveguide notch: Field values in the exterior domain computed by the complex deformed Rayleigh–Sommerfeld integral. Quasi–exact values are marked with + and ×.

The singular field $E_{y,s}$ is the Green's function to the Helmholtz equation in a homogeneous space with $\epsilon_d = \epsilon(x_d, z_d)$ and $\mu_d = \mu(x_d, z_d)$:

$$-\nabla \mu_d^{-1} \nabla E_{y,s} - \omega^2 \epsilon_d E_{y,s} = \delta(x - x_d, z - z_d).$$

$E_{y,s}$ is analytically available (cf. equation (1.26)). The correction field $E_{y,c}$ satisfies the above Helmholtz (4.22) but with the right hand side replaced by

$$f_c = \nabla(\mu^{-1} - \mu_d^{-1}) \nabla E_{y,s} + \omega^2 (\epsilon - \epsilon_d) E_{y,s}.$$

f_c is equal to zero in a vicinity of the dipole position. Hence the correction field $E_{y,c}$ is sufficiently smooth for an accurate discretization with finite elements.

The function f_c is possibly non–zero in the entire space $\mathbf{R}^2$. To suppress arising source terms in the PML we prefer to compute the correction field $E_{y,s}$ only in the interior domain. In the exterior domain Ω_{ext} we still use the total field $E_y = E_{y,s} + E_{y,c}$. This yields additional boundary terms on the interface $\partial\Omega$ of the computational domain to the exterior domain stemming from the coupling condition

$$\begin{aligned} E_y|_{\partial\Omega} &= E_{y,s}|_{\partial\Omega} + E_{y,c}|_{\partial\Omega} \\ \mu^{-1} \partial_{\mathbf{n}} E_y|_{\partial\Omega} &= \mu^{-1} \partial_{\mathbf{n}} E_{y,s}|_{\partial\Omega} + \mu^{-1} \partial_{\mathbf{n}} E_{y,c}|_{\partial\Omega}. \end{aligned} \tag{4.23}$$

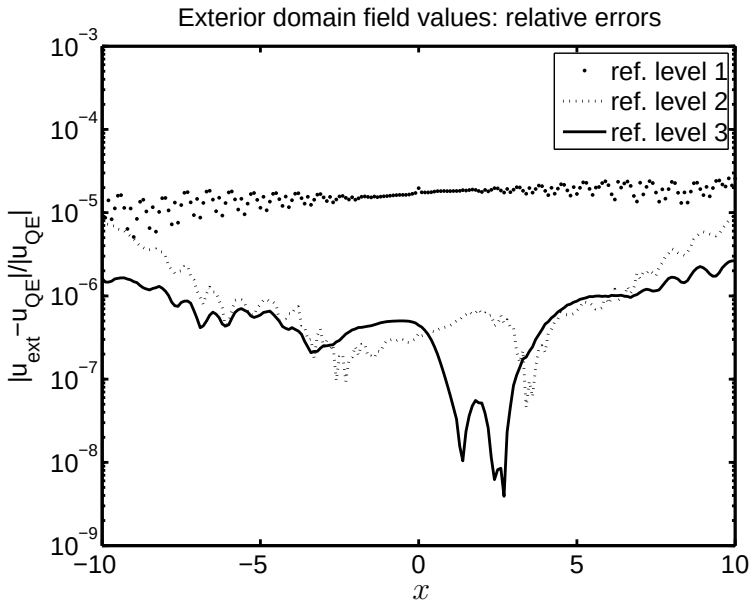

Figure 4.13: Waveguide notch: Error of exterior domain values u_{ext} to the quasi–exact solution u_{QE} for different refinement levels of the finite element mesh.

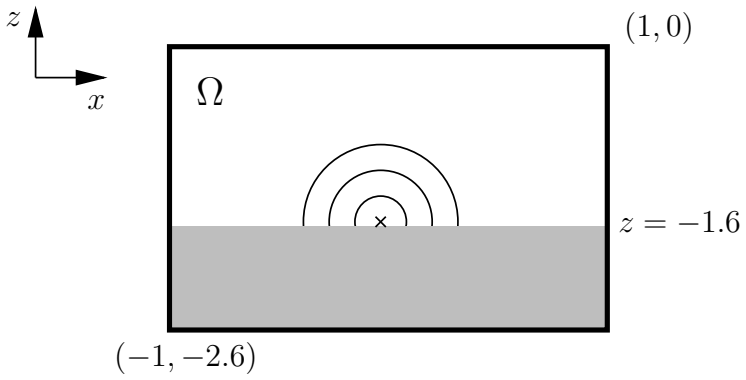

Figure 4.14: Point source above material interface: The material properties are as in Figure 4.11 but we removed the waveguide and the upper glass layer. No incoming field is prescribed. Instead a source dipole is placed above the material interface.

We already encountered such a coupling condition when prescribing the incoming field in a scattering problem in the scattering Problem 3.1. The numerical treatment of (4.23) is analog to that case.

The Fourier transform in x to the solution $E_y(x,z)$ of the above Helmholtz equation (4.22) is analytically given by Weyl's representation formula of a diverging spherical wave together with Fresnel's formula:

$$\hat{E}_y(k_x,z) = \frac{ie^{ik_z(z-z_d)}}{4\pi k_z}\left(1+e^{2\cdot ik_z d_{\mathrm{I}}}\frac{n_a\cos(\vartheta_a)-n_g\cos(\vartheta_g)}{n_a\cos(\vartheta_a)+n_g\cos(\vartheta_g)}\right) \tag{4.24}$$

with $k_z = \sqrt{k_0^2-k_x^2}$, $d_{\mathrm{I}} = 0.1$ (distance point source to the interface), $n_g = \sqrt{\epsilon_g\mu_g}$ (refractive index glass), $n_a = 1$ (refractive index air), $\vartheta_a = \mathrm{atan2}(k_x,k_z)$ and $\vartheta_g = \mathrm{asin}(\sin(\vartheta_a)n_a/n_g)$.

The Fourier transform has singularities at $k_x = \pm k_0$. We are only able to compute the band-limited Fourier transform which corresponds to upward traveling waves. This is not a severe restriction because in most scattering experiments one is only interested in the far field image. Hence, evanescent waves with $|k_x| > k_0$ do not play any role. Furthermore, the scattered wave typically passes an optical system (microscope, projector, *etc.*). Only those Fourier modes with $|k_x| \leq \mathrm{NA}\cdot k_0$ enter the optical system where NA is the numerical aperture of the optical system. In our numerical experiment we restricted the Fourier transform evaluation to $|k_x| \leq 0.9\cdot k_0$ which corresponds to a numerical aperture of $\mathrm{NA} = 0.9$.

The computed Fourier transform is given in Figure 4.15. To validate the accuracy and efficiency of the method we studied the convergence of the Fourier integrals with a growing integration interval $[0,\rho]$. We simultaneously reduced the finite element discretization error by a successive uniform mesh refinement.

Figures 4.16 and 4.17 give the results to this convergence study for $k_x/k_0 = 0$ and $k_x/k_0 = 0.88$, respectively. In both cases we observe an exponentially fast convergence of the complex deformed Fourier integrals with growing ρ until a saturation is reached. This saturation limit is caused by the finite element discretization error and therefore decreases under an uniform mesh refinement. As expected, the exponential convergence rate diminishes for the larger value $k_x/k_0 = 0.88$ compared to $k_x/k_0 = 0$.

We also computed the Fourier transform without the complex deformation techniques by setting $\sigma = 0$, see again Figures 4.16 and 4.17. The convergence is very slow without applying a complex deformation in accordance with the theoretical convergence behavior $\sim 1/\sqrt{\rho/\lambda_0}$.

For illustration, we want to use the gained Fourier transform to reconstruct the near field at $z = 0$ by an inverse Fourier transform. Since we only

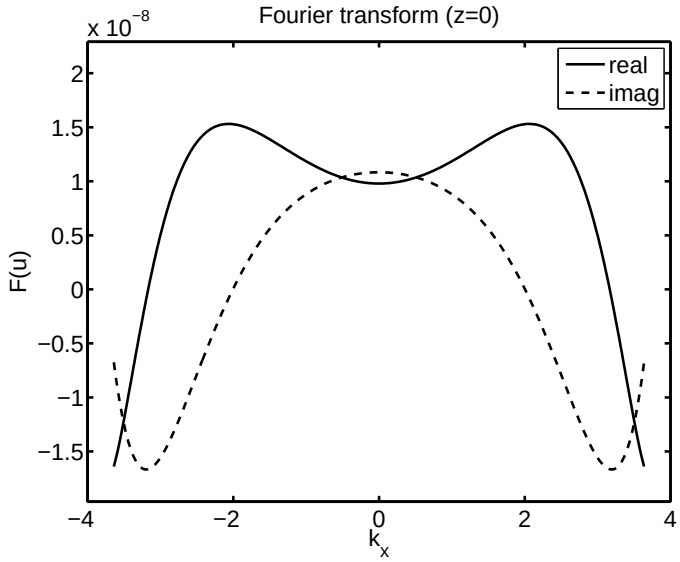

Figure 4.15: Computed Fourier transform of a scattered field to a point source located above a material interface.

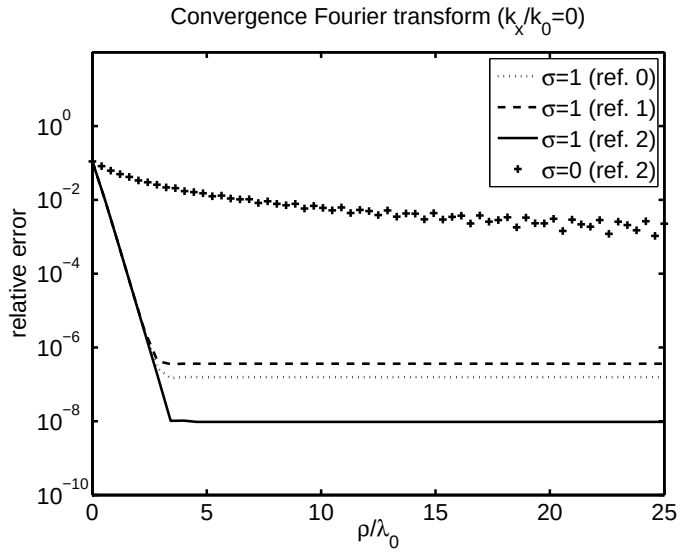

Figure 4.16: Point source above material interface: Convergence of the computed Fourier transform at $k_x/k_0 = 0$ with growing integration interval. "ref." denotes the finite element refinement level. σ is the PML damping factor used in the complex deformation of the Fourier integral.

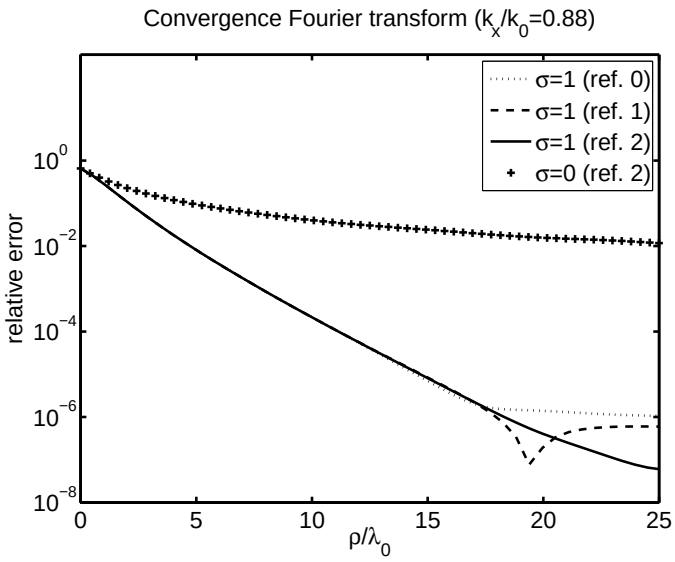

Figure 4.17: Point source above material interface: Convergence of the computed Fourier transform at $k_x/k_0 = 0.88$.

have the band–limited Fourier transform

$$\hat{u}_{\mathrm{NA}}(k_x, 0) = \chi_{[-k_0 \cdot \mathrm{NA}, k_0 \cdot \mathrm{NA}]}(k_x) \cdot \hat{u}(k_x, 0)$$

we are not able to reconstruct the true near–field. Instead of this, the inverse Fourier transform gives the image as seen by a perfect $1:1$ projection system with numerical aperture equal to 0.9. Figure 4.18 gives the results. The true near–field was computed on a sufficiently enlarged computational domain.

4.7.3 Point source near waveguide's tip

We deal with the geometry as given in Figure 4.19. Now, the dipole is placed close to the waveguide's tip. A quasi–analytic solution to this problem is not known.

We again use the subtraction approach to compute the singular solution to this problem as explained in the previous example. Figure 4.20 shows the computed band–limited Fourier transform $\hat{u}_{\mathrm{NA}}$ to this problem. The computed near field and the image gained by the inverse Fourier transform are shown in Figure 4.21.

Due to the lack of an analytic solution to this problem we want to cross-check the computed image by an alternative way to construct the image: We

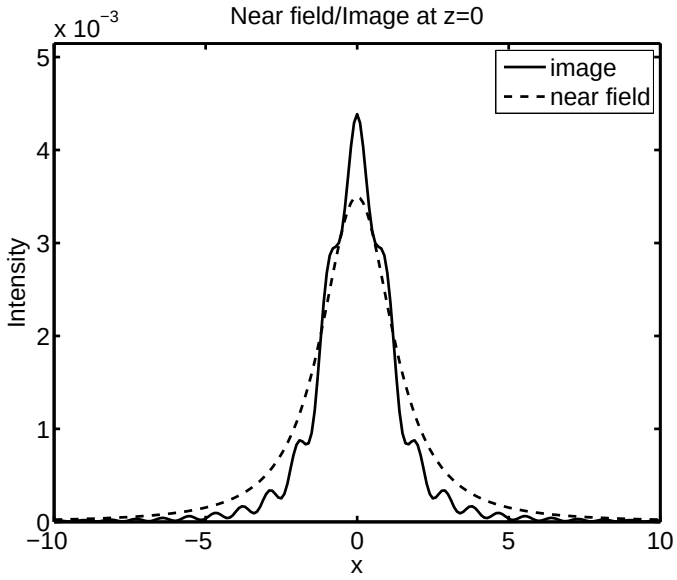

Figure 4.18: Point source above material interface: Image compared to true near–field. A perfect reconstruction is not possible due to the truncation of the Fourier transform.

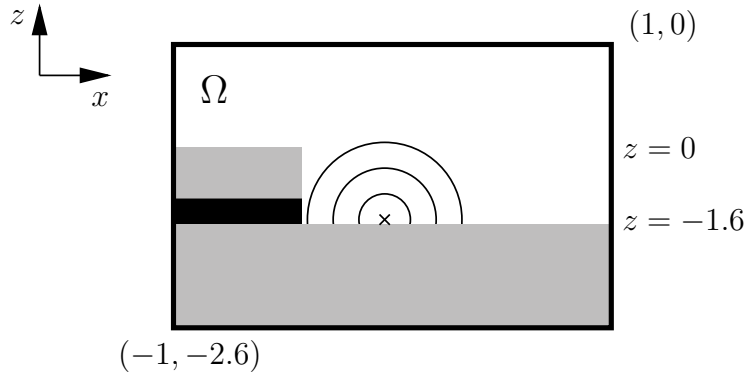

Figure 4.19: Point source near waveguide's tip: The material properties are as in Figure 4.11. In the right exterior domain we removed the waveguide and the upper glass layer. No incoming field is prescribed but a dipole is placed in front of the waveguide tip.

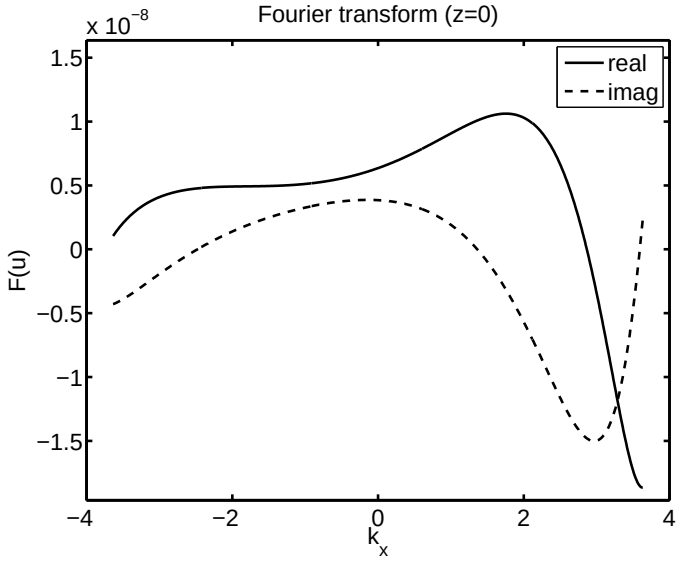

Figure 4.20: Point source at waveguide's tip: Computed Band–limited Fourier transform. An exact solution to this problem is not available.

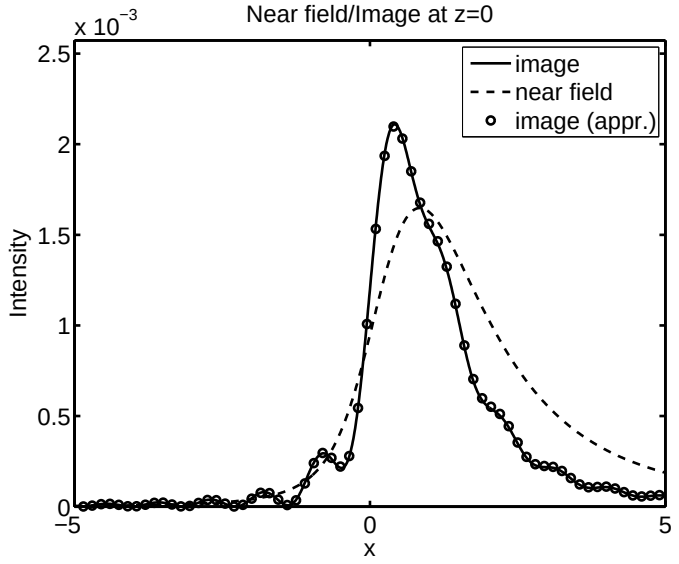

Figure 4.21: Point source above material interface: Image compared to true near–field at $z = 1$. Values marked with $\circ$ are computed by an alternative approach without the usage of the Fourier transform (cf. equation 4.25).

use the convolution theorem for the inverse Fourier transform to compute the image by

$$\begin{aligned} u_{\mathrm{I}}(x,0) &= \int_{-\infty}^{\infty} \chi_{[-k_0\mathrm{NA},k_0\mathrm{NA}]}(k_x) \cdot \hat{u}(k_x,0) e^{ik_x x} \mathrm{d}k_x \\ &= \frac{1}{2\pi} \int_{-\infty}^{\infty} u(x',0) \frac{2\sin(\mathrm{NA} \cdot k_0(x-x'))}{x-x'} \mathrm{d}x'. \end{aligned} \tag{4.25}$$

We remark that this integral needs a careful definition within the distribution theory, see for example Rudin [94, p. 166]. However, we commit the "integration"–crime and evaluate equation (4.25) numerically. The used near field data $u(x,0)$ were computed on an enlarged computational domain with $|x| \leq j\lambda_0$. Outside this interval we set $u(x,0) = 0$. This way we compute the following approximate image

$$u_{\mathrm{I},j}(x,0) = (\chi_{[-k_0\mathrm{NA},k_0\mathrm{NA}]}(\chi_{[-j\lambda_0,j\lambda_0]} u(\cdot,0))^{\wedge})^{\vee}, \tag{4.26}$$

where ' $^{\wedge}$' and ' $^{\vee}$' denote the Fourier transform and the inverse Fourier transform, respectively. From the convergence study in the previous example we expect a slow convergence of the approximate image $u_{\mathrm{I},j}$ towards the image u_{I}. Indeed, for $j = 20$ the approximate image $u_{\mathrm{I},20}(x,0)$ is qualitatively in a good agreement with the image $u_{\mathrm{I}}(x,0)$ we obtained directly from the band–limited Fourier transform, cf. Figure 4.21.

4.7.4 Glass fiber tip

This example serves the verification of the exterior domain evaluation formula (4.4) in three space dimensions. We deal with a 3D configuration as given in Figure 4.19. As explained in Section 2.5 we can exploit the rotational symmetry of the geometry to restrict the computational domain on a cross section given in Figure 4.23.

The incoming field is the fundamental propagating mode of the glass fiber. Hence, only the first Fourier mode is non-zero.

The incoming field is strongly confined within the glass fiber core. We have chosen the radial dimension of $\Omega_{\mathrm{ext},2}$ large enough, cf. Figure 4.23, so that the amplitude of the incoming field is smaller than the machine accuracy outside $\Omega_{\mathrm{ext},2}$. This way, it is sufficiently accurate to couple in the light only on the interface of the computational domain with $\Omega_{\mathrm{ext},2}$, cf. Figure 4.23. In the next chapter, when dealing with multiply structured exterior domains, we will get rid of this restriction, and we will be able to shrink the computational domain to the size of the glass fiber in radial direction.

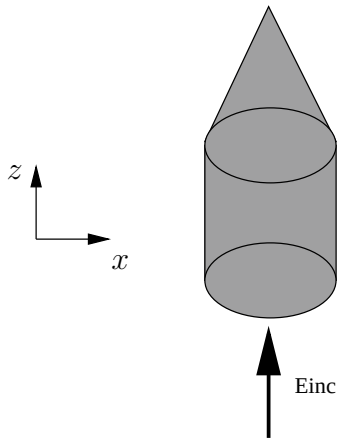

Figure 4.22: Glass fiber with pointed end face. For the precise geometry and material definitions we refer to Figure 4.23

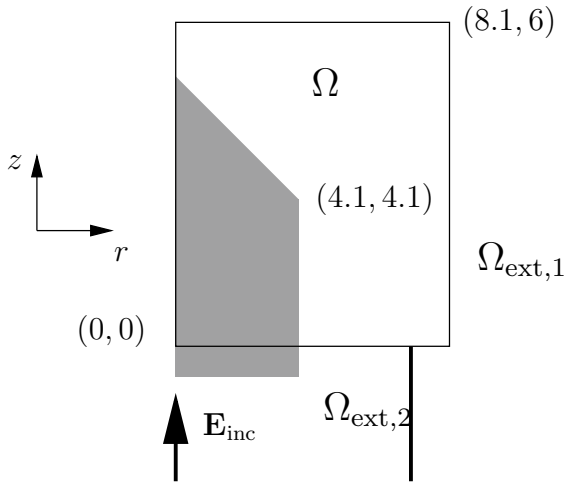

Figure 4.23: Cross section of glass fiber end face (scales are in μm). The glass has a refractive index $n_{\mathrm{g}} = \sqrt{2.113}$. The surroundings consist of air. The incoming glass fiber mode has a vacuum wavelength $\lambda_0 = 1.55$.

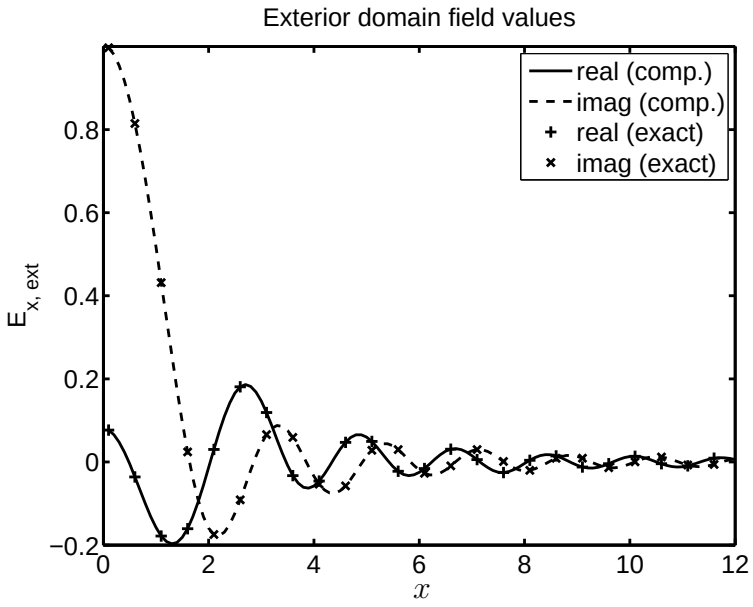

Figure 4.24: Glass fiber tip: Normalized field values (E_x–component) in the exterior domain computed with the exterior domain evaluation formula (4.4). Quasi–exact values are marked with + and ×. The z-coordinate of the evaluation point was chosen equal to 8.

In the numerical experiment we compared the exterior domain values computed by means of formula (4.4) with a quasi-exact solution obtained on an enlarged computational domain. Figure 4.24 confirms the accuracy of our exterior domain evaluation formula in three space dimensions. This is further validated by Figure 4.25, which shows the relative error in dependence on the evaluation point position and the used finite element order. As expected, the error in the exterior domain evaluation error decreases with the finite element order.

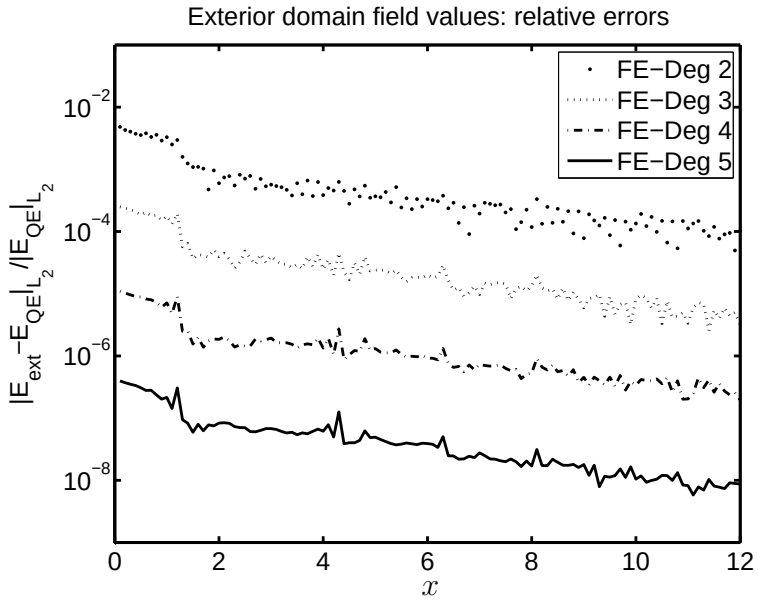

Figure 4.25: Glass: Field error of exterior domain values $\mathbf{E}_{\text{ext}}$ to the quasi–exact solution $\mathbf{E}_{\text{QE}}$ for different finite element orders.

Chapter 5

Multiply structured exterior domains

We have learned in the previous chapter how to exploit the PML solution for a field evaluation in the exterior domain. In this chapter we follow up the idea to consider the field within the PML not only as an artificial quantity only introduced for numerical purposes. This will help us to tackle scattering problems with exterior domains more complicated structured than regarded so far. For example we want to discuss a scattering problem as sketched in Figure 5.1. The exterior domain in this 2D setting is differently layered on the left and right horizontal half space. We assume that an incoming plane wave $\mathbf{E}_{\text{inc}}$ hits the scatterer from above. What makes this scattering problem difficult?

To give the answer we recall that in the scattering problem formulation (Problem 2.1 , Chapter 2) we need to know a reference field $\mathbf{E}_{\text{ref}}$ which satisfies Maxwell's equations in the entire exterior domain and which comprises the incoming plane wave. Such a reference field is easily constructed when the stratifications in the left and right horizontal domain coincide. In this simpler case one solves a 1D scattering problem for a stack layout in z–direction. To construct a reference field $\mathbf{E}_{\text{ref}}$ for the more sophisticated situation in Figure 5.1 one might fix a reference configuration as given in Figure 5.2 and might try to determine the reference field $\mathbf{E}_{\text{ref}}$. However, from a numerical point of view the computation of the reference field $\mathbf{E}_{\text{ref}}$ in this situation is not easier than solving the original scattering problem! To overcome this we will extend the scattering problem formulation from Chapter 2 to the situation of *multiply structured exterior domains* in this chapter.

Furthermore, the exterior domain evaluation and the far field extraction need also a revision to cover the case of multiply structured exterior domains. This is done in the section after next. To anticipate the discussion we mention

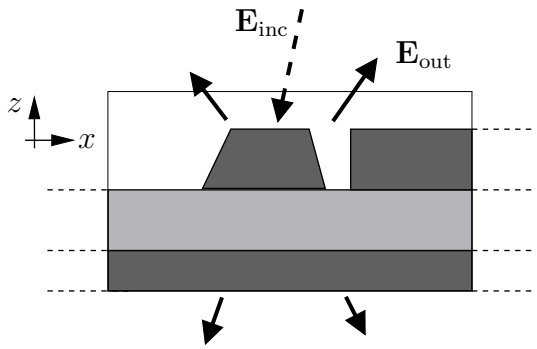

Figure 5.1: 2D scattering problem with complicated exterior domain. The exterior domain has different layered media on the left and right side. An incoming field $\mathbf{E}_{\text{inc}}$ gives rise to an outgoing field $\mathbf{E}_{\text{out}}$. The incoming field $\mathbf{E}_{\text{inc}}$ is typically a plane wave. In the standard scattering problem formulation we need to find a reference field $\mathbf{E}_{\text{ref}}$ which comprises the incoming field and which satisfies Maxwell's equations in the entire exterior domain. It is non–trivial to construct such a field $\mathbf{E}_{\text{ref}}$, cf. Figure 5.2.

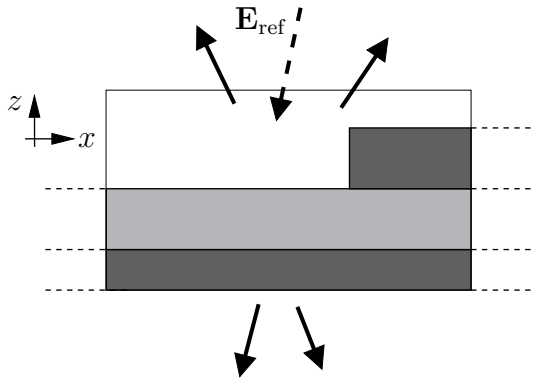

Figure 5.2: Reference field $\mathbf{E}_{\text{ref}}$ for scattering problem as sketched in Figure 5.1. The reference field $\mathbf{E}_{\text{ref}}$ comprises the incoming plane wave and the outgoing waves scattered off this reference configuration. Unfortunately, the reference field $\mathbf{E}_{\text{ref}}$ is numerically not available in this case.

that the distinction of the scattered field and the reference field in the far field regime gets more involved as we briefly explain here.

Recall that the actual far field consists of the scattered field $\mathbf{E}_{\text{sc}}$ and the outgoing waves of the reference field $\mathbf{E}_{\text{ref}}$. The scattered field gives rise to a continuous Fourier spectrum. In case of an uniformly layered exterior domain the contribution of the reference field to the Fourier spectrum is discrete for an incoming plane wave $\mathbf{E}_{\text{inc}} = \widehat{\mathbf{E}} \exp(i\mathbf{k} \cdot \mathbf{x})$. More precisely the reference field $\mathbf{E}_{\text{ref}}$ has a δ–distributed Fourier spectrum at $\mathbf{k}_{\text{inc},\perp}$. For the multiply structured exterior domain the situation changes. Firstly, there is no canonical choice to fix the reference field as in Figure 5.2. The precise position of the end face of the most upper right layer is arbitrary. Secondly, the contribution of the reference field $\mathbf{E}_{\text{ref}}$ to the Fourier spectrum also contains a continuous part. When changing the reference field $\mathbf{E}_{\text{ref}}$ the continuous spectrum $\mathbf{E}_{\text{sc}}$ also changes. To avoid these ambiguities we therefore want to base our consideration concerning the Fourier spectrum computation on the total field $\mathbf{E}_{\text{sc}} + \mathbf{E}_{\text{ref}}$. This requires to deal with the discrete part of the Fourier spectrum numerically.

5.1 Scattering problems with multiply structured exterior domains

We aim at a generalization of the scattering formulation Problem 2.1 in Chapter 2 for the case of multiply structured exterior domains as motivated above. As a general guideline we need to keep in mind that all quantities we use are numerically available. To satisfy this demand we sacrifice the construction of a single reference field $\mathbf{E}_{\text{ref}}$ and allows for a piecewise definition of reference fields $\mathbf{E}_{\text{ref},1}, \ldots, \mathbf{E}_{\text{ref},N}$ defined on a decomposition of the exterior domain into sub-domains that is $\Omega_{\text{ext}} = \Omega_{\text{ext},1} \cup \cdots \cup \Omega_{\text{ext},N}$.

Once the reference fields $\mathbf{E}_{\text{ref},1}, \ldots, \mathbf{E}_{\text{ref},N}$ are fixed the scattered field $\mathbf{E}_{\text{sc},j}$ on the exterior sub–domain $\Omega_{\text{ext},j}$ is defined as the difference of the reference field $\mathbf{E}_{\text{sc},j}$ and the total field that is $\mathbf{E}_{\text{sc},j} = \mathbf{E}_{\text{tot}} - \mathbf{E}_{\text{ref},j}$. Each scattered field $\mathbf{E}_{\text{sc},j}$ fulfills Maxwell's equations on the sub–domain $\Omega_{\text{sc},j}$. On the interface $\Gamma_{i,j} = \Omega_{\text{ext},i} \cap \Omega_{\text{ext},j}$ the scattered fields $\mathbf{E}_{\text{sc},i}$ and $\mathbf{E}_{\text{sc},j}$ as well as the field derivatives $\mu^{-1}\nabla \times \mathbf{E}_{\text{sc},i}$, $\mu^{-1}\nabla \times \mathbf{E}_{\text{sc},j}$ jump. More precisely we have that

$$\begin{aligned}(\mathbf{E}_{\text{sc},i} - \mathbf{E}_{\text{sc},j}) \times \mathbf{n} &= (\mathbf{E}_{\text{ref},j} - \mathbf{E}_{\text{ref},i}) \times \mathbf{n}, \\ (\mu^{-1}\nabla \times \mathbf{E}_{\text{sc},i} - \mu^{-1}\nabla \times \mathbf{E}_{\text{sc},j}) \times \mathbf{n} &= (\mu^{-1}\nabla \times \mathbf{E}_{\text{ref},j} - \mu^{-1}\nabla \times \mathbf{E}_{\text{ref},i}) \times \mathbf{n},\end{aligned}$$

where $\mathbf{n}$ denotes the normal on the interface $\Gamma_{i,j}$. Switching to the exterior

calculus notation we arrive at the following coupled system of equations,

$$d\mu^{-1}d\mathbf{e} - \omega^2\varepsilon\mathbf{e} = 0 \quad \text{in } \Omega, \tag{5.1a}$$
$$d\mu^{-1}d\mathbf{e}_{\mathrm{sc},j} - \omega^2\varepsilon\mathbf{e}_{\mathrm{sc},j} = 0 \quad \text{in } \Omega_{\mathrm{ext},j}, \tag{5.1b}$$
$$(\mathbf{e} - \mathbf{e}_{\mathrm{sc},j})|_{\Omega\cap\Omega_{\mathrm{ext},j}} = \mathbf{e}_{\mathrm{ref},j}|_{\Omega\cap\Omega_{\mathrm{ext},j}}, \tag{5.1c}$$
$$(\mu^{-1}d\mathbf{e} - \mu^{-1}d\mathbf{e}_{\mathrm{sc},j})|_{\Omega\cap\Omega_{\mathrm{ext},j}} = \mu^{-1}d\mathbf{e}_{\mathrm{ref},j}|_{\Omega\cap\Omega_{\mathrm{ext},j}}, \tag{5.1d}$$
$$(\mathbf{e}_{\mathrm{sc},i} - \mathbf{e}_{\mathrm{sc},j})|_{\Gamma_{i,j}} = (\mathbf{e}_{\mathrm{ref},j} - \mathbf{e}_{\mathrm{ref},i})|_{\Gamma_{i,j}}, \tag{5.1e}$$
$$(\mu^{-1}d\mathbf{e}_{\mathrm{sc},i} - \mu^{-1}d\mathbf{e}_{\mathrm{sc},j})|_{\Gamma_{i,j}} = (\mu^{-1}d\mathbf{e}_{\mathrm{ref},j} - \mu^{-1}d\mathbf{e}_{\mathrm{ref},i})|_{\Gamma_{i,j}}. \tag{5.1f}$$

Since we know the reference fields $\mathbf{e}_{\mathrm{ref},i}$ and $\mathbf{e}_{\mathrm{ref},j}$ all quantities on the right hand side of the above system of equations are numerically available.

The first two lines (5.1a) and (5.1b) state that the fields meet Maxwell's equations. Line three and four enforce the matching condition between the field $\mathbf{e}$ in the interior domain and the scattered field $\mathbf{e}_{\mathrm{sc},j}$ on the coupling boundary between the interior domain and the jth exterior domain. Special attention deserve the last two lines which realize the jump of the scattered fields $\mathbf{e}_{\mathrm{sc},i}$ and $\mathbf{e}_{\mathrm{sc},j}$ across a common interface $\Gamma_{i,j}$. The interface $\Gamma_{i,j}$ is infinitely extended so that the jump conditions in the last two lines give rise to additional right hand side terms within the exterior domain. In the next section we will introduce perfectly matched layers for the above system. Not surprisingly, the right hand side of the arising PML system will result from the interior–exterior domain coupling as well as from a complex stretched version of the jump matching condition on $\Gamma_{i,j}$.

We refer to Figure 5.3 for an illustration of the principle ideas in case of the 2D example from Figure 5.1. As in Figure 5.3 we regard the differently stratified left and right exterior domains separately and introduce two reference solutions $\mathbf{E}_{\mathrm{ref},1}$ and $\mathbf{E}_{\mathrm{ref},2}$. The reference solution $\mathbf{E}_{\mathrm{ref},1}$ solves Maxwell's equations for infinite media with the same stratification in the z–direction as the left exterior domain. To construct $\mathbf{E}_{\mathrm{ref},1}$ we only need to solve a Helmholtz equation in one space dimension for the given incoming plane wave $\mathbf{E}_{\mathrm{inc}}$. $\mathbf{E}_{\mathrm{ref},2}$ is defined accordingly by using the stratification of the right exterior domain.

A possible splitting of this multiply structured 2D domain is shown in Figure 5.4. The interface $\Gamma_{1,2}$ is given by the thick dashed lines. We have some freedom in fixing the position of the interface $\Gamma_{1,2}$. As a constraint we must only assure that $\mathbf{E}_{\mathrm{ref},1}$ and $\mathbf{E}_{\mathrm{ref},2}$ are solutions to Maxwell's equations in $\Omega_{\mathrm{ext},1}$ and $\Omega_{\mathrm{ext},2}$, respectively. Later in the PML method we will use this freedom to improve the exponential decay of the complex deformed jump $\mathbf{E}_{\mathrm{ref},j} - \mathbf{E}_{\mathrm{ref},i}$ which enters the right hand side of our scattering problem (5.1) in the equations (5.1e) and (5.1f).

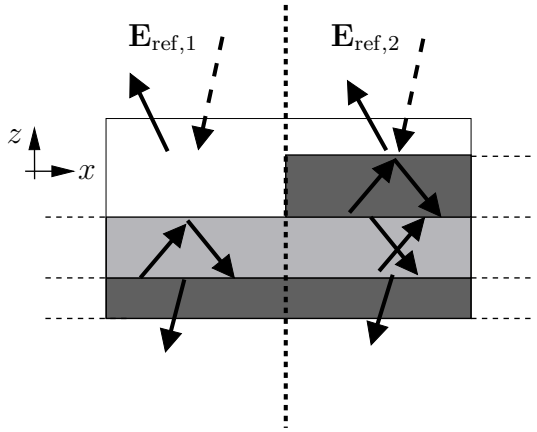

Figure 5.3: Choice of different reference fields for the split exterior domains. $\mathbf{E}_{\text{ref},1}$ and $\mathbf{E}_{\text{ref},2}$ are solutions to Maxwell's equations in the different layered media for a prescribed illuminating plane wave.

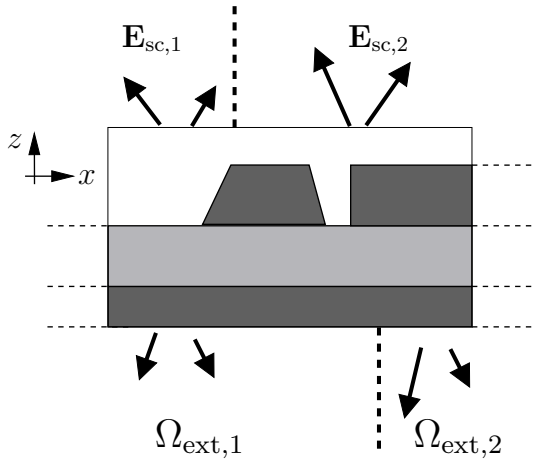

Figure 5.4: Exterior domain Ω_{ext} split into two separated exterior sub–domains $\Omega_{\text{ext},1}$ and $\Omega_{\text{ext},2}$. On each of the sub–domains we define scattered fields $\mathbf{E}_{\text{sc},1}$, $\mathbf{E}_{\text{sc},2}$ as the difference of the total field $\mathbf{E}_{\text{tot}}$ and $\mathbf{E}_{\text{ref1}}$, $\mathbf{E}_{\text{ref2}}$, respectively. Additional coupling conditions on the boundary $\Gamma_{1,2} = \Omega_{\text{ext},1} \cap \Omega_{\text{ext},2}$ are needed.

5.2 PMLs for multiply structured exterior domains

In Chapter 3 we explained in greater detail how to define a complex coordinate stretching which served as the starting point for the definition of *perfectly matched layers*. Especially, we carefully justified the step from a real coordinate stretching to a complex coordinate stretching by using a homotopy parameter which helped us to show the equivalence of the original scattering problem and the complex stretched version with arguments from complex function theory of one variable.

In this section we extend the PML concept to scattering problems with multiply structured exterior domains as given in the system of equations (5.1). Our goal is to derive a weak formulation of the system of equations (5.1) with PMLs. Many of the steps one has to perform to derive this weak formulation follow directly from the basic PML ideas. We therefore skip the details here and directly define the complex continuations $\mathbf{e}_{\gamma,j}$ of the scattered fields $\mathbf{e}_{\mathrm{sc},j}$ for a given PML path parameter γ. In the same way we define the complex continuation of the reference fields $\mathbf{e}_{\mathrm{ref},\gamma,j}$ and the *pulled back* material tensor ε_γ and μ_γ.

In the system of equations (5.1) for the scattering problem with multiply structured exterior domains various field matching conditions must be taken into account, see equations (5.1c)–(5.1f). For notational purposes we find it more convenient to give up the special role of the interior domain Ω and introduce the following notations $\Omega_0 = \Omega$ and $\Omega_j = \Omega_{\mathrm{ext},j}$. According to that we define $\mathbf{e}_{\gamma,0} = \mathbf{e}|_{\Omega_0}$ and set $\mathbf{e}_{\mathrm{ref},\gamma,0}$ equal to zero. This way the complex stretched version of the system of equations (5.1) can now be written as follows

$$d\mu_\gamma^{-1} d\mathbf{e}_{\gamma,j} - \omega^2 \varepsilon_\gamma \mathbf{e}_{\gamma,j} = 0 \quad \text{in } \Omega_j, \tag{5.2a}$$

$$(\mathbf{e}_{\gamma,i} - \mathbf{e}_{\gamma,j})|_{\Gamma_{i,j}} = (\mathbf{e}_{\mathrm{ref},j} - \mathbf{e}_{\mathrm{ref},\gamma,i})|_{\Gamma_{i,j}}, \tag{5.2b}$$

$$(\mu_\gamma^{-1} d\mathbf{e}_{\gamma,i} - \mu_\gamma^{-1} d\mathbf{e}_{\gamma,j})|_{\Gamma_{i,j}} = (\mu_\gamma^{-1} d\mathbf{e}_{\mathrm{ref},j} - \mu_\gamma^{-1} d\mathbf{e}_{\mathrm{ref},\gamma,i})|_{\Gamma_{i,j}}, \tag{5.2c}$$

with $j = 0, \dots N$ and $i < j$. We remark that this system is similar to a domain decomposition formulation for a partial differential equation with multiply domains [91, equation 1.4.27].

To bring the above system (5.2) into variational form we apply the wedge product with a test function $\varphi \in H_{\mathrm{loc}}(\mathrm{curl}, \cup_{j\geq 0}\Omega_j)$ on the domain–wise defined Maxwell's equations (5.2a) and use the partial integration formula (1.45). Together with the matching condition of the Neumann data in equation (5.2c)

this yields the preliminary variational equation

$$\begin{aligned}\sum_{j=0}^{N}\int_{\Omega_j} d\overline{\varphi}\wedge\mu_\gamma^{-1}d\mathbf{e}_{\gamma,j}-\omega^2\overline{\varphi}\wedge\varepsilon_\gamma\mathbf{e}_{\gamma,j}=\\ \sum_{i=0}^{N}\sum_{j=i+1}^{N}\int_{\Gamma_{i,j}}\overline{\varphi}\wedge(\mu_\gamma^{-1}d\mathbf{e}_{\gamma,i}-\mu_\gamma^{-1}d\mathbf{e}_{\gamma,j})\\ =\sum_{i=0}^{N}\sum_{j=i+1}^{N}\int_{\Gamma_{i,j}}\overline{\varphi}\wedge(\mu_\gamma^{-1}d\mathbf{e}_{\mathrm{ref},\gamma,j}-\mu_\gamma^{-1}d\mathbf{e}_{\mathrm{ref},\gamma,i}).\end{aligned}\tag{5.3}$$

Due to the jump of the Dirichlet data across an interface $\Gamma_{i,j}$ the piecewise combination of the fields $\mathbf{e}_{\gamma,j}$ is not contained in $H_{\mathrm{loc}}(\mathrm{curl},\cup_{j\geq 0}\Omega_j)$. As usual we therefore add supplemental fields near the interfaces $\Gamma_{i,j}$ to enforce continuity.

To construct these supplemental fields we use sufficiently smooth functions $\chi_j:\cup_i\Omega_i\to[0,1]$ such that $\chi_j=1$ on $\partial\Omega_j$ and $\chi_j(\mathbf{x})=0$ when $\mathrm{dist}(\mathbf{x},\Omega_j)>\delta$. We now define the field $\mathbf{e}_\gamma$ on $\cup_{j\geq 0}\Omega_j$ by

$$\begin{aligned}\mathbf{e}_\gamma|_{\Omega_j}&=\mathbf{e}_{\gamma,j}+\sum_{k<j}\chi_k\prod_{k'<k}(1-\chi_{k'})(\mathbf{e}_{\mathrm{ref},\gamma,j}-\mathbf{e}_{\mathrm{ref},k})\\ &=\mathbf{e}_{\gamma,j}+\mathcal{I}_j(\mathbf{e}_{\mathrm{ref},\gamma,1},\ldots,\mathbf{e}_{\mathrm{ref},\gamma,j})\end{aligned}\tag{5.4}$$

and will show that $\mathbf{e}_\gamma\in H_{\mathrm{loc}}(\mathrm{curl},\cup_{j\geq 0}\Omega_j)$. As a convention the product over an empty set is equal to one. We agree that this definition looks tricky but we need to cope with the situation of edges or corner points where several domains Ω_j intersect.

We have to prove that $\mathbf{e}_\gamma$ is continuous across an interface $\Gamma_{i,j}$ with $i<j$. Let us denote $\widetilde{\mathbf{e}}_{\gamma,j}=\mathbf{e}_\gamma|_{\partial\Omega_j}$. It is sufficient to show that $\widetilde{\mathbf{e}}_{\gamma,j}|_{\Gamma_{i,j}}=\widetilde{\mathbf{e}}_{\gamma,i}|_{\Gamma_{i,j}}$. We will make use of the equality

$$\prod_{k'<i}(1-\chi_{k'})+\sum_{k<i}\chi_k\prod_{k'<k}(1-\chi_{k'})=1\tag{5.5}$$

which we will prove at the end of this section. We have

$$\begin{aligned}\widetilde{\mathbf{e}}_{\gamma,j}-\widetilde{\mathbf{e}}_{\gamma,i}=\ &\mathbf{e}_{\gamma,j}+\sum_{k<i+1}\chi_k\prod_{k'<k}(1-\chi_{k'})(\mathbf{e}_{\mathrm{ref},\gamma,j}-\mathbf{e}_{\mathrm{ref},\gamma,k})\\ &-\mathbf{e}_{\gamma,i}-\sum_{k<i}\chi_k\prod_{k'<k}(1-\chi_{k'})(\mathbf{e}_{\mathrm{ref},i}-\mathbf{e}_{\mathrm{ref},\gamma,k}),\end{aligned}$$

where we truncated the first sum from the original range $k < j$ in definition (5.4) to $k < i + 1$, because $\chi_i = 1$ on $\Gamma_{i,j}$. Rearranging the terms and using $\chi_i = 1$ on $\Gamma_{i,j}$, again, yields

$$\begin{aligned}\widetilde{\mathbf{e}}_{\gamma,j} - \widetilde{\mathbf{e}}_{\gamma,i} &= \mathbf{e}_{\gamma,j} - \mathbf{e}_{\gamma,i} + \\ &\qquad \Big(\prod_{k'<i} (1-\chi_{k'}) + \sum_{k<i} \chi_k \prod_{k'<k} (1-\chi_{k'}) \Big) (\mathbf{e}_{\mathrm{ref},\gamma,j} - \mathbf{e}_{\mathrm{ref},\gamma,i}) \\ &= \mathbf{e}_{\gamma,j} + \mathbf{e}_{\mathrm{ref},\gamma,j} - \mathbf{e}_{\gamma,i} - \mathbf{e}_{\mathrm{ref},\gamma,i},\end{aligned}$$

where the last equation follows from the partition of unity property in (5.5). With the Dirichlet matching condition equation (5.2b) we see that the last line is equal to zero and so the continuity of $\mathbf{e}_\gamma$ across interfaces $\Gamma_{i,j}$ is shown.

We are now in the position to define the variational form in $H_{\mathrm{loc}}(\mathrm{curl}, \Omega \cup \Omega_{\mathrm{ext}})$ by inserting $\mathbf{e}_{\gamma,j} = \mathbf{e}_\gamma - \mathcal{I}_j(\mathbf{e}_{\mathrm{ref},\gamma,1}, \ldots, \mathbf{e}_{\mathrm{ref},\gamma,j})$ into the preliminary variational equation (5.3). We recall that $\Omega \cup \Omega_{\mathrm{ext}} = \cup_{j\geq 0} \Omega_j$. As detailed in Chapter 3 we restrict the PML system to a bounded domain $\Omega \cup \Omega_{\mathrm{ext}}^{(\rho)} = \Omega \cup_{j\geq 1} \Omega_{\mathrm{ext},j}^{(\rho)}$ with PML thickness ρ.

Problem 5.1 (scattering problem with multiply structured exterior domain using PML)**.** *Regard an admissible geometry $\Omega \subset \mathbf{R}^3$, which allows for a non–overlapping decomposition of the exterior domain $\Omega_{\mathrm{ext}} = \cup_{j\geq 1} \Omega_{\mathrm{ext},j}$. Let reference fields $\mathbf{e}_{\mathrm{ref},j} \in H_{\mathrm{loc}}(\mathrm{curl}, \Omega_{\mathrm{ext},j})$ be given which satisfy Maxwell's equations in $\Omega_{\mathrm{ext},j}$, that is,*

$$\int_{\Omega_{\mathrm{ext},j}} \overline{d\varphi} \wedge \mu^{-1} d\mathbf{e}_{\mathrm{ref},j} - \omega^2 \overline{\varphi} \wedge \varepsilon \mathbf{e}_{\mathrm{ref},j} \;=\; \int_{\partial\Omega_{\mathrm{ext},j}} \overline{\varphi} \wedge \mu^{-1} d\mathbf{e}_{\mathrm{ref},j}$$

for all test functions $\varphi \in H(\mathrm{curl}, \Omega_{\mathrm{ext}})$ with compact support. For a given PML path $\hat{\xi}_\gamma$, a given thickness of the sponge layer ρ and with the notations above we seek $\mathbf{e}_\gamma^{(\rho)} \in H(\mathrm{curl}, \Omega \cup \Omega_{\mathrm{ext}}^{(\rho)})$ such that

$$\begin{aligned}\int_{\Omega \cup \Omega_{\mathrm{ext}}^{(\rho)}} \overline{d\varphi} \wedge \mu_\gamma^{-1} d\mathbf{e}_\gamma^{(\rho)} - \omega^2 \overline{\varphi} \wedge \varepsilon_\gamma \mathbf{e}_\gamma^{(\rho)} = \\ \sum_{j=1}^{N} \int_{\partial\Omega \cap \partial\Omega_{\mathrm{ext},j}} \overline{\varphi} \wedge \mu_\gamma^{-1} d\mathbf{e}_{\mathrm{ref},\gamma,j} + \\ \sum_{i=1}^{N} \sum_{j=i+1}^{N} \int_{\Gamma_{i,j}} \overline{\varphi} \wedge (\mu_\gamma^{-1} d\mathbf{e}_{\mathrm{ref},\gamma,j} - \mu_\gamma^{-1} d\mathbf{e}_{\mathrm{ref},\gamma,i}) + \\ \sum_{j=1}^{N} \int_{\Omega_{\mathrm{ext},j}^{(\rho)}} \Big(\overline{d\varphi} \wedge \mu_\gamma^{-1} d\mathcal{I}_j(\mathbf{e}_{\mathrm{ref},\gamma,1}, \ldots, \mathbf{e}_{\mathrm{ref},\gamma,j}) - \\ \omega^2 \overline{\varphi} \wedge \varepsilon_\gamma \mathcal{I}_j(\mathbf{e}_{\mathrm{ref},\gamma,1}, \ldots, \mathbf{e}_{\mathrm{ref},\gamma,j}) \Big)\end{aligned} \tag{5.6}$$

for all $\varphi \in H(\mathrm{curl}, \Omega \cup \Omega_{\mathrm{ext}}^{(\rho)})$.

Remarks 5.1

i) The variational equation (5.6) can be interpreted as Maxwell's equations in variational form with anisotropic material tensor and additional source terms on the interfaces of two adjacent sub–domains (first and second right hand side term) and within the exterior domain (last right hand side term). Therefore equation (5.6) allows for a discretization with finite elements in a standard way.

ii) The interpolation operators $\mathcal{I}_j$ are readily implemented in the finite element context. From the defining equation (5.4) one sees that on a common interface $\Gamma_{i,j}$ with $i < j$ the field values of the domain Ω_i are privileged. For an ansatz function which corresponds to a boundary node of the sub-domain Ω_j one simply interpolates the difference $\mathbf{e}_{\mathrm{ref},j} - \mathbf{e}_{\mathrm{ref},i}$, where i is the minimum index so that Ω_i shares the considered ansatz function.

iii) The additional right hand side terms have support in the entire truncated exterior domain $\Omega_{\mathrm{ext}}^{(\rho)}$. To keep the PML truncation error small it is therefore inevitable to assure an exponential decay of these additional source terms with the distance to the interior–exterior domain coupling boundary $\partial\Omega$. The additional right hand side terms are caused by the piecewise selection of the reference fields $\mathbf{e}_{\mathrm{ref},j}$. From the above variational equation (5.6) and with the definition of the interpolation operator $\mathcal{I}_j$ in equation (5.4) one observes that only the jumps $\mathbf{e}_{\mathrm{ref},j} - \mathbf{e}_{\mathrm{ref},i}$ across interfaces enter the right hand side terms. One must guarantee that the jump $\mathbf{e}_{\mathrm{ref},j} - \mathbf{e}_{\mathrm{ref},i}$ is an outgoing wave on the common interface $\Gamma_{i,j}$. If this is the case, a complex stretching yields exponentially damped right hand side terms in the PML. The actual decay rate of the additional terms depends on the present reference fields and the sub-domain decomposition. The prescribed incoming field $\mathbf{e}_{\mathrm{inc}}$ is canceled out in the difference $\mathbf{e}_{\mathrm{ref},j} - \mathbf{e}_{\mathrm{ref},i}$ in any case, because all reference fields share the same prescribed incoming wave $\mathbf{e}_{\mathrm{inc}}$. However, this is not sufficient to guarantee that $\mathbf{e}_{\mathrm{ref},j} - \mathbf{e}_{\mathrm{ref},i}$ is outgoing on $\Gamma_{i,j}$. To see this, we refer to the example at the end of the previous section. We assumed that the incoming field is a plane wave with wave vector $(k_x, 0, k_z)$. For a non-zero k_z the splitting in Figure 5.4 is suitable. But the splitting in Figure 5.5 gives rise to exponentially growing right hand side terms in the PML if $k_x \neq 0$. Indeed, on the upper part of the interface $\Gamma_{1,2}$ the jump $\Delta\mathbf{E}_{\mathrm{ref},1,2} = \mathbf{E}_{\mathrm{ref},2} - \mathbf{E}_{\mathrm{ref},1}$

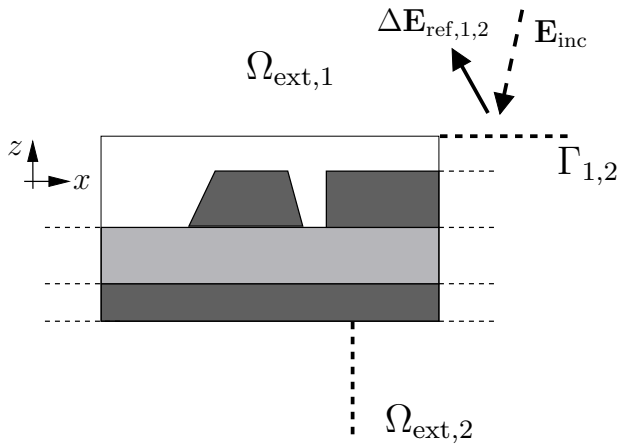

Figure 5.5: Inappropriate splitting. The complex continuation of the jump $\Delta\mathbf{E}_{\text{ref},1,2} = \mathbf{e}_{\text{ref},2} - \mathbf{e}_{\text{ref},1}$ grows exponentially with the distance to the computational domain.

is a plane wave with wave vector $(k_x, 0, -k_z)$. Hence, a PML based complex continuation in the x–coordinate, $x \to (1 + i\sigma)x$, results in a jump field which grows like $\exp(\sigma x)$ in the PML.

We have postponed to show the partition of unity property in equation (5.5),

$$\prod_{k'<i}(1-\chi_{k'}) + \sum_{k<i}\chi_k \prod_{k'<k}(1-\chi_{k'}) = 1,$$

which we now prove by induction of i. For $i = 0$, the equation is satisfied due to the convention that the product over an empty index set is equal to one. For the induction step $i \to i+1$, we split

$$\prod_{k'<i+1}(1-\chi_{k'}) + \sum_{k<i+1}\chi_k \prod_{k'<k}(1-\chi_{k'}) = (1-\chi_i)\prod_{k'<i}(1-\chi_{k'}) + \chi_i \prod_{k'<i}(1-\chi_{k'}) + \sum_{k<i}\chi_k \prod_{k'<k}(1-\chi_{k'})$$

Combining the first and the second terms yields the expression

$$\prod_{k'<i}(1-\chi_{k'}) + \sum_{k<i}\chi_k \prod_{k'<k}(1-\chi_{k'}),$$

which is equal to one due to induction hypothesis, so that (5.5) is shown for any $i \geq 0$.

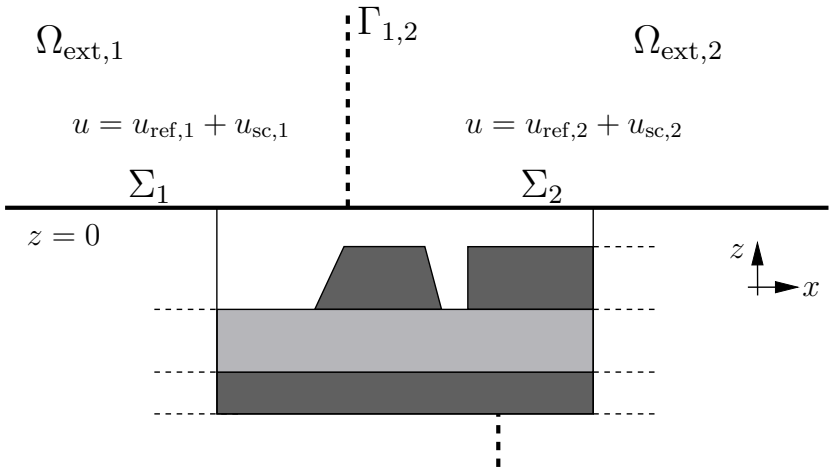

Figure 5.6: 2D setting for Fourier transform computation. We want to compute the Fourier transform of a scalar field u on the hyperplane $z = 0$. Since u is the total field the Fourier transform $u^\wedge(k_x, 0)$ is singular for $|k_x| \leq k_+$, where k_+ is the wave number in the upper half space.

5.3 Fourier transform with singular spectrum

We tackle now the vexed question on how to extract the angular spectrum representation (far field pattern) to the optical field $\mathbf{e}$ above a structure with a multiply structured exterior domain. We assume that the entire scatterer is contained in the lower half space $z < 0$. Hence for $z > 0$ the material parameters μ_+ and ε_+ are positive scalars. As usual we define the wave number in the upper half space by $k_+ = \omega\sqrt{\mu_+\epsilon_+}$. We have learned in Section 4.6 that the far field pattern is essentially the Fourier transform $\widehat{\mathbf{e}}(\mathbf{k}_\perp, 0)$ for $\|\mathbf{k}_\perp\| < k_+$ on the hyperplane $z = 0$. In real world applications the Fourier spectrum is further truncated by an aperture to $\|\mathbf{k}_\perp\| < \text{NA} \cdot k_+$, where $\text{NA} \leq 1$ is called numerical aperture.

We adopt the notation of the previous section. Additionally we set $\Sigma_j = \{\mathbf{x} \in \Omega_{\text{ext},j} \mid z = 0\}$. For the sake of a simpler notation we develop the essential ideas only for the scalar wave equation in two space dimensions and change the notation for the fields from $\mathbf{e}$ to u.

The situation we have in mind is sketched in Figure 5.6. There, the reference fields $u_{\text{ref},1}$ and $u_{\text{ref},2}$ are solutions to the 1D Helmholtz equation for a stack layout to an incoming plane wave

$$u_{\text{inc}}(x) = A_{\text{inc}} e^{i(k_{x,\text{inc}}x - k_z z)},$$

with $k_z = \sqrt{k_+^2 - k_{x,\text{inc}}^2}$. For $z > 0$ the reference solutions split into an down-

ward traveling wave (incoming) and a upward traveling wave (outgoing), that is

$$u_{\mathrm{ref},j}(x,z) = A_{\mathrm{inc}} e^{i(k_{x,\mathrm{inc}}x - k_z z)} + B_j e^{i(k_{x,\mathrm{inc}}x + k_z z)}.$$

The scattered fields $u_{\mathrm{sc},1}$ and $u_{\mathrm{sc},2}$ do not solve the Helmholtz equation in the upper half space. Indeed, they are discontinuous across the interface $\Gamma_{i,j}$. When regarded separately the Fourier spectrums of $u_{\mathrm{sc},1}$ and $u_{\mathrm{sc},2}$ do not carry any useful information on the optical field in the upper half space. We therefore consider the Fourier transform of the *outgoing* field $u_{\mathrm{out}}(x,z) = u(x,z) - u_{\mathrm{inc}}(x)$ on the hyperplane $z \geq 0$. The field u_{out} comprises the outgoing waves of the reference fields $u_{\mathrm{ref},j}$. Hence, the Fourier transform $\widehat{u}_{\mathrm{out}}(k_x, 0)$ is not a continuous, bounded function for $|k_x| \leq \mathrm{NA} \cdot k_+$ and requires therefore a careful treatment in the distributional sense.

By the definition of the Fourier transform we have

$$\begin{aligned} u_{\mathrm{out}}^{\wedge}(k_x, 0) &= \frac{1}{2\pi} \int_{-\infty}^{\infty} u_{\mathrm{out}}(x,0) e^{-ik_x x} \mathrm{d}x \\ &= \frac{1}{2\pi} \sum_{j=1}^{2} \int_{-\infty}^{\infty} \chi_{\Sigma_j}(x) u_{\mathrm{out}}(x,0) e^{-ik_x x} \mathrm{d}x. \end{aligned}$$

Our final goal is to compute the "image" field $u_{\mathrm{NA}}(x)$ given by the inverse Fourier transform of $u_{\mathrm{out}}^{\wedge}(k_x)$ limited to the band $|k_x| \leq \mathrm{NA} \cdot k_+$,

$$u_{\mathrm{NA}}(x) = (\chi_{[-\mathrm{NA}\cdot k_+, \mathrm{NA}\cdot k_+]}(k_x) \cdot u_{\mathrm{out}}^{\wedge}(k_x, 0))^{\vee}(x). \tag{5.7}$$

This formula describes intuitively what we aim to do. But a precise definition in the distributional sense is required. Since $u_{\mathrm{out}}^{\wedge}$ only exists as a tempered distribution the multiplication with the non–smooth characteristic function $\chi_{[-\mathrm{NA}\cdot k_+, \mathrm{NA}\cdot k_+]}$ is not trivially defined (cf. Rudin [94, Theorem 7.13]). To adopt to this, we replace the characteristic function χ_{Σ_j} by

$$\chi_{\Sigma_j,\epsilon}(x) = \begin{cases} 0, & x \notin \Sigma_j \\ e^{-\epsilon|x|}, & x \in \Sigma_j \end{cases}$$

for $\epsilon > 0$. Later we will discuss the limit $\epsilon \searrow 0$.

To gain a numerically feasible expression we insert

$$u_{\mathrm{out}}(x,0)|_{\Sigma_j} = u_{\mathrm{sc},j}(x,0) + u_{\mathrm{ref},j}(x,0) - u_{\mathrm{inc}}(x,0)$$

into the above integral over Σ_j. This yields

$$\begin{aligned}\frac{1}{2\pi}\int_{-\infty}^{\infty}\chi_{\Sigma_j,\epsilon}(x)u_{\text{out}}(x,0)e^{-ik_x x}\mathrm{d}x = \\ \frac{1}{2\pi}\int_{-\infty}^{\infty}\chi_{\Sigma_j,\epsilon}(x)u_{\text{sc},j}(x,0)e^{-ik_x x}\mathrm{d}x + \\ \frac{1}{2\pi}\int_{-\infty}^{\infty}\chi_{\Sigma_j,\epsilon}(x)(u_{\text{ref},j}(x,0)-u_{\text{inc}}(x,0))e^{-ik_x x}\mathrm{d}x.\end{aligned} \tag{5.8}$$

Both integrals on the right hand side are regular Fourier transforms which we denote by

$$\begin{aligned}u^{\wedge}_{\text{c},\epsilon}(k_x) =& \Big(\chi_{\Sigma_j,\epsilon}(x)u_{\text{sc},j}(x,0)\Big)^{\wedge}(k_x),\\ u^{\wedge}_{\text{s},\epsilon}(k_x) =& \Big(\chi_{\Sigma_j,\epsilon}(x)(u_{\text{ref},j}(x,0)-u_{\text{inc}}(x,0)\Big)^{\wedge}(k_x).\end{aligned}$$

In the following we will drop the sub-index "ϵ" for the case $\epsilon = 0$. The sub–indices "c" and "s" stand for *continuous* and *singular*, respectively, as we will explain soon.

We first consider $u^{\wedge}_{\text{c},\epsilon}$. We want to deal with the corresponding integral in the above equation (5.8) by the complex deformation technique we have developed in Section 4.6 of the previous chapter. To do so, we restrict k_x to the relevant spectrum $|k_x| \leq \text{NA}\cdot k_+$. We further need to make the assumption that there exist a $\kappa > \text{NA}\cdot k_+$ and a constant C such that

$$|u_{\gamma,j}(x,0)| \leq Ce^{-\kappa \text{Im}(\gamma)x}.$$

This is a requirement on the decay rate of the PML solution. Then, the Fourier integral $u^{\wedge}_{\text{c},\epsilon}$ can be replaced by an absolutely convergent integral which involves the PML solution $u_{\gamma,j}(x,0)$, cf. equation (4.20). The complex deformed integral has an exponentially fast convergence rate independently of ϵ. Hence, the Fourier transform $u^{\wedge}_{\text{c},\epsilon}(k_x)$ is continuous for $|k_x| < \kappa$. This allows to define the band limited Fourier transform as

$$u^{\wedge}_{\text{NA,c}}(k_x) = \chi_{[-\text{NA}\cdot k_+,\text{NA}\cdot k_+]}(k_x)u^{\wedge}_{\text{c}}(k_x).$$

Transforming back to the physical space by applying the inverse Fourier transform yields

$$u_{\text{NA,c}}(x) = (u^{\wedge}_{\text{NA,c}})^{\vee}(x). \tag{5.9}$$

We now turn to the second Fourier integral $u^{\wedge}_{\text{s},\epsilon}$. The corresponding integral in the above equation (5.8) (second term on the right hand side) involves

the reference field and is only defined in the distributional sense. We have that

$$u_{\mathrm{ref},j}(x,0) - u_{\mathrm{inc}}(x,0) = B_j e^{ik_{x,\mathrm{inc}}x}.$$

For the sake of a simpler notation we henceforth assume that $\Sigma_j = [0,\infty)$. This way, the considered integral is essentially the Fourier transform of the function $h(x)e^{i(k_{x,\mathrm{inc}}+i\epsilon)x}$, where $h(x)$ denotes the Heaviside step function. For $\epsilon = 0$ we have

$$\left(h(x)e^{ik_{x,\mathrm{inc}}x}\right)^{\wedge}(k_x) = \frac{1}{2}\delta(k_x - k_{x\cdot\mathrm{inc}}) - \frac{i}{2\pi}\mathrm{P.V.}\frac{1}{k_x - k_{x,\mathrm{inc}}},$$

see for example Benedetto [14]. Here, "P.V." denotes the Cauchy principal value.

But this is not our final result because it remains to discuss the restriction of the Fourier spectrum to the band $|k_x| \leq \mathrm{NA}\cdot k_+$. It is tempting to define the band–limited Fourier transform as

$$u^{\wedge}_{\mathrm{NA,s}}(k_x) = \chi_{[-\mathrm{NA}\cdot k_+,\mathrm{NA}\cdot k_+]}(k_x)u^{\wedge}_{\mathrm{s}}(k_x).$$

However, the multiplication of the tempered distribution $u^{\wedge}_{\mathrm{s}}$ with the non–smooth characteristic function $\chi_{[-\mathrm{NA}\cdot k_+,\mathrm{NA}\cdot k_+]}$ is not properly defined, as we already mentioned above. To understand the implications in greater detail we retreat to $\epsilon > 0$. We compute

$$\begin{aligned} u^{\wedge}_{\mathrm{s},\epsilon}(k_x) =& \frac{1}{2\pi}\int_0^{\infty} B_j e^{ik_x(\mathrm{inc})x}e^{-\epsilon x}e^{-ik_x x}\mathrm{d}x \\ =& \frac{1}{2\pi}\frac{B_j}{i(k_x - k_x^{(\mathrm{inc})} - i\epsilon)}. \end{aligned}$$

Now, we are allowed to form the product

$$u^{\wedge}_{\mathrm{NA,s},\epsilon} = \chi_{[-\mathrm{NA}\cdot k_+,\mathrm{NA}\cdot k_+]}u^{\wedge}_{\mathrm{s},\epsilon}.$$

We do not discuss the convergence of $u^{\wedge}_{\mathrm{NA,s},\epsilon}$ for $\epsilon \searrow 0$ in the weak*–topology of tempered distributions. Instead, we apply the inverse Fourier transform on $u^{\wedge}_{\mathrm{NA,s},\epsilon}$ and discuss the convergence

$$\lim_{\epsilon\searrow 0}(u^{\wedge}_{\mathrm{NA,s},\epsilon})^{\vee}(x) = u_{\mathrm{NA,s}}(x) \tag{5.10}$$

in the physical space. To give a motivation we recall that the "image"–field

$$u_{\mathrm{NA}}(x) = u_{\mathrm{NA,s}}(x) + u_{\mathrm{NA,c}}(x)$$

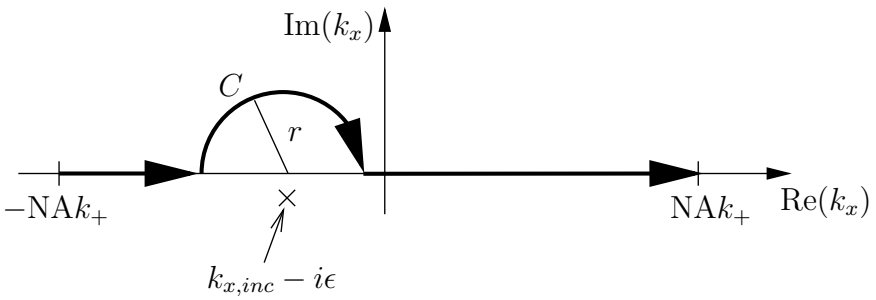

Figure 5.7: Contour integrals in the complex k_x–plane for the evaluation of the inverse Fourier transform.

is the relevant output of a scattering experiment.

To study the convergence in equation (5.10) we use classical arguments from function theory, see for example Young [115]. We have that

$$(u^{\wedge}_{\mathrm{NA,s},\epsilon})^{\vee}(x) = \frac{-iB_j}{2\pi} \int_{-\mathrm{NA}\cdot k_+}^{\mathrm{NA}\cdot k_+} \frac{1}{k_x - k_{x,\mathrm{inc}} - i\epsilon} e^{ik_x x} \mathrm{d}k_x$$

We start with the case $|k_x^{(\mathrm{inc})}| < \mathrm{NA}\cdot k_+$. Applying Cauchy's integral theorem with contours in the complex k_x–plane as depicted Figure 5.7 yields

$$\begin{aligned}(u^{\wedge}_{\mathrm{NA,s},\epsilon})^{\vee}(x) = &\frac{-iB_j}{2\pi} \int_C \frac{1}{s - k_{x,\mathrm{inc}} - i\epsilon} e^{isx} \mathrm{d}s + \\ &\frac{-iB_j}{2\pi} \Bigg(\int_{-\mathrm{NA}\cdot k_+}^{k_{x,\mathrm{inc}}-r} \frac{1}{k_x - k_{x,\mathrm{inc}} - i\epsilon} e^{ik_x x} \mathrm{d}k_x + \\ &\int_{k_{x,\mathrm{inc}}+r}^{\mathrm{NA}\cdot k_+} \frac{1}{k_x - k_{x,\mathrm{inc}} - i\epsilon} e^{ik_x x} \mathrm{d}k_x \Bigg).\end{aligned} \tag{5.11}$$

For a fixed $r > 0$ we are allowed to perform the limit process $\epsilon \searrow 0$. Setting $\epsilon = 0$, the first integral over the semicircle C is equal to $B_j/2 \exp(ik_x x)$ independently of r. The second and third integral diverge as $r \searrow 0$, but the sum of both remains finite. In this context, the Cauchy principal value is defined as the sum two integrals. For $|k_x^{(\mathrm{inc})}| < \mathrm{NA}\cdot k_+$ we have shown that

$$\begin{aligned}u_{\mathrm{NA,s}}(x) = &\frac{B_j}{2} e^{ik_x x} + \frac{-iB_j}{2\pi} \lim_{r \searrow 0} \Big(\int_{-\mathrm{NA}\cdot k_+}^{k_{x,\mathrm{inc}}-r} \frac{1}{k_x - k_{x,\mathrm{inc}}} e^{ik_x x} \mathrm{d}k_x + \\ &\int_{k_{x,\mathrm{inc}}+r}^{\mathrm{NA}\cdot k_+} \frac{1}{k_x - k_{x,\mathrm{inc}}} e^{ik_x x} \mathrm{d}k_x \Big).\end{aligned} \tag{5.12}$$

For the case $|k_x^{(\mathrm{inc})}| > \mathrm{NA} \cdot k_+$ the limit process $\epsilon \searrow 0$ is trivial. We have

$$u_{\mathrm{NA,s}}(x) = \frac{-iB_j}{2\pi} \int_{-\mathrm{NA}\cdot k_+}^{\mathrm{NA}\cdot k_+} \frac{1}{k_x - k_{x,\mathrm{inc}}} e^{ik_x x} \mathrm{d}k_x. \tag{5.13}$$

Both formulas (5.12) and (5.13) undesirably diverge for $(\mathrm{NA} \cdot k_+) \nearrow |k_{x,\mathrm{inc}}|$. This mirrors the mathematical difficulties we had to define the product of a distribution with a non–smooth function.

However, equations (5.12) and (5.13) are useful when $|k_{x,\mathrm{inc}} \pm \mathrm{NA} \cdot k_+|$ is sufficiently large. What *sufficiently large* means depends on the type of the application. To explain this, we need to make some deeper considerations on the physical background of scattering problems. Especially, we will take into account that one deals with two length scales in a scattering problem. The scatterer has a microscopic length scale with feature sizes in the dimension of the wavelength. On the other hand, the scatterer and the aperture are millions of wavelengths apart. So, the aperture (or the optical system in general) has a macroscopic length scale.

The misbehavior of equations (5.12) and (5.13) for $k_{x,\mathrm{inc}}$ near $\pm\mathrm{NA} \cdot k_+$ is not a flaw of our analysis but reflects the breakdown of our idealized scattering modeling. We used a monochromatic plane wave $A_{\mathrm{inc}} e^{i(k_{x,\mathrm{inc}} x - k_z z)}$ as the incoming field. But from a physical point of view this is not a reasonable model in a macroscopic sense, e.g., the energy transported by an ideal plane wave is infinite. A realistic incoming wave like a laser beam is a superposition (Fourier integral) of plane waves. This way the scalar A_{inc} is replaced by a function $a_{\mathrm{inc}}(k_x)$ centered near $k_{x,\mathrm{inc}}$. Accordingly, the scalar B_j is transfered to a function $b_j(k_x)$ and we need to integrate the expressions in equations (5.12) and (5.13) over $k_{x,\mathrm{inc}}$. With this *smoothing* our mathematically difficulties with the divergent integrals disappear.

The applicability of this smoothing approach depends on the physical situation. Firstly, the precise form of the function $b_j(k_{x,\mathrm{inc}})$ is often unknown due to thermal fluctuation, *etc.* Then we need further arguments from statistics. For this topic we refer to the comprehensive book by Mandel and Wolf [72] which also covers statistical fluctuations in the angular frequency ω.

Secondly, for imaging systems as used in micro-lithography applications the function $b_j(k_x)$ is extremely concentrated near $k_{x,\mathrm{inc}}$. Also here, the precise form of the function $b_j(k_x)$ is unknown, but let us assume that we can write

$b_j(k_x) = B_j\psi(k_x)$ with

$$\int_{|k_{x,\mathrm{inc}}-k_x|\leq\Delta} \psi(k_x)\mathrm{d}k_x = 1,$$
$$\int_{|k_{x,\mathrm{inc}}-k_x|>\Delta} \psi(k_x)\mathrm{d}k_x \ll 1,$$

with $\Delta \ll k_+$. For $\Delta \searrow 0$ the function ψ converges to the δ-distribution at $k_{x,\mathrm{inc}}$. This way we regain our idealized model with a plane wave as the incoming field. For a small but finite value of Δ, the incoming field still looks like a beam from the macroscopic point of view. But near the scatterer the incoming field looks like a plane wave over a distance of a huge number of wavelengths.

It is still in front of us to explain what happens when $k_{x,\mathrm{inc}}$ is close to $\mathrm{NA}\cdot k_+$. Conversely, one verifies that for $|k_{x,\mathrm{inc}} \pm \mathrm{NA}\cdot k_+| > \Delta$, the precise shape of the function $\psi(k_x)$ does not matter in the equations (5.12) and (5.13) because $\Delta \ll k_+$, and we can perform the limit process $\Delta \searrow 0$. But this is not the case when $|k_{x,\mathrm{inc}} \pm \mathrm{NA}\cdot k_+| < \Delta$. Then, the precise form of the function $\psi(k_x)$ matters. Since $\psi(k_x)$ is typically unknown, statistics comes into play at this point again. In brief, the critical scenario, $|k_{x,\mathrm{inc}} \pm \mathrm{NA}\cdot k_+| < \Delta$, cannot be treated without taking the incoherence of the light source into account. But this is out of the scope of this thesis and we again refer to Mandel and Wolf [72].

5.4 Numerical examples

Before we start with the discussion of the numerical examples we comment on the computation of the inverse Fourier transform with a spectrum defined in the distributional sense only. In the discussion of the singular Fourier spectrum in Section 5.3 we first mollified the Fourier transform by introducing a small perturbation ϵ and discussed the limit $\epsilon \searrow 0$ afterward. A possible way for a numerical evaluation is to use a finite but small value for ϵ. Doing so, it is necessary to cautiously monitor arising round–off errors.

When the Fourier transform is defined as a Cauchy principal value, more accurate and stable approaches are available. In our implementation we followed Noble [86] and used an *even*–order Gauss–Legendre formula for the principal value integral evaluation. To improve the efficiency of the numerical integration the usage of an adaptive integration method is advisable, see Deuflhard and Hohmann [38].

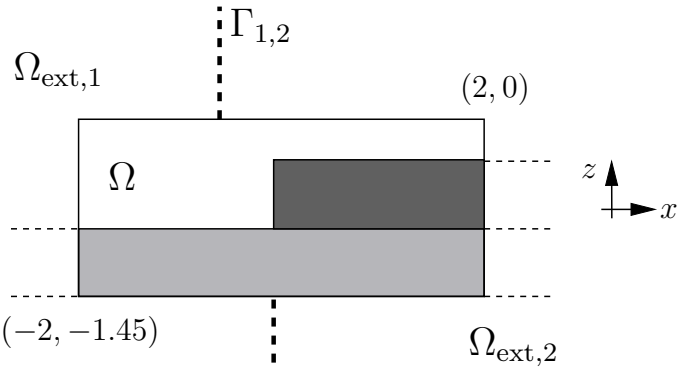

Figure 5.8: Plane wave diffraction by a semitransparent half-plane. The lower domain is a glass substrate with $\epsilon_g = 2.34273636$. The upper domain consists of air. A semi-transparent screen with height $h = 0.65$ and $\epsilon_{\text{s}} = -0.923115 + 5.204948i$ is placed on top of the glass substrate in the right infinite half-space.

5.4.1 Diffraction of a plane wave by a semitransparent half–plane

With this simple example we want to verify our scattering problem approach for multiply structured exterior domain. Moreover, we will validate the Fourier transform computation in the presence of a non-trivial distributional spectrum.

Figure 5.8 gives the geometry of this example. The structure is illuminated from below by a y–polarized plane wave with vacuum wavelength $\lambda_0 = 1.26$ propagating in the direction $(\sin(\alpha), 0, \cos(\alpha))^{\text{T}}$. The actual value of the incident angle α is given below.

The exterior domain was split into two compartments $\Omega_{\text{ext},1}$ and $\Omega_{\text{ext},1}$ as shown in Figure 5.8 in the simulation. The structure consists of two differently layered media. The reference fields $\mathbf{e}_{\text{ref},1}$ and $\mathbf{e}_{\text{ref},2}$ are the solutions to Maxwell's equations in the left hand side and right hand side layered media, respectively.

In the upper half space, the reference fields $\mathbf{e}_{\text{ref},1}$ and $\mathbf{e}_{\text{ref},2}$ are plane waves with different amplitudes but with the same propagation direction $(\sin(\beta), 0, \cos(\beta))^{\text{T}}$. The incident angle α was chosen so that $\beta = 30\,^\circ$.

We compared the solution $\mathbf{e}_{\text{mult}}$ obtained with our new approach to $\mathbf{e}_{\text{per},L}$ and $\mathbf{e}_{\text{tr},L}$, where $\mathbf{e}_{\text{per},L}$ was computed on an enlarged computational domain with range $[-L, L]$ in x and with periodic boundary conditions in x–direction. For the computation of $\mathbf{e}_{\text{tr},L}$ we also increased the computational domain ac-

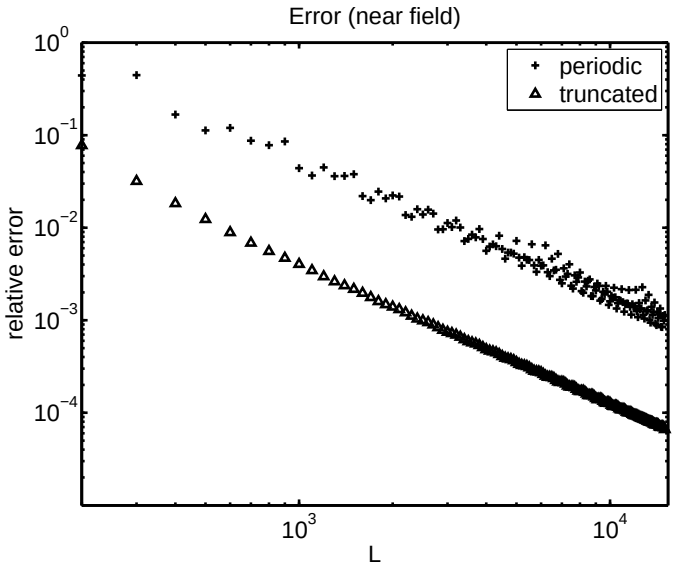

Figure 5.9: Plane wave diffraction by a semitransparent half-plane: Convergence of $\mathbf{e}_{\mathrm{per},L}$ and $\mathbf{e}_{\mathrm{tr},L}$ towards $\mathbf{e}_{\mathrm{mult}}$. The solution $\mathbf{e}_{\mathrm{mult}}$ was obtained on a small computational domain with our new method. For the computation of $\mathbf{e}_{\mathrm{per},L}$ and $\mathbf{e}_{\mathrm{tr},L}$ we increased the computational domain to the range $[-L, L]$ in x. For $\mathbf{e}_{\mathrm{per},L}$ periodic boundary conditions in x were used, whereas for $\mathbf{e}_{\mathrm{tr},L}$ semi-transparent layer was truncated to fit into the enlarged computational domain.

cordingly, but truncated the semi-transparent top layer to the computational domain and used transparent boundary conditions in x–direction. From physical insight one expects that $\mathbf{e}_{\mathrm{per},L}$, $\mathbf{e}_{\mathrm{tr},L}$ converges to $\mathbf{e}_{\mathrm{mult}}$ within Ω with a growing computational domain size L. Actually, scattering off a multiply structured exterior domain is traditionally simulated by using a large value L. Figure 5.9 approves the convergences

$$\lim_{L\to\infty} \mathbf{e}_{\mathrm{per},L} = \mathbf{e}_{\mathrm{mult}}$$
$$\lim_{L\to\infty} \mathbf{e}_{\mathrm{tr},L} = \mathbf{e}_{\mathrm{mult}}.$$

The relative differences $\mathbf{e}_{\mathrm{per},L} - \mathbf{e}_{\mathrm{mult}}$ and $\mathbf{e}_{\mathrm{tr},L} - \mathbf{e}_{\mathrm{mult}}$ on top of Ω are plotted in the L^2–norm. We observe a clear but very slow convergence of $\mathbf{e}_{\mathrm{per},L}$, $\mathbf{e}_{\mathrm{tr},L}$ to $\mathbf{e}_{\mathrm{mult}}$. This justifies our new approach and shows the tremendous performance gain compared to the traditional approach.

We now turn to the Fourier transform evaluation. The practically relevant

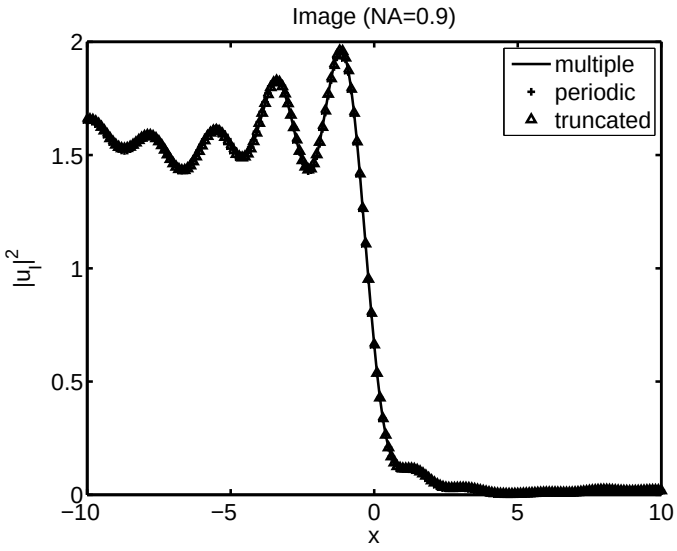

Figure 5.10: Plane wave diffraction by a semitransparent half-plane: Computed image fields for a numerical aperture NA = 0.9.

field is the image

$$\mathbf{e}_{\mathrm{NA}}(x) = (\chi_{[-\mathrm{NA}\cdot k_0,\mathrm{NA}\cdot k_0]}(k_x)(\mathbf{e}_{\mathrm{mult}}(x,0))^\wedge(k_x))^\vee,$$

where $k_0 = 2\pi/\lambda_0$ is the wavenumber in the air–filled, upper domain. This image is formed by a perfect $1:1$ projection system with numerical aperture NA. We will again compare $\mathbf{e}_{\mathrm{NA}}(x)$ to the images formed by the periodified problem and the truncated problem,

$$\begin{aligned}\mathbf{e}_{\mathrm{NA,per},L}(x) =&(\chi_{[-\mathrm{NA}\cdot k_0,\mathrm{NA}\cdot k_0]}(k_x)(\mathbf{e}_{\mathrm{per},L}(x,0))^\wedge(k_x))^\vee,\\ \mathbf{e}_{\mathrm{NA,tr},L}(x) =&(\chi_{[-\mathrm{NA}\cdot k_0,\mathrm{NA}\cdot k_0]}(k_x)(\mathbf{e}_{\mathrm{tr},L}(x,0))^\wedge(k_x))^\vee.\end{aligned}$$

We learned in Section 5.3 of this chapter that the image formation is ill-conditioned when the numerical aperture coincides with $\sin(\beta) = 0.5$.

Figure 5.10 gives the image fields for NA = 0.9, where $\mathbf{e}_{\mathrm{NA}}$ is compared to $\mathbf{e}_{\mathrm{NA,per},L}$ and $\mathbf{e}_{\mathrm{NA,tr},L}$ with $L = 5200\lambda_0$. All three fields are in a good agreement. More quantitatively, Figure 5.11 shows the convergences of $\mathbf{e}_{\mathrm{NA,per},L}$ and $\mathbf{e}_{\mathrm{NA,tr},L}$ to $\mathbf{e}_{\mathrm{NA}}$ with growing computational domain size L.

We repeated the image formation for a smaller numerical aperture NA = 0.45. In this case, we observe much larger differences between $\mathbf{e}_{\mathrm{NA}}$ and $\mathbf{e}_{\mathrm{NA,per},L}$ or $\mathbf{e}_{\mathrm{NA,tr},L}$, cf. Figure 5.12. Even for a 4000 times enlarged computational domain for the artificially periodified problem significant derivations are present. Nevertheless, Figure 5.13 affirms the convergences of $\mathbf{e}_{\mathrm{NA,per},L}$ and $\mathbf{e}_{\mathrm{NA,tr},L}$ to $\mathbf{e}_{\mathrm{NA}}$ with a growing computational domain size L.

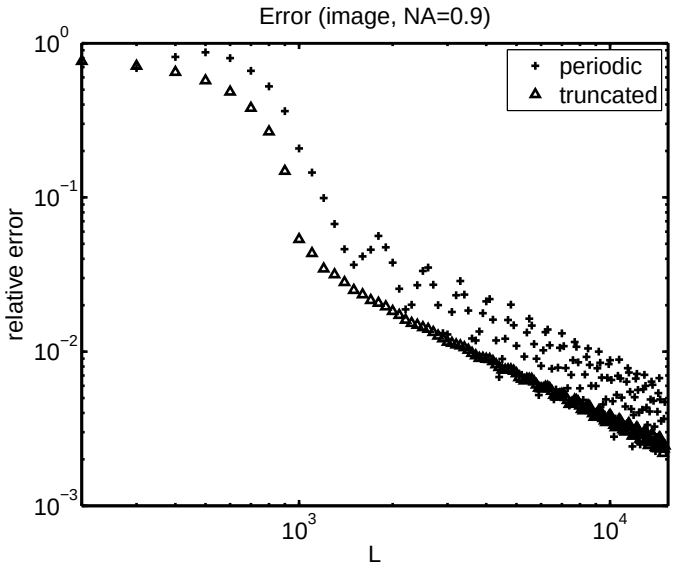

Figure 5.11: Plane wave diffraction by a semitransparent half-plane: Convergence of $\mathbf{e}_{\mathrm{NA,per},L}$ and $\mathbf{e}_{\mathrm{NA,tr},L}$ to $\mathbf{e}_{\mathrm{NA}}$ with growing computational domain size L. (NA $= 0.9$)

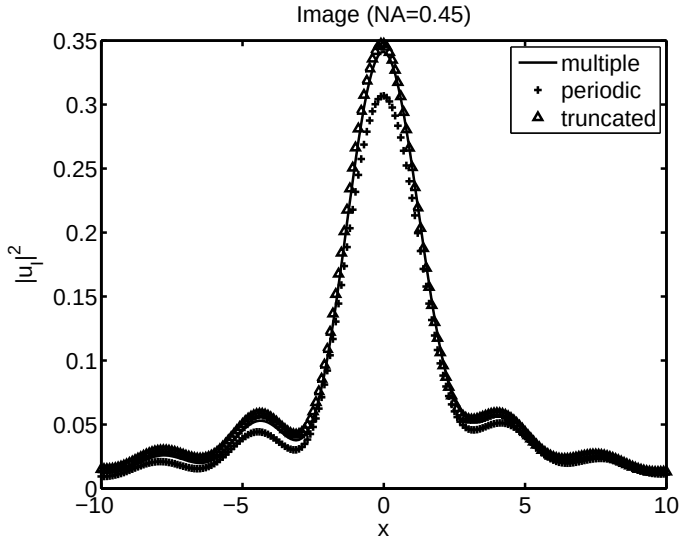

Figure 5.12: Plane wave diffraction by a semitransparent half-plane: Computed image fields for a numerical aperture NA $= 0.45$.

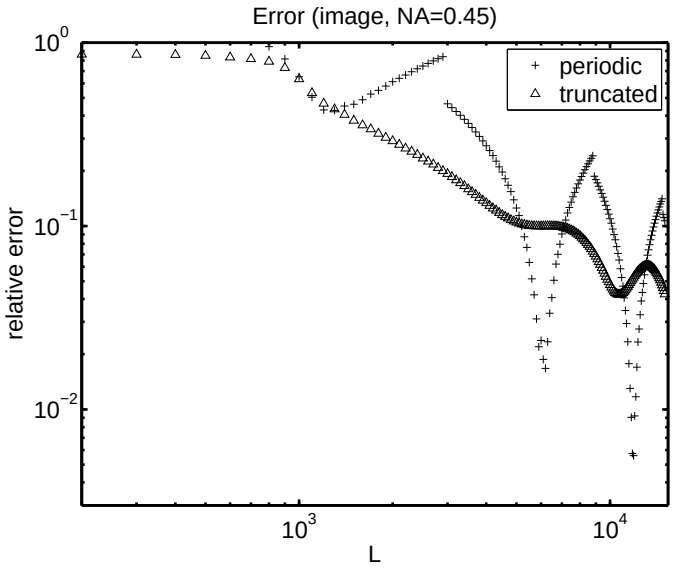

Figure 5.13: Plane wave diffraction by a semitransparent half-plane: Convergence of $\mathbf{e}_{\mathrm{NA,per},L}$ and $\mathbf{e}_{\mathrm{NA,tr},L}$ to $\mathbf{e}_{\mathrm{NA}}$ with growing computational domain size L. ($\mathrm{NA} = 0.45$)

5.4.2 Oblique line crossing

This 2D example is a test for the PML method applied to a scattering problem with a fairly complicated, multiply structured exterior domain. The geometry parameters are given in Figure 5.14 which is a true–to–scale plot. The incoming field is a y–polarized plane wave with vacuum wavelength $\lambda = 1.93$ and normalized amplitude which travels in the $(-1/\sqrt{2}, 0, 1/\sqrt{2})^{\mathrm{T}}$–direction.

The exterior domain is split into three compartments as shown in Figure 5.14. The reference fields $\mathbf{e}_{\mathrm{ref},1}$, $\mathbf{e}_{\mathrm{ref},2}$ in $\Omega_{\mathrm{ext},1}$ and $\Omega_{\mathrm{ext},2}$, respectively, are constructed in a straightforward way: In both cases, we extend the half infinite structures so that layered media are formed, cf. Figure 5.15. As reference fields $\mathbf{e}_{\mathrm{ref},1}$, $\mathbf{e}_{\mathrm{ref},2}$ we use the exact solutions for a field propagation in layered media with prescribed incoming plane wave $\mathbf{e}_{\mathrm{inc}}$. The difference field $\mathbf{e}_{\mathrm{ref},1} - \mathbf{e}_{\mathrm{ref},2}$ is outward radiating on the interface $\Gamma_{1,2}$, so that the right hand side terms stemming from the matching condition on $\Gamma_{1,2}$ are exponentially damped when applying a complex continuation.

The construction of the reference field $\mathbf{e}_{\mathrm{ref},3}$ is more involved. The trivial choice $\mathbf{e}_{\mathrm{ref},3} = \mathbf{e}_{\mathrm{inc}}$ gives rise to coupling terms on $\Gamma_{1,3}$ and $\Gamma_{2,3}$ which *grow*

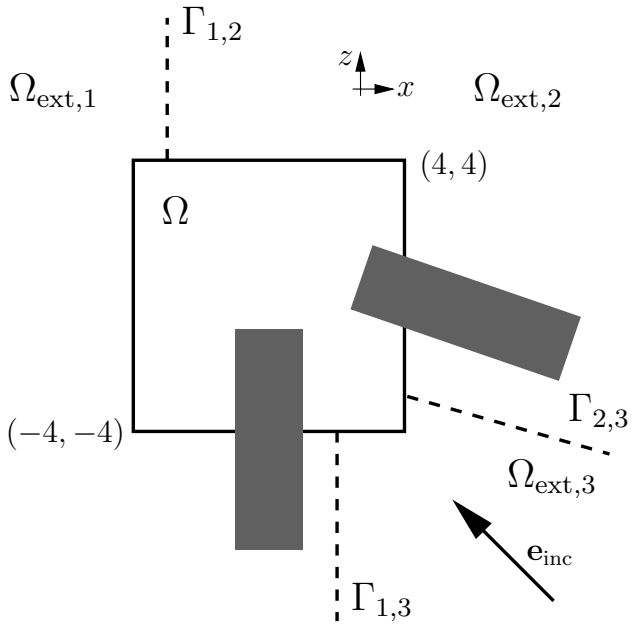

Figure 5.14: Oblique line crossing: The structures painted in dark gray are semitransparent with permittivity $\epsilon_l = 5.995184 + 3.00384i$ and are infinitely extended within the exterior domain. The background consists of air.

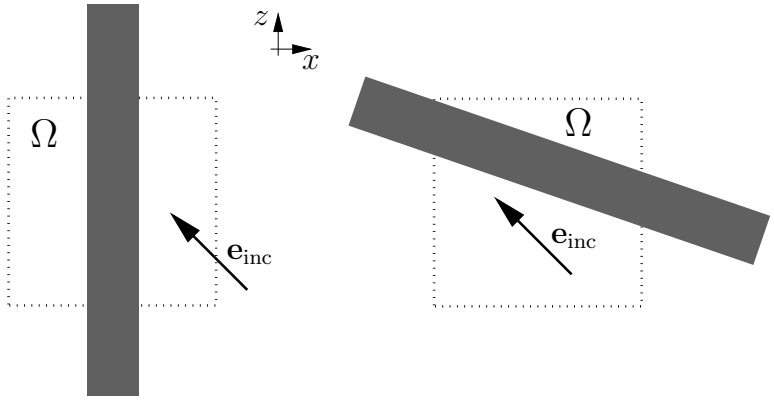

Figure 5.15: Oblique line crossing: Construction of reference fields $\mathbf{e}_{\text{ref},1}$ (right plot) and $\mathbf{e}_{\text{ref},2}$ (left plot). In both cases, the reference field is a solution to Maxwell's equations in layered media with prescribed incoming plane wave $\mathbf{e}_{\text{inc}}$.

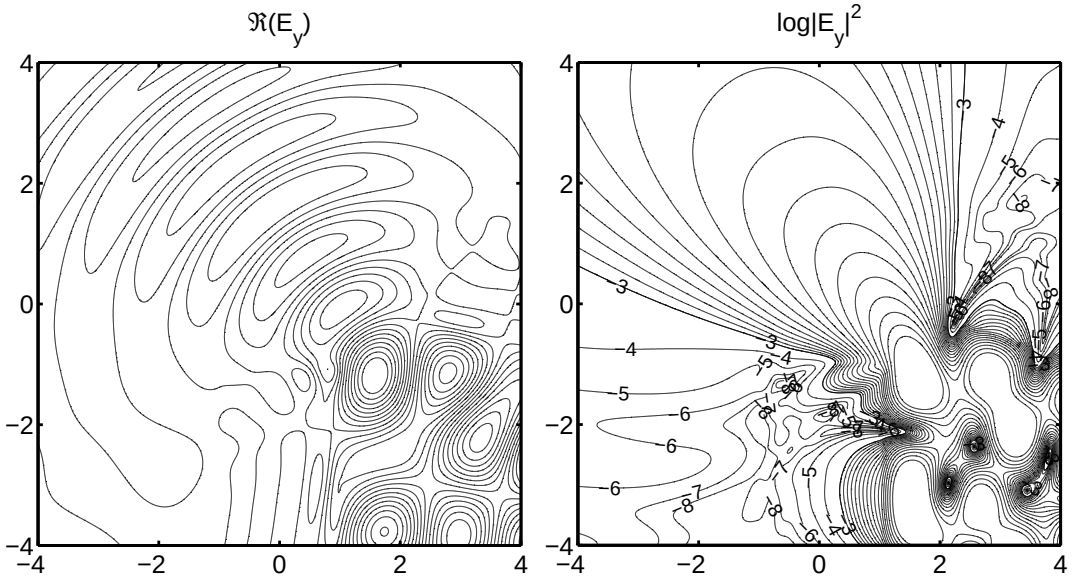

Figure 5.16: Oblique line crossing: Isoline plots of the computed field E_y. The figure on the left shows the real part. In the right figure the intensity $\log(|E_y|^2)$ is plotted.

exponentially when the PML method is applied. To circumvent this we use

$$\begin{aligned}\mathbf{e}_{\mathrm{ref},3} &= \mathbf{e}_{\mathrm{inc}} + (\mathbf{e}_{\mathrm{ref},1} - \mathbf{e}_{\mathrm{inc}}) + (\mathbf{e}_{\mathrm{ref},2} - \mathbf{e}_{\mathrm{inc}}) \\ &= \mathbf{e}_{\mathrm{ref},1} + \mathbf{e}_{\mathrm{ref},2} - \mathbf{e}_{\mathrm{inc}}.\end{aligned}$$

Surely, $\mathbf{e}_{\mathrm{ref},3}$ is a solution to Maxwell's equations in $\Omega_{\mathrm{ext},3}$. Moreover, since $(\mathbf{e}_{\mathrm{ref},1} - \mathbf{e}_{\mathrm{inc}})$ and $(\mathbf{e}_{\mathrm{ref},2} - \mathbf{e}_{\mathrm{inc}})$ are outward radiating in $\Omega_{\mathrm{ext},3}$, we infer that the incoming part of $\mathbf{e}_{\mathrm{ref},3}$ is equal to $\mathbf{e}_{\mathrm{inc}}$ as desired. The field jump on $\Gamma_{1,3}$ is given by

$$\mathbf{e}_{\mathrm{ref},3} - \mathbf{e}_{\mathrm{ref},1} = \mathbf{e}_{\mathrm{ref},2} - \mathbf{e}_{\mathrm{inc}},$$

which is the outgoing part of $\mathbf{e}_{\mathrm{ref},2}$. Hence, the coupling terms on $\Gamma_{1,3}$ are also exponentially damped under a complex continuation. The damping property of $\mathbf{e}_{\mathrm{ref},3} - \mathbf{e}_{\mathrm{ref},2}$ on $\Gamma_{2,3}$ is shown just as well. Hence, the PML formulation as posed in Problem 5.1 applies.

The computed field is shown in Figure 5.16. The left plot shows the real part of the total field E_y within the computational domain. The intensity $|E_y|^2$ is given in the logarithmic plot on the right, where we labeled some isolines corresponding to small intensities.

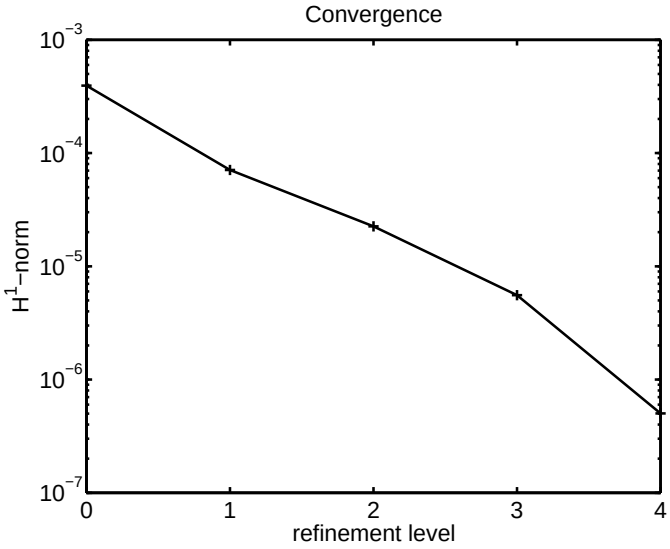

Figure 5.17: Oblique line crossing: Convergence of the computed field within the computational domain for successive finite element mesh refinements.

In our simulation we used the adaptive PML method as described in Chapter 3. The actual damping rate of the PML method depends on the coupling terms arising on the interfaces $\Gamma_{1,2}$, $\Gamma_{1,3}$ and $\Gamma_{2,3}$. Hence, a proper and automatic adaption of the PML thickness is indeed required for an optimal choice of the PML discretization parameters. In Figure 5.16 we observe no disturbances near the coupling interfaces $\Gamma_{1,2}$, $\Gamma_{1,3}$ and $\Gamma_{2,3}$.

Figure 5.17 shows the finite element convergence. We used second order finite elements and refined the mesh uniformly. In Figure 5.17, we observe an excellent agreement with the theoretical convergence behavior of finite elements. We remark that the PML discretization was automatically adapted during the refinement process, so that this example demonstrates the accuracy of our adaptive PML method again.

For a further validation we increased the computational domain to $\Omega_L = [-4, L] \times \{0\} \times [-L, 4]$ and truncated the infinite lines to fit into Ω_L. For this setting, the exterior domain is homogeneous and the standard PML method applies for the computation of the scattering of the prescribed incoming plane wave $\mathbf{e}_{\text{inc}}$ by the truncated structures. This yields the fields $\mathbf{e}_{\text{tr},L}$. From physical insight we expect that

$$\lim_{L\to\infty} \mathbf{e}_{\text{tr},L} = \mathbf{e}_{\text{mult}},$$

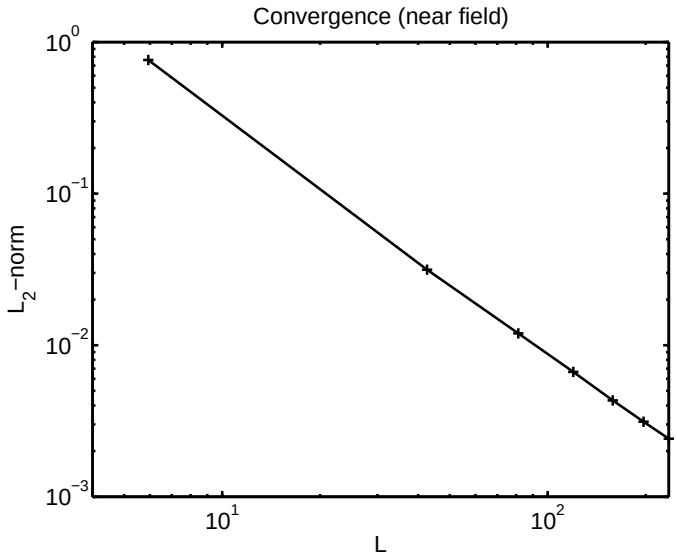

Figure 5.18: Oblique line crossing: Convergence of $\mathbf{e}_{\mathrm{tr},L}$ towards $\mathbf{e}_{\mathrm{mult}}$. The solution $\mathbf{e}_{\mathrm{mult}}$ was computed on the computational domain Ω in Figure 5.15 applying our new method. For the computation of $\mathbf{e}_{\mathrm{tr},L}$ we increased the computational domain diameter with the parameter L and truncated the infinite structures to fit into the enlarged computational domain.

where $\mathbf{e}_{\mathrm{mult}}$ is the solution obtained with our new PML method for multiply structured exterior domains. This is indeed approved in Figure 5.18 which shows the truncation error

$$\|\mathbf{e}_{\mathrm{tr},L} - \mathbf{e}_{\mathrm{mult}}\|_{L^2(\Omega)}.$$

For the computation of $\mathbf{e}_{\mathrm{tr},L}$ we used fourth order finite elements and refined the mesh sufficiently, so that the finite element approximation error was suppressed.

As in the previous example, we observe a clear but very slow convergence of $\mathbf{e}_{\mathrm{tr},L}$ to $\mathbf{e}_{\mathrm{mult}}$. This justifies our new approach for the numerical treatment of scattering problems with multiply structured exterior domains again. The performance gain in this example is tremendous. Without the new method we are forced to increase the diameter of the computational domain by a factor larger than 20 to reach a relative accuracy of 10^{-2}.

5.4.3 Plane wave scattering off glass cone

The geometry of this 3D example is shown in Figure 5.19. The geometry

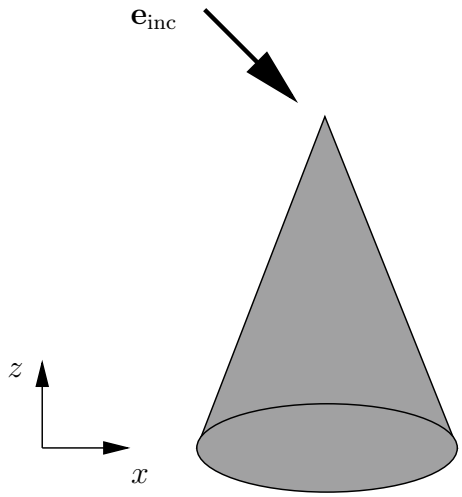

Figure 5.19: Infinite glass cone. The apex angle of the glass cone is equal to 40°. The glass has a refractive index $n_{\text{g}} = \sqrt{2.113}$. The surroundings consist of air. The cone is illuminated by a plane wave from above with incidence angle equal to 45°.

exhibits a rotational symmetry. After transforming the problem to cylinder coordinates (r, ϕ, z), it is possible to separate this type of 3D scattering problem into discrete Fourier modes with respect to the ϕ coordinate, cf. Section 2.5. The solution expands into a sum

$$\mathbf{e}(r, \phi, z) \quad = \quad \sum_{n=-\infty}^{\infty} \mathbf{e}_n(r, z) e^{in\phi}.$$

Each of the fields $\mathbf{e}_n(r, z)$ satisfies a Maxwell scattering problem on a two dimensional cross section domain sketched in Figure 5.20. In classical notation, we have

$$\begin{pmatrix} \partial_r \\ in \\ \partial_z \end{pmatrix} \times \mu^{-1}(r) \begin{pmatrix} \partial_r \\ in \\ \partial_z \end{pmatrix} \times \begin{pmatrix} E_r \\ E_\phi \\ E_z \end{pmatrix} - \omega^2 \varepsilon(x) \begin{pmatrix} E_r \\ E_\phi \\ E_z \end{pmatrix} = 0,$$

which is precisely of the same form as the 2D Maxwell's equations (2.8), but with transformed tensors

$$\varepsilon(r) = \varepsilon \text{diag}([\ r, \quad 1/r, \quad r\ ]), \quad \mu(r) = \mu \text{diag}([\ r, \quad 1/r, \quad r\ ]).$$

To fix the incoming field $\mathbf{e}_{n,\text{inc}}(r, z)$ for the nth cross section problem we utilize the Jacobi-Anger formula to decompose the incoming plane wave into Fourier

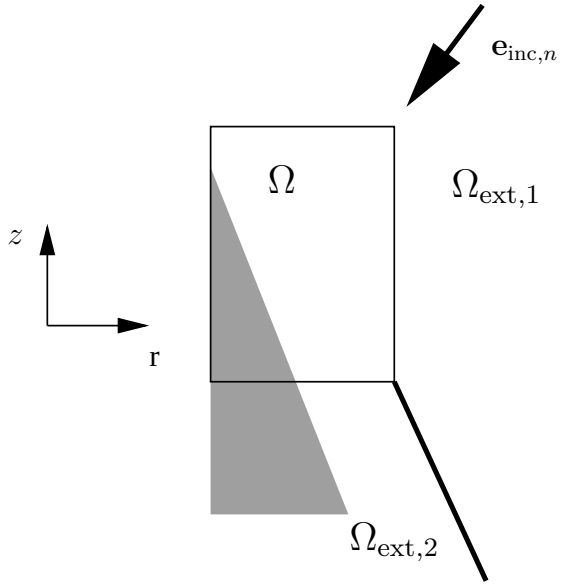

Figure 5.20: Infinite glass cone: cross section computational domain.

modes, see Colton and Kress [32, p. 32]. Since the series $\|\mathbf{e}_{n,\mathrm{inc}}(r,z)\|$ decays quickly with n, it is possible to truncate the above Fourier mode expansion in a numerical simulation.

Figure 5.20 also shows the used splitting of the multiply structured exterior domain. The incoming light is a solution to Maxwell's equations in the sub-domain $\Omega_{\mathrm{ext},1}$ only. Within $\Omega_{\mathrm{ext},2}$ the incoming field is set equal to zero. One verifies that the arising coupling terms on the interface $\Gamma_{1,2}$ decay exponentially with the distance to the computational domain.

Carrying out numerical experiments as in the previous example – checking convergence with the finite element refinement level, comparing with scattering off a truncated but large cone – one again validates the accuracy of the method. Since the convergence plots resemble those of the previous example too much, they are not presented here. Instead, it is time to give an illustrative false color plot of the field amplitude $|\mathbf{e}(x,y,z)|$. We refer to the title page of this thesis.

Zusammenfassung

In dieser Arbeit wurden numerische Konzepte zur Berechnung der Lichtausbreitung in kompliziert strukturierten optischen Bauteilen weiter- und neuentwickelt. Neben der Berechnung des Nahfeldes, das heißt der Berechnung der Lichtverteilung in einem kleinen Ausschnitt eines optischen Bauteiles, stand die Entwicklung einer Darstellungsformel im Vordergrund, die es erlaubt, das elektromagnetische Feld auch außerhalb dieses eigentlichen Rechengebietes auszuwerten. Im Einzelnen wurden folgende Aspekte behandelt:

Lichtstreuprobleme werden mathematisch durch die Maxwell'schen Gleichungen auf dem gesamten Raum beschrieben. Die Einschränkung auf ein endliches Rechengebiet erfordert mathematisch die Formulierung geeigneter Randbedingungen für das Rechengebiet. Dabei ist es entscheidend, ein mathematisches Kriterium für die Unterscheidung von ein- und auslaufenden Wellen bereitzustellen. In dieser Arbeit wurde dies konsequent mit Hilfe der sogenannten Polbedingung bewerkstelligt. Dies knüpft an bisherige Arbeiten zur skalaren Helmholtzgleichung an. Auf diese Weise wurde eine klare Problemstellung für komplizierte Streuprobleme gegeben, deren mathematische Lösungstheorie nach wie vor unvollständig ist.

Die Perfectly-Matched-Layer Methode (PML) ist sehr weit verbreitet, um ein Streuproblem numerisch auf ein endliches Rechengebiet zu beschränken. Es wurde in dieser Arbeit der tiefe Zusammenhang zwischen der Polbedingung als theoretisches Konzept und der PML Methode erhellt. Auf Grundlage dessen konnte eine integrale Darstellungsformel der Streufeldlösung im Außenraum motiviert werden, die es erlaubte, eine adaptive PML Methode zu entwickeln. Die Adaptivität ist wichtig für einen effizienten Einsatz der PML Methode in relevanten Ingenieursproblemen, da kleine Änderungen der physikalischen Umgebungsparameter große Auswirkungen auf die numerischen Steuerungsparameter nach sich ziehen können. Es konnte gezeigt werden, dass mit der adaptiven PML Methode kritische Probleme akkurat numerisch gelöst werden können, bei denen bisherige Implementierungen der PML Me-

thode zu großen Fehlern führten.

Ein weiterer wichtiger Aspekt dieser Arbeit war die Bereitstellung einer Außenraumlösungsformel auf Grundlage der berechneten Innenraumdaten und den zusätzlichen PML Freiheitsgraden. Dies stellt einen großen technischen Fortschritt dar, weil in einem Streuexperiment häufig die Fernfelddaten entscheidend sind. Bisherige Ansätze zur Berechnung der Fernfelddaten beschränkten sich auf einfache Geometrien, wie etwa den homogenen Raum oder geschichtete Außenräume. Für komplizierter strukturierte Außenräume musste man sich bislang mit approximativen Resultaten zufrieden geben, die man nur durch Vergrößerung des Rechengebietes kostspielig verbessern konnte.

Abschließend wurde gezeigt, wie die PML Methode erweitert werden kann, damit auch mehrfach strukturierte Außenräume behandelt werden können. Der Begriff "mehrfach strukturierter Außenraum" wurde in dieser Arbeit geprägt und soll zum Ausdruck bringen, dass der Außenraum mehrere halb–unendliche Strukturen besitzt, die es unter anderem verhindern, analytische Lösungen der Maxwell'schen Gleichungen zu Lichtquellen im Außenraum zu finden. In diesem Sinne liegt für solche Geometrien auch keine numerisch brauchbare Beschreibung des einfallenden Lichts vor, was aber bislang Voraussetzung für die mathematische Beschreibung eines Streuproblems war. Entsprechend wurde die Streuproblemformulierung auf den Fall mehrfach strukturierter Außenräume erweitert. Dabei wurde an klassische Arbeiten von Sommerfeld und Wiener–Hopf angeknüpft, die allerdings nur idealisierte Strukturen behandeln konnten, wie zum Beispiel einen halbunendlichen, infinitesimal dünnen, lichtundurchlässigen Schirm. Es wurde des Weiteren gezeigt, wie auch für mehrfach strukturierte Außenräume eine Außenraum- und Fernfeldauswertung erfolgen kann.

Bibliography

[1] M. Abramowitz and I. A. Stegun. *Pocketbook of mathematical functions*. Verlag Harri Deutsch, 1984.

[2] J. Aguilar and J. M. Combes. A class of analytic perturbations for one-body Schrödinger Hamiltonians. *Commun. Math. Phys.*, 22:269–279, 1971.

[3] M. Ainsworth and J. Coyle. Hierarchic finite element bases on unstructured tetrahedral meshes. *Int. J. Numer. Methods Eng.*, 2003.

[4] X. Antoine, A. Arnold, C. Besse, M. Ehrhardt, and A. Schädle. A review of transparent and artificial boundary conditions techniques for linear and nonlinear Schrödinger equations. *Commun. Comput. Phys.*, 4:729–796, 2008.

[5] X. Antoine, M. Darbas, and Y. Y. Lu. An improved surface radiation condition for high-frequency acoustics scattering problems. *Comput. Methods Appl. Mech. Eng.*, 195:4060–4074, 2006.

[6] T. Arens, S. N. Chandler-Wilde, and A. Meier. Integral equation methods for scattering by one-dimensional rough surfaces. In A. Bermúdez, D. Gómez, C. Hazard, P. Joly, and J. E. Roberts, editors, *Proceedings of the 5th International Conference on Mathematical and Numerical Aspects of Wave Propagation, Santiago de Compostela, Spain*, pages 3–13, 2000.

[7] T. Arens and T. Hohage. On radiation conditions for rough surface scattering problems. *IMA J. Appl. Math.*, 70:839–847, 2005.

[8] D. N. Arnold, R.S. Falk, and R. Winther. Multigrid in H(div) and H(curl). *Numer. Math.*, 85:197–217, 2000.

[9] K. A. Awada, D. R. Jackson, J. T. Williams, and D. R. Wilton. Computational aspects of finite element modeling in EEG source localization. *IEEE Trans. Biomed. Eng.*, 44:736–752, 1997.

[10] G. Bao, Z. Chen, and H. Wu. An adaptive finite element method for diffraction gratings. *J. Opt. Soc. Am. A*, 22:1106–1114, 2005.

[11] A. Bayliss, M. Gunzburger, and E. Turkel. Boundary conditions for the numerical solution of elliptic equations in exterior regions. *SIAM J. Appl. Math.*, 42:430–451, 1982.

[12] R. Beck. Algebraic multigrid by component splitting for edge elements on simplicial triangulations. Preprint SC 99-40, Zuse Institute Berlin, 1999.

[13] R. Beck, P. Deuflhard, R. Hiptmair, R. Hoppe, and B. Wohlmuth. Adaptive multilevel methods for edge element discretizations of Maxwell's equations. *Surv. Math. Ind.*, 8:271–312, 1998.

[14] J. J. Benedetto. *Harmonic analysis and applications*. CRC Press, 1997.

[15] J.-P. Bérenger. A perfectly matched layer for the absorption of electromagnetic waves. *J. Comput. Phys.*, 114(2):185–200, 1994.

[16] A. Bermúdez, L. Hervella-Nieto, A. Prieto, and R. Rodríguez. An optimal perfectly matched layer with unbounded absorbing function for time-harmonic acoustic scattering problems. *J. Comput. Phys.*, 223(2):469–488, 2007.

[17] M. Bollhöfer, M. J. Grote, and O. Schenk. Algebraic multilevel preconditioner for the Helmholtz equation in heterogeneous media. Preprint 2008-3, Department Mathematics, Universität Basel, 2008.

[18] M. Born and E. Wolf. *Principle of optics*. Pergamon Press, 1993 (1959).

[19] C. Bourlier, Gildas Kubické, and Nicolas Déchamps. A fast method to compute scattering by a buried object under a randomly rough surface: PILE combined to FB-SA. *J. Opt. Soc. Am. A*, 25(4):891–902, 2008.

[20] S. Burger, R. Köhle, L. Zschiedrich, W. Gao, F. Schmidt, R. März, and C. Nölscher. Benchmark for FEM, waveguide and FDTD algorithms for rigorous mask simulation. In J.T. Weed and P. M. Martin, editors, *25th annual BACUS Symposium on photomask technology*, volume 5992, pages 378–389. Proc. SPIE, 2005.

[21] W. Cecot, L. Demkowicz, and W. Rachowicz. Three dimensional infinite element for Maxwell's equations. *Int. J. Numer. Methods Eng.*, 57:899–921, 2003.

[22] S. N. Chandler-Wilde. The impedance boundary value problem for the Helmholtz equation in a half–plane. *Math. Methods Appl. Sci.*, 20:813–840, 1997.

[23] S. N. Chandler-Wilde and P. Monk. Existence, uniqueness and variational methods for scattering by unbounded rough surfaces. *SIAM J. Math. Anal.*, 37:598–618, 2005.

[24] S. N. Chandler-Wilde, P. Monk, and M. Thomas. The mathematics of scattering by unbounded, rough, inhomogeneous layers. *J. Comput. Appl. Math.*, 204:549–559, 2007.

[25] Z. Chen and X. Liu. An adaptive perfectly matched layer technique for time-harmonic scattering problems. *Numer. Math.*, 103:667–689, 2006.

[26] Z. Chen and H. Wu. An adaptive finite element method with perfectly matched Absorbing layers for the wave scattering by periodic structures. *SIAM J. Numer. Anal.*, 43:799–826, 2003.

[27] W. C. Chew. *Waves and fields in inhomogeneous media*. IEEE Press, 1995.

[28] W. C. Chew and W. H. Weedon. 3D perfectly matched medium from modified Maxwells equations with stretched coordinates. *MOTL*, 7:599–604, 1994.

[29] P. C. Clemmow. *The plane wave spectrum representation of electromagnetic fields*. Pergamon Pres, 1966.

[30] F. Collino and P. Monk. Optimizing the perfectly matched layer. *Comput. Methods Appl. Mech. Eng.*, 164:157–171, 1998.

[31] F. Collino and P. Monk. The perfectly matched layer in curvilinear coordinates. *SIAM J. Sci. Comput.*, 19:2061–2090, 1998.

[32] D. Colton and R. Kreß. *Inverse acoustic and electromagnetic scattering theory*. Springer-Verlag, 1992.

[33] N. Déchamps, N. De Beaucoudrey, C. Bourlier, and S. Toutain. A fast numerical method for electromagnetic scattering by rough layered interfaces: Propagation-inside-layer expansion (PILE) method. *J. Opt. Soc. Am. A*, 23(2):359–369, 2006.

[34] N. Déchamps and C. Bourlier. Electromagnetic scattering from a rough layer: Propagation-inside-layer expansion method combined to the forward-backward novel-spectral acceleration. *IEEE Trans. Antennas Propag.*, 50(12):3576–3586, 2007.

[35] L. Demkowicz and F. Ihlenburg. Analysis of a coupled finite-infinite element method for exterior Helmholtz problems. *Numer. Math.*, 88:43–73, 2001.

[36] L. Demkowicz and M. Pal. An infinite element for Maxwell's equations. *Comput. Methods Appl. Mech. Eng.*, 164:77–94, 1998.

[37] L. Demkowicz and L. Vardapetyan. hp-adaptive finite elements in electromagnetics. *Comput. Methods Appl. Mech. Eng.*, 169:331–344, 1999.

[38] P. Deuflhard and A. Hohmann. *Numerical Analysis in Modern Scientific Computing. An Introduction.* Spinger, 2003.

[39] D. C. Dobson and J. E. Pasciak. Analysis of an algorithm for computing electromagnetic Bloch modes using Nédélec spaces. *Comp. Meth. App. Math.*, 1:138–153, 2001.

[40] M. Ehrhardt, H. Han, and C. Zheng. Numerical simulation of waves in periodic structures. *Commun. Comput. Phys.*, 5:849–872, 2008.

[41] M. Ehrhardt and C. Zheng. Exact artificial boundary conditions for problems with periodic structures. *J. Comput. Phys.*, 227:6877–6894, 2008.

[42] J. Elschner, R. Hinder, and G. Schmidt. Finite element solution of conical diffraction problems. *AICM*, 16:139–156, 2002.

[43] J. Elschner and G. Schmidt. Inverse scattering for periodic structures: Stability of polygonal interfaces. *Inverse Problems*, 17:1817–1829, 2001.

[44] J. Elschner and M. Yamamoto. An inverse problem in periodic diffractive optics: Reconstruction of Lipschitz grating profiles. *Applicable Analysis*, 81:1307–1328, 2002.

[45] B. Engquist and A. Majda. Absorbing boundary conditions for the numerical simulation of waves. *Math. Comp.*, 31:629–651, 1977.

[46] F. L. Teixeira and W. C. Chew. Unified analysis of perfectly matched layers using differential forms. *MOTL*, 20:124–126, 1999.

[47] J. W. Goodman. *Introduction to Fourier optics*. McGraw-Hill, 1968.

[48] M. J. Grote and J. B. Keller. On nonreflecting boundary conditions. *J. Comput. Phys.*, 122:231–243, 1995.

[49] M. J. Grote and C. Kirsch. Far–field evaluation via nonreflecting boundary conditions. In T. Y. Hou and E. Tadmor, editors, *Hyperbolic Problems: Theory, Numerics, Applications (Proc. 9th Internat. Conf. on Hyperbolic Problems, HYP 2002)*, pages 195–204. Springer, 2003.

[50] M. Hammer. Hybrid analytical/numerical coupled-mode modeling of guided wave devices. *J. Lightwave Technol.*, 25:2287–2298, 2007.

[51] B. Heubeck, C. Pflaum, and G. Steinle. New finite elements for large-scale simulation of optical waves. Technical Report 07-8, Friedrich–Alexander–Universität Erlangen–Nürnberg, 2007.

[52] R. Hiptmair. Multigrid method for Maxwell's equations. *SIAM J. Numer. Anal.*, 36:204–225, 1999.

[53] R. Hiptmair and P. D. Ledger. Computation of resonant modes for axisymmetric cavities using hp-version finite elements. Technical report, ETH, Eidgenössische Technische Hochschule Zürich, 2003.

[54] P. D. Hislop and I. Sigal. *Introduction to spectral theory: With applications to Schrödinger operators*. Springer, 1996.

[55] T. Hohage and L. Nannen. Hardy space infinite elements for scattering and resonance problems. *SIAM J. Numer. Anal.*, at press.

[56] T. Hohage, F. Schmidt, and L. Zschiedrich. Solving time-harmonic scattering problems based on the pole condition. I: Theory. *SIAM J. Math. Anal.*, 35:183–210, 2003.

[57] T. Hohage, F. Schmidt, and L. Zschiedrich. Solving time-harmonic scattering problems based on the pole condition. II: Convergence of the PML method. *SIAM J. Math. Anal.*, 35(3):547–560, 2003.

[58] J. P. Hugonin and P. Lalanne. Perfectly matched layers as nonlinear coordinate transforms: A generalized formalization. *J. Opt. Soc. Am. A*, 22(9):1844–1849, 2005.

[59] F. Ihlenburg. *Finite element analysis of acoustic scattering*. Springer, 1998.

[60] J. D. Jackson. *Classical electrodynamics, 3rd edition*. John Wiley & Sons, 1998.

[61] K. Jänich. *Vector analysis*. Springer, 2001.

[62] O. T. A. Janssen, S. van Haver, A. J. E. M. Janssen, J. J. M. Braat, H. P. Urbach, and S. F. Pereira. Extended Nijboer–Zernike based mask imaging: Efficient coupling of electromagnetic field solvers and the ENZ imaging algorithm. In H. J. Levinson and M. V. Dusa, editors, *Optical Microlithography XXI*, volume 6924. SPIE Proc., 2008.

[63] J. Jin. *The finite element method in electromagnetics*. John Wiley and Sons, Inc, 1993.

[64] P. Joly, J.-R. Li, and S. Fliss. Exact boundary conditions for periodic waveguides containing a local perturbation. *Commun. Comput. Phys.*, 1:945–973, 2006.

[65] J. B. Keller and D. Givoli. Exact non–reflecting boundary conditions. *J. Comput. Phys.*, 82:172–192, 1989.

[66] B. Kettner. Ein Algorithmus zur prismatoidalen Diskretisierung von unbeschränkten Außenräumen in 2D und 3D unter Einhaltung von Nebenbedingungen. Diploma thesis, Freie Universität Berlin, 2006.

[67] M. Lassas, J. Liukkonen, and E. Somersalo. Complex Riemannian metric and absorbing boundary condition. *J. Math. Pures Appl.*, 80(7):739–768, 2001.

[68] M. Lassas and E. Somersalo. On the existence and convergence of the solution of PML equations. *Computing*, 60(3):229–241, 1998.

[69] M. Lassas and E. Somersalo. Analysis of the PML equations in general convex geometry. In *Proc. Roy. Soc. Edinburgh Sect. A 131*, volume 131, pages 1183–1207, 2001.

[70] R. Leis. *Initial Boundary Value Problems in Mathematical Physics*. Wiley, 1986.

[71] M. Lohmeyer. Mode expansion modeling of rectangular integrated optical microresonators. *Opt. Quant. Electron.*, 34:541–557, 2002.

[72] L. Mandel and E. Wolf. *Optical coherence and quantum optics*. Cambridge University Press, 1995.

[73] O. J. F. Martin and N. B. Piller. Electromagnetic scattering in polarizable backgrounds. *Physical Review E*, 58(3):3909–3915, 1998.

[74] V. P. Maslov and M. V. Fedoriuk. *Semi-classical approximation in quantum mechanics*. Reidel, Dordrecht, 1981.

[75] J. C. Maxwell. *A treatise on electricity and magnetism*. Clarendon Press, Oxford, 1873.

[76] A. Meier, T. Arens, S. N. Chandler-Wilde, and A. Kirsch. A Nyström method for a class of integral equations on the real line with applications to scattering by diffraction gratings and rough surfaces. *Journal of Integral Equations and Applications*, 12:281–321, 2000.

[77] E. Meister, F.-O. Speck, and F. S. Teixeira. Wiener-Hopf-Hankel operators for some wedge diffraction problems with mixed boundary conditions. *J. Integral Equations Appl.*, 4:229–255, 1992.

[78] C. Michler, L. Demkowicz, J. Kurtz, and D. Pardo. Improving the performance of perfectly matched layers by means of hp-adaptivity. *Numerical Methods for Partial Differential Equations*, 23:832–858, 2007.

[79] P. Monk. *Finite element methods for Maxwell's equations*. Oxford University Press, 2003.

[80] P. Monk and A. K. Parrot. Phase–accuracy comparisons and improved far–field estimates for 3D–edge elements on tetrahedral meshes. *J. Comput. Phys.*, 170:614–41, 2001.

[81] P. Monk, J. Schöberl, and A. Sinwel. Hybridizing Raviart-Thomas elements for the Helmholtz equation. Preprint 2008-22, RICAM, 2008.

[82] P. Monk and E. Süli. The adaptive computation of far–field patterns by a posteriori error estimation of linear functionals. *SIAM J. Numer. Anal.*, 36:614–41, 1998.

[83] L. Nannen. *Hardy-Raum Methoden zur numerischen Lösung von Streu- und Resonanzproblemen auf unbeschränkten Gebieten*. Dissertation thesis, Universität Göttingen, 2008.

[84] J.-C Nédélec. *Acoustic and electromagnetic equations: Integral Representations for Harmonic Problems*. Springer, 2001.

[85] B. Noble. *Methods based on the Wiener-Hopf technique for the solution of partial differential equations*. Pergamon Press, 1958.

[86] J. V. Noble. Gauss-legendre principal value integration. *Computing in Science and Engineering*, 2:92–95, 2000.

[87] A. F. Oskooi, L. Zhang, Y. Avniel, and S. G. Johnson. The failure of perfectly matched layers, and towards their redemption by adiabatic absorbers. *Optics Express*, 16(15):11376–11392, 2008.

[88] M. Paulus, P. Gay-Balmaz, and O. J. F. Martin. Accurate and efficient computation of the green's tensor for stratified media. *Physical Review E*, 62(4):5797–5807, 2000.

[89] M. Paulus and O. J. F. Martin. Green's tensor technique for scattering in two-dimensional stratified media. *Physical Review E*, 63(6):066615.1–066615.8, 2001.

[90] T. Pollok. Separabilität von Helmholtz- und Maxwellgleichungen über unbeschränkten heterogenen Gebieten. Diploma thesis, Freie Universität Berlin, 2007.

[91] A. Quarteroni. *Domain decomposition methods for partial differential equations*. Clarendon Press, Oxford, 1999.

[92] S. Reitzinger and J. Schöberl. Algebraic multigrid for edge elements. *Numerical Linear Algebra with Applications*, 9:223–238, 2002.

[93] M. Renardy and R. Rogers. *An introduction to partial differential equations*. Springer, 1992.

[94] W. Rudin. *Functional analysis*. Tata McGraw-Hill, 1974.

[95] W. Rudin. *Real and complex analysis*. McGraw-Hill international editions, 1987.

[96] D. Ruprecht, A. Schädle, F. Schmidt, and L. Zschiedrich. Transparent boundary conditions for time-dependent problems. *SIAM J. Sci. Comput*, 30:2358–2385, 2008.

[97] O. Schenk and K. Gärtner. Solving unsymmetric sparse systems of linear equations with PARDISO. *Future Gener. Comput. Syst.*, 20(3):475–487, 2004.

[98] F. Schmidt. *Solution of interior-exterior Helmholtz-type problems based on the pole condition concept: Theory and algorithms*. Habilitation thesis, Freie Universität Berlin, 2002.

[99] F. Schmidt, T. Friese, L. Zschiedrich, and P. Deuflhard. Adaptive multigrid methods for the vectorial Maxwell eigenvalue problem for optical waveguide design. In W. Jäger, editor, *Mathematics - Key Technology for the Future: Joint Problems between Universities and Industry*, pages 270–292. Springer, 2003.

[100] F. Schmidt, T. Hohage, R. Klose, A. Schädle, and L. Zschiedrich. A numerical method for Helmholtz-type scattering problems with inhomogeneous exterior domain. *J. Comput. Appl. Math.*, 218:61–69, 2008.

[101] F. Shen and A. Wang. Fast-Fourier-transform based numerical integration method for the Rayleigh-Sommerfeld diffraction formula. *Applied Optics*, 45(6):1102–1110, 2005.

[102] W. Singer, M. Totzeck, and H. Gross. *Handbook of optical systems, volume 2: Physical image formation*. Wiley-VCH, Berlin, 2005.

[103] S. Soussi. Wave propagation in periodic media. http://num.math.uni-goettingen.de/~soussi/simulations.php.

[104] F. L. Teixeira. Differential form approach to the analysis of electromagnetic cloaking and masking. *MOTL*, 49(8):2051–2053, 2007.

[105] F. L. Teixeira and W. C. Chew. Systematic derivation of anisotropic PML absorbing media in cylindrical and spherical coordinates. *IEEE Microwave Guided Wave Letters*, 7(11):371–373, 1997.

[106] F. L. Teixeira and W. C. Chew. Analytical derivation of a conformal perfectly matched absorber for electromagnetic waves. *MOTL*, 17(4):231–236, 1998.

[107] E. C. Titchmarsh. *Introduction to the theory of Fourier integrals*. Clarendon Press, Oxford, 1937.

[108] A. Toselli. Overlapping Schwarz methods for Maxwell's equations in three dimensions. *Numer. Math.*, 86(4):733–752, 2000.

[109] J. A. C. Veerman, J. J. Rusch, and H. P. Urbach. Calculation of the Rayleigh-Sommerfeld diffraction integral by exact integration of the fast oscillating factor. *J. Opt. Soc. Am. A*, 22(4):636–646, 2005.

[110] H. Weyl. Ausbreitung elektromagnetischer Wellen über einem ebenen Leiter. *Ann. d Physik*, 365(21):481–500, 1919.

[111] S. Wilcox, L. C. Botten, R. C. McPhedran, C. G. Poulton, and C. M. de Sterke. Modeling of defect modes in photonic crystals using the fictitious source superposition method. *Physical Review E*, 71, 2005.

[112] E. Wolf. *Theory of coherence and polarization of light*. Cambridge University Press, 2007.

[113] C. Wolters. *Influence of Tissue Conductivity Inhomogeneity and Anisotropy on EEG/MEG based Source Localization in the Human Brain*. Dissertation thesis, Universität Leipzig, 2003.

[114] A. Kwok-Kit Wong. *Resolution enhancement techniques in optical lithography*. SPIE, 2001.

[115] P. Young. Singular fourier transforms. http://www.apyoung.com/-˜peter/250/sing_ft.pdf, 2007.

[116] S. Zaglmayr. *High order finite elements for electromagnetic field computation*. Dissertation thesis, Johannes Kepler Universität Linz, 2006.

[117] L. Zschiedrich, S. Burger, B. Kettner, and F. Schmidt. Advanced finite element method for nano-resonators. In M. Osinski et. al., editor, *Physics and Simulation of Optoelectronic Devices XIV*, volume 6115, pages 164–174. Proc. SPIE, 2006.

[118] L. Zschiedrich, S. Burger, R. Klose, A. Schädle, and F. Schmidt. JCMmode: An adaptive finite element solver for the computation of leaky modes. In Y. Sidorin and C. A. Wächter, editors, *Integrated Optics: Devices, Materials, and Technologies IX*, volume 5728, pages 192–202. Proc. SPIE, 2005.

[119] L. Zschiedrich, S. Burger, J. Pomplun, and F. Schmidt. Goal oriented adaptive finite element method for the precise simulation of optical components. In Y. Sidorin and C. A. Wächter, editors, *Integrated Optics: Devices, Materials, and Technologies XI*, volume 6475, pages 64750H.1–64750H.9. SPIE Proc., 2007.

[120] L. Zschiedrich, S. Burger, A. Schädle, and F. Schmidt. Domain decomposition method for electromagnetic scattering problems: Application to EUV lithography. In *Numerical Simulation of Optoelectronic Devices*, pages 55–56, www.nusod.org/nusod05/WB5.pdf. Numerical Simulation of Optoelectronic Devices, 2005. NUSOD, 2005.

[121] L. Zschiedrich, R. Klose, A. Schädle, and F. Schmidt. A new finite element realization of the perfectly matched layer method for Helmholtz scattering problems on polygonal domains in 2D. *J. Comput. Appl. Math.*, 188:12–32, 2006.

[122] L. Zschiedrich, R. März, S. Burger, and F. Schmidt. Efficient 3D Finite Element Simulation of Fiber-Chip Coupling. In *Integrated Photonics Research and Applications/Nanophotonics, Technical Digest*. Optical Society of America, 2006.

[123] L. Zschiedrich and F. Schmidt. Evaluation of Rayleigh-Sommerfeld diffraction formula for PML solutions. In N. Biggs, editor, *The 8th International Conference on Mathematical and Numerical Aspects of Waves*, page 253. Univ. of Reading, 2007.

[124] L. Zschiedrich and F. Schmidt. Finite Element Simulation of Light Propagation in Non-Periodic Mask Patterns. In *Photomask and Next-Generation Lithography Mask Technology XV*, volume 7028, page 702831. Proc. SPIE, 2008.